

Modeling of Fluid Flow and Heat Transfer for Optimization of Pin-Fin Heat Sinks

by

Waqar Ahmed Khan

A thesis

presented to the University of Waterloo

in fulfillment of the

thesis requirement for the degree of

Doctor of Philosophy

in

Mechanical Engineering

Waterloo, Ontario, Canada, 2004

©Waqar Ahmed Khan, 2004

I hereby declare that I am the sole author of this thesis. This is a true copy of the thesis, including any required final versions, as accepted by my examiners.

I understand that my thesis may be made electronically available to the public.

Waqar Ahmed Khan

Abstract

In this study, an entropy generation minimization procedure is employed to optimize the overall performance (thermal and hydrodynamic) of isolated fin geometries and pin-fin heat sinks. This allows the combined effects of thermal resistance and pressure drop to be assessed simultaneously as the heat sink interacts with the surrounding flow field. New general expressions for the entropy generation rate are developed using mass, energy, and entropy balances over an appropriate control volume. The formulation for the dimensionless entropy generation rate is obtained in terms of fin geometry, longitudinal and transverse pitches, pin-fin aspect ratio, thermal conductivity, arrangement of pin-fins, Reynolds and Prandtl numbers. It is shown that the entropy generation rate depends on two main performance parameters, i.e., thermal resistance and the pressure drop, which in turn depend on the average heat transfer and friction coefficients. These coefficients can be taken from fluid flow and heat transfer models. An extensive literature survey reveals that no comprehensive analytical model for any one of them exists that can be used for a wide range of Reynolds number, Prandtl number, longitudinal and transverse pitches, and thermal conductivity.

This study is one of the first attempts to develop analytical models for the fluid flow and heat transfer from single pins (circular and elliptical) with and without blockage as well as pin-fin arrays (in-line and staggered). These models can be used for the entire laminar flow range, longitudinal and transverse pitches, any material (from plastic com-

posites to copper), and any fluid having Prandtl numbers ≥ 0.71 . In developing these models, it is assumed that the flow is steady, laminar, and fully developed. Furthermore, the heat sink is fully shrouded and the thermophysical properties are taken to be temperature independent. Using an energy balance over the same control volume, the average heat transfer coefficient for the heat sink is also developed, which is a function of the heat sink material, fluid properties, fin geometry, pin-fin arrangement, and longitudinal and transverse pitches. The hydrodynamic and thermal analyses of both in-line and staggered pin-fin heat sinks are performed using parametric variation of each design variable including pin diameter, pin height, approach velocity, number of pin-fins, and thermal conductivity of the material.

The present analytical results for single pins (circular and elliptical) and pin-fin-arrays are in good agreement with the existing experimental/numerical data obtained by other investigators. It is shown that the present models of heat transfer and pressure drop can be applied for a wide range of Reynolds and Prandtl numbers, longitudinal and transverse pitches, aspect ratios, and thermal conductivity. Furthermore, selected numerical simulations for a single circular cylinder and in-line pin-fin heat sink are also carried out to validate the present analytical models. Results of present numerical simulations are also found to be in good agreement.

Contents

Abstract	iii
1 Introduction	1
1.1 Motivation	6
1.2 Problem Definition	7
1.2.1 Geometry	7
1.2.2 Flow Description	8
1.2.3 Assumptions	12
1.2.4 Governing Equations	14
1.2.5 Fluid Friction	15
1.2.6 Heat Transfer	15
1.2.7 Entropy Generation Minimization (EGM)	16
1.3 Objectives	17
1.4 Organization of the Thesis	19
2 Literature Review	22
2.1 Fluid Flow	24

2.1.1	Analytical Studies	24
2.1.2	Experimental/ Numerical Studies	24
2.2	Heat Transfer	31
2.2.1	Analytical Studies	31
2.2.2	Experimental and Numerical Studies	33
2.3	Optimization	48
2.4	Comparison of Existing Models and Data	50
2.5	Summary	54
3	Fluid Flow Modeling	55
3.1	Introduction	55
3.2	Circular Pin in an Infinite Flow	56
3.2.1	Analysis	56
3.2.2	Boundary-Layer Parameters	59
3.2.3	Fluid Friction	62
3.3	Single Elliptical Pin in an Infinite Flow	66
3.3.1	Analysis	66
3.3.2	Boundary-Layer Parameters	67
3.3.3	Fluid Friction	68
3.4	Circular Pin Between Two Parallel Planes	75
3.4.1	Analysis	75
3.4.2	Boundary-Layer Parameters	76
3.4.3	Fluid Friction	76

3.5	Pin-Fin Arrays	81
3.5.1	Analysis	81
3.5.2	Fluid Friction	86
3.6	Model Verification	93
3.6.1	Single Circular Pin in an Infinite Flow	93
3.6.2	Single Elliptical Pin in an Infinite Flow	93
3.6.3	Single Circular Pin Between Two Parallel Planes	98
3.7	Summary and Concluding Remarks	99
4	Heat Transfer Modeling	104
4.1	Introduction	104
4.2	Circular Pin-Fin in an Infinite Flow	107
4.2.1	Isothermal Boundary Condition	107
4.2.2	Isoflux Boundary Condition	110
4.3	Elliptical Pin-Fin in an Infinite Medium	115
4.3.1	Isothermal Boundary Condition	115
4.3.2	Isoflux Boundary Condition	118
4.4	Circular Pin Confined Between Two Parallel Planes	122
4.4.1	Isothermal Boundary Condition	122
4.4.2	Isoflux Boundary Condition	123
4.5	Pin-Fin Heat Sinks	124
4.5.1	Pin-Fin Arrays	126
4.5.2	Base Plate	135

4.6	Model Verification	135
4.6.1	Single Circular Pin in an Infinite Flow	135
4.6.2	Single Elliptical Pin in an Infinite Flow	135
4.6.3	Circular Pin Between Parallel Planes	143
4.6.4	Pin-Fin Arrays	148
4.7	Summary	154
5	Numerical Validation	155
5.1	Introduction	155
5.2	Single Circular Cylinder in an Infinite Flow	155
5.2.1	Problem Description	155
5.2.2	Specifying Problem Parameters	159
5.2.3	Building the Model	159
5.2.4	Generating the Mesh	160
5.2.5	Calculating the Solution	161
5.2.6	Examining the Results	163
5.3	Pin-Fin Heat Sinks	168
5.3.1	Problem Description	168
5.3.2	Specifying Problem Parameters	169
5.3.3	Building the Model	169
5.3.4	Generating the Mesh	170

6	Heat Sink Analysis	174
6.1	Introduction	174
6.2	Heat Sink Model	176
6.2.1	Overall Heat Transfer Coefficient for Heat Sink	179
6.2.2	Temperature Distribution	180
6.3	Performance of Heat Sinks	183
6.3.1	Heat Sink Resistance	183
6.3.2	Total Heat Sink Pressure Drop	192
6.4	Case Studies and Discussion	195
6.5	Summary	205
7	Optimization	206
7.1	Introduction	206
7.2	Optimization	207
7.2.1	Selection of Independent Variables	208
7.2.2	Performance Criterion	208
7.2.3	Model Development	210
7.2.4	Problem Formulation	216
7.2.5	Optimization Technique	218
7.2.6	Optimal Solution and Sensitivity	219
7.3	Results and Discussion	220
7.3.1	Optimization	220
7.3.2	Sensitivity Analysis	251
7.4	Summary	251

8	Summary and Conclusions	253
	References	258
A	Equations of Motion	271
A.1	Plane Polar Coordinates	271
A.2	Curvilinear Coordinates	274
A.3	Elliptical Coordinates	278
B	Boundary Conditions	279
B.1	Hydrodynamic Boundary Conditions	279
B.2	Thermal Boundary Conditions	280
B.3	Boundary Conditions for Control Volume	281
C	Velocity and Temperature Distributions	282
C.1	Velocity Distribution	282
C.2	Temperature Distribution	283
D	Potential Flow Velocity	284
D.1	Circular Pin in Infinite Flow	284
D.2	Elliptical Pin in Infinite Flow	285
D.3	Circular Pin Between Two Parallel Planes	286
D.4	Cylindrical Pin-Fins in In-Line Arrangement	288
D.5	Cylindrical Pin-Fins in Staggered Arrangement	290

E	Fluid Friction and Heat Transfer	292
E.1	Fluid Friction	292
E.2	Heat Transfer	293
E.2.1	Isothermal Boundary Condition	293
E.2.2	Isoflux Boundary Condition	294
F	Entropy Generation Rate Model	295
F.1	Model for Fin Geometry	295
F.2	Model for Pin-Fin Heat Sinks	299
F.3	Optimization Code	303
G	Boundary-Layer Parameters	304

List of Tables

2.1	Summary of Numerical Results of Drag Coefficients for Laminar Flow Over a Circular Cylinder	26
2.2	Recommended Relationships for In-Line Tube Banks	29
2.3	Recommended Relationships for Staggered Tube Banks	30
2.4	Summary of Previous Experimental/Numerical Correlations and Models for Air	33
2.5	Summary of Previous Experimental Correlations for Air ($Pr = 0.71$)	34
2.6	Constants for Grimison Correlation (Eq. 2.11)	40
2.7	Correction Factor for Grimison Correlation when $N_L \leq 10$	41
2.8	Constants for Žukauskas Correlation (Eq. 2.18)	42
2.9	Correction Factor F for Žukauskas Correlation when $N_L \leq 16$	43
2.10	Summary of Previous Experimental/Numerical Correlations for Pin-Fin Heat Sinks	45
2.11	Constants for Hamilton et al. (2002) Correlation (Eq. 2.19)	46
3.1	Coefficients in Eqs. (3.19) and (3.20)	61
3.2	Angle of Separation for Different Axis Ratios of Elliptic Pin	70

5.1	Results of Average Heat Transfer Coefficients for Circular Cylinder	166
5.2	Dimensions Used to Determine Performance of Heat Sinks	170
5.3	Results of Average Heat Transfer Coefficients for In-Line Pin-Fin Heat Sink	172
6.1	Dimensions Used to Determine Performance of Heat Sinks	195
6.2	Performance Parameters for In-Line and Staggered Heat Sinks	196
7.1	Parameters for Different Geometries of Pin-Fins	213
7.2	Quantities Used to Determine Performance of Pin-Fin Geometry	226
7.3	Dimensions Used to Determine Performance of Heat Sinks	233
7.4	Results For Optimization of Three Parameters for In-Line Arrangement .	248
7.5	Results For Optimization of Three Parameters for Staggered Arrangement	249
7.6	Results For Optimization of Four Parameters	250
G.1	Boundary-Layer Parameters For a Circular Pin	305
G.2	Boundary-Layer Parameters For an Elliptical Pin With $\epsilon = 1/2$	307
G.3	Boundary-Layer Parameters For an Elliptic Pin with $\epsilon = 1/3$	309
G.4	Boundary-Layer Parameters For an Elliptical Pin With $\epsilon = 1/4$	311
G.5	Boundary-Layer Parameters For a Circular Pin Between Parallel Planes for $b=0.8$	313
G.6	Boundary-Layer Parameters For a Circular Pin Between Parallel Planes for $b=0.5$	315
G.7	Boundary-Layer Parameters For a Circular Pin Between Parallel Planes for $b=0.2$	317

List of Figures

1.1	Low Density / High Density Pin-Fin Heat Sinks	2
1.2	In-Line Pin-Fin Heat Sink	3
1.3	Schematics of In-Line Pin-Fin Heat Sinks	4
1.4	Schematics of Staggered Pin-Fin Heat Sinks	5
1.5	Flow Past a Circular Cylinder: (A) $Re_D = 1.54$; (B) $Re_D = 9.6$; (C) $Re_D = 13.1$; (D) $Re_D = 26$ (Van Dyke, 1982)	9
2.1	Flow Chart Showing Procedure for Literature Review	23
2.2	Comparison of Drag Data for a Single Circular Cylinder	51
2.3	Variation of Average Nusselt Number with Reynolds Number for Isothermal Boundary Condition	52
2.4	Variation of Average Nusselt Number with Reynolds Number for Isoflux Boundary Condition	53
3.1	Flow Chart for Calculating Drag Coefficients	56
3.2	Cylindrical Pin-Fin in Cross Flow	57
3.3	Curvilinear Coordinates for Flow Over a Circular Pin	58
3.4	Friction and Pressure Drag Coefficients for Flow Over a Circular Pin	64

3.5	Ratio of Friction Drag to Pressure Drag for a Single Circular Pin	65
3.6	Curvilinear Coordinates For the Flow Over an Elliptic Pin	67
3.7	Variation of Skin Friction for Elliptical Pins of Different Axis Ratios . . .	69
3.8	Variation of Total Drag Coefficients with the Axis Ratio	71
3.9	Variation of Total Drag with Reynolds Number for Elliptical Pins of Different Axis Ratios	74
3.10	Physical Model and Coordinate System	75
3.11	Effect of Blockage Ratio on the Angle of Separation	77
3.12	Effects of Blockage Ratio on Drag Coefficients for Different Reynolds Numbers	79
3.13	Effects of Reynolds Number on Drag Coefficients for Different Blockage Ratios	80
3.14	In-Line Pin-Fin Heat Sink	82
3.15	Nomenclature for In-Line and Staggered Arrangements	83
3.16	Control Volume for Prediction of Fluid Flow from a Pin-Fin Heat Sink . .	84
3.17	Effects of Transverse Pitch on Skin Friction in In-Line Arrays	88
3.18	Effects of Longitudinal Pitch on Skin Friction in In-Line Arrays	89
3.19	Effects of Transverse Pitch on Skin Friction in Staggered Arrays	90
3.20	Effects of Longitudinal Pitch on Skin Friction in Staggered Arrays	91
3.21	Coefficients of Friction for In-Line and Staggered Arrangements	92
3.22	Distribution of Shear Stress on a Circular Pin in Air	94
3.23	Drag Coefficient as a Function of Re_D for a Circular Pin	95
3.24	Variation of Total Drag Coefficients with the Reynolds Numbers	96

3.25	Comparison of Friction Drag Coefficients of a Finite Plate-Fin	97
3.26	Effect of Blockage Ratio on the Velocity Distribution Outside the Boundary Layer	100
3.27	Distribution of Dimensionless Shear Stress on a Circular Pin for a Given Blockage Ratio	101
3.28	Drag Coefficient as a Function of Re_D for Different Blockage Ratios . . .	102
3.29	Distribution of $C_f\sqrt{Re_D}$ on Pin in Staggered Array	103
4.1	Types of Fins: (a) Longitudinal Fin, (b) Cylindrical Fin, and (c) Radial Fin	105
4.2	Flow Chart for Calculating Average Heat Transfer Coefficient	106
4.3	Local Heat Transfer Coefficients For Various Reynolds Numbers	109
4.4	Average Heat Transfer Coefficients For Air and Water	111
4.5	Local Nusselt Numbers for Different Thermal Boundary Conditions	113
4.6	Average Nusselt Numbers for Different Thermal Boundary Conditions . .	114
4.7	Variation of Average Nusselt Number with Axis Ratio for an Isothermal Elliptic Pin	117
4.8	Comparison of Local Nusselt Numbers for Both Thermal Boundary Con- ditions	120
4.9	Comparison of Average Nusselt Numbers for Both Thermal Boundary Con- ditions	121
4.10	Effect of Blockage Ratio on Heat Transfer and Thermal Boundary Conditions	125
4.11	Effect of Blockage Ratio and Reynolds Number on Average Nusselt Numbers	126
4.12	A) Aligned Pins with Fluid Flow B) Staggered Pins with Fluid Flow .	127
4.13	Comparison of Both Arrangements for 1.25×1.25	128

4.14	Comparison of Both Arrangements for 1.5×1.5	129
4.15	Comparison of Both Arrangements for 2×2	130
4.16	Comparison of Both Arrangements for 3×3	131
4.17	Effect of Pitches on Heat Transfer in In-Line Arrangement	133
4.18	Effect of Transverse Pitch on Heat Transfer in Staggered Arrangement . .	134
4.19	Variation of Average Nusselt Number with Reynolds Number for Isothermal Circular Pin	136
4.20	Variation of Average Nusselt Number with Reynolds Number for Isoflux Circular Pin	137
4.21	Variation of Average Nusselt Number with Reynolds Number for Isothermal Elliptic Pin With $\epsilon = 0.5$	138
4.22	Variation of Average Nusselt Number with Reynolds Number for Isoflux Elliptic Pin With $\epsilon = 0.5$	140
4.23	Variation of Average Nusselt Number with Reynolds Number for Isothermal Elliptic Pin	141
4.24	Variation of Average Nusselt Number with Axis Ratio for an Isothermal Elliptic Pin	142
4.25	Local Nusselt Numbers for Different Thermal Boundary Conditions	144
4.26	Average Nusselt Numbers for Isoflux Boundary Condition for Water	145
4.27	Average Nusselt Numbers for Isoflux Pin	146
4.28	Effect of Blockage Ratio on Average Nusselt Numbers	147
4.29	Average Nusselt Numbers for In-Line Arrangement 1.25×1.25	148
4.30	Average Nusselt Numbers for In-Line Arrangement 1.25×2	149
4.31	Average Nusselt Numbers for In-Line Arrangement 1.5×1.5	150

4.32	Average Nusselt Numbers for Staggered Arrangement 2×1.5	151
4.33	Average Nusselt Numbers for Staggered Arrangement 2×2	152
4.34	Average Nusselt Numbers for Staggered Arrangement 2×3	153
5.1	Flow Chart for Numerical Simulations	157
5.2	Model for Flow Over Circular Cylinder	158
5.3	Mesh on YZ-Plane	161
5.4	Residuals	162
5.5	Velocity Vectors on the Cylinder Side of the Enclosure	163
5.6	Grid Convergence for Circular Cylinder ($Re_D = 400$)	164
5.7	Variation of Average Heat Transfer Coefficients with Reynolds Numbers .	165
5.8	Numerical Model for In-Line Pin-Fin Heat Sink	168
5.9	Velocity Vectors in In-Line Pin-Fin Heat Sink	171
5.10	Comparison of Average Heat Transfer Coefficients for In-Line Pin-Fin Heat Sink	173
6.1	Flow Chart for System Resistance	175
6.2	Control Volume for Pin-Fin Heat Sink	177
6.3	Geometry of Pin-Fin Heat Sink	178
6.4	Control Volumes for Energy Balances	179
6.5	Control Volume for Analysis of Pin-Fin Heat Sinks	181
6.6	Thermal Resistance Network for a Heat Sink	184
6.7	Interface Between Heat Source and Baseplate	186
6.8	Interface Contact Resistance of Aluminum Heat Sink-Ceramic Package . .	188

6.9	Temperature Distribution of Fluid in Heat Sink	198
6.10	Temperature of Air Leaving Heat Sink versus N_T	199
6.11	Temperature of Air Leaving Heat Sink versus H	200
6.12	Performance of PFHS as Function of Number of Fins	201
6.13	Performance of PFHS as Function of Pin Diameter	202
6.14	Performance of PFHS as Function of Approach Velocity	203
6.15	Performance of PFHS as Function of Thermal Conductivity	204
7.1	Cross Sections of Selected Geometries	214
7.2	Shrouded Heat Sink	215
7.3	Dimensionless Entropy Generation Rate vs Approach Velocity	221
7.4	Effect of Axis Ratio on Dimensionless Entropy Generation Rate	222
7.5	Effect of Aspect Ratio on Dimensionless Entropy Generation Rate	223
7.6	Effect of Approach Velocity on Heat Transfer and Friction Irreversibilities	224
7.7	Effect of Perimeter on Dimensionless Entropy Generation Rate	225
7.8	Selected Pin-Fin Heat Sink for Optimization	227
7.9	Effect of Pin Diameter on Dimensionless Entropy Generation Rate	228
7.10	Effect of Pin Height on Dimensionless Entropy Generation Rate	229
7.11	Effect of Approach Velocity on Dimensionless Entropy Generation Rate	230
7.12	Effect of Number of Pins on Dimensionless Entropy Generation Rate	231
7.13	Dimensionless Entropy Generation Rate as Function of Pin Diameter and Approach Velocity	234
7.14	Dimensionless Entropy Generation Rate as Function of Pin Diameter and Number of Pins in Transverse Direction	236

7.15	Dimensionless Entropy Generation Rate as Function of Reynolds Number	237
7.16	Dimensionless Entropy Generation Rate as Function of Aspect Ratio and Reynolds Number	238
7.17	Dimensionless Entropy Generation Rate as Function of Aspect Ratio and Thermal Conductivity of Material	239
7.18	Effect of Pin Diameter and Number of Pins on Dimensionless Entropy Generation Rate	240
7.19	Effect of Pin Height and Diameter on Dimensionless Entropy Generation Rate	241
7.20	Effect of Approach Velocity and Pin Height on Dimensionless Entropy Generation Rate	242
7.21	Effect of Approach Velocity and Number of Pins on Dimensionless Entropy Generation Rate	243
7.22	Comparison of In-Line and Staggered Arrangements for Optimum Diameter	244
7.23	Comparison of In-Line and Staggered Both Arrangements for Optimum Height	245
7.24	Comparison of In-Line and Staggered Arrangements for Optimum Approach Velocity	246
7.25	Comparison of In-Line and Staggered Arrangements for Optimum Number of Pins	247
B.1	Velocity Distribution in Viscous and Inviscid Regions	280
D.1	Transverse Row of Doublets or Circular Pins	287
F.1	Control Volume for Calculating \dot{S}_{gen} for Single Circular Pin	296

F.2	Control Volume for Calculating \dot{S}_{gen} for Pin-Fin Heat Sink	300
F.3	Dimensionless Pressure Drop Components	301

Chapter 1

Introduction

The continuing increase of power densities in microelectronics and the simultaneous drive to reduce the size and weight of electronic products have led to the increased importance of thermal management issues in this industry. The temperature at the junction of an electronics package (chip temperature) has become the limiting factor determining the lifetime of the package. The most common method for cooling packages is the use of aluminum pin-fin heat sinks. These heat sinks provide a large surface area for the dissipation of heat and effectively reduce the thermal resistance of the package. They often take less space and contribute less to the weight and cost of the product. For these reasons, they are widely used in applications where heat loads are substantial and/or space is limited. They are also found to be useful in situations where the direction of the approaching flow is unknown or may change. They offer a low cost, convenient method for lowering the thermal resistance and in turn maintaining junction temperature at a safe level for long term, reliable operation.

The overall performance of a pin-fin heat sink depends on a number of parameters including the dimensions of the baseplate and pin-fins, thermal joint resistance, location and concentration of heat sources. These parameters make the optimal design of a heat sink very difficult. Traditionally, the performance of heat sinks is measured experimen-

tally or numerically and the results are made available in the form of design graphs in heat sink catalogues. Analytical and empirical models for the fluid friction and heat transfer coefficients are used to determine optimal heat sink design.

Pin-fin heat sinks consist of a base and an array of integral attached pins. They can be classified in many ways, e.g. (i) low or high density (Fig. 1.1) and (ii) in-line or staggered (Figs. 1.2 - 1.4). The effective cooling scheme for pin-fin heat sinks is forced convection where forced air creates a significant amount of air in between the pins and enhancing the heat sink's efficiency.

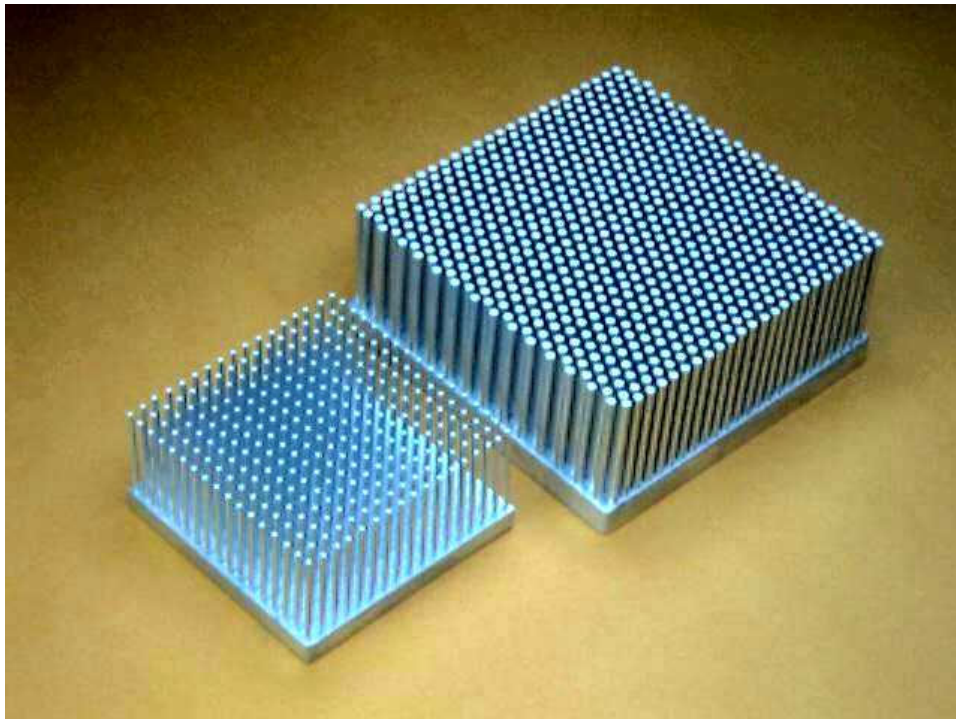


Figure 1.1: Low Density / High Density Pin-Fin Heat Sinks

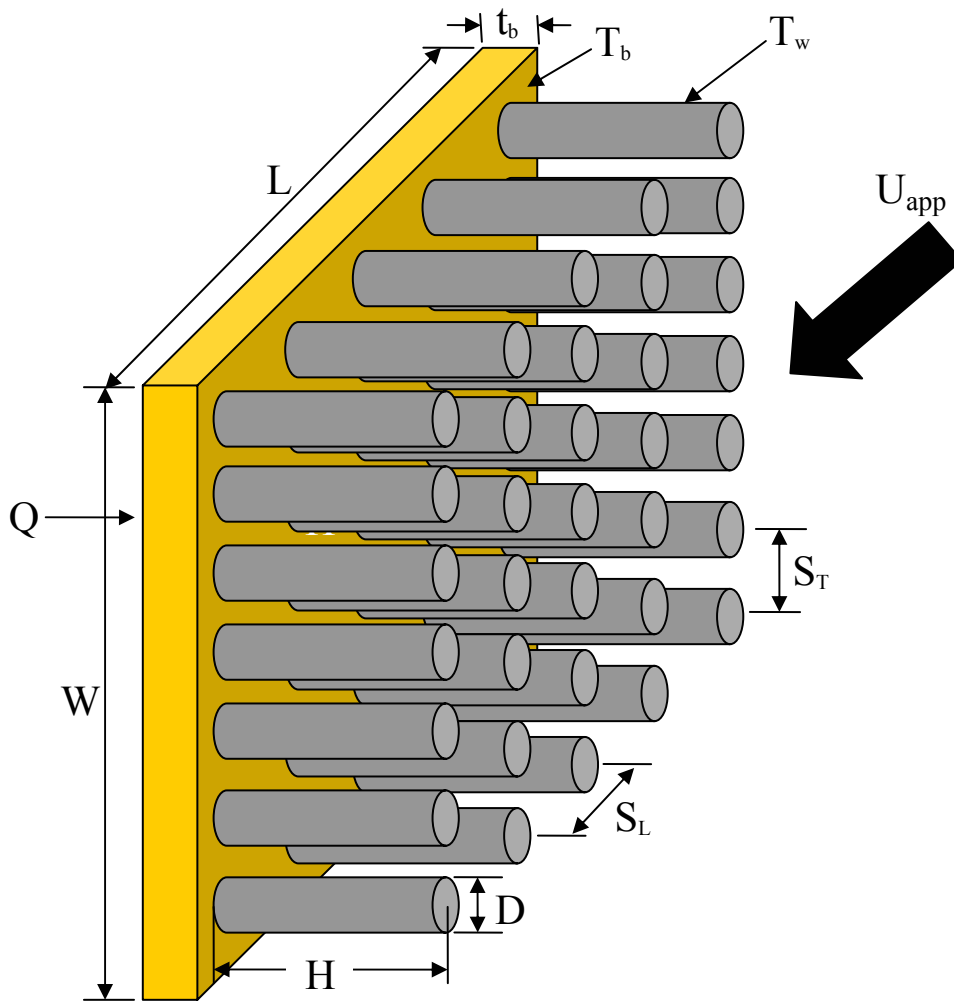


Figure 1.2: In-Line Pin-Fin Heat Sink

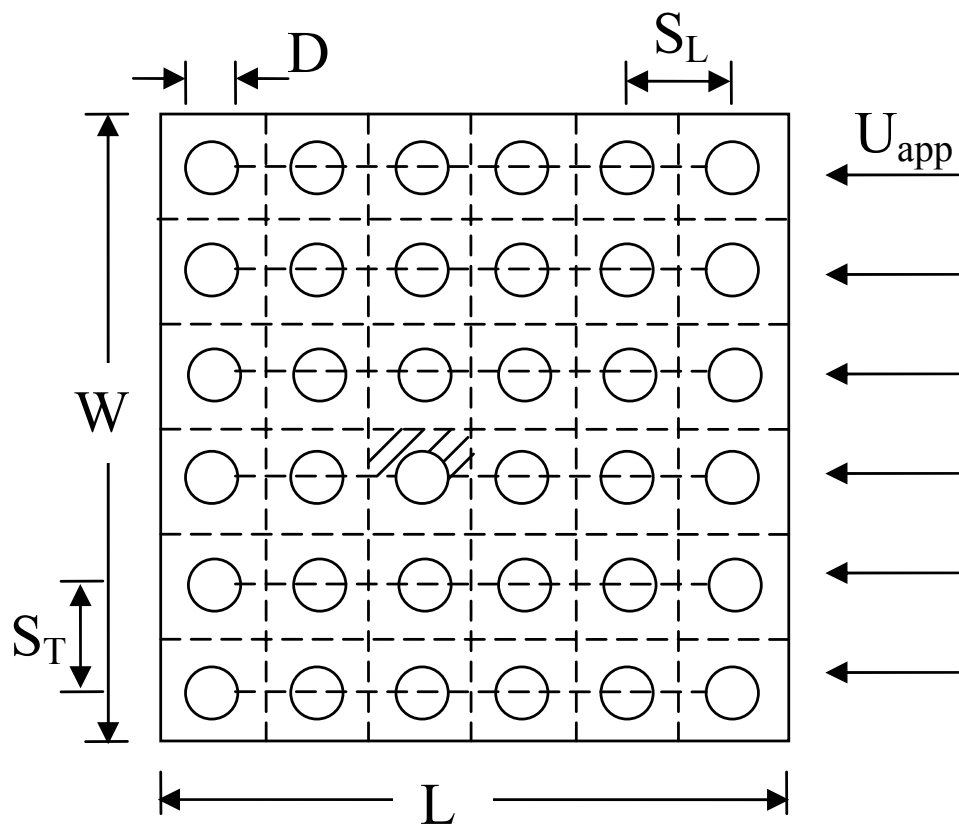


Figure 1.3: Schematics of In-Line Pin-Fin Heat Sinks

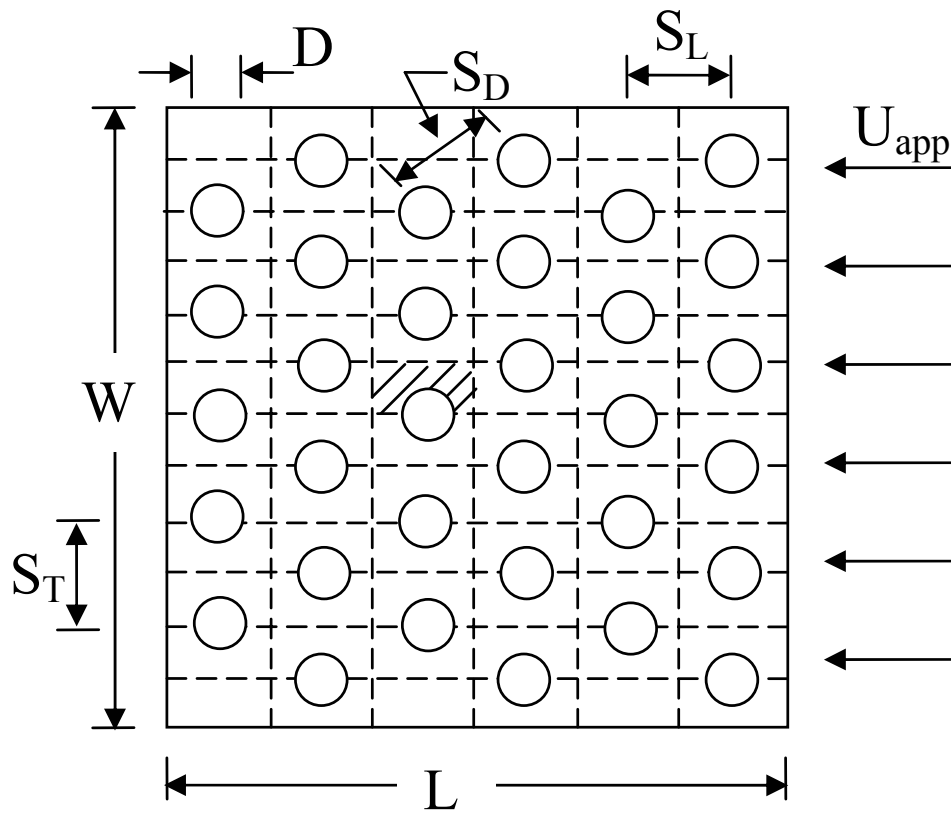


Figure 1.4: Schematics of Staggered Pin-Fin Heat Sinks

1.1 Motivation

The basic equations describing fluid flow and heat transfer in forced convection (Appendix A) are complicated by being non-linear in nature. These non-linearities arise from the inertial and convective terms in the momentum and energy equations respectively. From a mathematical point of view, the presence of a pressure gradient term in the momentum equation for forced convection further complicates the solution of the problem. The energy equation is, in turn, dependent on the velocity (inside the boundary layer) through the convective terms and is coupled with the momentum equation through the pressure gradient.

Because of these mathematical difficulties, the theoretical investigations for fluid flow and heat transfer from cylinders have mainly centered upon asymptotic solutions. These solutions are well documented in the open literature and are valid for very large or very small Reynolds numbers. For moderate Reynolds numbers, there has been heavy reliance on both experiments and numerical methods. These approaches are not only expensive and time consuming but their results are only applicable over a limited range of conditions. They do not provide the values of all the relevant variables throughout the domain of interest. For each new heat sink, a new model has to be constructed and experiments run. No analytical study related to the fluid flow and heat transfer could be found that can be used for low to moderate Reynolds numbers as well as for a wide range of Prandtl numbers.

Unfortunately, many situations arise where solutions are required for low to moderate Reynolds numbers, between the diffusive and laminar boundary layer regimes. Such solutions are of particular interest to thermal engineers involved with cylinders or pin-fin heat sinks. In light of these facts, it is necessary to develop analytical models for the fluid flow and heat transfer from single cylinders (circular and elliptical) and pin-fin heat sinks for a range of Reynolds numbers, Prandtl numbers, pin aspect ratio, baseplate thickness, longitudinal and transverse spacings. Although it is very difficult to obtain an analytical

solution due to the non-linear governing differential equations and complex geometry, it is the challenge in solving this problem analytically that provides the motivation for this work.

1.2 Problem Definition

1.2.1 Geometry

Two schematics of the pin fin heat sinks used in this study are shown in Figs. 1.3 and 1.4. The dimensions of the baseplate are $W \times L \times t_b$, where W is the width of the entrance, L is the length measured in the downstream direction and t_b is the thickness of the base plate. Each pin fin has diameter D and height H . The dimensionless longitudinal and transverse pitches are $\mathcal{S}_L = S_L/D$ and $\mathcal{S}_T = S_T/D$. The source of heat is applied to the bottom of the heat sink. The approach velocity of the fluid is U_{app} and the ambient temperature is T_a . The surface temperature of the pin is $T_w (> T_a)$ in the case of the isothermal fin and the heat flux is q for the isoflux boundary condition. Following restrictions are imposed on the analysis:

$$Pr \geq 0.71 \tag{1.1}$$

$$40 \leq Re_D \leq 1000 \tag{1.2}$$

$$1 \leq U_{app} (m/s) \leq 6 \tag{1.3}$$

$$1 \leq D (mm) \leq 3 \tag{1.4}$$

$$1.25 \leq \mathcal{S}_L \leq 3 \tag{1.5}$$

$$1.25 \leq \mathcal{S}_T \leq 3 \tag{1.6}$$

$$3 \leq \gamma \leq 8 \tag{1.7}$$

1.2.2 Flow Description

The following description of the flow field around a single cylinder and in tube banks/pin-fin heat sinks depends on the understanding based on the previous experimental work of Chang (1970), Zukauskas (1972), Zukauskas and Ziugzda (1985), Pierson (1937), Hoge (1937), and Zukauskas et. al (1988).

Single Cylinder

The fluid dynamics of flow around a single cylinder is highly complicated, due to the combined effects of the Reynolds number, the level of free-stream turbulence, and a number of other factors. It has been observed experimentally by Incropera (1999) that the flow around a cylinder can be approximated as the flow around a single pin in cross flow, which has been discussed in many fluid mechanics and heat transfer books.

When a cylinder is placed in crossflow of a real fluid, a laminar boundary layer is formed on the leading surface as a result of the viscous forces. It is commonly accepted that, in the lower range of Reynolds number $Re_D = DU_{app}/\nu < 3$, the cylinder is enveloped by a laminar boundary layer, which separates from its surface only at the rear stagnation point (Fig. 1.5 A). An increase of $Re_D (< 40)$ leads to an increase in the effect of inertial forces, so that the laminar boundary layer separates from the surface at a certain distance from the rear stagnation point, and a complex vortex structure is formed in the wake (Figs. 1.5 B, C, D). With a further increase of $Re_D (> 40)$, the boundary layer gradually becomes turbulent, and its separation point is shifted upstream. The wake behind the cylinder becomes unstable and vortex shedding is initiated. In the range $150 < Re_D < 300$, periodic irregular disturbances are observed in the wake. In this range the flow is transitional, and gradually becomes turbulent as Re_D increases. A 3-D structure has been observed in this flow range by Gerrard (1966). As Re_D increases further, the point of separation gradually moves forward. At $Re_D \cong 1.2 \times 10^4$ the point of separation attains a maximum

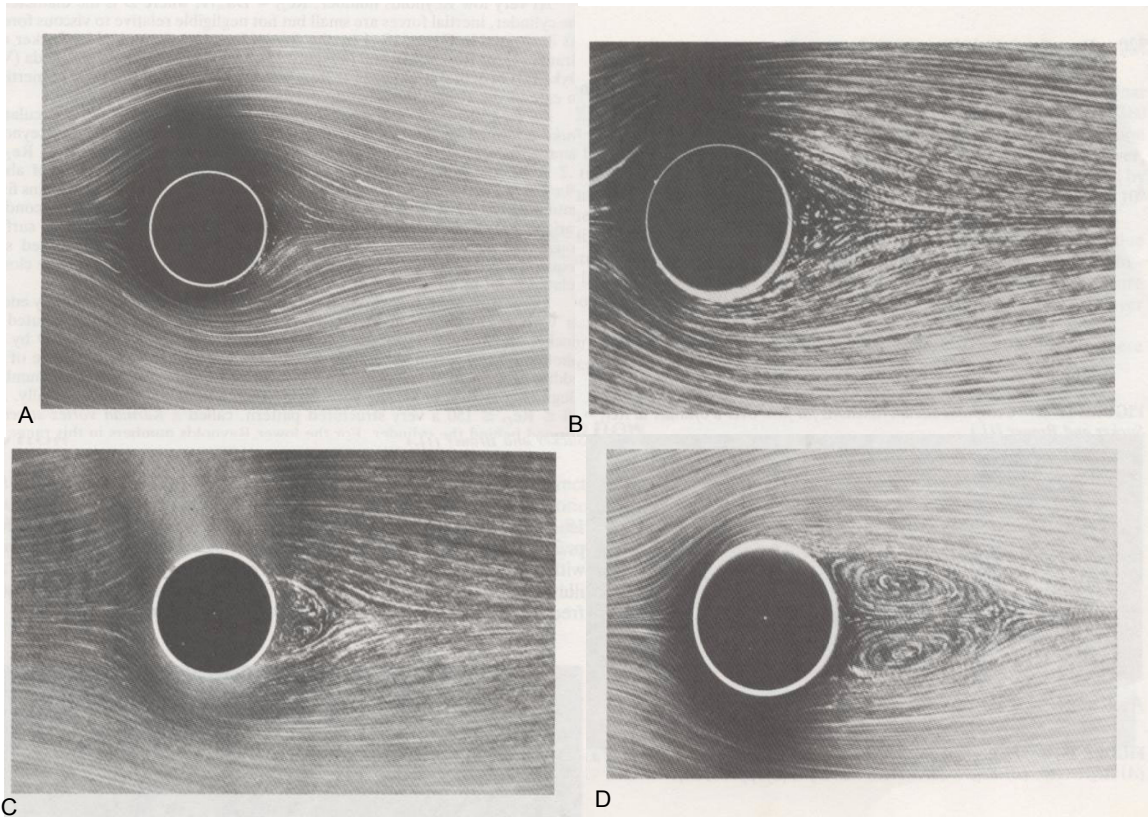


Figure 1.5: Flow Past a Circular Cylinder: (A) $Re_D = 1.54$; (B) $Re_D = 9.6$; (C) $Re_D = 13.1$; (D) $Re_D = 26$ (Van Dyke, 1982)

advancement of about 99° and remains fixed until $Re_D \geq 1.2 \times 10^5$. The exact point of separation depends on secondary variables such as the intensity and scale of free-stream turbulence, surface roughness, and the length of the cylinder. When Re_D increases further, the point of separation starts moving backward. At $Re_D \cong 3 \times 10^5$ it reaches 110° from the front stagnation point. This complex fluid dynamic behavior is reflected in the heat transfer between the cylinder and the fluid.

Pin-Fin Heat Sinks

The experimental work of Pierson (1937), Hoge (1937), Zukauskas (1972), and Zukauskas et. al (1988) for tube banks provides some guidance in understanding the flow behavior in a pin-fin heat sink. Their experiments show that the flow over tubes is controlled by the pressure gradient, the fluid viscosity, and the Reynolds number. This flow is more complex than that over a single tube, due to nonuniformity of the velocity field, high turbulence, and other factors including longitudinal and transverse pitches. Flow over tubes within a bank involves significant blockage of the flow passage; the pressure gradient at the tube surfaces is affected by the degree of flow constriction. Nonisotropic turbulence with discrete eddies prevails within the bank where the mean flow has a non uniform velocity profile. For this reason, the flow structure near the tube surfaces differs from that of a single tube; consequently, the location of the boundary layer separation shifts downstream and affects the flow in the near wake.

At low $Re_D < 10^3$, the mainstream within the bank is laminar with regions of circulating macroscale eddies whose effect on the boundary layer over the front part of tubes is attenuated by viscous forces and by the favorable pressure gradient. The boundary layer flow is laminar whereas the trailing part of the tube lies in a region of circulating flow. This flow pattern over a tube bank which occurs at $Re_D < 10^3$ can be regarded as predominantly laminar.

The studies of Zukauskas et. al (1988) show that the flow pattern within the bank changes significantly for $Re_D > 10^3$. The flow in the space between the tubes becomes turbulent, that depends on their configuration and the relative longitudinal and transverse pitches. At a relatively small S_T , intensive fluctuations are generated at the exit from an upstream row of tubes. However, when the flow enters the next row of tubes these eddies are damped out more rapidly than in the case of large S_T , due to the favorable pressure gradient.

In banks with larger S_L , transition from laminar to turbulent flow in the space between

tubes occurs gradually with increasing Re_D . In banks with small S_L this occurs over a narrower range of Re_D : small eddies are generated at $Re_D \simeq 10^3$. In this case, the flow in the space between the tubes becomes turbulent very rapidly.

The applicability of the previous experimental work regarding heat transfer from cross flow of tube banks has definite limitations when it comes to the analysis of pin fin heat sinks. There are two major differences between the pin fins and tube banks. One difference is that in tube banks, the tube array consists of very long hollow cylinders that generally carry some fluid internally. As a result, the surface temperature of the cylinder surface can be assumed isothermal along its length. Whereas, in a pin fin heat sink, the so-called “fin effect” results in a very definite temperature gradient along the height of the pins. The other difference is that in tube banks, nearly all of the heat transfer occurs along the cylinders which have an aspect ratio $H/D > 20$, so end-wall effects can be neglected. In a pin fin heat sink, considered in this study, the pins are relatively short, therefore, the empirical heat transfer correlations derived for the tube bundle analysis are not generally applicable to pin fin arrays.

Due to the complexity of the flow around a single cylinder or a cylindrical pin in a pin-fin heat sink, it is necessary to make some assumptions to simplify the analysis. These assumptions with their possible justifications are listed in the next section.

1.2.3 Assumptions

This study assumes the following design considerations:

1. Each pin is of uniform diameter, D , and height, H , with circular cross section.
2. The pins are uniformly spaced on the base plate.
3. The fin tips are adiabatic.
4. There is no airflow bypass, i.e. the heat sink is fully ducted.
5. The airflow is normal to the pin-axis.
6. The approach velocity is uniform for each row in a heat sink.

It was observed experimentally by Zukauskas et. al (1988) that the tubes located in the inner part of a bundle are subjected to a highly turbulent flow with a nonuniform velocity profile. This velocity profile depends on many factors including Reynolds number, longitudinal and transverse pitches as well as the method of tubes arrangement. No empirical correlation of the velocity profile could be found that depends on the above mentioned factors. In order to proceed analytically, it is therefore assumed that the approach velocity is uniform. Due to this assumption, it is possible that the local drag and heat transfer coefficients are higher than the experimental/numerical values. In averaging the heat transfer coefficients, they are brought down to some extent. The only risk in using uniform approach velocity is 7 – 8% higher heat transfer coefficients for single cylinders as well as pin-fin arrays.

7. Flow is steady, laminar and two dimensional.

Steady flow shows that there is no variation with time either of the external flow or of flow within the boundary layer. The restriction on the Reynolds number ($40 \leq Re_D \leq 1000$) ensures that the flow is laminar. Other influences, such as sudden changes in surface geometry, which can disturb the flow, are not present in

case of an isolated cylinder. So, these assumptions are valid for isolated cylinders. In case of pin-fin heat sinks, strong 3-D flow patterns exist due to the baseplate but away from the baseplate the flow field is predominantly 2-D over most of the pin length. So the assumptions of laminar and 2-D flow are also acceptable in case of pin-fin heat sinks. However, the assumption of steady flow, in the case of pin-fin heat sinks, is not true due to significant blockage of the flow passage. The assumption of steady flow in a pin-fin heat sink makes the analysis possible.

8. Radiation heat transfer is negligible.
9. The fluid is considered incompressible with constant properties.

From experiments, it is observed that enormous changes of pressure are required to produce measurable changes in the volumes and densities of liquids (Evans, 1968). Since the flow conditions in this study will not contain such extreme pressure differences, liquids can be regarded as incompressible. In a gaseous medium, experiments have shown that the effects of the compressible nature of the medium begin to appear at high speeds (speed of sound). Since laminar flow is assumed in this study, where the fluid velocity is well below high speeds, the assumption of incompressibility for gases is also retained. The assumption of constant properties also appears to be soundly based because experimental measurement does confirm that for most common gases and liquids, the coefficients of viscosity are indeed very small.

10. There is no energy dissipation in the boundary layer.

In flows at high speed there is a viscous dissipation of energy in the boundary-layer region; the interests are, therefore, confined to flows at relatively low speeds.

11. Body forces are negligible.

The effects of gravitational or buoyancy forces are omitted due to forced convection. Any effects produced by the buoyancy of the fluid due to temperature differences will be assumed to be very small.

12. Temperature differences are small.

A large temperature difference between the fluid and the cylinder surface over which it flows could produce extraneous effects which are avoided in this study.

13. The region of viscous flow is thin.

This is also an observed experimental fact which is important because it leads to a considerable simplification of the equations which govern boundary-layer flow. This simplification leads, in turn, of the possibility of obtaining the solutions which will be the concern of Chapter 3.

14. There is no slip at the baseplate and the fin surface.

The condition of no slip is confirmed by previous experimental studies and it is acceptable, at least for the fluid flows considered in this study. The solid surface of the cylinder always contains minute projections and indentations, and under normal conditions of temperature and pressure, some fluid will be trapped within these small cavities. Such trapped fluid, which can be regarded as forming part of the surface, does not move with respect to the surface. Also, the nearest high projections in the surface can be regarded on a macroscopic scale as forming the outer limit of the surface, and the fluid is also stationary with respect to the surface. It is therefore a more satisfactory approach on physical grounds to accept the no slip condition at the wall.

15. Outside the hydrodynamic boundary layer the fluid is inviscid.

1.2.4 Governing Equations

The governing equations of continuity, momentum and energy for steady state forced convection in a Newtonian, constant property fluid with no heat generation can be expressed

in vector form as follows:

$$\nabla \cdot \vec{V} = 0 \quad (1.8)$$

$$\vec{V} \cdot \nabla \vec{V} = -\frac{1}{\rho} \nabla P + \nu \nabla^2 \vec{V} \quad (1.9)$$

$$\vec{V} \cdot \nabla T = \alpha \nabla^2 T \quad (1.10)$$

where \vec{V} is the velocity vector showing the flow field, ∇P is the pressure gradient for forced convection, and T is the fluid temperature. The governing equations are simplified using the order-of-magnitude analysis and are presented in Appendix A.

1.2.5 Fluid Friction

The fluid friction is an important characteristic of heat sinks, because of its association to the power required to move the fluid across the fin arrays and plays a major operating expense, which is directly proportional to the pressure drop. This pressure drop across the heat sink is also known as the hydraulic resistance of the system. It affects the overall performance of the heat sink. Higher hydraulic resistance causes less airflow through the heat sink channel, attaining lower convection heat transfer rate between the fins and the surrounding air and increases fin thermal resistance.

Experiments show that the pressure drop across heat sinks is proportional to the number of rows in the flow direction and is determined by the pin-fins arrangement. With a decreasing number of rows, the entrance and exit conditions in the heat sink contribute more to the total loss of kinetic energy. These effects are described in Chapter 6. Fluid friction factors will be discussed in Chapter 3.

1.2.6 Heat Transfer

The second parameter of interest in this study is the total heat transfer rate through the heat-sink. This parameter is determined mainly by the flow velocity, aspect ratio of

the fin $\gamma = H/D$, thermophysical properties of the fluid, the thermal conductivity of the heat sink material, and the arrangement of the pins. In dimensionless form, it can be expressed by the following relationship:

$$Nu_D = f(\mathcal{S}_L, \mathcal{S}_T, \gamma, k_f/k, Re_D, Pr) \quad (1.11)$$

The heat transfer of a pin-fin in a heat sink depends on the longitudinal and transverse pitches. From the heat transfer standpoint, the staggered arrangement is found to be more effective than the in-line arrangement. In the open literature many experimental/numerical heat transfer models are available but no analytical model exists that can be used for a wide range of parameters discussed above. Heat transfer models for single fins and fin arrays will be developed in Chapter 4.

1.2.7 Entropy Generation Minimization (EGM)

In the present study EGM criterion is used to determine the overall performance of fin geometry and pin-fin heat sink, which allows the combined effect of thermal resistance and pressure drop to be assessed through the simultaneous interaction with the heat sink. A general expression for the entropy generation rate is obtained by using the conservation equations for mass and energy with the entropy balance. The formulation for the dimensionless entropy generation rate is developed in terms of dimensionless variables, including the aspect ratio, Reynolds number, Nusselt number and the friction coefficient. Following Bejan (1996) and applying the laws of conservation of mass and energy with entropy balance for a fluid flowing across a heat sink, one can obtain an expression for the entropy generation rate:

$$\dot{S}_{gen} = \left(\frac{Q^2}{T_a T_b} \right) R_{hs} + \frac{\dot{m} \Delta P}{\rho T_a} \quad (1.12)$$

where Q is the total heat dissipated by the heat sink, T_a is the inlet temperature, T_b is the baseplate temperature, \dot{m} is the mass flow rate through the heat sink, and ρ is the

density of the fluid. Equation (1.12) shows that the entropy generation rate depends on the heat sink resistance R_{hs} and the pressure drop ΔP across the heat sink, provided that the heat load, mass flow rate and ambient conditions are specified. The optimal overall performance of the heat sink can be calculated by minimizing \dot{S}_{gen} subject to constraints such as heat sink resistance, fluid flow, pin-fin dimensions, material, base heat flux, longitudinal and transverse spacings and so forth.

The heat sink resistance R_{hs} consists of several components such as joint resistance R_j , spreading resistance R_s , material resistance R_m , contact resistance R_c , fin resistance R_{fin} , film resistance R_{film} and that the pressure drop include the friction, entrance and the exit effects of the heat sink. There is, at present, no compact and comprehensive model for R_{hs} and ΔP for the pin-fin heat sinks. These two important heat sink performance parameters will be discussed in Chapter 6.

1.3 Objectives

The objectives of this study are to develop:

1. analytical models that can be used to predict fluid flow and heat transfer from single cylinders and pin-fin heat sinks for a range of materials, Reynolds numbers, Prandtl numbers, pin aspect ratios, baseplate thicknesses, longitudinal and transverse spacings, and
2. an entropy generation minimization model that can be used to optimize the overall performance of the heat sink for a wide range of parameters mentioned above.

To accomplish these objectives, the work is divided into the four tasks which can be described as follows:

TASK 1 Conduct an extensive literature survey of forced convection heat transfer from pin-fin heat sinks.

This task is accomplished in the following two steps:

1. In the first step, a literature survey of forced convection heat transfer from single and multiple cylinders (circular and elliptical) is conducted which is a critical step for developing fluid friction and heat transfer models for arrays of pin fins. A single cylinder study can provide insights into convection heat transfer effects due to boundary-layer separation, Reynolds number, and Prandtl number.
2. In the next step, a literature survey of an array of pin fins as well as pin-fin heat sinks is conducted which will help achieve the first task of the current study. This task will be achieved in Chapter 2.

TASK 2 Develop analytical forced convection models capable of predicting fluid flow and average heat transfer for a pin-fin heat sink.

Fluid flow and heat transfer models are first developed for a single isolated cylinder under different thermal boundary conditions. These models are then modified to include blockage effects on the cylinder. Finally, models are developed to determine fluid friction and heat transfer from pin-fin arrays. These models can be applied to the design of pin-fin heat sinks. The fluid flow and convection heat transfer from the base plate of a heat sink can be modeled by considering a finite flat plate under forced convection. This task will be discussed in Chapters 3 and 4.

TASK 3 Conduct a simplified heat sink analysis and determine heat sink performance.

Energy balances will be performed first to determine the overall heat transfer coefficient and temperature distribution of the fluid. Then, heat sink performance will be ana-

lyzed by using fluid flow and heat transfer models. Heat sink performance is analyzed in Chapter 5.

TASK 4 Develop entropy generation minimization (EGM) model for optimization of pin-fin heat sinks.

Combining laws of conservation of mass and energy with the entropy balance across the heat sink, an optimization model will be developed. This model can be used to optimize any or all design parameters in a pin-fin heat sink. Parametric optimization was performed on the model using entropy generation minimizing techniques with the help of MAPLE 9.

Based on the parametric studies performed in the previous task for the selected heat sink, important parameters governing the overall performance will be identified. Parametric studies will be conducted to examine the influence of governing parameters on overall performance. Based on these studies, optimal selection of materials and heat sink configurations will be investigated for various operating conditions. This task will be discussed in Chapter 7.

TASK 5 Conduct numerical validation using a CFD and heat transfer software package ICEPAK.

Finally, the results of heat transfer from single pins and pin-fin arrays will be validated using a CFD and heat transfer software package ICEPAK. Two separate CFD models, based on a finite volume method, will be presented in Chapter 5. The multigrid solver algorithm will be used to find the solution.

1.4 Organization of the Thesis

The thesis is organized as follows. Chapter 2 is a review of literature containing relevant material, and is subdivided according to the contents of the thesis. The contents of the thesis are divided into three major parts.

The first part concerns modeling of fluid flow and heat transfer for different geometries (single cylindrical and elliptical pins, circular pin between two parallel planes and pin-fin arrays) and their numerical validation using ICEPAK. Modeling part is further divided into four sections. In each section, an integral approach of the boundary layer analysis is employed to derive closed form expressions for the calculation of drag coefficients (Chapter 3) and the average heat transfer coefficients (Chapter 4) under both isothermal and isoflux thermal boundary conditions. The Von Karman-Pohlhausen method is used to solve the momentum integral equation, whereas the energy integral equation is solved for both thermal boundary conditions. A fourth order velocity profile in the hydrodynamic boundary layer and a third order temperature profile in the thermal boundary layer are used to study the fluid flow and heat transfer characteristics in each case. In the first two sections, circular and elliptical pins in an infinite medium are discussed. In the third section, the effects of blockage on the fluid flow and heat transfer from a circular cylinder are investigated, where the potential flow velocity is obtained by the method of images. In the fourth section, the same integral analysis is applied on a control volume selected from the third row of a pin-fin array (in-line or staggered). The mean velocity in the minimum free cross section of the control volume, U_{max} , is used as a reference velocity in the calculations of fluid flow and heat transfer for both types of arrangements. The potential flow velocity outside the boundary layer is obtained by using complex variable theory for both arrangements. Comparisons are made with existing experimental/ numerical data obtained by other investigators. It is shown that the results of the present method are in good agreement with the others. In Chapter 5, some numerical simulations for single circular cylinder and in-line pin-fin heat sink are carried out to validate the present analytical results. Results of numerical simulations are presented herein and all are shown to be satisfactory.

The second part of this thesis (Chapter 6) incorporates the fluid flow and heat transfer models, developed in the first part, to analyze the performance of a heat sink. Fully developed heat and fluid flow are assumed in the analysis, and the thermophysical prop-

erties are taken to be temperature independent. Energy balances and thermal circuit concepts are used to develop models for thermal and hydraulic resistances of the heat sink. The analysis of both in-line and staggered pin-fin heat sinks is performed by using parametric variation of thermal and hydraulic resistances. It is shown that thermal resistance decreases whereas pressure drop increases for each design variable which gives optimum value of that variable. The effect of thermal conductivity is also observed in both arrangements.

The third part of this thesis (Chapter 7) is devoted to the optimization of pin-fin geometry and pin-fin heat sinks using entropy generation minimization technique. For convenience, this part is divided into two sections. The first section will examine the effect on overall thermal/fluid performance associated with different fin geometries, including, rectangular plate-fins as well as square, circular and elliptical pin-fins, whereas the second one will deal with cylindrical pin-fin heat sinks. The use of entropy generation minimization, EGM, allows the combined effect of thermal resistance and pressure drop to be assessed through the simultaneous interaction with the heat sink. A general expression for the entropy generation rate is obtained in each case by using the conservations equations for mass and energy with entropy balance. The formulation for the dimensionless entropy generation rate is developed in terms of dimensionless variables, including the aspect ratio, Reynolds number, Nusselt number and the drag coefficient. Both in-line and staggered arrangements are studied and their relative performance is compared on the basis of equal foot print area of heat sinks. It is shown that all relevant design parameters for pin-fin heat sinks, including geometric parameters, material properties and flow conditions can be simultaneously optimized. In Chapter 8, a summary of the entire work is presented.

Chapter 2

Literature Review

An extensive literature survey of fluid flow and heat transfer from single isolated cylinders (circular and elliptical), cylinder/ pin-fin arrays and tube banks is conducted which is a critical step for developing fluid friction and heat transfer models for pin-fin heat sinks. A single cylinder study can provide insights into convection heat transfer effects due to boundary-layer separation, Reynolds number, and Prandtl number. Due to similarities between the geometry of a heat exchanger tube bundle and pin-fin arrays, previous work related to cylinder arrays and tube banks can also provide some guidance in modeling pin-fin heat sinks. Depending upon the objectives of this study, mentioned in the previous chapter, the literature review is divided into three main sections, i.e. fluid flow (hydrodynamic), heat transfer (thermal) and optimization. Each section will review analytical and experimental/ numerical studies about single cylinders and arrays of cylinders/ tube banks/ pin-fin heat sinks in detail. The following flow chart (Fig. 2.1) explains the procedure to review the available literature.

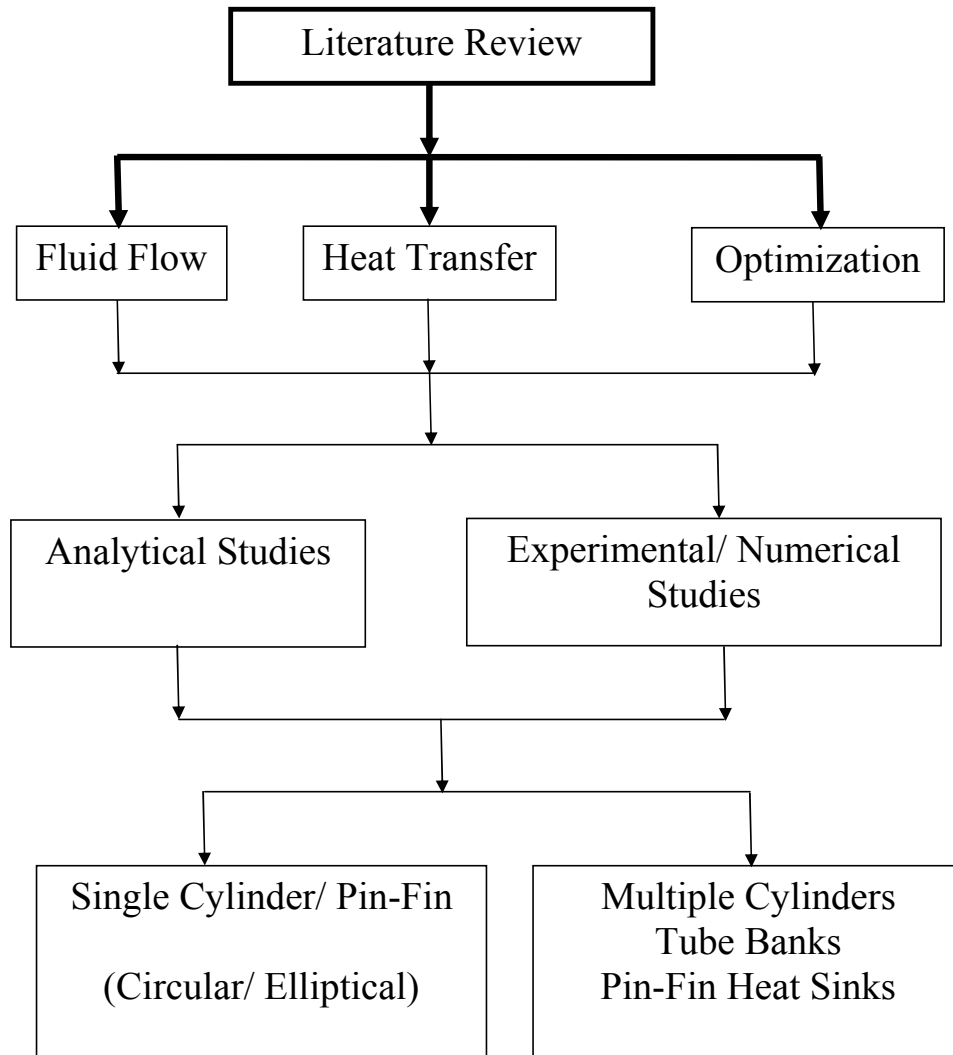


Figure 2.1: Flow Chart Showing Procedure for Literature Review

2.1 Fluid Flow

2.1.1 Analytical Studies

Single Cylinders in an Infinite Flow

Fluid friction manifests itself in the form of the drag force F_D , where F_D is the sum of the skin friction drag D_f and pressure drag D_p . No analytical study could be found for the drag coefficients for a single circular or elliptical cylinder in an infinite flow.

Array of Cylinders / Pin-Fin Heat Sinks

To the author's knowledge, no analytical work exists for the fluid friction for an array of cylinders or pin-fin heat sinks either. The early studies of Howland (1934), Howland and McMullen (1936) and Knight and McMullen (1937) provide only the potential functions for different groups of circular cylinders. These functions can be used to determine the velocity of fluid on the surface of the cylinder in the arrays of cylinders. Following these studies, Beale (1992) proposed expressions for the complex potentials in the form of power series. Based on the method of images, Streeter (1948), Milne-Thomson (1968), and Suh et al.(1989) developed closed form expressions for the complex potential for a group of cylinders.

2.1.2 Experimental/ Numerical Studies

Numerous numerical and experimental studies have been conducted on fluid flow and heat transfer from a single cylinder, tube banks, arrays of cylinders and pin-fin heat sinks. Some authors including Kays and London (1964), Žukauskas (1972), Žukauskas and Žiugžda (1985), Žukauskas and Ulinskas (1988), and Zdravkovich (1997) have published books on fluid flow and heat transfer from a single cylinder, tube banks and arrays of

cylinders or pin fins. In the following two sections, a brief review of previous numerical and experimental work related to fluid flow from single and multiple cylinders as well as tube banks and pin-fin heat sinks will be presented.

Single Cylinders

Flow past a single circular cylinder has been investigated experimentally/ numerically by numerous authors. Žukauskas (1972), Lamb (1957), Roshko (1961), Achenbach (1975), and Schlichting (1979) studied the influence of Reynolds number on the separation point, skin friction, pressure distribution as well as the local velocity around the cylinder. Wieselsberger (1921), and according to Schlichting (1979), Flachsbart (1932) and Roshko (1961) investigated the influence of Reynolds number on the drag coefficients. Wieselsberger (1921) performed extensive experimental work and showed that almost all the experimental points for the drag coefficient of circular cylinders of widely different diameters fall on a single curve. This curve is recognized as a standard curve to determine the drag coefficients of a circular cylinder.

Numerical work for laminar flow around a circular cylinder includes that of Takami and Keller (1969), Dennis and Chang (1970), Nieuwstadt and Keller (1973), Sucker and Brauer (1975), and D'Alessio and Dennis (1994). The numerical results of drag coefficients, obtained from these studies, are compared in Table 2.1

Regarding single elliptical cylinders in infinite flow, the following related experimental/numerical studies are found:

Schubauer (1934, 1939) conducted experiments to determine velocity distribution in the laminar boundary layer on the surface of an elliptic cylinder with axis ratio 1 : 3. He found that the velocity distribution in the boundary layer, its thickness, and its tendency to separate from the surface of the body are governed almost entirely by the velocity distribution in the region of potential flow outside the layer. He got good agreement with

Table 2.1: Summary of Numerical Results of Drag Coefficients for Laminar Flow Over a Circular Cylinder

Re_D	C_D				
	Takami and Keller (1969)	Dennis and Chang (1970)	Nieuwstadt and Keller (1973)	Sucker and Brauer (1975)	D'Allesio and Dennis (1994)
10	2.750	2.846	2.828	2.831	2.719
20	2.024	2.045	2.053	2.178	1.969
30	1.717	-	1.733	1.825	1.673
40	1.524	1.522	1.550	1.633	1.451
70	-	1.212	-	1.371	-
100	-	1.056	-	1.243	-

the approximate method, developed by Pohlhausen (1921), for the forward part of the cylinder. The same approximate method was used by Schlichting and Ulrich (1942) to calculate the boundary layer parameters on elliptical cylinders of different axis ratios, mentioned by Schlichting (1979).

Modi et al. (1992) studied experimentally the aerodynamics of a set of two-dimensional, stationary elliptic cylinders with different axis ratios in the subcritical Reynolds number range of $3 \times 10^3 - 10^5$. They presented extensive results on static pressure distribution, Strouhal number and near wake geometry as functions of the angle of attack and Reynolds number. They also determined the separation points using the analytical Gortler series solution approach.

Jackson (1987), D'Allesio and Dennis (1994, 1995), and D'Allesio (1996) studied numerically the flow of a viscous incompressible fluid past an inclined elliptic cylinder. They obtained solutions for Reynolds numbers up to 100 and for various inclinations. Good agreement in the steady state results is found with the existing results.

Arrays of Cylinders / Pin-Fin Heat Sinks

A review of existing literature reveals that many experimental/ numerical studies exists regarding arrays of cylinders or pin-fin heat sinks. Zdravkovich (1977, 1987) investigated the effects of interference between two circular cylinders in various arrangements. Igarashi (1981) investigated experimentally the characteristics of the flow around two and three circular cylinders arranged in tandem. Aiba et al. (1976, 1980, 1981) measured the heat transfer around three and four circular cylinders closely spaced in a cross flow of air, whereas Igarashi and Nishikawa (1975) investigated the structure of the flow around five tubes. Igarashi and Suzuki (1984) investigated the vortex-shedding frequency, drag and flow structures of three cylinders in line. Kundu et al. (1991) studied numerically the fluid flow and heat transfer from a row of in-line cylinders placed between two parallel plates. Fowler and Bejan (1993) studied the pressure drop and heat transfer through bundles of parallel cylinders at low Reynolds numbers. Their numerical results cover the range $1 \leq Re_D \leq 30$ and $0.72 \leq Pr \leq 100$.

Chilton and Genereaux (1933) reviewed the existing data on the pressure drop across tube banks and recalculated the data to a common basis from the original sources. They recommended the following correlations of friction factors for $40 \leq Re_D \leq 30000$:

$$f = 0.75Re_D^{-0.2} \quad (2.1)$$

for staggered tube banks, and

$$f = 0.33Re_D^{-0.2} \quad (2.2)$$

for in-line tube banks. In both equations, Reynolds number Re_D is based on transverse spacing S_T .

Grimison (1937) produced a complete friction-factor plot for flow across in-line and staggered tube banks based on the available data of Huger (1937) and Pierson (1937). Jakob (1938) studied the same data and obtained the friction factors for in-line and staggered arrangements in terms of longitudinal and transverse pitches and the Reynolds

number based on the tube diameter ($2000 \leq Re_D \leq 40000$) and the mean velocity in the minimum free cross section between two tubes, U_{max} as:

$$f = \left\{ 0.25 + \frac{0.1175}{(a-1)^{1.08}} \right\} Re_{Dmax}^{-0.16} \quad (2.3)$$

for staggered tube arrangement, and

$$f = \left\{ 0.044 + \frac{0.08b}{(a-1)^{0.43+1.13/b}} \right\} Re_{Dmax}^{-0.15} \quad (2.4)$$

for in-line arrangement.

Gunter and Shaw (1945) used extensive friction data, on both in-line and staggered arrangements, produced by a number of authors including Sieder and Scott (1932), Norris and Spofford (1942), Hoge (1937), Pierson (1937), and Wallis and White (1938) to establish the following equation for pressure drop in crossflow over tubes for $0.01 \leq Re_D \leq 3 \times 10^5$:

$$\frac{f}{2} = \frac{\Delta P g D_v}{\rho U_{max}^2 L} \left(\frac{\mu}{\mu_w} \right)^{0.14} \left(\frac{D_v}{S_T} \right)^{-0.4} \left(\frac{S_L}{S_T} \right)^{-0.6} \quad (2.5)$$

For the viscous range, the function of the Reynolds number is $f/2 = 90/Re_{Dmax}$ and in turbulent range, $f/2 = 0.96/Re_{Dmax}^{-0.145}$.

For in-line and staggered tube banks, Zukauskas and Ulinskas (1983) recommended following empirical relations based on Reynolds numbers and longitudinal and transverse pitches:

Table 2.2: Recommended Relationships for In-Line Tube Banks

S_L	Re_D Range	f/K_1	K_1
1.25	$3 < Re_D < 2000$	$0.272 + \frac{207}{Re_D} + \frac{102}{Re_D^2} - \frac{286}{Re_D^3}$	$1.009 \left(\frac{S_T-1}{S_L-1} \right)^{-0.744}$ for $Re_D = 10^3$
		$0.263 + \frac{86.7}{Re_D} - \frac{2.02}{Re_D^2}$	
1.50	$3 < Re_D < 2000$	$0.188 + \frac{56.6}{Re_D} - \frac{646}{Re_D^2} + \frac{6010}{Re_D^3} - \frac{18300}{Re_D^4}$	$1.007 \left(\frac{S_T-1}{S_L-1} \right)^{-0.655}$ for $Re_D = 10^4$
		$0.247 - \frac{0.595 Re_D}{10^6} + \frac{0.15 Re_D^2}{10^{11}} - \frac{0.137 Re_D^3}{10^{17}} - \frac{0.396 Re_D^4}{10^{24}}$	
2.0	$7 < Re_D < 800$	$0.177 - 0.311 \times 10^{-6} Re_D + 0.11710^{-11} Re_D^2$	$1.004 \left(\frac{S_T-1}{S_L-1} \right)^{-0.539}$ for $Re_D = 10^5$
2.5	$600 < Re_D < 2 \times 10^5$		

Table 2.3: Recommended Relationships for Staggered Tube Banks

S_T	Re_D Range	f/K_1	K_1
1.25	$3 < Re_D < 1000$	$0.795 + \frac{247}{Re_D} + \frac{335}{Re_D^2} - \frac{1550}{Re_D^3} + \frac{2410}{Re_D^4}$	$\left(\frac{S_T}{S_L}\right)^{-0.048}$ (for $Re_D = 10^3$) and $0.5 < \frac{S_T}{S_L} < 3.5$
	$10^3 < Re_D < 2 \times 10^6$	$0.245 + \frac{3390}{Re_D} - \frac{0.984 \times 10^7}{Re_D^2} + \frac{0.132 \times 10^{11}}{Re_D^3} - \frac{0.599 \times 10^{13}}{Re_D^4}$	
1.50	$3 < Re_D < 1000$	$0.684 + \frac{111}{Re_D} - \frac{97.3}{Re_D^2} + \frac{426}{Re_D^3} - \frac{574}{Re_D^4}$	$1.28 - \frac{0.708}{(S_T/S_L)} + \frac{0.55}{(S_T/S_L)^2} - \frac{0.113}{(S_T/S_L)^3}$ (for $0.45 < \frac{S_T}{S_L} < 3.5$, and $Re_D = 10^4$)
	$10^3 < Re_D < 2 \times 10^6$	$0.203 + \frac{2480}{Re_D} - \frac{0.758 \times 10^7}{Re_D^2} + \frac{0.104 \times 10^{11}}{Re_D^3} - \frac{0.482 \times 10^{13}}{Re_D^4}$	
2.0	$7 < Re_D < 100$	$0.713 + \frac{44.8}{Re_D} - \frac{126}{Re_D^2} - \frac{582}{Re_D^3}$	$0.93 \left(\frac{S_T}{S_L}\right)^{0.48}$ (for $1.25 < \frac{S_T}{S_L} < 3.5$ and $Re_D = 10^2$)
	$100 < Re_D < 1 \times 10^4$	$0.343 + \frac{303}{Re_D} - \frac{0.717 \times 10^5}{Re_D^2} + \frac{0.88 \times 10^7}{Re_D^3} - \frac{0.38 \times 10^9}{Re_D^4}$	
2.5	$100 < Re_D < 5000$	$0.33 + \frac{98.9}{Re_D} - \frac{0.148 \times 10^5}{Re_D^2} + \frac{0.192 \times 10^7}{Re_D^3} - \frac{0.862 \times 10^8}{Re_D^4}$	$0.951 \left(\frac{S_T}{S_L}\right)^{0.284}$ (for $1.25 < \frac{S_T}{S_L} < 3.5$ and $Re_D = 10^3$)
	$5000 < Re_D < 2 \times 10^6$	$0.119 + \frac{4980}{Re_D} - \frac{0.507 \times 10^8}{Re_D^2} + \frac{0.251 \times 10^{12}}{Re_D^3} - \frac{0.463 \times 10^{15}}{Re_D^4}$	

2.2 Heat Transfer

2.2.1 Analytical Studies

Single Cylinders

Few analytical studies are available for the local and average heat transfer from a single isolated circular cylinder.

Refai Ahmed and Yovanovich (1995) proposed an analytical method to predict forced convection heat transfer from isothermal cylinders for a wide range of Reynolds number and Prandtl number. They transformed the linear energy equation into an equivalent transient heat conduction equation and gave a final expression as a function of the effective velocity that is defined in the limits of $Pr \rightarrow \infty$ and $Pr \rightarrow 0$ using scaling analysis. They presented an analytical solution in closed form based on the square root of area \sqrt{A} , where A is the surface area of the cylinder:

$$Nu_{\sqrt{A}} = Nu_{\sqrt{A}}^0 + 1.015(H/D)^{0.25} Re_{\sqrt{A}}^{0.5} F(Pr, \gamma_{\sqrt{A}}) \quad (2.6)$$

where $Nu_{\sqrt{A}}^0$ is the diffusive limit for the circular cylinder and is given by:

$$Nu_{\sqrt{A}}^0 = \begin{cases} 3.5(H/D)^{0.02} & 0 < H/D \leq 1 \\ 3.385 + 0.082(H/D) & 1 < H/D \leq 8 \\ 4\sqrt{H/D}/\ln 2(H/D) & 8 < H/D \end{cases} \quad (2.7)$$

and $F(Pr, \gamma_{\sqrt{A}})$ is a function that depends on fluid properties and velocity profiles through the parameter $\gamma_{\sqrt{A}}$ and is given by:

$$F(Pr, \gamma_{\sqrt{A}}) = \frac{Pr^{1/3}}{\left[(2\gamma_{\sqrt{A}} + 1)^3 + \frac{1}{Pr} \right]^{1/6}}, \quad 0 < Pr < \infty \quad (2.8)$$

The parameter $\gamma_{\sqrt{A}}$ is given by:

$$\gamma_{\sqrt{A}} = \frac{1}{\left[1 + 0.49Re_{\sqrt{A}}^{1.25} \right]^{1/5}} \quad (2.9)$$

Eckert (1952) presented a method for the calculation of local heat transfer around the periphery of cylinders of arbitrary cross section in the laminar region for flow of a fluid with constant thermophysical properties. This method was based on exact solutions of the boundary-layer equations for incompressible wedge-type flow and on the postulate that on any location of the cylinder the boundary-layer growth is the same as that on the wedge with comparable flow conditions.

Drake et al. (1950) solved the energy equation in cylindrical coordinates for an infinite isothermal cylinder placed normal to a uniform stream of incompressible fluid transferring heat by laminar convection and obtained an approximate solution for the average heat transfer coefficient. They found excellent agreement with the experimental data for air over a wide range of Reynolds number.

Arrays of Cylinders

To the author's knowledge, no analytical work exists for the heat transfer from arrays of cylinders or pin-fin heat sinks either. The early studies of Howland (1934), Howland and McMullen (1936) and Knight and McMullen (1937) provide only the potential functions for different groups of circular cylinders. These functions can be used to determine the

velocity of fluid on the surface of the cylinder in the arrays of cylinders. Following these studies, Hsu (1964) obtained theoretical expressions for Nusselt numbers for cross flow of liquid metals through rod bundles.

2.2.2 Experimental and Numerical Studies

Single Cylinders

Heat transfer from a circular cylinder in an infinite flow has been investigated also by many researchers. A summary of experimental/numerical correlations of heat transfer from a single cylinder is given in Tables 2.2 and 2.3.

Table 2.4: Summary of Previous Experimental/Numerical Correlations and Models for Air

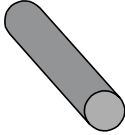
Configuration	Authors	Correlations / Models	Re _D Range
Single Cylinder 	Refai Ahmed and Yovanovich (1997)	$Nu_D = 0.76 + 0.73Re_D^{1/2}F(Pr, \gamma_D)$ $F(Pr, \gamma_D) = \frac{Pr^{1/3}}{\left[(2\gamma_D + 1)^3 + \frac{1}{Pr}\right]^{1/6}}$ $\gamma_D = \frac{1}{[1 + (Re_D^{0.75}/300)^5]^{1/5}}$	10 ⁴ – 10 ⁵
	Quarmby and Fakhri (1980)	$Nu_D = 0.123Re_D^{0.651} +$ $0.00416 \left(\frac{D}{H}\right)^{0.85} Re_D^{0.792}$	1 – 2 × 10 ⁵
	Churchill and Bernstein (1977)	$Nu_D = 0.3 + \frac{0.62Re_D^{1/2}Pr^{1/3}}{[1 + (0.4/Pr)^{2/3}]^{1/4}} \cdot$ $\left[1 + \left(\frac{Re_D}{282000}\right)^{5/8}\right]^{4/5}$	10 ² – 10 ⁷

Table 2.5: Summary of Previous Experimental Correlations for Air ($Pr = 0.71$)

	$Nu_D = CRe_D^n$			Boundary Condition
	C	n	Re_D Range	
Žukauskas (1972)	0.6607	0.4	1 – 40	Isothermal
	0.4493	0.5	$40 - 1 \times 10^3$	
	0.2290	0.6	$1 \times 10^3 - 2 \times 10^5$	
	0.0669	0.7	$2 \times 10^5 - 1 \times 10^6$	
Morgan (1975)	0.795	0.384	4 – 40	Isothermal
	0.583	0.471	$40 - 4 \times 10^3$	
	0.148	0.633	$4 \times 10^3 - 4 \times 10^4$	
	0.0208	0.814	$4 \times 10^4 - 4 \times 10^5$	
Hilpert (1933)	0.891	0.33	1 – 4	Isothermal
	0.821	0.385	4 – 40	
	0.615	0.466	$40 - 4 \times 10^3$	
	0.174	0.618	$4 \times 10^3 - 4 \times 10^4$	
	0.0239	0.805	$4 \times 10^4 - 4 \times 10^5$	
Eckert and Soehngren(1952)	0.57	0.473	$1 \times 10^4 - 1 \times 10^5$	Isothermal
Žukauskas and Žiugžda (1985)	0.29	0.6	$1 \times 10^3 - 2 \times 10^5$	Isoflux
Sarma and Sukhatme (1977)	0.62	0.505	1200 – 4700	Isoflux

Other numerical / experimental studies and their findings related to heat transfer from a single circular cylinder in an infinite flow are described below.

According to Žukauskas and Žiugžda (1985), Kruzhilin (1936), Frossling (1940), and Eckert (1942), Drake et al. (1950), Eckert and Soehngen (1952), and recently, Refai Ahmed and Yovanovich (1995) presented a number of calculation techniques, which involved analytical solutions of the boundary layer equations or of integral equations with the corresponding limiting conditions. Žukauskas and Žiugžda (1985) presented a semi-analytical solution for the boundary-layer equations in the laminar, transitional, and turbulent parts of the boundary layer, taking into account the effects of free-stream turbulence, blockage factor, and Reynolds number on the heat transfer and fluid dynamics for a cylinder in cross flow. They found their results in good agreement with the numerical results of Jones and Launder (1973) and Karyakin and Sharov (1974).

Quarmby and Fakhri (1980) investigated experimentally the effect of aspect ratio, i.e. L/D , on forced convection heat transfer from single cylinders of finite length in cross flow. They proposed a correlation for heat transfer from cylinders of low aspect ratio which in the limit agrees with the Žukauskas (1972) and Morgan (1975) correlations for large aspect ratio.

Eckert and Soehngren (1952) investigated experimentally the distribution of heat transfer coefficients around circular cylinders in crossflow at Reynolds numbers from 20 to 500. They found that the thermal boundary layers were quite thick, especially for the lower Reynolds numbers, with separation occurring further downstream than at high Reynolds numbers. Furthermore, the contribution of the stagnant region at the downstream side of the cylinder to the over-all heat transfer was low ($\cong 15\%$), but the heat flow into the upstream side was much higher than into the downstream side.

Giedt (1940) performed experiments to obtain data on the variation of the rate of heat transfer around a cylinder with a non isothermal surface. His experimental data included a point unit heat-transfer coefficient and static-pressure distributions around a

cylinder circumference throughout a range of Reynolds number from 70,800 to 219,000.

Spalding and Pun (1962) carried out a survey, in which they compared fifteen general numerical methods by applying them to the calculation of heat transfer from the front half of a circular cylinder in cross flow. They found that while several methods appeared to give accuracies of $\pm 3\%$ or better, one of the most accurate was that proposed by Merk (1959). This method has a sound theoretical basis because it is derived directly from the boundary-layer equations and involves no drastic assumptions about the behavior of the boundary-layer fluid. This method is reliable and accurate but it requires knowledge of the distribution of the mainstream velocity outside the boundary layer. Krall and Eckert (1970), Cebeci and Smith (1974), Lin et al. (1976), and Chun and Boehm (1989) obtained various finite difference solutions for low Reynolds numbers.

Žukauskas (1972) analyzed the work of Akilba'yev et al. (1966) about the influence of channel blockage on the flow and heat transfer of a tube in a restricted channel. According to Žukauskas (1972), they showed that the increasing channel blockage ratio from 0 to 0.8 caused the minimum pressure point to be displaced from $\phi = 70^\circ$ to 90° , and the separation point moved downstream to $\phi = 100^\circ$. Their theoretical calculations, by the method of Merk (1959) using the potential flow velocity distribution, showed that the heat transfer on the front portion of the tube increased with an increase in blockage ratio. Žukauskas and Žiugžda (1985) performed a series of experiments with different free stream geometries to investigate the effects of channel blockage. They expressed the Hiemenz velocity distribution in the outer boundary layer in terms of channel blockage and used it to estimate the heat transfer behavior of a cylinder. Vaitiekūnas et al. (1985) investigated numerically the effects of the channel blockage on the dimensionless shear stress, location of U_{max} , point of boundary layer detachment, and the local heat transfer coefficients. They approximated the velocity distribution outside the boundary layer by the modified Hiemenz polynomial in which the coefficients are functions of channel blockage. These functions were based on the analysis of the experimental data of Žukauskas and Žiugžda (1985). They found satisfactory agreement with the experimental results of

Žukauskas and Žiugžda (1985).

Hattori and Takahashi (1993) performed experiments on forced convection heat transfer from a single row of circular cylinders in cross flow. They measured local and average Nusselt numbers for a cylinder in the Reynolds number range from 80 to 6×10^3 and gave a correlation for the average Nusselt number. Later Yamamoto and Hattori (1996) verified numerically their heat transfer values for the same arrangement. They found good agreement with those obtained from experiments in water by Hattori and Takahashi (1993).

Regarding single elliptical cylinders in infinite flow, the following related experimental/numerical studies are found:

Ota et al. (1983, 1984) studied experimentally heat transfer and flow around an elliptical cylinder of axes ratios 1 : 2 and 1 : 3. Their experimental results show that the heat transfer coefficient of the elliptical cylinder is higher than that of a circular one with equal circumference and the pressure drag coefficients of the former are much lower than that of the later. Žukauskas and Žiugžda (1985) studied experimentally the fluid flow and heat transfer from an elliptical cylinder with 1 : 2 ratio between minor and major axes, and with air flow parallel to either axis. They found higher heat transfer coefficients for elliptical cylinders. Their studies of heat transfer with various fluids showed that the elliptical cylinder gave no effects regarding thermophysical properties.

Kondjoyan and Daudin (1995) measured experimentally the effect of free stream turbulence intensity on heat and mass transfers at the surface of a circular and elliptical cylinder with axis ratio 1 : 4. They found that the effect of turbulence intensity appeared to be as important as the influence of velocity and seemed to be independent of the pressure gradient and of the degree of turbulence intensity. Li et al. (1998) showed experimentally that the heat transfer rate with elliptical pin fins is higher than that with circular pin fins while the resistance of the former is much lower than that of the latter in the Reynolds number range from 1000 to 10000.

Arrays of Cylinders/ Tube Banks/ Pin-Fin Heat Sinks

Hattori and Takahashi (1993) performed experiments on forced convection heat transfer from a single transverse row of circular cylinders in cross flow. They measured local and average Nusselt numbers for a cylinder in the Reynolds number range from 80 to 6×10^3 and gave a correlation for average Nusselt number. Later Yamamoto and Hattori (1996) verified numerically their heat transfer values for the same arrangement. They found good agreement with those obtained from experiments in water by Hattori and Takahashi (1993).

Wang and Sangani (1997) conducted a numerical study to determine the Nusselt number for flow perpendicular to arrays of cylinders in the limit of small Reynolds and large Peclet numbers. They obtained a formula for relating the Nusselt number and the Darcy permeability of the arrays by fitting the results of their numerical simulations.

Based on the pertinent data available up to 1933, Colburn (1933) proposed a simple correlation of heat transfer data for flow across banks of staggered tubes as follows:

$$Nu_D = 0.33 Re_{Dmax}^{0.6} Pr^{1/3} \quad (2.10)$$

This correlation works well for 10 or more rows of tubes in the staggered arrangement and for $10 < Re_D < 40000$. Then Huge (1937), Pierson (1937), Omohundro et al. (1949), Bergelin et al. (1949, 1950, 1952), Jones and Monroe (1958), Gram et al. (1958), Žukauskas (1972), Aiba et al. (1981, 1982), and Žukauskas and Ulinskas (1988) reported extensive experimental data on heat transfer and fluid friction during viscous flow across in-line and staggered banks of tubes under different thermal boundary conditions. Grimison (1937) correlated the experimental data of Huge (1937) and Pierson (1937) for both arrangements and gave an equation of the form:

$$Nu_D = C Re_{Dmax}^n \quad (2.11)$$

His empirical relation pertain to tube banks having ten or more rows of tubes in the flow direction. The values of C and n are given in Table 2.4 for both in-line and staggered

arrangements. For fewer rows, Kays and Lo (1952) gave a correction factor C_2 (Table 2.5) such that:

$$Nu_D|_{N_L < 10} = C_2 Nu_D|_{N_L \geq 10} \quad (2.12)$$

Grimison (1937) also correlated the test measurements of Pierson (1937) and Hoge (1937) by a second method and derived the following expression:

$$Nu_D = 0.32 F_a Re_{Dmax}^{0.61} Pr^{0.31} \quad (2.13)$$

where the arrangement factor F_a was set out graphically by Grimison (1937) for the various values of Re_D dependent on the dimensionless transverse and longitudinal pitches.

Hausen (1983) modified slightly the above correlation and set out an empirical formula for the tubes arrangement factor F_a instead of the graphical representation by Grimison (1937). For an in-line arrangement:

$$Nu_D = 0.34 F_a Re_D^{0.61} Pr^{0.31} \quad (2.14)$$

can be used with

$$F_a = 1 + \left[a + \frac{7.17}{a} - 6.52 \right] \left[\frac{0.266}{(b-0.8)^2} - 0.12 \right] \sqrt{\frac{1000}{Re_D}} \quad (2.15)$$

and for a staggered arrangement:

$$Nu_D = 0.35 F_a Re_D^{0.57} Pr^{0.31} \quad (2.16)$$

can be employed with

$$F_a = 1 + 0.1a + \frac{0.34}{b} \quad (2.17)$$

where a and b are the dimensionless transverse and longitudinal pitches respectively. Žukauskas (1972) gave the following experimental correlation for the average Nusselt number for a tube bank consisting of 16 or more rows:

$$Nu_D = FC Re_{Dmax}^n Pr^m \quad (2.18)$$

Table 2.6: Constants for Grimison Correlation (Eq. 2.11)

$S_T/D \rightarrow$	1.25		1.5		2		3	
	C	n	C	n	C	n	C	n
Staggered								
0.600	-	-	-	-	-	-	.213	.636
0.900	-	-	-	-	0.446	0.571	0.401	0.581
1.000	-	-	0.497	0.558	-	-	-	-
1.125	-	-	-	-	0.478	0.565	0.518	0.560
1.25	0.518	0.556	0.505	0.554	0.519	0.556	0.522	0.562
1.5	0.451	0.568	0.460	0.562	0.452	0.568	0.488	0.568
2.000	0.404	0.572	0.416	0.568	0.482	0.556	0.449	0.570
3.000	0.310	0.592	0.356	0.580	0.440	0.562	0.421	0.574
In-Line								
1.250	0.348	0.592	0.275	0.608	0.100	0.704	0.0633	0.752
1.500	0.367	0.586	0.250	0.620	0.101	0.762	0.0678	0.744
2.000	0.418	0.570	0.299	0.602	0.229	0.632	0.198	0.648
3.000	0.290	0.601	0.357	0.584	0.374	0.581	0.286	0.608

Table 2.7: Correction Factor for Grimison Correlation when $N_L \leq 10$

Rows→	1	2	3	4	5	6	7	8	9	10
In-Line	0.64	0.80	0.87	0.90	0.92	0.94	0.96	0.98	0.99	1.00
Staggered	0.68	0.75	0.83	0.89	0.92	0.95	0.97	0.98	0.99	1.00

where the coefficients C , m , and n are given in Table 2.6 and the parameter F , given in Table 2.7, is a correction factor that accounts for fewer than 16 rows in the tube bank.

Lauder and Massey (1978), Fujii et al. (1984), Dhaubhadel et al. (1987), Wung and Chen (1989), Murray (1993), and Franz et al. (1995) presented numerical solutions of local heat transfer for the tube bank problem for a wide range of longitudinal and transverse pitches, Reynolds and Prandtl numbers.

Beale (1992) conducted a detailed numerical study of fluid flow and heat transfer in tube banks. Using complex function theory, he obtained a potential flow solution in the form of a power series. He presented his results in the form of skin friction, pressure drop, and heat transfer for different thermal boundary conditions. He got good agreement with the existing experimental and numerical data. Later Beale and Spalding (1998, 1999) extended the previous work for the laminar fully-developed cross flow and heat transfer in tube-bank heat exchangers. They obtained a wide range of results for in-line square, rotated square, and equilateral triangle configurations.

Gowda et al. (1998) carried out finite element simulations of transient laminar flow past an in-line tube bank. They solved two-dimensional unsteady Navier-Stokes and energy equations using an explicit and a semi-implicit algorithms for selected Reynolds and Prandtl numbers. They determined local and average Nusselt numbers, pressure, and shear stress distributions around the tubes.

Table 2.8: Constants for Žukauskas Correlation (Eq. 2.18)

Geometry	C	n	m	Conditions
In-Line				
	0.9	0.4	0.36	$10 \leq Re_{Dmax} \leq 100$
	0.52	0.5	0.36	$100 \leq Re_{Dmax} \leq 10^3$
	0.27	0.63	0.36	$10^3 \leq Re_{Dmax} \leq 2 \times 10^5$
	0.21	0.84	0.4	$Re_{Dmax} > 2 \times 10^5$
Staggered				
	1.04	0.4	0.36	$10 \leq Re_{Dmax} \leq 500$
	$0.35(S_T/S_L)^{0.2}$	0.60	0.36	$S_T/S_L < 2$ $10^3 \leq Re_{Dmax} \leq 2 \times 10^5$
	0.40	0.60	0.36	$S_T/S_L > 2$ $10^3 \leq Re_{Dmax} \leq 2 \times 10^5$
	0.022	0.84	0.36	$Re_{Dmax} > 2 \times 10^5$

Table 2.9: Correction Factor F for Žukauskas Correlation when $N_L \leq 16$

Rows→	1	2	3	4	5	7	10	13	16
In-Line	0.70	0.80	0.86	0.90	0.93	0.96	0.98	0.99	1.00
Staggered	0.64	0.76	0.84	0.89	0.93	0.96	0.98	0.99	1.00

Wilson and Bassiouny (2000) developed a mathematical model to simulate the laminar and turbulent flow fields inside tube banks. They solved the conservation equations of mass, momentum and energy using an implicit finite volume procedure. They found that the pressure drop and friction factor increased with the longitudinal pitch. They recommended the use of a longitudinal pitch ratio, $a \leq 3$ to obtain the best performance and to achieve a high degree of compactness in an in-line arrangement whereas $a \leq 1.5$ was needed to reduce friction and enhance Nu_D in the staggered arrangement.

Mandhani et al. (2002) solved the fluid flow and energy equations numerically to obtain detailed temperature fields and the distribution of Nusselt number on the surface of a typical cylinder in a cylinder bundle for the steady incompressible flow of Newtonian fluids. They found that the surface averaged value of Nusselt number increases with decreasing values of porosity and increasing values of Prandtl and Reynolds numbers. Their results were found in satisfactory agreement with the previous numerical and experimental data for a single cylinder and for the tube banks.

A summary of previous experimental/ numerical correlations for pin-fin arrays is presented in Table 2.8 and the other related studies are given below.

Hamilton et al. (2002) used a 3-D finite element based numerical simulation to model the heat transfer characteristics of a staggered short pin-fin array heat exchanger. The simulation was validated against available experimental data, and then used to estimate

overall array averaged heat transfer coefficient and pressure drop for various pin-fin configurations and Reynolds numbers. They proposed the following Nusselt number correlation for a limited range of configurations and Reynolds numbers:

$$Nu_D = C Re_{Dmax}^n \quad (2.19)$$

where the values of C and n are given in Table 2.9. This correlation works only for $3500 < Re_{Dmax} < 14000$.

Dvinsky et al. (2000) performed a numerical study of two square pin fin heat sinks using the commercial CFD software Coolit. They found that the in-line design was thermally superior to the staggered design for all but the fully-shrouded heat sinks. They also found that in a given geometry the non-dimensional pressure drop over a heat sink was almost constant, which indicates small viscous drag.

Jung and Maveety (2000) performed numerical experiments to investigate the turbulent fluid flow and heat transfer from three pin-fin heat sink geometries over the range of Re_D from 7,800 to 19,700 with air impingement cooling. They used a standard $\kappa - \epsilon$ turbulence model in predicting the Reynolds stresses. They found that the maximum heat transfer dissipated from a heat sink was obtained under turbulent flow conditions.

You and Chang (1997) predicted numerically the forced convection heat transfer rate for a cooling fluid through a pin-fin porous channel. They found that the flow inside the pin-fin channel reaches the fully developed thermal state in the early downstream region.

Wirtz et al. (1997) reported experimental results on the thermal performance of model pin-fin fan-sink assemblies. They used cylindrical, square, and diamond shape cross section pin-fins and found that cylindrical pin-fins give the best overall fan-sink performance. Furthermore, the overall heat sink thermal resistance decreases with an increase in either applied pressure rise or fan power and fin height.

Jonsson and Bjorn (1996) performed experiments to compare the thermal performance of the heat sinks with different fin designs including straight fins and pin fins with

Table 2.10: Summary of Previous Experimental/Numerical Correlations for Pin-Fin Heat Sinks

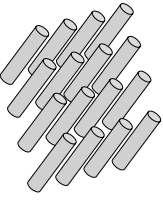
Configuration	Authors	Correlations/Models	Conditions
Pin-Fin Arrays 	Tahat et al. (2000)	$Nu_D = 0.00902 Re_D^{1.011} \left(\frac{S_T}{W}\right)^{0.285} \left(\frac{S_L}{H}\right)^{0.212}$ $Nu_D = 0.00704 Re_D^{0.953} \left(\frac{S_T}{W}\right)^{0.091} \left(\frac{S_L}{H}\right)^{0.053}$	<p>In-Line Arrangement</p> $3341.4 \leq Re_D \leq 6683$ $0.004 \leq \frac{S_T}{W} \leq 0.332$ $0.033 \leq \frac{S_L}{H} \leq 0.212$
	Wang and Sangani (1997)	$Nu_D = \frac{1}{N} \sum_{\alpha=1}^N \frac{q'}{2\pi\alpha\kappa(T_w - T_\infty)}$	<p>Staggered Arrangement</p> $3138 \leq Re_D \leq 4980$ $0.004 \leq \frac{S_T}{W} \leq 0.332$ $0.033 \leq \frac{S_L}{H} \leq 0.1522$
	Maudgal and Sunderland (1996)	$Nu_D = 0.003 Re_D^{1.197}$ $Nu_D = 0.032 Re_D^{0.964}$ $Nu_D = 0.066 Re_D^{0.894}$	$Re_D \rightarrow 0$ and $Pe_D \rightarrow 0$
	Wung and Chen (1989)	$Nu_D = 0.8 Re_D^{0.4} Pr^{0.37}$ $Nu_D = 0.78 Re_D^{0.45} Pr^{0.38}$	$Re_D = 2531, 3796, 5062$ $\frac{S_L}{D} = 1.5, 2, 3.0$
			For in-line array For staggered array

Table 2.11: Constants for Hamilton et al. (2002) Correlation (Eq. 2.19)

$S_T/D \rightarrow$	1.25		1.5		2		3	
	C	n	C	n	C	n	C	n
1.25	0.0905	0.7140	0.1024	0.7099	0.0860	0.7355	0.1377	0.6832
1.5	0.1881	0.6277	0.1247	0.6850	0.1465	0.6696	0.1826	0.6476
2.000	0.1406	0.6542	0.0813	0.7297	0.1203	0.6935	0.1619	0.6621
3.000	-	-	0.0750	0.7309	0.1504	0.6692	0.1094	0.7019

circular, quadratic and elliptical cross sections. They evaluated the thermal performance by comparing the thermal resistance of the heat sinks at equal average velocity and equal pressure drop. They recommended elliptical pin-fin heat sinks at high velocities and circular pin-fin heat sinks at mid-range velocities.

Babus’Haq et al. (1995) investigated experimentally the thermal performance of a shrouded vertical Duralumin pin-fin assembly in the in-line and staggered configurations. They found that under similar flow conditions and for an equal number of pin-fins, the staggered configuration yields a higher steady-state rate of heat transfer than the in-line configuration. They studied the effect of changing the thermal conductivity of the pin-fin material and found that the optimal separation between the pin-fins in the streamwise direction increased with the thermal conductivity of the pin-fin material, whereas the optimal separations in the spanwise direction remained invariant.

Azar and Mandrone (1994) investigated the effect of pin-fin density on thermal performance of unshrouded pin-fin heat sinks. They found an optimal number of pin fins

beyond which thermal resistance actually increased. They also found that thermal resistance was a function of the approach velocity and the governing flow pattern. Further, pin-fin heat sinks with a small number of pins had the best performance at low and moderate forced convection cooling.

Minakami and Iwasaki (1994) conducted experiments to investigate the pressure loss characteristics and heat transfer performance of pin-fin heat sinks exposed to air flow in a cross-flow direction, varying the pin pitch as a parameter. They found that as the longitudinal pitch increased, the heat transfer coefficient increased and the pressure loss also increased. Further, as the transverse pitch decreased, the heat transfer coefficient increased, but the pressure loss increased drastically compared to the Nu_D .

The steady-state thermal and air-flow resistance performances of horizontally-based pin-fin assemblies were investigated experimentally by Tahat et al. (1994). They studied the effects of varying the geometrical configurations of the pin-fins and found the optimal pin-fin separation in both streamwise as well as spanwise directions to achieve maximum heat transfer rate. They established a general empirical correlation for the average Nusselt number which can be used for both in-line and staggered arrangements.

$$Nu_D = 0.355 \left(\frac{S_T}{W} \right)^{0.0446} \left(\frac{S_L}{L} \right)^{0.048} Re_{Dmax}^{0.585} \quad (2.20)$$

Later Tahat et al. (2000) repeated previous experiments for a wider range of Re_{Dmax} , S_T/W , and S_L/L to give separate correlations for the in-line and staggered arrangements.

Damerow et al. (1972) studied pin fin channels with ten rows of pins. Their aspect ratio H/D varied from 2 to 4 with various pin spacing geometries. They found that H/D had no effect on the friction factor and that their data were well above the long tube correlation of Jakob (1938). They suggested the following correlation for the friction factor:

$$f = 2.06(S_L/D)^{-1.1} Re_{Dmax}^{-0.16} \quad (2.21)$$

Van Fossen (1982) and Metzger et al. (1981, 1982a, 1982b, 1983, 1986) have done similar but independent studies of short pin fin banks with various aspect ratios and

spacings for the staggered array. VanFossen studied the average heat transfer effects of the first four rows of pins and deduced the heat transfer coefficients of the pins relative to the endwalls whereas Metzger and his co-workers studied the row-by-row variation of average heat transfer and characterized that variation with a single curve. They also studied the relative effects of streamwise pin spacing and end wall on array heat transfer.

Armstrong and Winstanley (1988) presented a review of works specifically on short pin fin arrays. They showed that not only is the existence of an active bounding wall a significant departure from the classical tube bundle situations, but also that the heat transfer from the pins themselves is lower than from long pin fins/cylinders. Heat transfer for short pin fin arrays has been found to be a function of Reynolds number Re_D , Prandtl number Pr , longitudinal pitch S_L/D , transverse pitch S_T/D , and the aspect ratio H/D .

And while a limited number of correlations have been proposed based on the analysis of pin fin arrays, there is currently no known analytical correlation in the open literature suitable for the analysis of the pin fin heat sink geometry considered in this study which encompasses all the effects.

2.3 Optimization

The following studies on optimization of pin-fin heat sink geometries were found in the literature:

Poulikakos and Bejan (1982) established a theoretical framework to determine the optimum fin dimensions for minimum entropy generation in forced convection. They first developed an expression for the entropy generation rate for a general fin and then applied it to select the optimum dimensions of pin fins, rectangular plate fins, plate fins with trapezoidal cross section, and triangular plate fins with rectangular cross section. Their study seems to be inconclusive as to which geometry offers advantages over others.

Bejan and Morega (1993) reported the optimal geometry of an array of fins that

minimizes the thermal resistance between the substrate and the forced flow through the fins. They modeled pin-fin arrays as the Darcy-flow porous medium and expressed the local thermal conductance in dimensionless form.

Jubran et al. (1993) performed an experimental investigation on the effects of inter-fin spacing, shroud clearance, and missing pins on the heat transfer from cylindrical pin fins arranged in staggered and in-line arrays. They found that the optimum inter-fin spacing in both span wise and stream wise directions is $2.5D$ regardless of the type of array and shroud clearance used. They also found the effect of missing fins to be negligible for the in-line array but more significant for the staggered arrays. Later, Bejan (1995) extended the previous work of Jubran et al. and proved the existence of an optimal spacing between the cylinders. He showed that this optimal spacing increases with the length of the bundle and decreases with the applied pressure difference and the Prandtl number.

Stanescu et al. (1996) performed an experimental, numerical and analytical study of the optimal spacing between cylinders in crossflow forced convection. They determined optimal cylinder-to-cylinder spacing by maximizing the overall thermal conductance between all the cylinders and the free stream. They found that the optimal spacing decreases as the Re_D increases, and as the flow length of the array L decreases.

Shaukatuallah et al. (1996) performed a study to optimize the design of pin fin heat sinks for use in low velocity applications typically encountered in personal computers and low end work stations. They found that for pin fin heat sinks up to 15 mm high and base sizes of about 25×25 mm, the 6×6 pin fin configuration with fin cross sections of 1.5×1.5 mm appears to be a good practical choice for use in low velocity, open flow type conditions.

Rocha et al. (1997) performed a comparative study of elliptical and circular sections in one- and two row tubes. They used experimentally determined heat transfer coefficients from a heat and mass transfer analogy. They observed a relative fin efficiency gain of up to 18% in the sections, as compared to the circular ones.

Lin and Lee (1997) performed a second law analysis on a pin-fin array under forced flow conditions. They evaluated optimal operational/design conditions for both the in-line and staggered fin alignments. They considered the heat transfer contributions from the base wall as well as from the fin surface and found the optimal Re_D values as 2068 for the in-line and 1974 for the staggered alignment. It is also noted that in the range where $Re_D < Re_{Dopt}$, the in-line array would generate more entropy than does the staggered arrays and that Re_{Dopt} increases with the decreasing slenderness ratio, whereas the corresponding entropy generation number decreases only slightly.

Zapach (2000) verified experimentally a model for the optimization of pin-fin heat sinks. This model was based on Žukauskas (1972) correlations of flow resistance and heat transfer from studies of tube bank heat exchangers. With some minor modification to the heat transfer correlation, he presented a model that can be used to optimize inter-pin spacing based on a constant fluid velocity or a fan curve.

Kondo et al. (2000) presented a semi-empirical zonal approach for the design and optimization of pin-fin heat sinks cooled by impingement. They calculated the thermal resistance and pressure drop for an air-cooled heat sink and performed experiments and flow visualization to validate the model predictions.

2.4 Comparison of Existing Models and Data

The variation of the total drag coefficient C_D with Re_D is shown in Fig. 2.2 for an infinite cylinder. The numerical results of Takami and Keller (1969), Dennis and Chang (1970), Nieuwstadt and Keller (1973), Sucker and Brauer (1975), and D’Alessio and Denis (1994) are compared with the experimental data of Wieselsberger (1921). It is clear that all the results are in good agreement.

The average Nusselt numbers for the isothermal boundary condition are compared in Fig. 2.3. It shows that the correlations of Churchill and Bernstein (1977), Žukauskas

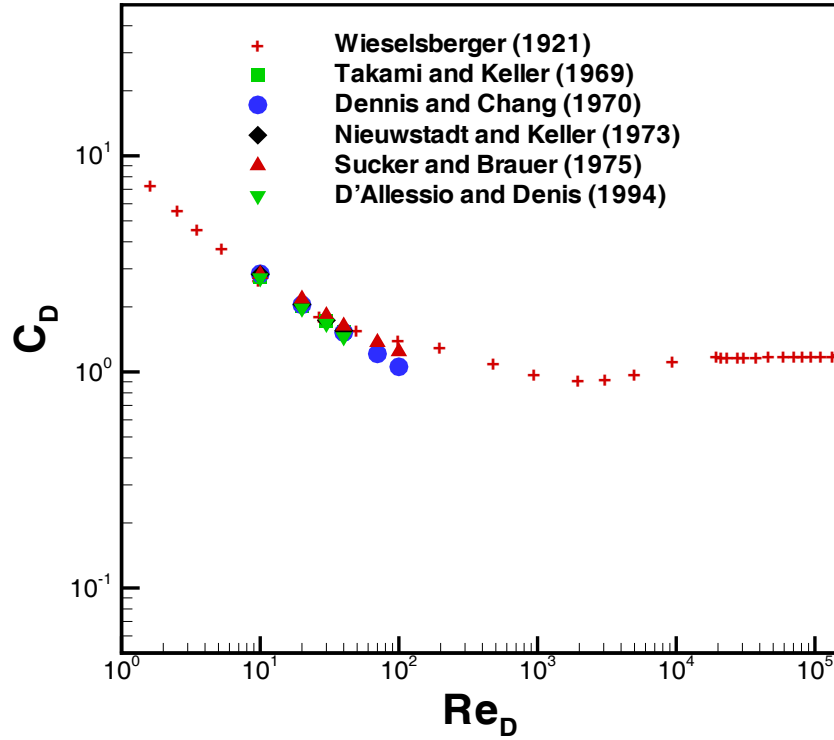


Figure 2.2: Comparison of Drag Data for a Single Circular Cylinder

(1972), Morgan (1975), and of Hilpert (1933) are in good agreement for the whole laminar range.

Previous experimental/numerical data of average Nusselt numbers for the isoflux boundary condition is plotted in Fig. 2.4. Numerical results of Krall and Eckert (1973) and Chun and Boehm (1989) are found in good agreement with the experimental data of Sarma and Sukhatme (1977).

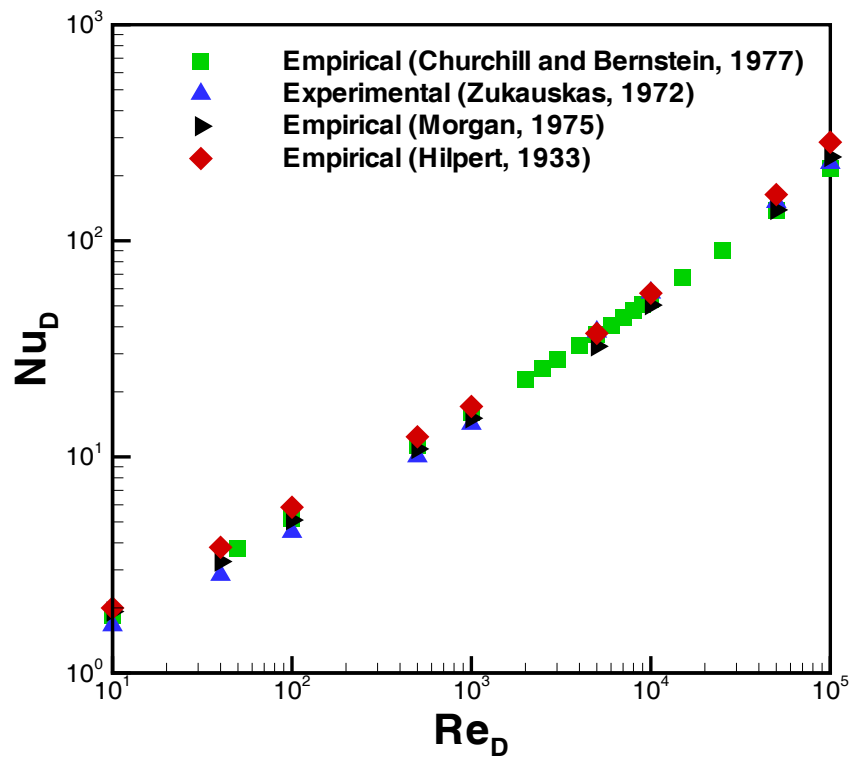


Figure 2.3: Variation of Average Nusselt Number with Reynolds Number for Isothermal Boundary Condition

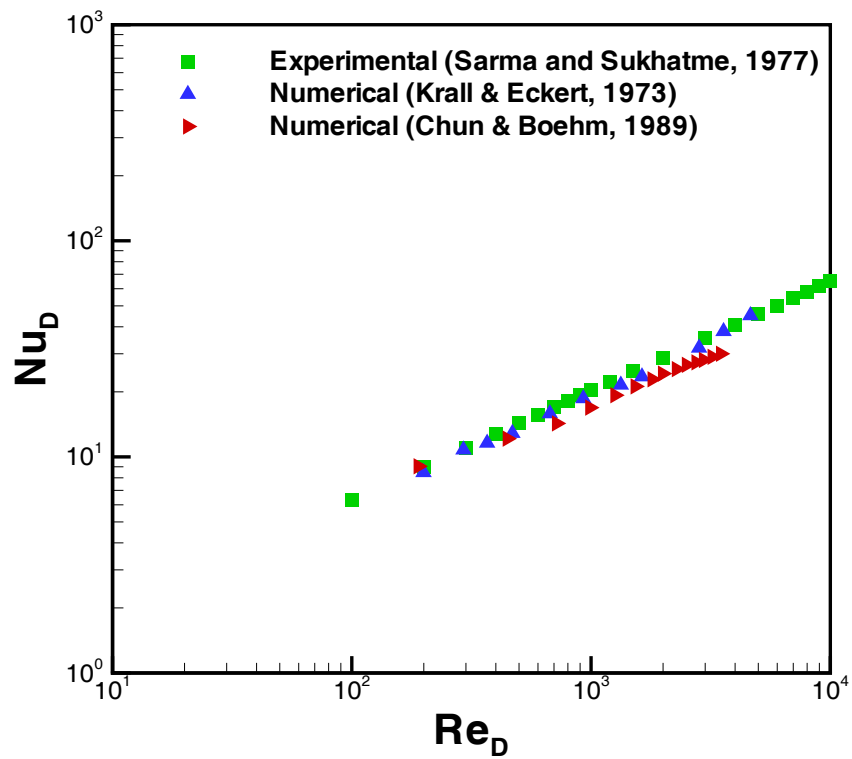


Figure 2.4: Variation of Average Nusselt Number with Reynolds Number for Isoflux Boundary Condition

2.5 Summary

A description of the models and data available in the literature for a single (circular and elliptical) and multiple cylinders, including tube bundles, pin-fin arrays and pin-fin heat sinks has been presented. The majority of the data belongs to experimental or numerical simulations for all the geometries and is only applicable over a limited range of conditions. The available empirical heat transfer correlations are valid only for a limited range of Reynolds numbers and are applicable for air only. No single correlation exists for fluid friction or heat transfer that could be used for a single pin (circular or elliptical) or pin-fin arrays for a wide range of parameters like Reynolds numbers, Prandtl numbers, longitudinal and transverse pitches. The lack of such important correlations for fluid friction and heat transfer motivated the current author to start this work analytically which is declared in most of the heat transfer books (like Holman, 1992, Žukauskas and Žiugžda, 1985) “that due to non linear momentum and energy equations, it is not possible to calculate analytically the average heat transfer coefficients for circular cylinders in cross flow.”

Chapter 3

Fluid Flow Modeling

3.1 Introduction

It has been observed experimentally by Incropera and DeWitt (1999) that the flow around a cylinder can be approximated as the flow around a single pin in cross flow, which has been discussed in many fluid mechanics and heat transfer books. Due to the pressure gradient, the flow is complicated by boundary layer separation, which yields a wake region immediately behind the pin. Flow separation from a cylindrical pin produces pressure drag that dominates the pressure drop around the pin rather than skin friction. Viscous losses in the wake behind the pin combined with the pressure drag result in higher pressure drop than that caused by the viscous effects.

The flow field adjacent to the pin should be strongly affected by the fact that one end of the pin is wall-attached while the other end is free. This arrangement should give rise to a transverse flow component (in the direction of the pin axis) superposed on the main flow that passes around the periphery. As a consequence, the wake flow should be strongly 3-D. In order to simplify the analysis, it is assumed that the flow is laminar, steady, and 2-D.

In this chapter an approximate analytical method, known as the Von Karman-Pohlhausen

method, is used to investigate fluid flow over isolated circular and elliptical pins. A fourth order velocity profile in the hydrodynamic boundary layer is used to obtain a closed form solution for the fluid flow. Figure 3.1 shows the flow chart for the calculation of drag coefficients for the flow over a cylindrical/ elliptical pin. The momentum equation in the integral form is used to obtain the solution. Finally, in-line and staggered arrangements are studied.

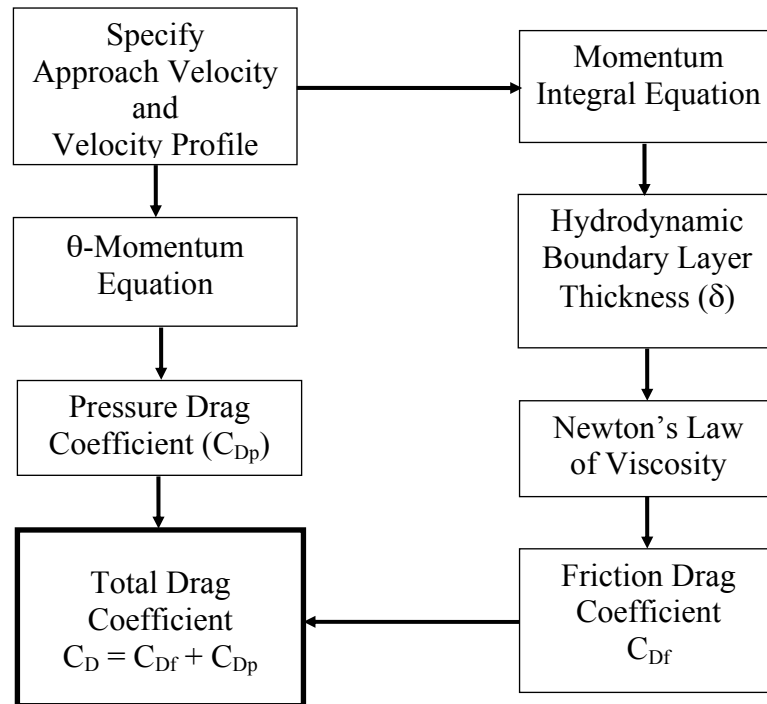


Figure 3.1: Flow Chart for Calculating Drag Coefficients

3.2 Circular Pin in an Infinite Flow

3.2.1 Analysis

Consider a circular pin of diameter D , which is extended from a wall at temperature T_b and situated in cross flow with vanishing circulation around it, as shown in Fig. 3.2.

The approaching velocity of the air is U_{app} and the ambient temperature of the air is assumed to be T_a . The surface temperature of the pin wall is $T_w (> T_a)$ in the case of the isothermal pin and the heat flux is q for the isoflux boundary condition.

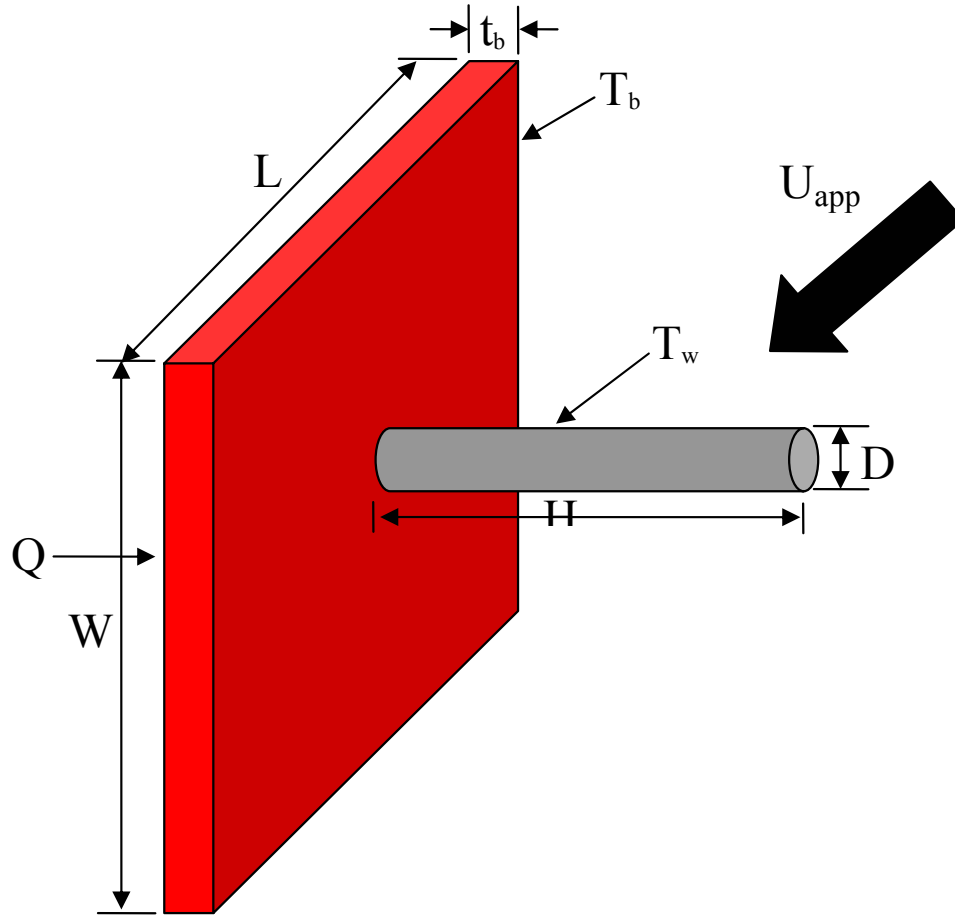


Figure 3.2: Cylindrical Pin-Fin in Cross Flow

Using an order-of-magnitude analysis (Appendix A), the reduced equations of continuity and momentum in a curvilinear system (Fig. 3.3) are written as:

Continuity:

$$\frac{\partial u}{\partial s} + \frac{\partial v}{\partial \eta} = 0 \quad (3.1)$$

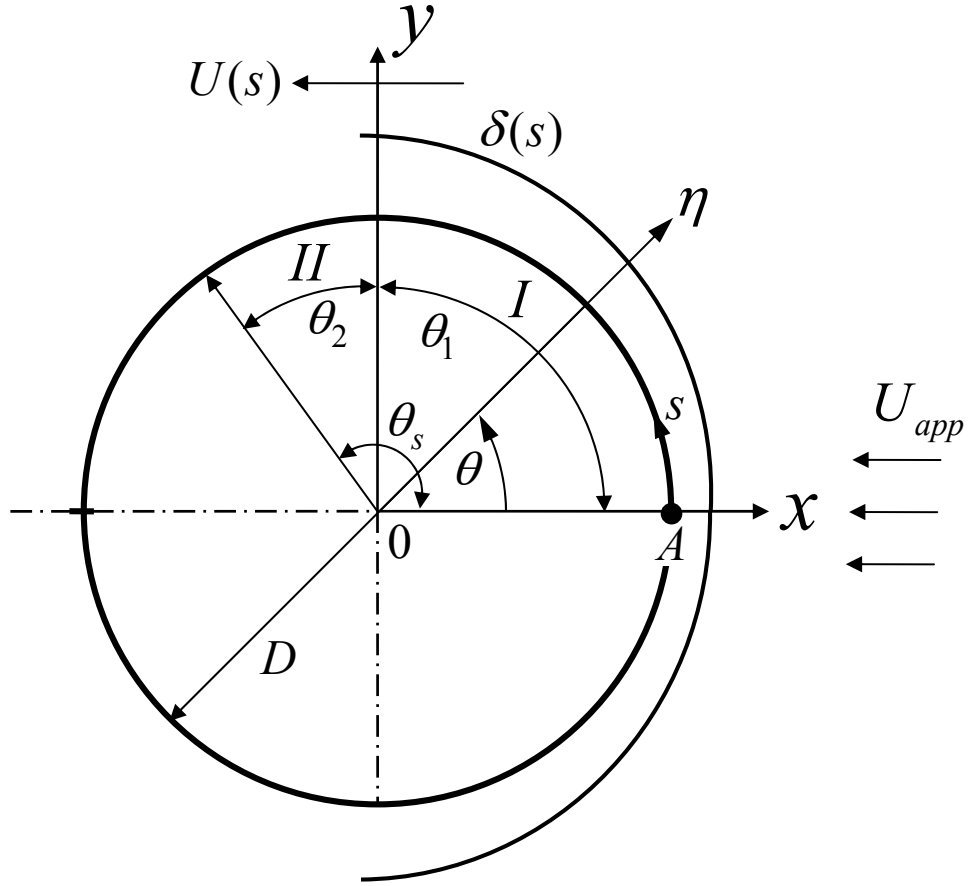


Figure 3.3: Curvilinear Coordinates for Flow Over a Circular Pin

s-Momentum:

$$u \frac{\partial u}{\partial s} + v \frac{\partial u}{\partial \eta} = -\frac{1}{\rho} \frac{dP}{ds} + \nu \frac{\partial^2 u}{\partial \eta^2} \quad (3.2)$$

η -Momentum:

$$\frac{dp}{d\eta} = 0 \quad (3.3)$$

Bernoulli Equation:

$$-\frac{1}{\rho} \frac{dP}{ds} = U(s) \frac{dU(s)}{ds} \quad (3.4)$$

where $U(s)$ is the potential flow velocity which is obtained from the complex potential for a circular pin of diameter D in a uniform flow (Appendix D).

3.2.2 Boundary-Layer Parameters

In dimensionless form, the momentum integral equation can be written as:

$$\frac{U \delta_2}{\nu} \frac{d\delta_2}{ds} + \left(2 + \frac{\delta_1}{\delta_2}\right) \frac{\delta_2^2}{\nu} \frac{dU}{ds} = \frac{\delta_2}{U} \frac{\partial u}{\partial \eta} \Big|_{\eta=0} \quad (3.5)$$

where δ_1 and δ_2 are the displacement and momentum thicknesses, given by:

$$\delta_1 = \delta \int_0^1 \left[1 - \frac{u}{U(s)}\right] d\eta_H \quad (3.6)$$

$$\delta_2 = \delta \int_0^1 \frac{u}{U(s)} \left[1 - \frac{u}{U(s)}\right] d\eta_H \quad (3.7)$$

Using the velocity distribution inside the boundary layer, Eq. (C-2), Eqs. (3.6) and (3.7) can be written as:

$$\delta_1 = \frac{\delta}{10} \left(3 - \frac{\lambda}{12}\right) \quad (3.8)$$

$$\delta_2 = \frac{\delta}{63} \left(\frac{37}{5} - \frac{\lambda}{15} - \frac{\lambda^2}{144}\right) \quad (3.9)$$

Assuming,

$$Z = \frac{\delta_2^2}{\nu} \quad \text{and} \quad K = Z \frac{dU}{ds}$$

Equation (3.5) can be reduced to a non-linear differential equation of the first order for Z :

$$\frac{dZ}{ds} = \frac{H(K)}{U} \quad (3.10)$$

where $H(K) = 2f_2(K) - 2K[2 + f_1(K)]$ is a universal function and is approximated by Walz (1941) using a straight line:

$$H(K) = 0.47 - 6K \quad (3.11)$$

with

$$f_1(K) = \frac{63(3 - \lambda/12)}{10(37/5 - \lambda/15 - \lambda^2/144)} \quad (3.12)$$

$$f_2(K) = \frac{1}{63} \left(2 + \frac{\lambda}{6}\right) \left(\frac{37}{5} - \frac{\lambda}{15} - \frac{\lambda^2}{144}\right) \quad (3.13)$$

$$K = \frac{\lambda}{3963} \left(\frac{37}{5} - \frac{\lambda}{15} - \frac{\lambda^2}{144} \right)^2 \quad (3.14)$$

Solving Eq. (3.10) with Eq. (3.11), the local dimensionless momentum thickness can be written as:

$$\frac{\delta_2}{D} = \frac{0.3428}{\sqrt{Re_D}} \sqrt{\frac{1}{\sin^6 \theta} \int_0^\theta \sin^5 \zeta d\zeta} \quad (3.15)$$

where ζ is a dummy variable and Re_D is the Reynolds number which is defined as:

$$Re_D = \frac{U_{app} D}{\nu} \quad (3.16)$$

From Eq. (C-3), the local dimensionless boundary layer thickness can be written as:

$$\frac{\delta}{D} = \sqrt{\frac{\lambda}{4 Re_D \cos \theta}} \quad (3.17)$$

The point of separation is defined as the point where the velocity gradient normal to the pin wall surface is zero, i.e.:

$$\left. \frac{\partial u}{\partial \eta} \right|_{\eta=0} = 0 \quad (3.18)$$

which gives the angle of separation as $\theta_s = 107.71^\circ$. The angle of separation, calculated in this study, depends closely on the velocity distribution inside the boundary layer (Eq. C-2). Schoenauer (1964) found (numerically) that the separation angle, for a circular pin, is at $\theta_s = 104.5^\circ$ as against $\theta_s = 109.5^\circ$ obtained by Schlichting (1979) with the aid of the Pohlhausen approximation and $\theta_s = 108.8^\circ$ suggested by the Blasius series expansion up to x^{11} terms. Žukauskas and Žiugžda (1985) found the separation angle as $\theta_s = 82^\circ$ using Hiemenz (1911) experimental velocity distribution and as $\theta_s = 105^\circ$ using potential flow velocity (Eq. D-7).

By solving Eqs. (3.9) and (3.17) and comparing the results with Eq. (3.15), the values of the pressure gradient parameter λ are obtained corresponding to each position along the pin surface. These values are found to be positive from $0 \leq \theta \leq \pi/2$ (region I) and negative from $\pi/2 < \theta \leq \theta_s = 107.71^\circ$ (region II). So the whole range of interest $0 \leq \theta \leq \theta_s$ can be divided into two regions and the λ values can be fitted separately by the least

Table 3.1: Coefficients in Eqs. (3.19) and (3.20)

j	0	1	2	3	4	5
a_j	1.000	-0.0053	-0.1344	-0.2998	0.6335	-0.7937
b_j	-2521.735	2834.998	-219.186	-262.703	109.967	-349.374

j	6	7	8	9	10
a_j	0.4583	-0.1123	-	-	-
b_j	131.419	-7.360	43.564	-21.629	1.564

squares method into two polynomials, i.e., for region I:

$$\lambda_1 = 7.239 \sum_{j=0}^7 a_j \theta^j \quad (3.19)$$

and for region II:

$$\lambda_2 = 0.3259 \sum_{j=0}^{10} b_j \theta^j \quad (3.20)$$

where a_j and b_j are the coefficients given in Table 3.1 and θ is the angle measured from the front stagnation point in radians. These polynomials will be used to determine the drag and the local heat transfer coefficients in both regions. The values of the boundary layer parameters for a circular pin are presented in Appendix G (Table G.1).

3.2.3 Fluid Friction

For a circular pin, the area of a small surface element per unit length of the pin can be written as:

$$dA = \frac{D}{2} d\theta \quad (3.21)$$

and the characteristic area is the projected area per unit length of the pin, which can be written as:

$$A = D \quad (3.22)$$

So, the skin friction and the friction drag coefficients can be determined from Eqs. (E-5) and (E-6):

$$C_f = \frac{4}{3\sqrt{Re_D}} (\lambda + 12) \sin \theta \sqrt{\frac{\cos \theta}{\lambda}} \quad (3.23)$$

and

$$\begin{aligned} C_{Df} &= \frac{4}{3\sqrt{Re_D}} \int_0^\pi (\lambda + 12) \sin^2 \theta \sqrt{\frac{\cos \theta}{\lambda}} d\theta \\ &= \frac{4}{3\sqrt{Re_D}} \left\{ \int_0^{\theta_s} (\lambda + 12) \sin^2 \theta \sqrt{\frac{\cos \theta}{\lambda}} d\theta + \int_{\theta_s}^\pi (\lambda + 12) \sin^2 \theta \sqrt{\frac{\cos \theta}{\lambda}} d\theta \right\} \end{aligned} \quad (3.24)$$

Since no shear stress acts on the pin surface after boundary layer separation, the friction drag coefficient can be written as:

$$\begin{aligned} C_{Df} &= \frac{4}{3\sqrt{Re_D}} \int_0^{\theta_s} (\lambda + 12) \sin^2 \theta \sqrt{\frac{\cos \theta}{\lambda}} d\theta \\ &= \frac{4}{3\sqrt{Re_D}} \left\{ \int_0^{\pi/2} (\lambda_1 + 12) \sin^2 \theta \sqrt{\frac{\cos \theta}{\lambda_1}} d\theta + \int_{\pi/2}^{\theta_s} (\lambda_2 + 12) \sin^2 \theta \sqrt{\frac{\cos \theta}{\lambda_2}} d\theta \right\} \\ &= \frac{5.784}{\sqrt{Re_D}} \end{aligned} \quad (3.25)$$

where the pressure gradient parameters λ_1 and λ_2 are given by Eqs. (3.19) and (3.20).

For the circular pin, pressure difference ΔP can be obtained by integrating the θ -momentum equation, Eq. (A-6) with respect to θ . Using the velocity components u_r and

u_θ , Eq. (D-5), and their derivatives with respect to r and θ in Eq. (A-6), we get:

$$\frac{dP}{d\theta} = -(2\rho U_{app}^2) \sin 2\theta - \frac{\nu U_{app} \rho}{D} \sin \theta \quad (3.26)$$

Integrating both sides w. r. t. θ and simplifying, we get:

$$\Delta P = -(\rho U_{app}^2)(\cos 2\theta - 1) - \frac{4\nu U_{app} \rho}{D}(\cos \theta - 1) \quad (3.27)$$

In dimensionless form, it can be written as:

$$C_p = \frac{\Delta P}{\frac{1}{2}\rho U_{app}^2} = -2(1 - \cos \theta) - \frac{8}{Re_D}(1 - \cos \theta) \quad (3.28)$$

Thus, the pressure drag coefficient for the circular pin up to the separation point is:

$$\begin{aligned} C_{Dp} &= \int_0^{\theta_s} C_p \cos \theta d\theta \\ &= 1.152 + \frac{1.260}{Re_D} \end{aligned} \quad (3.29)$$

Equations (3.25) and (3.29) show the effects of Reynolds number on the friction and pressure drags. At low Reynolds number the pressure drag is insignificant and is proportional to $1/Re_D$, but at high Reynolds numbers it is independent of Re_D . This behavior is shown in Fig. 3.4. The contribution of the friction drag to the pressure drag was found to be in the range 50 to 2% for Re_D from 30 to 10^4 by Goldstein (1965), 3 to 1% for Re_D from 5×10^3 to 10^6 by Žukauskas and Žiugžda (1985). Figure 3.5 shows similar results of the contribution of the friction drag to the pressure drag obtained in the present analysis.

The total drag coefficient C_D can be written as the sum of both drag coefficients:

$$\begin{aligned} C_D &= C_{Df} + C_{Dp} \\ &= \frac{5.784}{\sqrt{Re_D}} + 1.152 + \frac{1.260}{Re_D} \end{aligned} \quad (3.30)$$

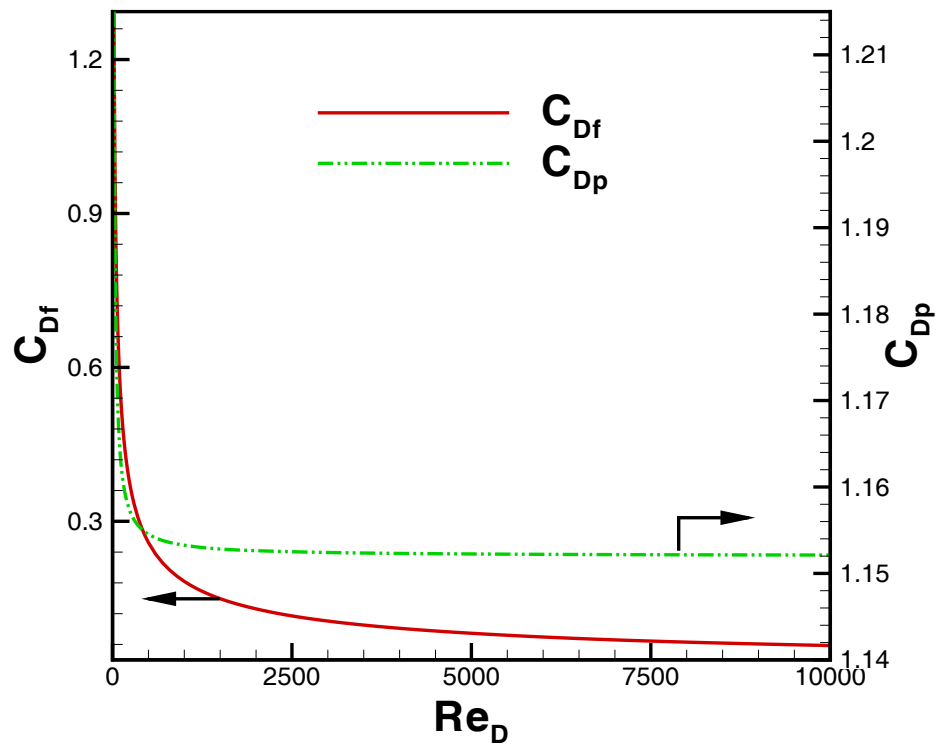


Figure 3.4: Friction and Pressure Drag Coefficients for Flow Over a Circular Pin

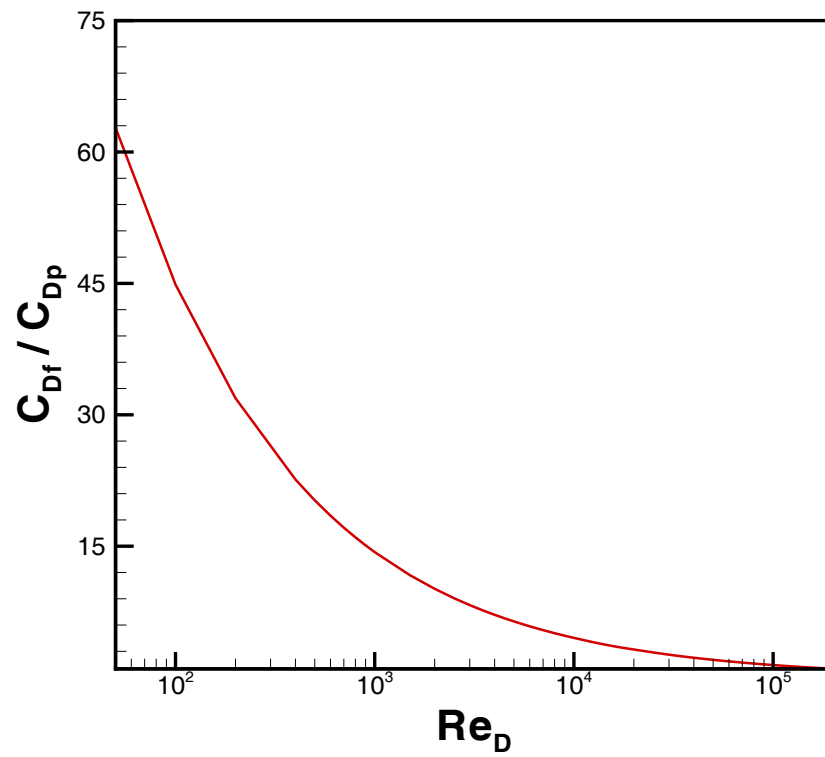


Figure 3.5: Ratio of Friction Drag to Pressure Drag for a Single Circular Pin

3.3 Single Elliptical Pin in an Infinite Flow

Elliptical pins provide more general geometrical configurations than circular pins. In the limiting cases, they represent a horizontal plate-fin when the minor-major axis ratio $\epsilon \rightarrow 0$, and a circular pin when the axis ratio $\epsilon \rightarrow 1$. Thus a systematic analytical investigation of elliptical geometries can provide not only flow and heat transfer characteristics from elliptical pins of different axis ratios but also from circular pins and finite plate-fins. In this section, closed form expressions will be derived for the drag coefficients of elliptical pins of arbitrary axis ratio and for the limiting cases they will be used for the circular pins and finite plates. The basic parameters involved in this case are the axis ratio ϵ , and the Reynolds numbers.

3.3.1 Analysis

Consider uniform flow of a Newtonian fluid past a fixed elliptical pin with a major axis of $2a$ and a minor axis of $2b$. The pin is oriented so that the major axis is parallel to the direction of the net flow in the main stream, thus making one end of the major axis a point of stagnation (Fig. 3.6). The flow conditions are the same as mentioned for circular pins.

The radius of curvature of the surface is denoted by r . For a fair comparison of fluid flow and heat transfer from an elliptical pin with that of a circular pin and a plate-fin, an appropriate characteristic length is used in both the Reynolds and the Nusselt numbers. This characteristic length \mathcal{L} is defined as the equivalent diameter of a circular pin, whose perimeter is the same as that of the elliptical pin and that of the plate-fin. In this case, the distance covered by the flow will be the same along the surface of the three geometries. This length is given by:

$$\mathcal{L} = 4a E(e)/\pi \quad (3.31)$$

where $e = \sqrt{1 - \epsilon^2}$ is the eccentricity and $E(e)$ is an associated complete elliptic integral

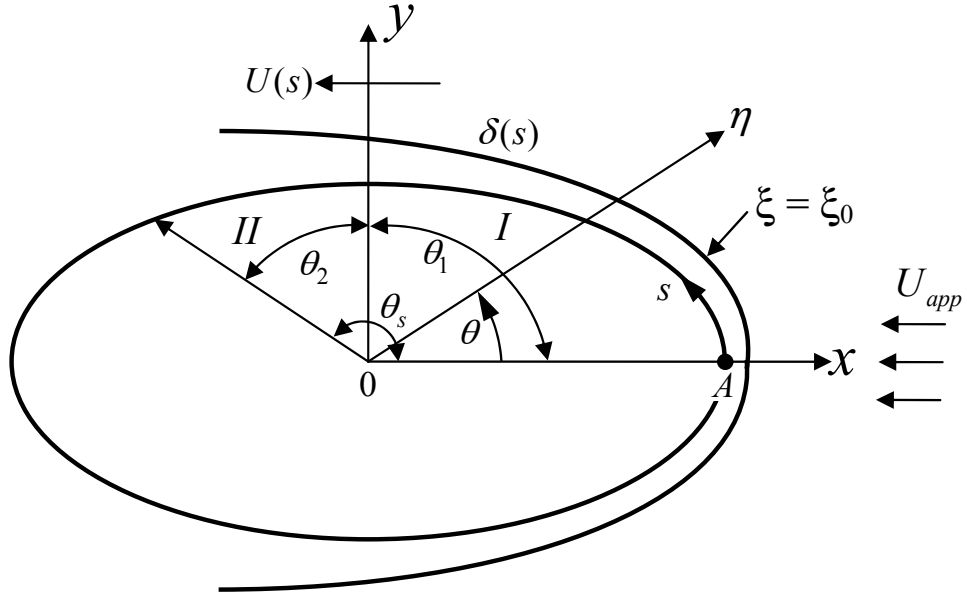


Figure 3.6: Curvilinear Coordinates For the Flow Over an Elliptic Pin

of the second kind. In the limiting cases, this characteristic length gives the diameter of a circular pin and the finite length of a plate-fin.

The potential flow velocity just outside the boundary layer is given by Eq. (D-20) and the simplified boundary layer equations, in curvilinear coordinates, are the same as mentioned in section 3.1.

3.3.2 Boundary-Layer Parameters

Using Eq. (D-20) and following the same procedure, as for the circular pin, the dimensionless momentum and hydrodynamic boundary layer thicknesses can be written as:

$$\frac{\delta_2}{\mathcal{L}} = \frac{0.6076}{\sqrt{Re_{\mathcal{L}}}} \sqrt{\frac{(1 - e^2 \cos^2 \theta)^3}{(1 + \epsilon)E(e) \sin^6 \theta} \int_0^\theta \frac{\sin^5 \theta d\theta}{(1 - e^2 \cos^2 \theta)^2}} \quad (3.32)$$

$$\frac{\delta}{\mathcal{L}} = \frac{0.8862}{Re_{\mathcal{L}}} \sqrt{\frac{\lambda}{\cos\theta} \frac{(1 - e^2 \cos^2\theta)}{\sqrt{\epsilon^2(1+\epsilon)E(e)}}} \quad (3.33)$$

By solving Eqs. (3.9) and (3.33) and comparing the results with Eq. (3.32), the values of the pressure gradient parameter λ are obtained corresponding to each position along the elliptic pin surface for different axis ratios. Again the whole range of interest $0 \leq \theta \leq \theta_s$ is divided into two regions and the λ values are fitted separately using a least squares procedure into two polynomials for each axis ratio.

3.3.3 Fluid Friction

In the case of the elliptical geometry, the radial distance to any point on the ellipse surface $\xi = \xi_0$ is not constant with θ and is given by:

$$r = a \sqrt{1 - e^2 \cos^2\theta} \quad (3.34)$$

therefore, the length ds of the small element will be:

$$ds = a \sqrt{1 - e^2 \cos^2\theta} d\theta \quad (3.35)$$

Using the potential flow velocity Eq. (D-20), the dimensionless shear stress on the elliptic surface can be determined from Eq. (E-5):

$$C_f = \frac{\tau_w}{\frac{1}{2}\rho U_{app}^2} = \frac{1}{3} \frac{\epsilon(1+\epsilon)(\lambda+12)\sin\theta}{\sqrt{Re_{\mathcal{L}}}(1-e^2\cos^2\theta)^{3/2}} \sqrt{\frac{2(1+\epsilon)\cos\theta}{\lambda}} \quad (3.36)$$

The dimensionless shear stress, $C_f \sqrt{Re_D}$, at the wall of pins of different axis ratios is shown in Fig. 3.7. It shows that C_f is zero at the stagnation point for each case and reaches a maximum at a certain angles which decrease with the axis ratio. The increase in shear stress is caused by the deformation of the velocity profiles in the boundary layer, a higher velocity gradient at the wall and a thicker boundary layer. In the region of decreasing C_f preceding the separation point, the pressure gradient decreases further

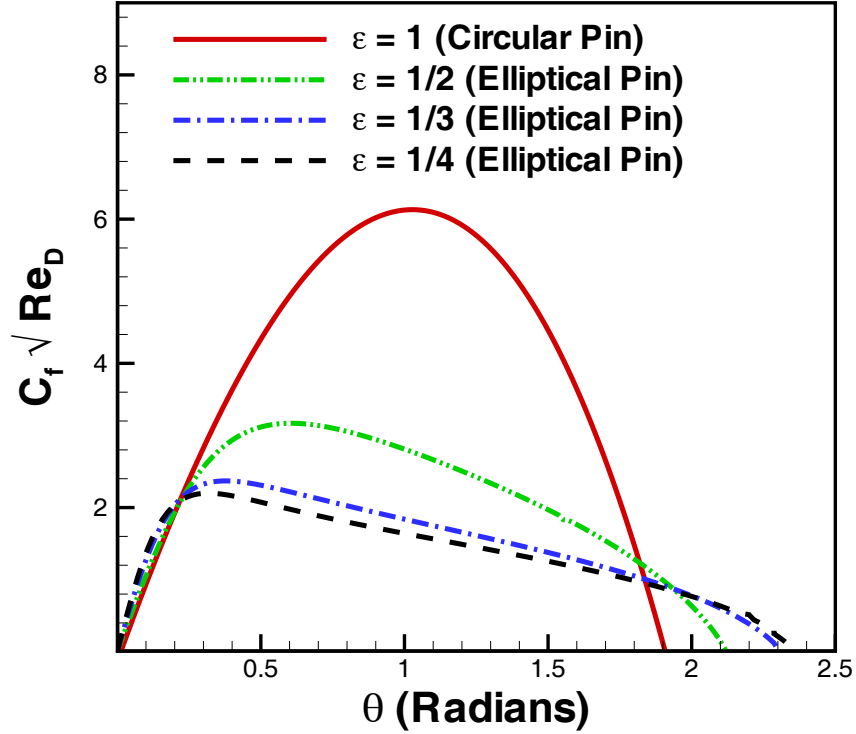


Figure 3.7: Variation of Skin Friction for Elliptical Pins of Different Axis Ratios

and finally C_f falls to zero at the separation angle which increases with the axis ratio. These angles are presented in Table 3.2. Beyond the separation point, C_f remains close to zero up to the rear stagnation point. The results for the circular pin are also shown in Fig. 3.7 for the purpose of comparison. The boundary layer parameters, for different axis ratios of elliptical pins, are presented in Appendix G (Tables 2-4). The total drag coefficients versus axis ratio are plotted in Fig. 3.8 for different Reynolds numbers. It is clear that the total drag coefficient decreases from circular pin ($\epsilon = 1$) to finite plate-fin ($\epsilon = 0.01$) and then it becomes constant. For high axis ratios, these coefficients depend upon the Reynolds numbers but for lower axis ratios the coefficients are independent of Reynolds numbers.

Table 3.2: Angle of Separation for Different Axis Ratios of Elliptic Pin

ϵ	1	0.9	0.8	0.6	0.5	0.4	0.3	0.2	0.1	0.01
θ_s	107.7	109.5	111.7	117.6	121.5	126.4	132.6	140.6	151.7	171.0

The friction drag coefficient can be determined from Eq. (E-6):

$$\begin{aligned}
 C_{Df} &= \int_0^\pi C_f \sin \theta d\theta \\
 &= \int_0^{\theta_s} C_f \sin \theta d\theta + \int_{\theta_s}^\pi C_f \sin \theta d\theta
 \end{aligned} \tag{3.37}$$

Since no shear stress acts on the pin surface after boundary layer separation, the second integral will be zero and the friction drag coefficient can be written as:

$$C_{Df} = \int_0^{\theta_s} C_f \sin \theta d\theta \tag{3.38}$$

where θ_s is the angle of separation which depends upon the velocity distribution, Eq. (C-2), chosen inside the boundary layer. These angles of separation, for different axis ratios, are given in Table 3.3. It is important to note that these results follow the trend of Schlichting and Ulrich (1942) and Schubauer (1935), but do not confirm the trend of Modi et. al (1992). The friction drag coefficients are calculated for different axis ratios and a general correlation is deduced in terms of arbitrary axis ratio and Reynolds number:

$$C_{Df} = \frac{1.353 + 4.43\epsilon^{1.35}}{\sqrt{Re_L}} \tag{3.39}$$

In the limiting case when $\epsilon \rightarrow 1$, it gives $5.783/\sqrt{Re_D}$ for a circular pin, and when $\epsilon \rightarrow 0$, it gives $1.353/\sqrt{Re_L}$ for a finite horizontal plate-fin.

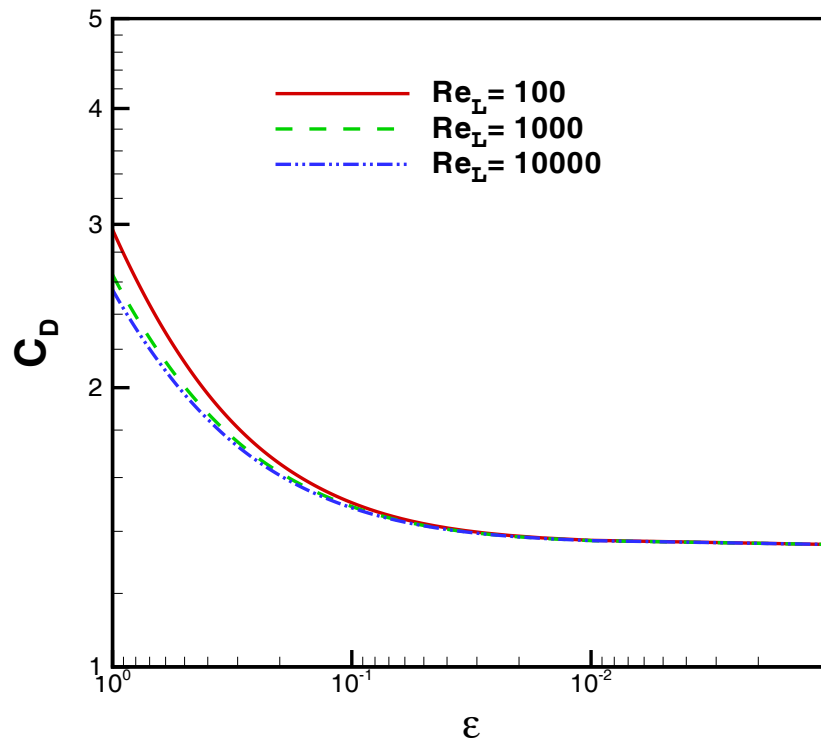


Figure 3.8: Variation of Total Drag Coefficients with the Axis Ratio

For the elliptic pin, pressure difference ΔP can be obtained by integrating the θ -momentum equation, Eq. (A-29), with respect to θ . Using velocity components u_ξ and u_θ , Eqs. (D-15) and (D-16), and their derivatives with respect to ξ and θ in Eq. (A-29), and simplifying, we get:

$$C_p = 2\epsilon^2(1 + \epsilon)^2 f_1(\theta) - \frac{8E(e)}{\pi Re_{\mathcal{L}}}(1 + \epsilon) f_2(\theta) \quad (3.40)$$

where

$$f_1(\theta) = \int_0^\theta \frac{\sin \theta \cos \theta}{(1 - e^2 \cos^2 \theta)^2} d\theta \quad (3.41)$$

$$f_2(\theta) = \int_0^\theta \frac{\sin \theta (\epsilon^2 - e^2 \cos^2 \theta)}{(1 - e^2 \cos^2 \theta)^2} d\theta \quad (3.42)$$

Thus, the pressure drag coefficient for an elliptical pin of arbitrary axis ratio will be:

$$C_{Dp} = 2\epsilon^2(1 + \epsilon)^2 \int_0^{\theta_s} f_1(\theta) \cos \theta \sqrt{1 - e^2 \cos^2 \theta} d\theta - \frac{8E(e)}{\pi Re_{\mathcal{L}}}(1 + \epsilon) \int_0^{\theta_s} f_2(\theta) \cos \theta \sqrt{1 - e^2 \cos^2 \theta} d\theta \quad (3.43)$$

Using these coefficients, a general correlation is determined in terms of the axis ratio and the Reynolds number:

$$C_{Dp} = \left(1.1526 + \frac{1.26}{Re_{\mathcal{L}}} \right) \epsilon^{0.95} \quad (3.44)$$

The total drag coefficient C_D can be written as the sum of the both drag coefficients:

$$C_D = \frac{1.353 + 4.43\epsilon^{1.35}}{\sqrt{Re_{\mathcal{L}}}} + \left(1.1526 + \frac{1.26}{Re_{\mathcal{L}}} \right) \epsilon^{0.95} \quad (3.45)$$

In the limiting cases when $\epsilon \rightarrow 1$, it gives:

$$C_D = \frac{5.786}{\sqrt{Re_D}} + 1.152 + \frac{1.260}{Re_D} \quad (3.46)$$

for a circular pin, and when $\epsilon \rightarrow 0$, it gives:

$$C_D = \frac{1.353}{\sqrt{Re_L}} \quad (3.47)$$

for a finite horizontal plate-fin. The variation of drag coefficients with Reynolds numbers is shown in Fig. 3.9 for different axis ratios of elliptical pins. It is clear that the drag coefficients decrease with the Reynolds numbers as well as with the axis ratio. They range from circular pin-fin to plate-fin.

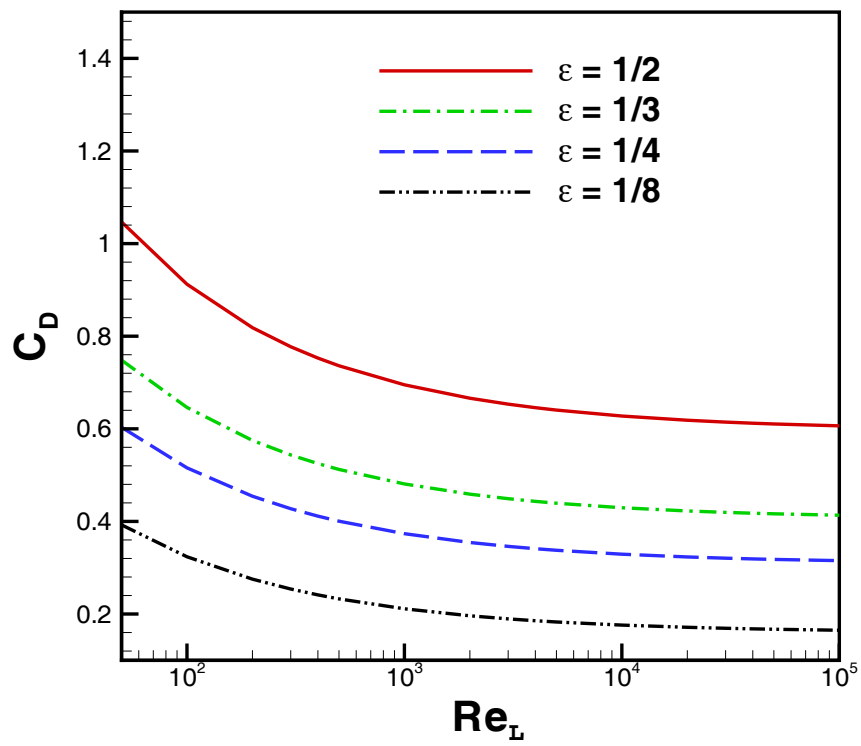


Figure 3.9: Variation of Total Drag with Reynolds Number for Elliptical Pins of Different Axis Ratios

3.4 Circular Pin Between Two Parallel Planes

In this section, the effects of blockage on fluid flow over a circular pin, confined between parallel planes, will be investigated. The momentum equation is solved by the same modified Von Karman-Pohlhausen method as described in section 3.1. The potential flow velocity, outside the boundary layer, is obtained by the method of images, Eq. D-33. The reciprocal of the dimensionless distance between two planes S_T/D is defined as the blockage ratio $b = D/S_T$. This parameter plays an important role in determining the fluid flow past a pin confined between two parallel planes. In practice, a pin is placed in flows restricted by walls. This configuration is found in many applications, such as cross flow heat exchangers, shrouded heat sinks, and electric heating elements in boilers.

3.4.1 Analysis

Consider a uniform flow of a Newtonian fluid past a fixed circular pin of diameter D , confined between two parallel planes. The vertical distance between these planes is S_T , as shown in Fig. 3.10. The flow conditions and the boundary layer equations are the same as described in section 3.1.

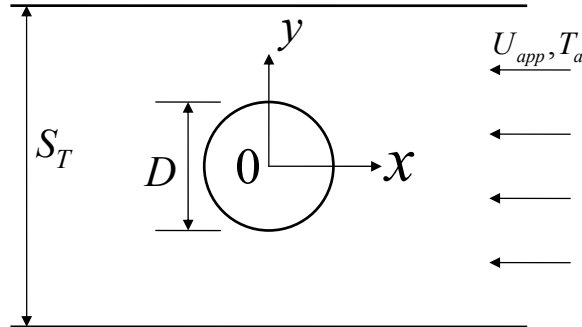


Figure 3.10: Physical Model and Coordinate System

3.4.2 Boundary-Layer Parameters

Using potential flow velocity, Eq. (D-33) with Eq. (D-32), Eqs. 3.10 and 3.11 can be solved to determine the dimensionless hydrodynamic boundary layer and momentum thicknesses:

$$\frac{\delta_2}{D} = \frac{0.485}{\sqrt{Re_D}} \sqrt{\frac{1}{f^6(\theta)} \int_0^\theta f^5(\zeta) d\zeta} \quad (3.48)$$

$$\frac{\delta}{D} = \sqrt{\frac{\lambda}{2Re_D g(\theta)}} \quad (3.49)$$

where $g(\theta)$ is the first derivative of $f(\theta)$ w.r.t. θ and $f(\theta)$ is given by Eq. (D-32). By solving Eqs. (3.9) and (3.49) and comparing the results with Eq. (3.48), the values of the pressure gradient parameter λ are obtained corresponding to each position along the pin surface for different transverse spacings. Again the range of interest $0 \leq \theta \leq \theta_s$ is divided into two regions and the λ values can be fitted separately for each transverse spacing by the least squares method into two polynomials. These polynomials will be used to determine the drag and the local heat transfer coefficients in both regions.

3.4.3 Fluid Friction

Using potential flow velocity, Eq. (D-33) with Eq. (D-32), the dimensionless shear stress on the pin surface, Eq. (E-5), can be written as:

$$C_f = \frac{\tau_w}{\frac{1}{2}\rho U_{app}^2} = \frac{1}{3} \frac{\lambda + 12}{\sqrt{Re_D}} f(\theta) \sqrt{\frac{2g(\theta)}{\lambda}} \quad (3.50)$$

The angle of separation depends on the velocity distribution outside the boundary layer as well as the blockage ratio. The boundary layer parameters for specific blockage ratios are presented in Appendix G (Tables 5-7). Figure 3.11 clearly shows that the angle of separation depends upon the blockage ratio. As the blockage ratio increases, the location of the boundary layer separation moves forward. This movement is due to the change in the velocity distribution inside the boundary layer. The friction drag coefficient can be

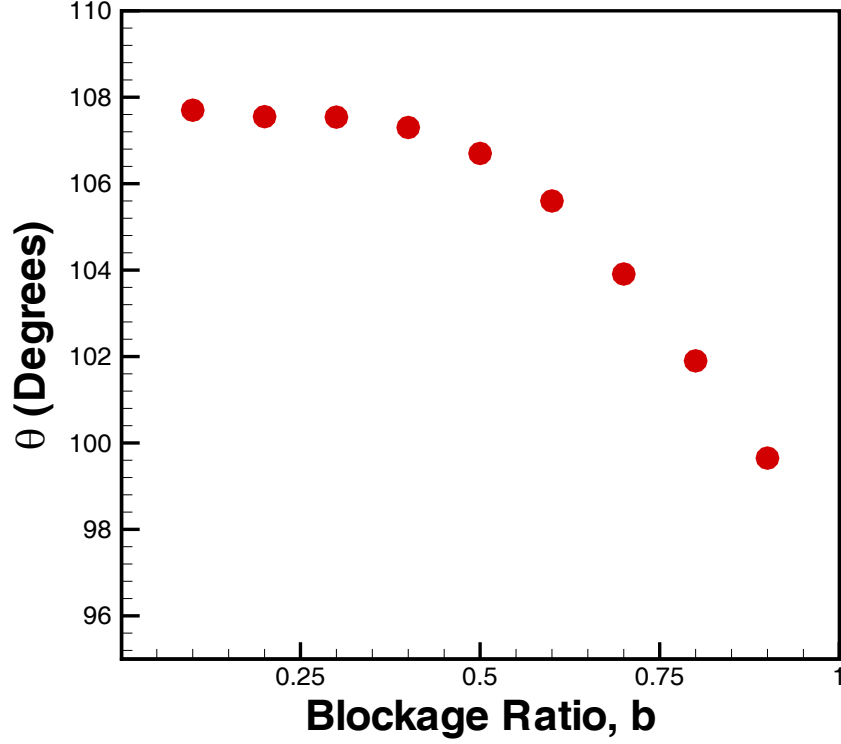


Figure 3.11: Effect of Blockage Ratio on the Angle of Separation

determined from Eq. (E-6):

$$C_{Df} = \frac{1}{3\sqrt{Re_D}} \left[\int_0^{\theta_1} (\lambda_1 + 12) f(\theta) \sin \theta \sqrt{\frac{2g(\theta)}{\lambda_1}} d\theta + \int_{\theta_1}^{\theta_s} (\lambda_2 + 12) f(\theta) \sin \theta \sqrt{\frac{2g(\theta)}{\lambda_2}} d\theta \right] \quad (3.51)$$

The drag coefficient C_{Df} is calculated for different blockage ratios and correlated as a single expression:

$$C_{Df} = \left[45.72 - 39.9 \exp(-0.95b^{3.44}) \right] / \sqrt{Re_D} \quad (3.52)$$

The pressure difference ΔP can be obtained by integrating Eq. (A-10) w.r.t. θ . In

dimensionless form, it can be written as:

$$\frac{\Delta P}{\frac{1}{2}\rho U_{app}^2} = 2f(\theta)g(\theta) - \frac{4}{Re_D} \left[j(\theta) + \frac{1}{R}h(\theta) - \frac{1}{R^2}f(\theta) \right] \quad (3.53)$$

where $h(\theta)$ and $j(\theta)$ are the first and second derivatives of $f(\theta)$ w.r.t. r . Substituting these derivatives in Eq. (3.54) and integrating w.r.t. θ , we get

$$C_p = 2F(\theta) - \frac{4}{Re_D}G(\theta) \quad (3.54)$$

where

$$F(\theta) = \int_0^\theta f(\theta)g(\theta)d\theta \quad (3.55)$$

and

$$G(\theta) = \int_0^\theta \left[j(\theta) + \frac{1}{R}h(\theta) - \frac{1}{R^2}f(\theta) \right] d\theta \quad (3.56)$$

So, the pressure drag coefficient for the pin up to the separation point will be:

$$C_{Dp} = \int_0^{\theta_s} \left[2F(\theta) - \frac{4}{Re_D}G(\theta) \right] \cos\theta d\theta \quad (3.57)$$

This drag coefficient is calculated for different blockage ratios and correlated as a single expression:

$$C_{Dp} = \left[6.1 - 4.95 \exp(-0.76b^{2.63}) \right] + \left[1.49 - 0.23 \exp(-5.81b^{2.15}) \right] / Re_D \quad (3.58)$$

The total drag coefficient C_D can be written as the sum of both drag coefficients:

$$C_D = \left[45.72 - 39.9 \exp(-0.95b^{3.44}) \right] / \sqrt{Re_D} + \left[6.1 - 4.95 \exp(-0.76b^{2.63}) \right] + \left[1.49 - 0.23 \exp(-5.81b^{2.15}) \right] / Re_D \quad (3.59)$$

Figure 3.12 shows the effects of blockage ratio on the drag coefficient for different Reynolds numbers. It shows that the drag coefficient decreases with the blockage ratio and Reynolds number. For zero blockage, it gives the value for an isolated pin. In Fig. 3.13, the effects of Reynolds number on the drag coefficients are shown for various blockage ratios. It is clear that the drag coefficients decrease when the Reynolds number increase.

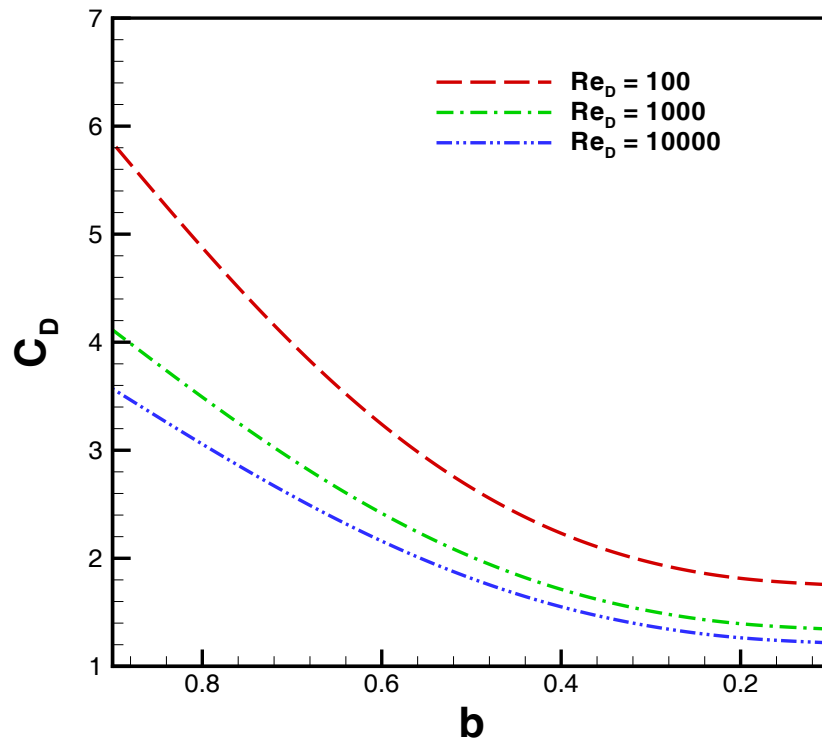


Figure 3.12: Effects of Blockage Ratio on Drag Coefficients for Different Reynolds Numbers

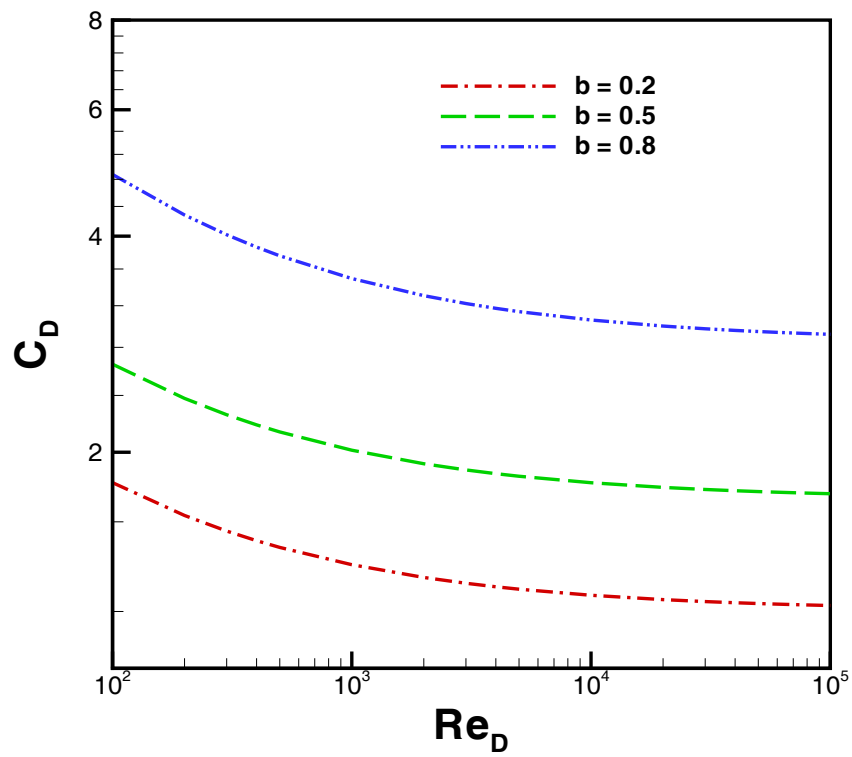


Figure 3.13: Effects of Reynolds Number on Drag Coefficients for Different Blockage Ratios

3.5 Pin-Fin Arrays

3.5.1 Analysis

A single pin-fin is rarely used in heat transfer applications, but is, instead, used in array form. Heat sinks, used in microelectronics, usually consist of arrays of pin-fins in in-line or staggered arrangements. The pins are attached to a common base of dimension $L \times W \times t_b$, and the geometry of the array is determined by the fin diameter D , pin height H , longitudinal spacing S_L , and transverse spacing S_T (Fig. 3.14). The approach velocity of the air is U_{app} and the ambient temperature of the air is T_a . The surface temperature of the pin wall is $T_w (> T_a)$ in the case of the isothermal pin and the heat flux is q for the isoflux boundary condition. The nomenclature of both arrangements, in-line and staggered, is shown in Fig. 3.15. In this section, fluid flow will be analyzed for both arrangements.

You and Chang (1997) found numerically that the flow inside the pin-fin channel reaches the fully developed thermal state in the early downstream region whereas Žukauskas (1972) showed experimentally that the heat transfer becomes stable from the third or fourth row depending upon the Reynolds number. Depending on this information, a control volume (CV) is selected from the third row as a typical cell (Fig. 3.16) to study the fluid flow through an array of in-line or staggered pin fins. The width of the control volume is taken as unity for convenience and the length and height, in dimensionless form, are taken as \mathcal{S}_L and $\mathcal{S}_T/2$ ($\equiv S_T/2D$) respectively. Because the flow is symmetrical about the horizontal center-line, the solution has only been obtained for half of the flow domain i.e. for ABCDEFG in Fig. 3.16. The control volume surface can be regarded as impermeable, adiabatic and shear free (no mass transfer and shear work transfer across the boundary). The heat transfer between the pin and stream is Q and the wall temperature is T_w . The boundary conditions for the selected control volume are described in Appendix B.

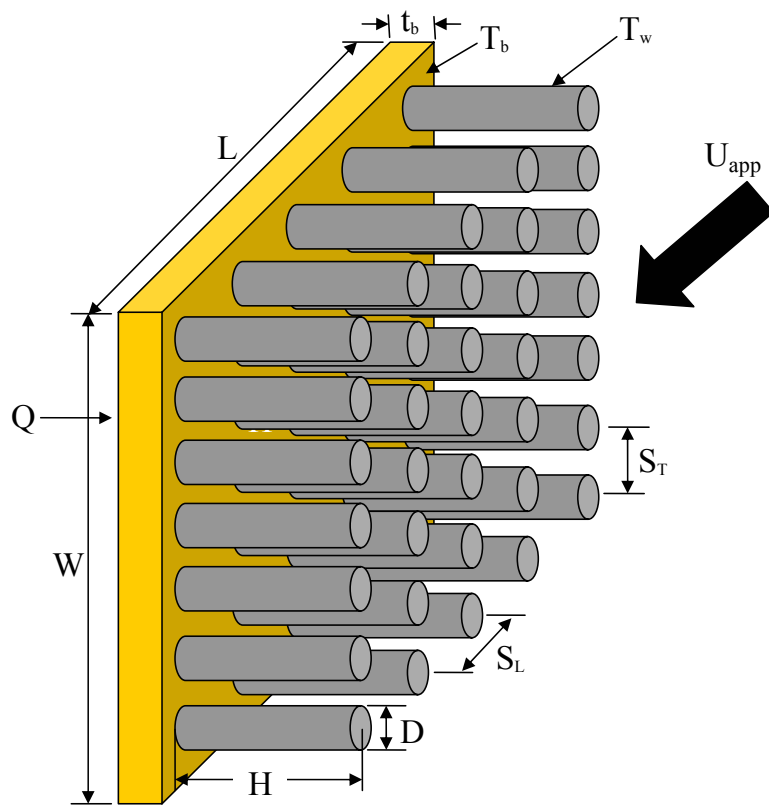
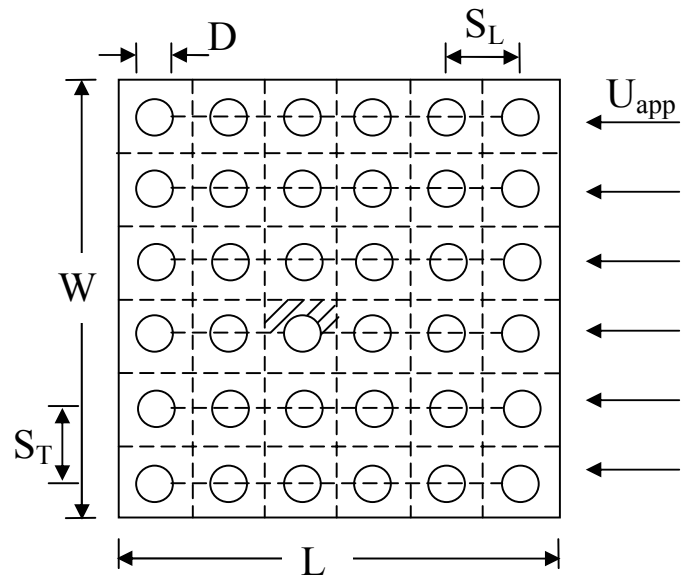
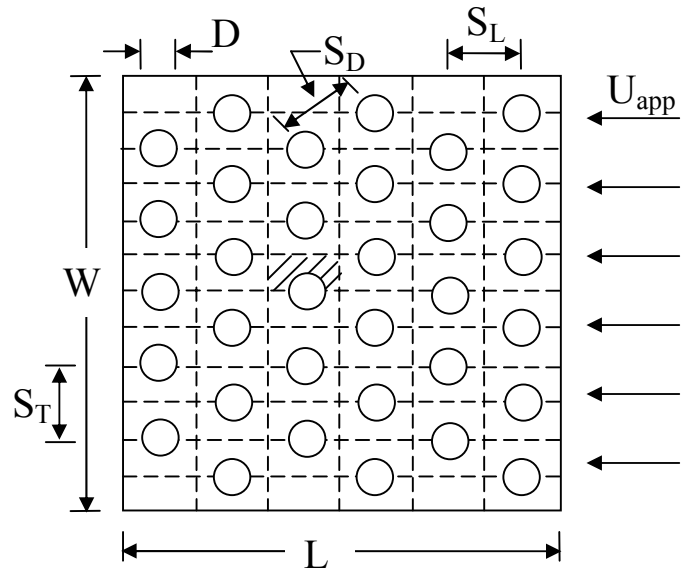


Figure 3.14: In-Line Pin-Fin Heat Sink



a) In-Line Arrangement



b) Staggered Arrangement

Figure 3.15: Nomenclature for In-Line and Staggered Arrangements

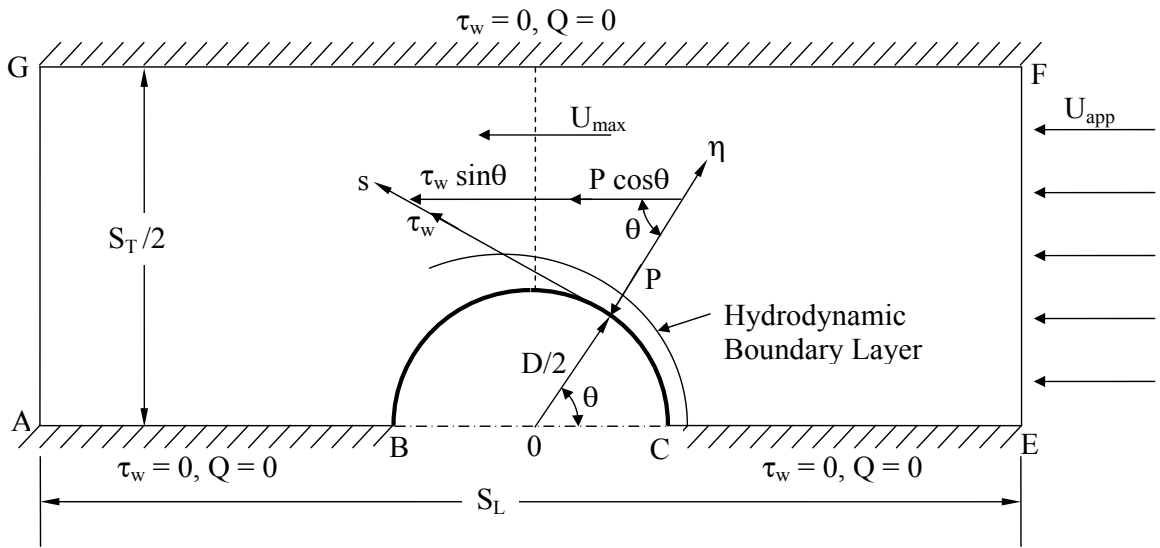


Figure 3.16: Control Volume for Prediction of Fluid Flow from a Pin-Fin Heat Sink

The mean velocity in the minimum free cross section of the CV, U_{max} , is used as a reference velocity in the calculations of fluid flow and heat transfer for both types of arrangements, and is given by:

$$U_{max} = \max \left[\frac{S_T}{S_T - 1} U_{app}, \frac{S_T}{S_D - 1} U_{app} \right] \quad (3.60)$$

where $S_D = \sqrt{S_L^2 + (S_T/2)^2}$ is the dimensionless diagonal pitch in the case of the staggered arrangement. Depending upon the maximum velocity, the Reynolds number for the in-line arrangement can be defined as:

$$Re_{Dmax} = Re_D \frac{S_T}{S_T - 1} \quad (3.61)$$

and for the staggered arrangement, it is defined as:

$$Re_{Dmax} = \max \left[Re_D \frac{S_T}{S_T - 1}, Re_D \frac{S_T}{S_D - 1} \right] \quad (3.62)$$

The flow conditions, governing equations, velocity and temperature distributions inside the boundary layer are the same as described in Section 1. The potential flow velocity outside the boundary layer is derived in Appendix D for both arrangements. Using potential flow velocity, Eq. (D-46) with Eq. (D-45) for the in-line arrangement and Eq. (D-53) with Eq. (D-52) for the staggered arrangement, Eqs. (3.10 and 3.11) can be solved again to determine the dimensionless hydrodynamic boundary layer and momentum thicknesses for a pin-fin taken from in-line or staggered arrays:

$$\frac{\delta_2}{D} = \frac{0.485}{\sqrt{Re_D}} \sqrt{\frac{1}{f^6(\theta)} \int_0^\theta f^5(\zeta) d\zeta} \quad (3.63)$$

$$\frac{\delta}{D} = \sqrt{\frac{\lambda}{2 Re_D g(\theta)}} \quad (3.64)$$

where $g(\theta)$ is the first derivative of $f(\theta)$ w.r.t. θ and $f(\theta)$ is given by Eq. (D-45) or Eq. (D-53) depending upon the geometry of the array.

By solving Eqs. (3.9) and (3.64) and comparing the results with Eq. (3.63), the values of the pressure gradient parameter λ can be obtained corresponding to each position along the pin surface for different longitudinal and transverse spacings in both arrangements.

3.5.2 Fluid Friction

In pin-fin arrays in cross flow, the total drag also consists of friction and pressure drag. The drag on a pin in an array is described by its skin friction coefficient C_f and the pressure drag coefficient C_p . These coefficients are defined in Appendix E and, for both arrangements, can be written as:

$$C_f = \frac{\tau_w}{\frac{1}{2}\rho U_{max}^2} = \frac{1}{3} \frac{\lambda + 12}{\sqrt{Re_D}} f(\theta) \sqrt{\frac{2g(\theta)}{\lambda}} \quad (3.65)$$

$$C_p = \frac{\Delta p}{\frac{1}{2}\rho U_{max}^2} = 2f(\theta)g(\theta) - \frac{4}{Re_D} \left[j(\theta) + \frac{1}{R}h(\theta) - \frac{1}{R^2}f(\theta) \right] \quad (3.66)$$

where $g(\theta)$ is the first derivative of $f(\theta)$ w.r.t. θ , $h(\theta)$ and $j(\theta)$ are the first and second derivatives of $f(\theta)$ w.r.t. r , and $f(\theta)$ is given by Eq. (D-45) for in-line arrangement and by Eq. (D-52) for staggered arrangement. The coefficients of friction are plotted in Figs. 3.17-3.20 for different longitudinal and transverse pitches for both arrangements. They show the effects of S_T and S_L on skin friction in each arrangement. It can be seen again that $C_f = 0$ at the points of stagnation and separation. With an increase of θ , the value of C_f increases and reaches a maximum at θ from 50 to 80°, depending upon Re_D , S_T , and S_L . Also the values of C_f are higher for the staggered arrangement. This fact can also be observed in Fig. 3.21, where a direct comparison is made between two arrangements for the same pitches. The combined friction and pressure drag over a pin in an array in cross flow is known as drag coefficient and it is written as:

$$C_D = \int_0^{\theta_s} C_f \sin \theta d\theta + \int_0^{\theta_s} C_p \cos \theta d\theta$$

$$= \frac{1}{3} \frac{\lambda + 12}{\sqrt{Re_D}} f(\theta) \sin \theta \sqrt{\frac{2g(\theta)}{\lambda}} + \int_0^{\theta_s} \left[2F(\theta) - \frac{4}{Re_D} G(\theta) \right] \cos \theta d\theta \quad (3.67)$$

where

$$F(\theta) = \int_0^\theta f(\theta) g(\theta) d\theta \quad (3.68)$$

$$G(\theta) = \int_0^\theta \left\{ j(\theta) + \frac{1}{R} h(\theta) - \frac{1}{R^2} f(\theta) \right\} d\theta \quad (3.69)$$

The drag coefficients for both arrangements can be determined from Eq. (3.67) for different longitudinal and transverse pitches. These coefficients are not generally used in heat sink terminology, but instead a pressure drop is used, which will be discussed in Chapter 5.

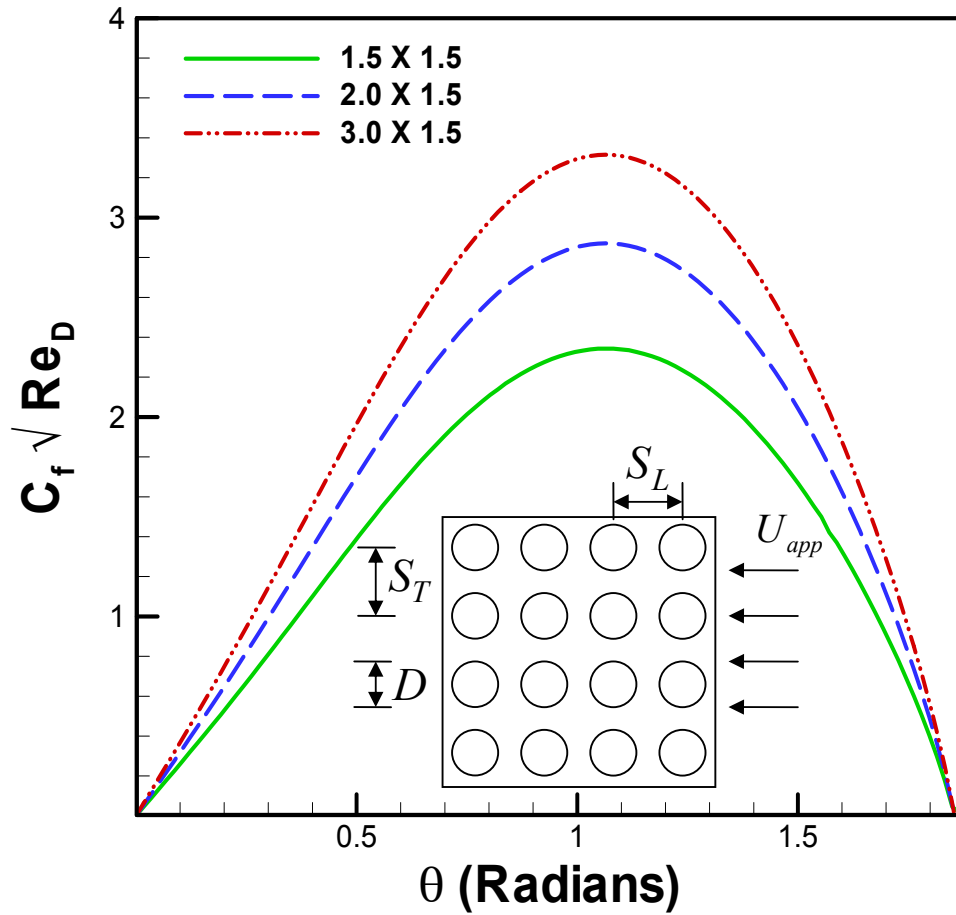


Figure 3.17: Effects of Transverse Pitch on Skin Friction in In-Line Arrays

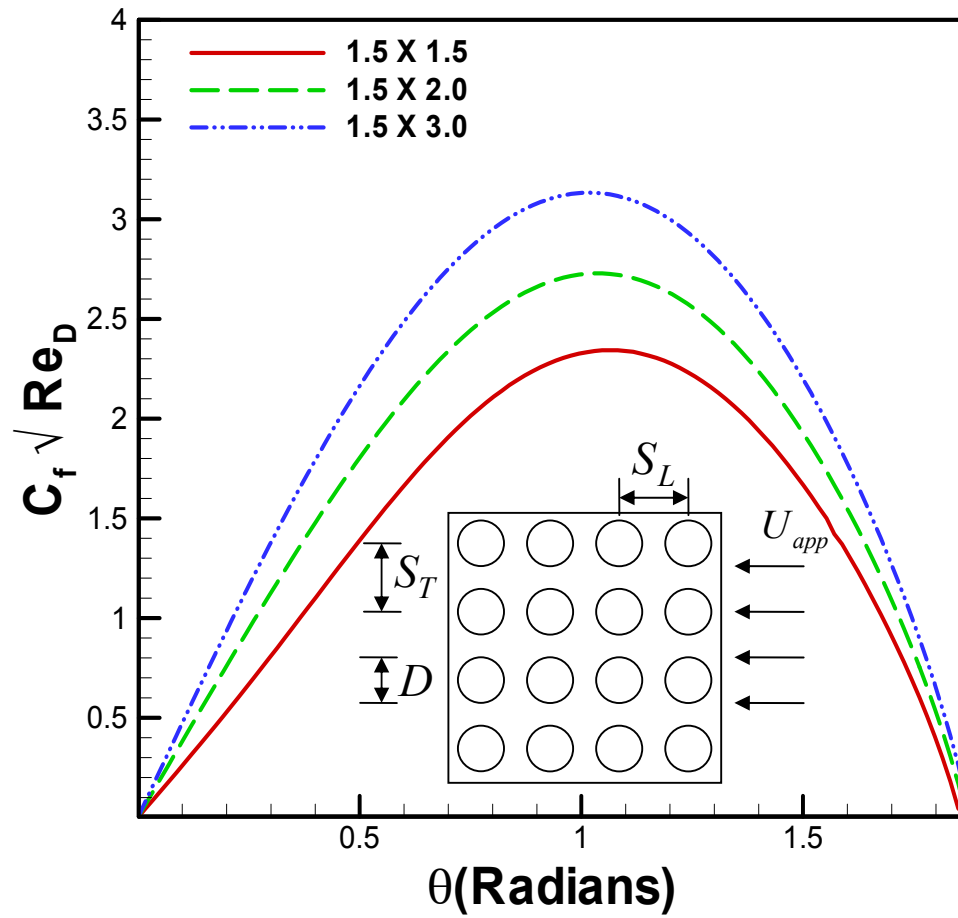


Figure 3.18: Effects of Longitudinal Pitch on Skin Friction in In-Line Arrays

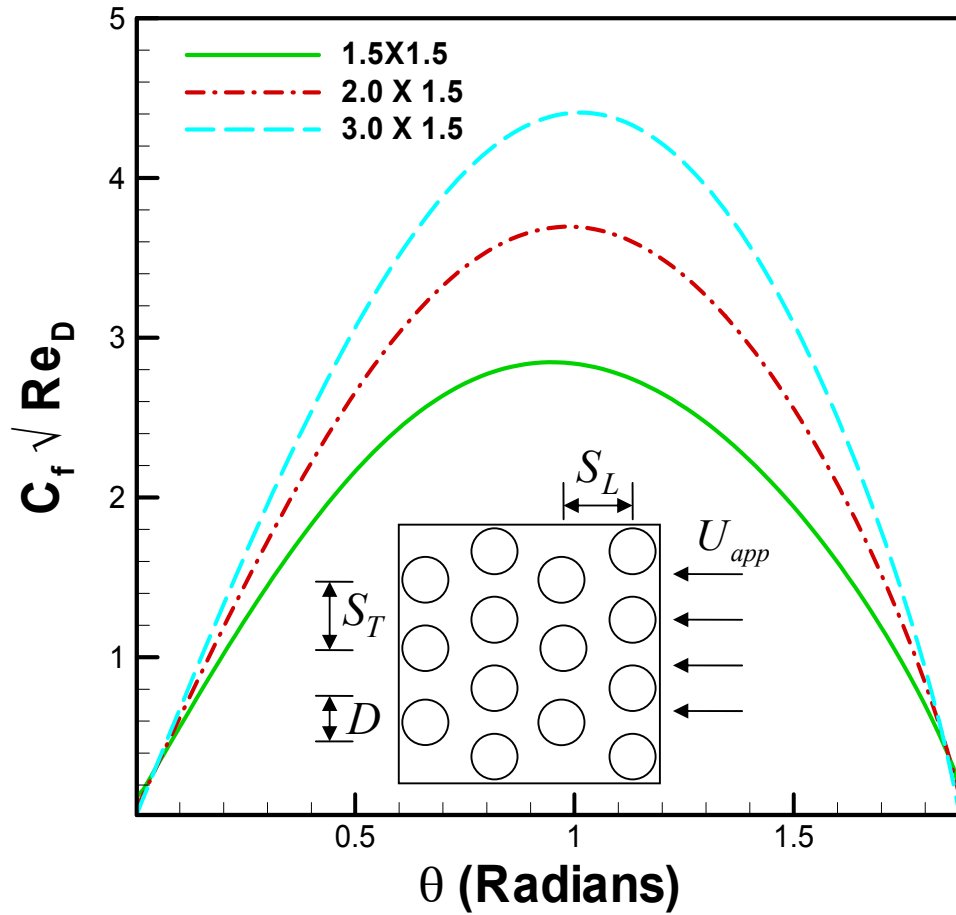


Figure 3.19: Effects of Transverse Pitch on Skin Friction in Staggered Arrays

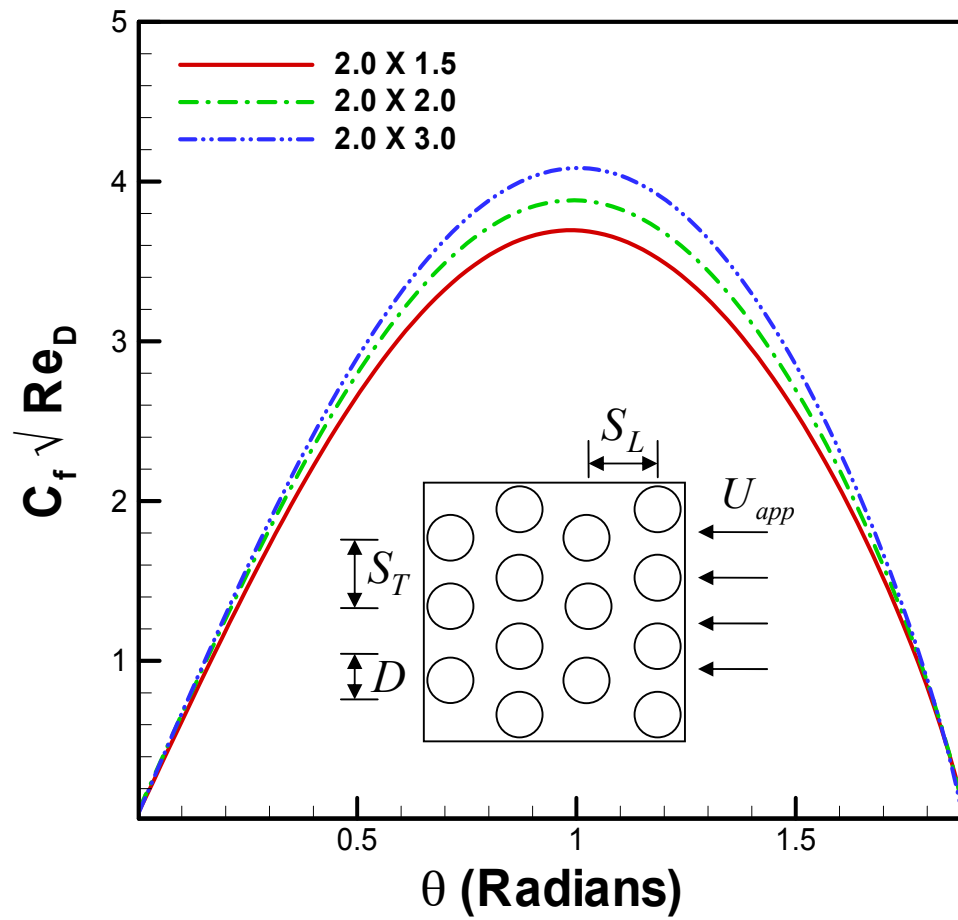


Figure 3.20: Effects of Longitudinal Pitch on Skin Friction in Staggered Arrays

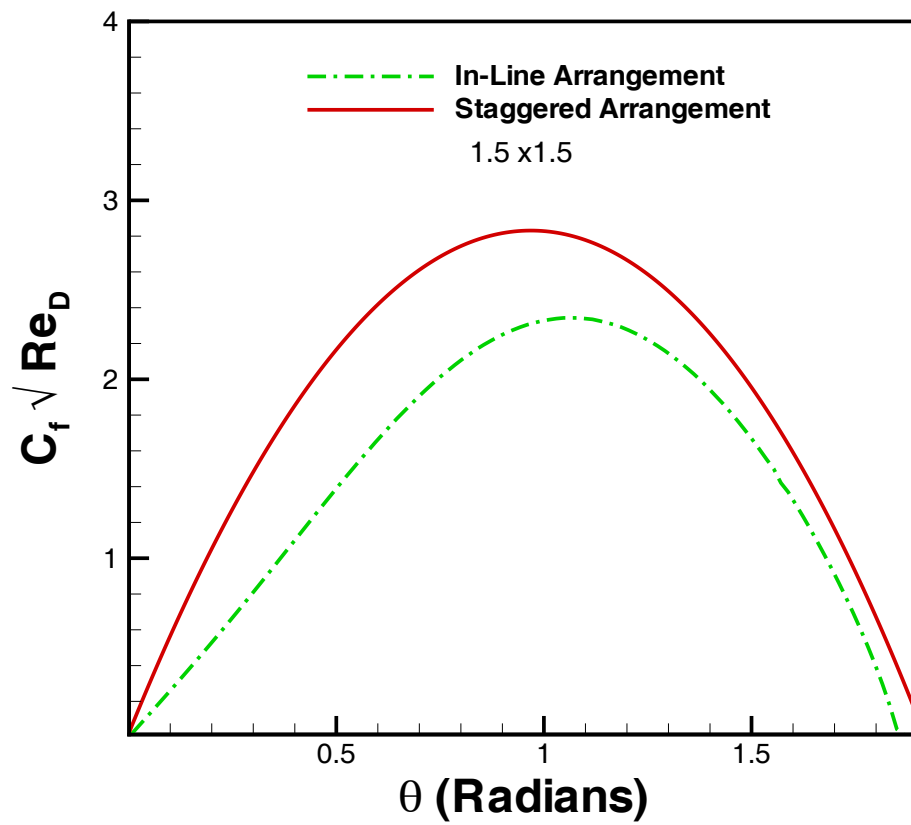


Figure 3.21: Coefficients of Friction for In-Line and Staggered Arrangements

3.6 Model Verification

Experimental and numerical data are available in the literature for specific ranges of Reynolds number, longitudinal and transverse pitches and aspect ratios of pins. In this section, the preliminary models for single pins as well as for pin-fin arrays for the fluid flow will be validated with these data.

3.6.1 Single Circular Pin in an Infinite Flow

The dimensionless local shear stress, $C_f \sqrt{Re_D}$, is plotted for a single circular pin in Fig. 3.22. It shows that C_f is zero at the stagnation point and reaches a maximum at $\theta \approx 60^\circ$. The increase in shear stress is caused by the deformation of the velocity profiles in the boundary layer, a higher velocity gradient at the wall and a thicker boundary layer. In the region of decreasing C_f preceding the separation point, the pressure gradient decreases further and finally C_f falls to zero at $\theta = 107.7^\circ$, where the boundary-layer separation occurs. Beyond this point, C_f remains close to zero up to the rear stagnation point. These results show good agreement with the experimental results of Žukauskas and Žiugžda (1985) for a single circular pin.

The variation of the total drag coefficient C_D with Re_D , for the same pin, is shown in Fig. 3.23. The present results are compared with the experimental results of Wieselsberger (1921). It is clear that the present results are in good agreement except at $Re_D = 2 \times 10^3$, where a downward deviation (23.75%) in the experimental results was noticed. No physical explanation could be found in the literature for this deviation.

3.6.2 Single Elliptical Pin in an Infinite Flow

Figure 3.24 shows the total drag coefficients of elliptical pins vs Reynolds numbers for different axis ratios. The present results of drag coefficients for circular pin and finite plate-fin are compared with the experimental data of Wieselsberger (1921) and Janour

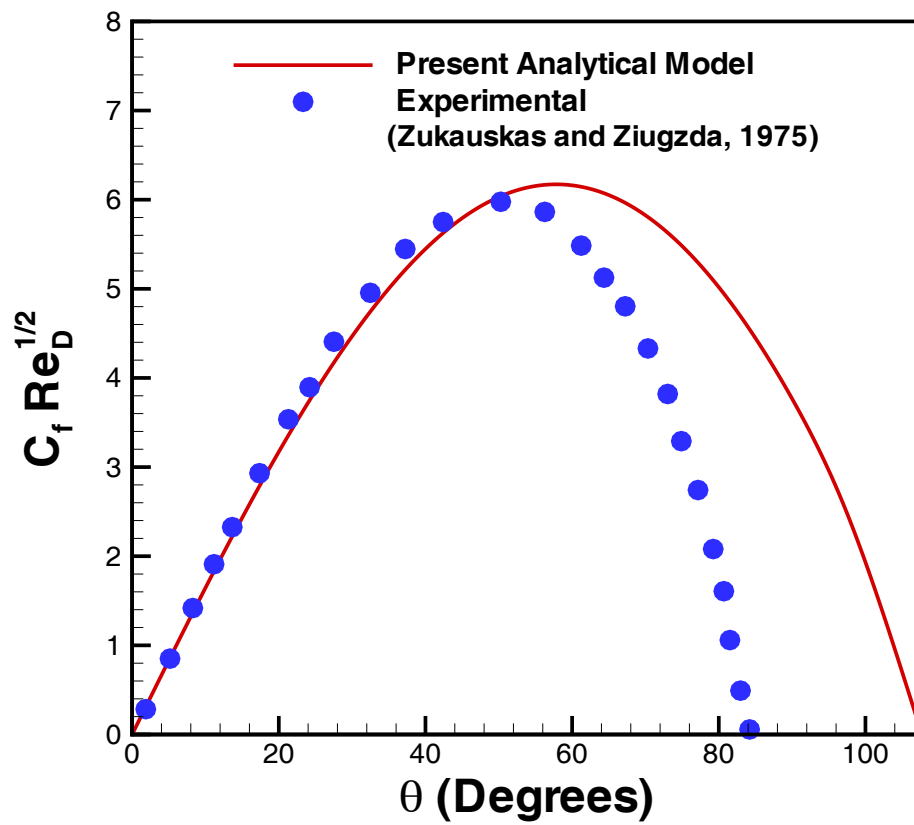


Figure 3.22: Distribution of Shear Stress on a Circular Pin in Air

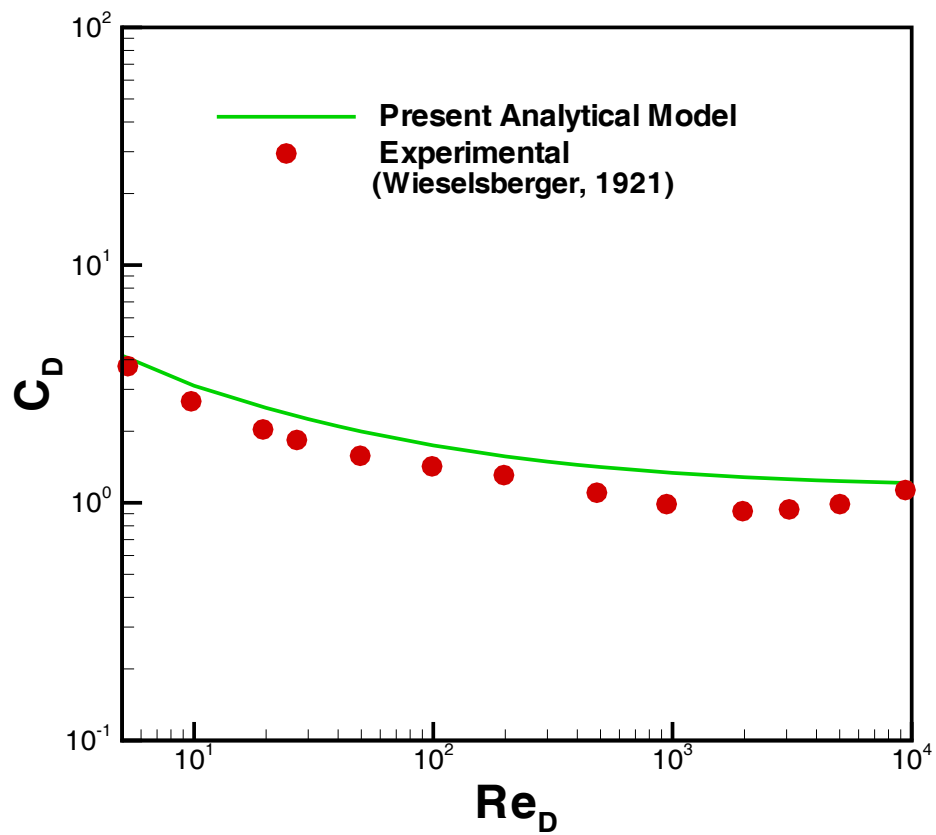


Figure 3.23: Drag Coefficient as a Function of Re_D for a Circular Pin

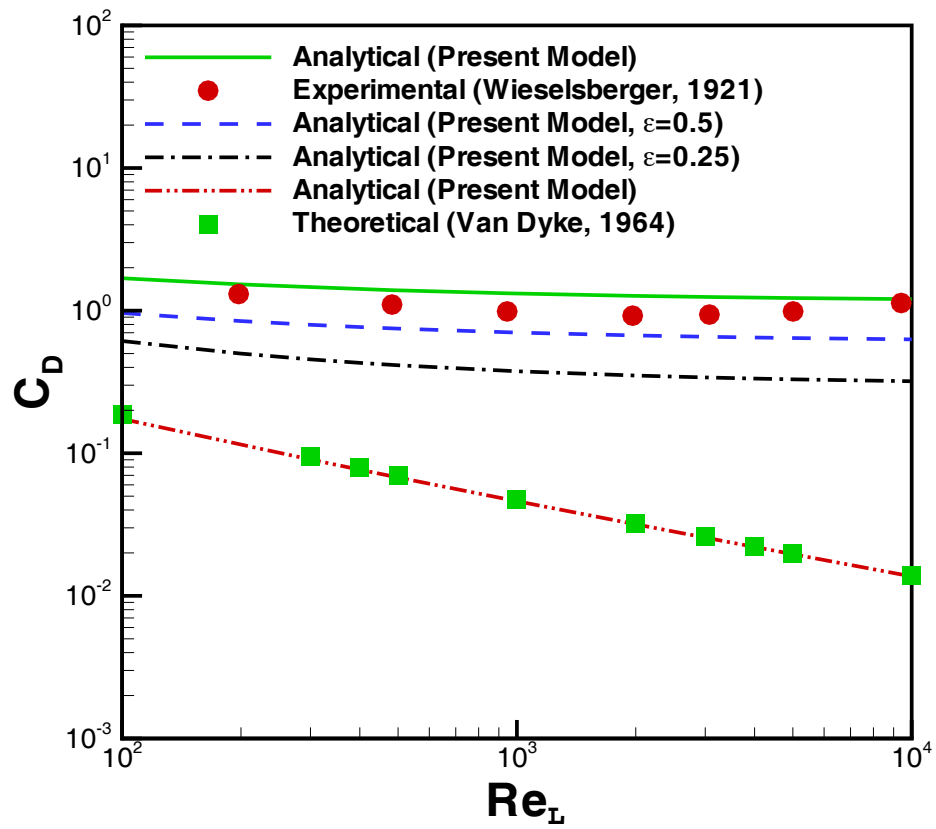


Figure 3.24: Variation of Total Drag Coefficients with the Reynolds Numbers

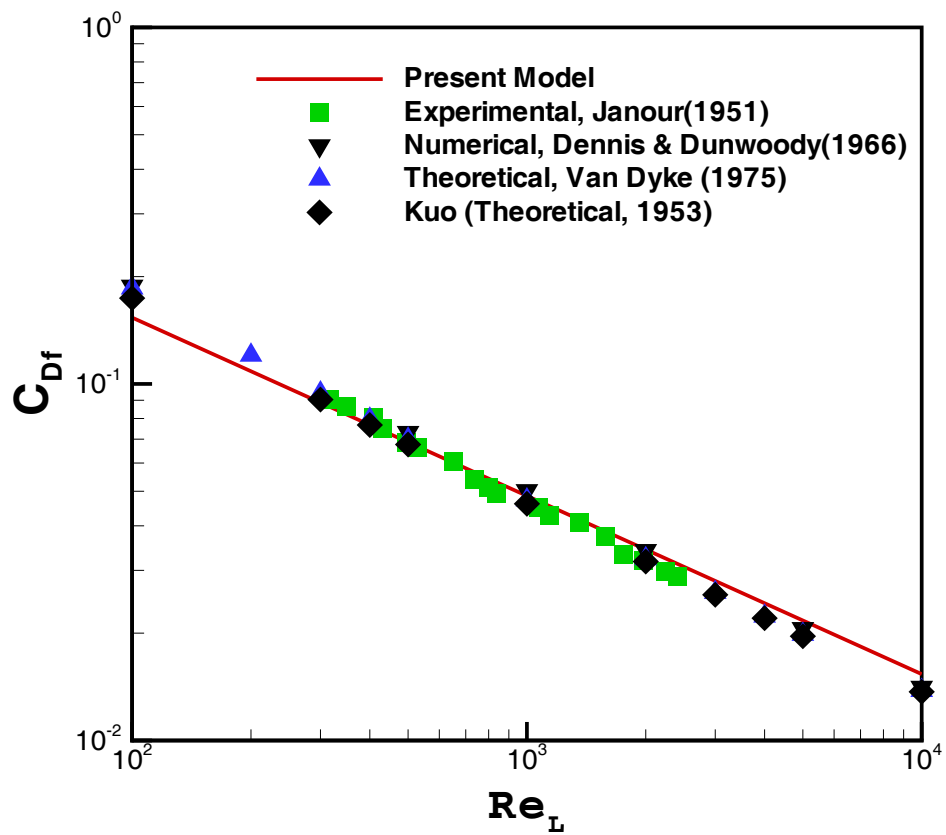


Figure 3.25: Comparison of Friction Drag Coefficients of a Finite Plate-Fin

(1951). As expected, the drag coefficients are the highest for the circular pin and lowest for the plate-fin. The drag coefficients of the elliptical pin lie between these two limits and decrease with the Reynolds numbers but the slope of the curves is smaller than the circular pin. It is clear that the present results are in good agreement with the experimental data.

The friction drag coefficients of finite plate-fin, obtained from the present model, are compared with the experimental (Janour, 1951) and numerical (Dennis and Dunwoody, 1966) data in Fig. 3.25. The theoretical correlations of Van Dyke (1964) and Kuo (1953) are also plotted on the same figure. The present results are in good agreement with the existing data.

3.6.3 Single Circular Pin Between Two Parallel Planes

The effects of blockage ratio $b = D/S_T$ on the velocity distribution outside the boundary layer are shown in Fig. 3.26. It shows that as the blockage ratio increases, the velocity outside the boundary layer increases. These results are compared with the experimental data of Akilba'yev et. al (1966) (reported by Žukauskas, 1972) for two blockage ratios. A good agreement between potential theory and experiment is observed for the front part of the pin where laminar boundary layer flow exists.

The dimensionless local shear stress, $C_f \sqrt{Re_D}$, is plotted in Fig. 3.27 for $b = 0.4$. It shows that C_f is zero at the stagnation point and reaches a maximum at $\theta \approx 60^\circ$. The increase in shear stress is caused by the deformation of the velocity profiles in the boundary layer, a higher velocity gradient at the wall and a thicker boundary layer. In the region of decreasing C_f preceding the separation point, the pressure gradient decreases further and finally C_f falls to zero, where the boundary-layer separation occurs. Beyond this point, C_f remains close to zero up to the rear stagnation point. These results are compared with the numerical results of Vaitiekūnas et al. (1985) for the same blockage ratio. The results are again in good agreement for the front part of the pin.

The variation of the total drag coefficient C_D with Re_D for different blockage ratios is illustrated in Fig. 3.28. The present results are compared with the experimental results of Wieselsberger [6] for infinite flow conditions. The present results, for infinite flow conditions, are found to be in good agreement except at $Re_D = 2 \times 10^3$, where a downward deviation (23.75%) in the experimental results was noticed. The coefficients of skin friction are plotted in Fig. 3.29 for staggered arrays. They are compared with the experimental data of Achenbach (1969). The agreement for the front part of the pins is found to be good.

3.7 Summary and Concluding Remarks

The Von Karman-Pohlhausen method was used to investigate the fluid flow for each case (single circular or elliptical pins, a circular pin confined between two parallel planes, and pin-fin arrays). Different correlations are obtained for each case to determine the drag coefficients. It was found that the drag coefficients depend on the Reynolds number, the axis ratio ϵ in case of elliptical pin, the blockage ratio b in case of a circular pin between two parallel planes, and S_L and S_T in case of pin-fin arrays. The present results are in good agreement with the experimental/numerical results for a wide range of axis ratios, blockage ratios, and Reynolds numbers. The velocity distributions and hydrodynamic boundary layer thickness obtained in this chapter will be incorporated into the energy equation to obtain solutions for the local and average heat transfer coefficients as a function of the Reynolds and Prandtl numbers for single circular and elliptical pins and pin-fin arrays. These solutions are presented in the next Chapter.

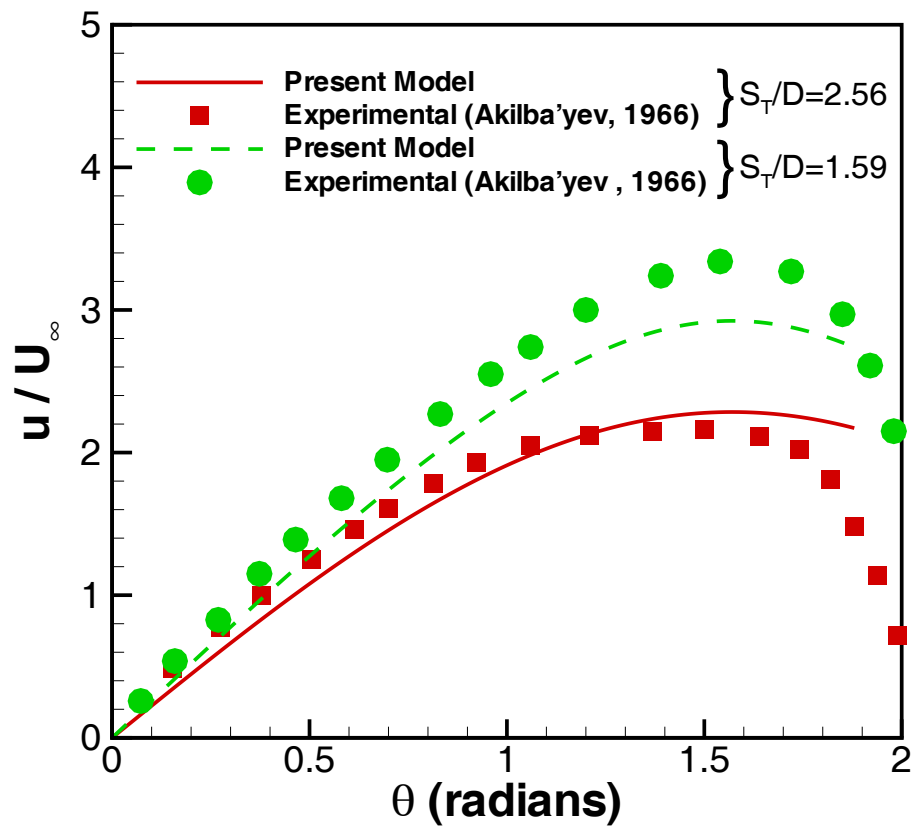


Figure 3.26: Effect of Blockage Ratio on the Velocity Distribution Outside the Boundary Layer

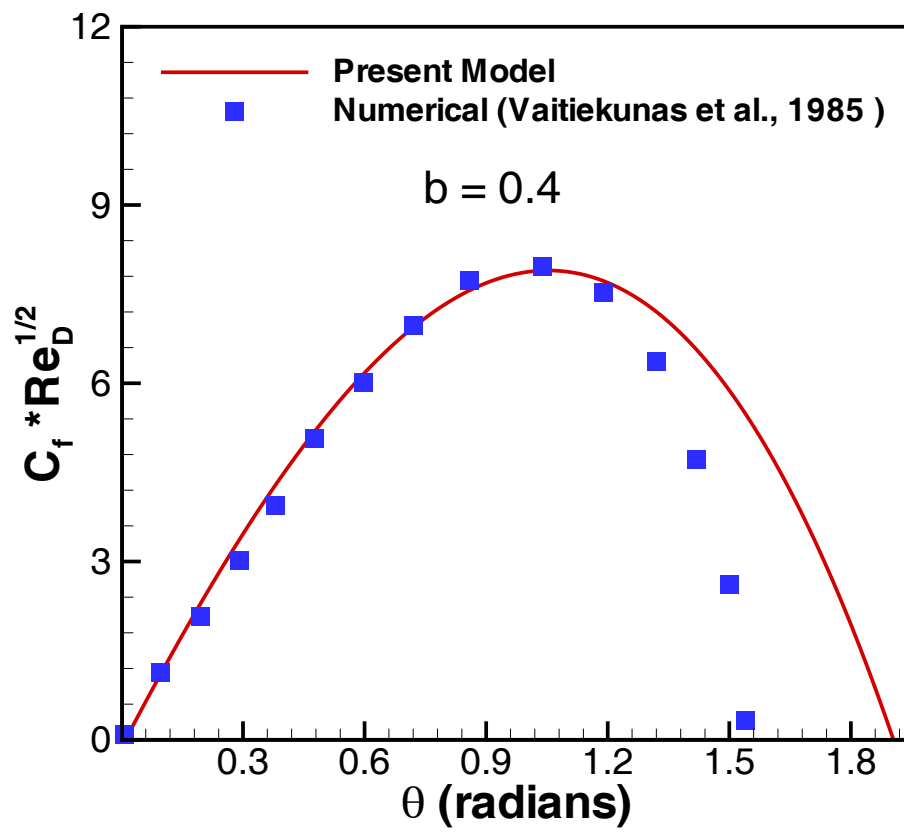


Figure 3.27: Distribution of Dimensionless Shear Stress on a Circular Pin for a Given Blockage Ratio

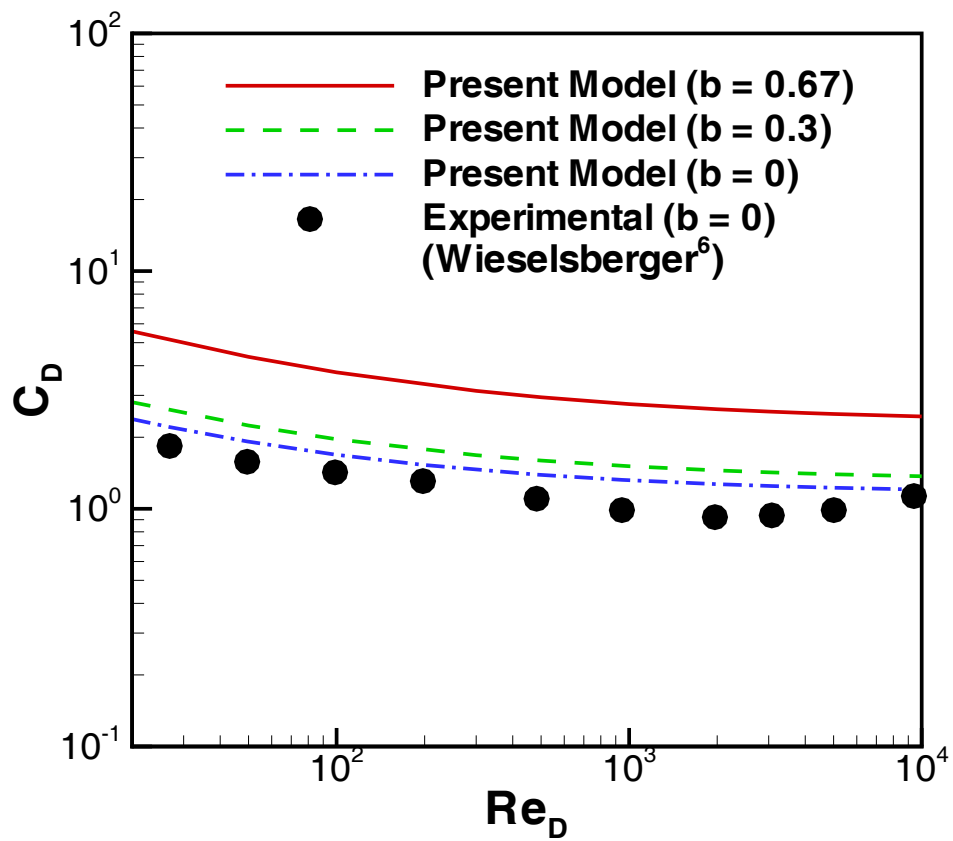


Figure 3.28: Drag Coefficient as a Function of Re_D for Different Blockage Ratios

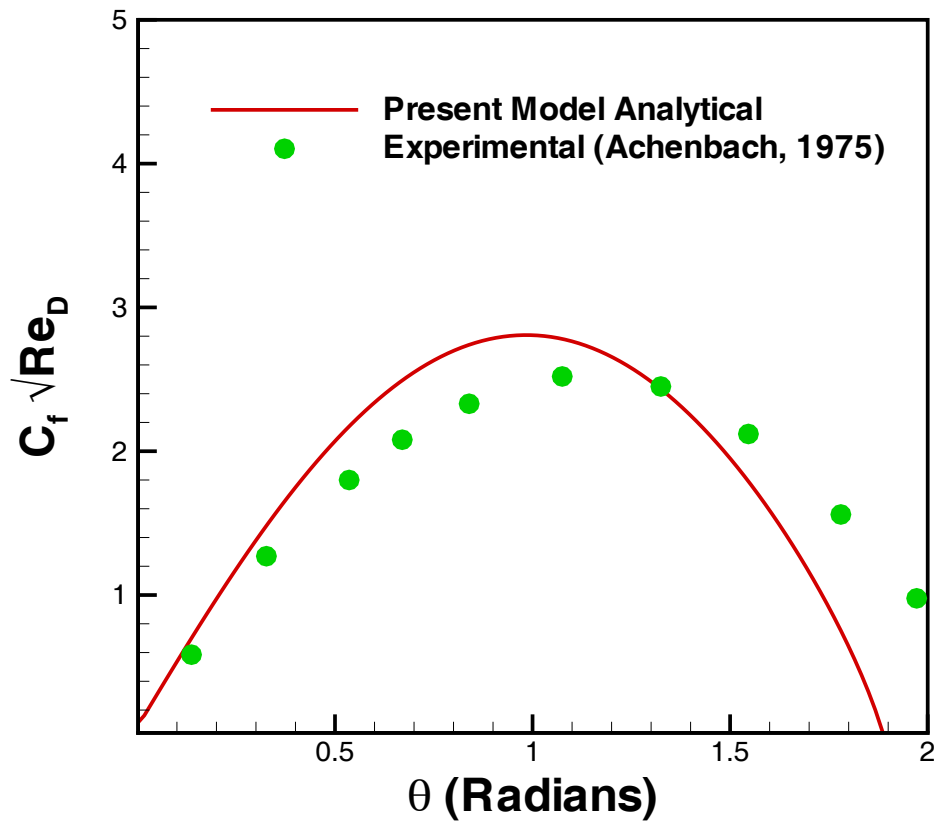


Figure 3.29: Distribution of $C_f \sqrt{Re_D}$ on Pin in Staggered Array

Chapter 4

Heat Transfer Modeling

4.1 Introduction

Pin fins are widely used to increase the rate of heat transfer from a wall. They come in many shapes and forms, a few of them are shown in Fig. 4.1. The selection of a suitable fin geometry requires a compromise among the available space, weight, cost, and the pressure drop of the fluid as well as the heat transfer characteristics of the fin surface. The fins increase the hA product and hence decrease the convective thermal resistance $1/hA$, where h is the convective heat transfer coefficient and A is the surface area of the fin.

Assuming constant thermophysical properties, heat transfer coefficient, thermal conductivity and homogeneous and isotropic material for the fin, an integral approach of the boundary layer analysis is employed to derive closed-form expressions for the calculation of local and average heat transfer from single isolated pins (circular and elliptical), and cylindrical pin-fin arrays. The flow chart (Fig. 4.2) shows the procedure for calculating the average heat transfer coefficient.

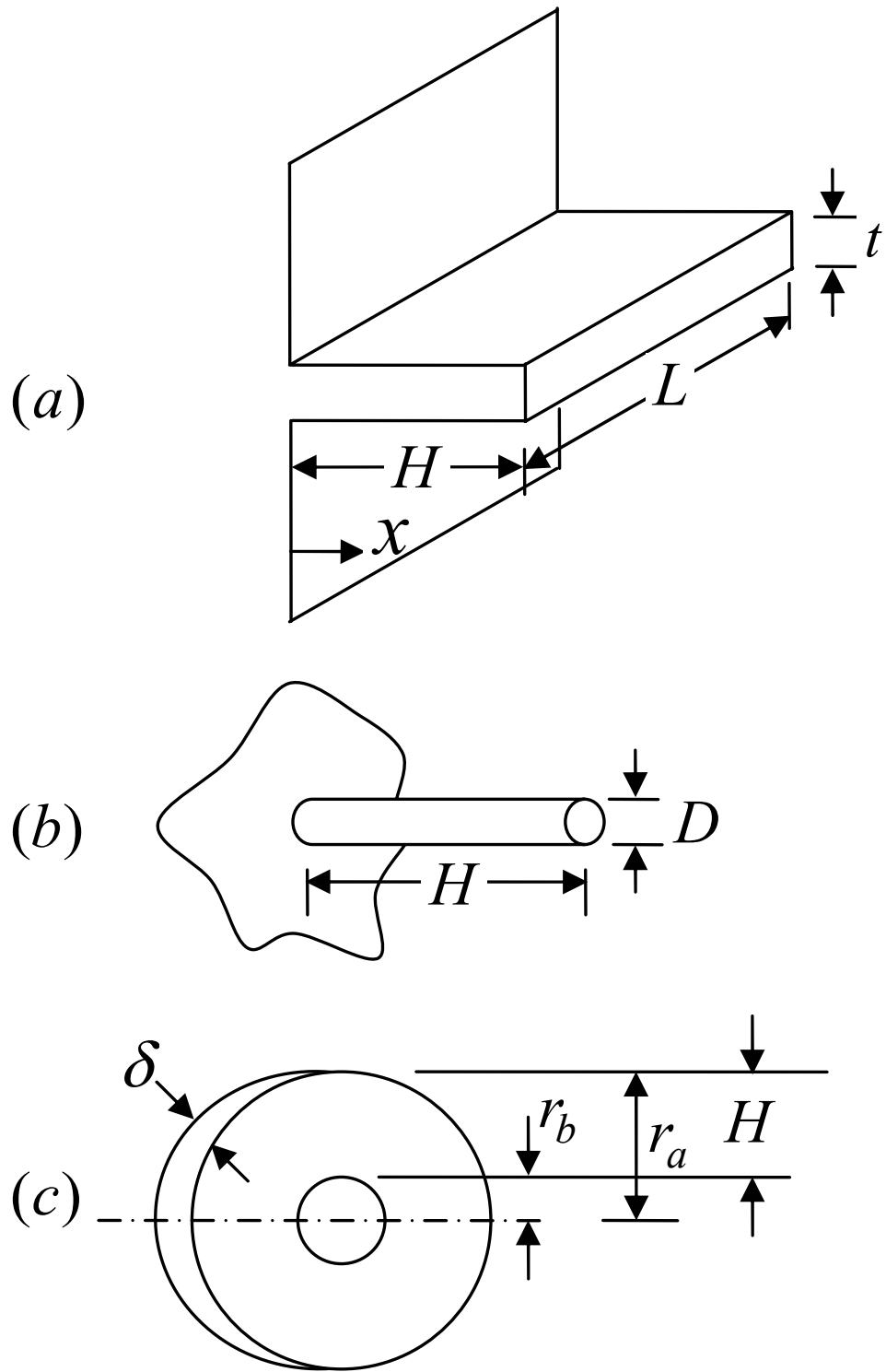


Figure 4.1: Types of Fins: (a) Longitudinal Fin, (b) Cylindrical Fin, and (c) Radial Fin

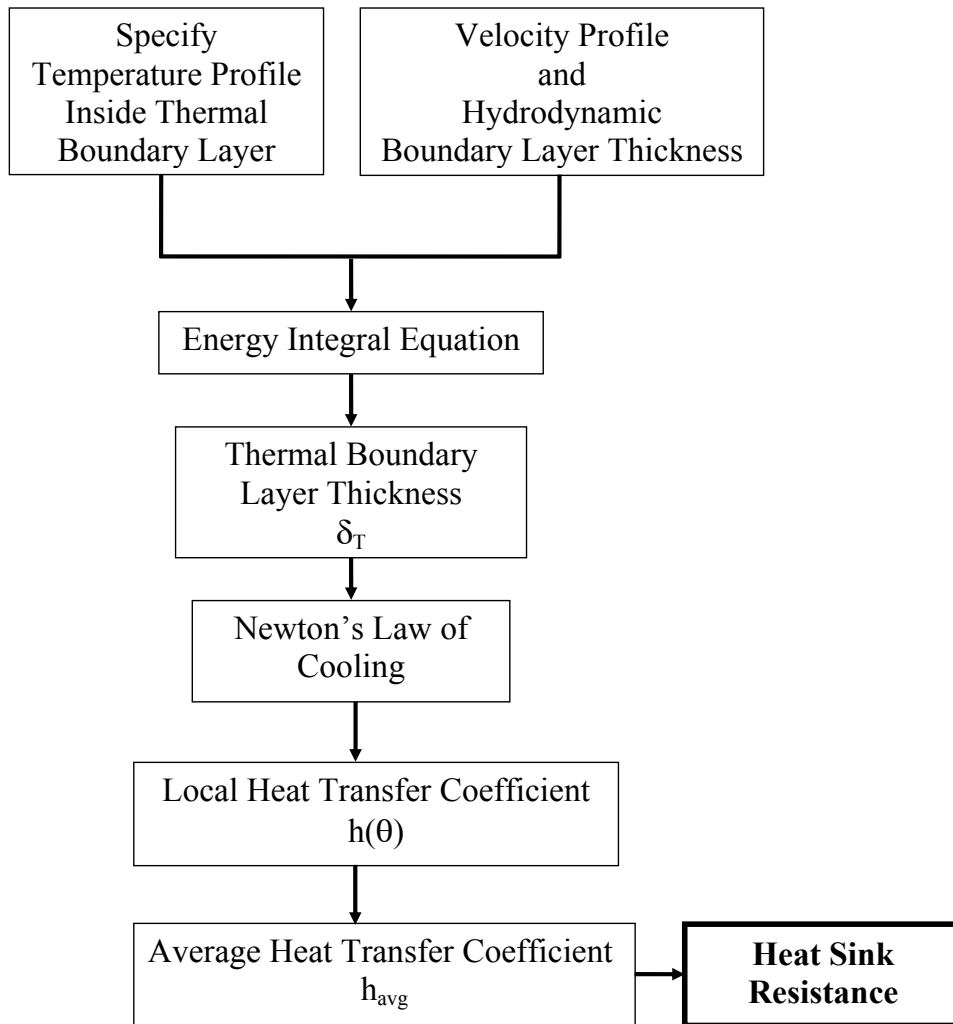


Figure 4.2: Flow Chart for Calculating Average Heat Transfer Coefficient

The effects of blockage on the heat transfer from pins will also be examined in this Chapter. A fourth order velocity profile in the hydrodynamic boundary layer and a third order temperature profile (Appendix C) in the thermal boundary layer are used for the pins under isothermal and isoflux boundary conditions. The thermal boundary conditions are described in Appendix B.

4.2 Circular Pin-Fin in an Infinite Flow

Consider a circular pin of diameter D which is extended from a wall at temperature T_b and situated in cross flow with air, as shown in Figure 3.2. The approaching velocity of the air is U_{app} and the ambient temperature of the air is assumed to be T_a . The surface temperature of the pin wall is $T_w (> T_a)$ in the case of the isothermal pin and the heat flux is q for the isoflux boundary condition. Using an order-of-magnitude analysis, the energy equation in the curvilinear coordinates system (Fig. 3.3) can be written as (Appendix A):

$$u \frac{\partial T}{\partial s} + v \frac{\partial T}{\partial \eta} = \alpha \frac{\partial^2 T}{\partial \eta^2} \quad (4.1)$$

This energy equation is solved for two thermal boundary conditions (as described in Appendix E):

4.2.1 Isothermal Boundary Condition

For an isothermal pin, Eqs. (E-11) and (E-12) can be integrated to determine the dimensionless thermal boundary layer thicknesses in the two regions:

$$\left(\frac{\delta_T(\theta)}{D}\right) \cdot Re_D^{1/2} Pr^{1/3} = \begin{cases} \sqrt[3]{\frac{45f_1(\theta)}{2(\lambda_1 + 12)^2 \sin^2 \theta} \sqrt{\frac{\lambda_1}{\cos \theta}}} & \text{for Region I} \\ \sqrt[3]{\frac{45f_3(\theta)}{2\sin^2 \theta} \sqrt{\frac{\lambda_2}{\cos \theta}}} & \text{for Region II} \end{cases} \quad (4.2)$$

where the functions $f_1(\theta)$ and $f_3(\theta)$ are given by:

$$f_1(\theta) = \int_0^\theta \sin \theta (\lambda_1 + 12) d\theta \quad (4.3)$$

and

$$f_3(\theta) = \frac{f_1(\theta)}{\lambda_1 + 12} + \frac{f_2(\theta)}{\lambda_2 + 12} \quad (4.4)$$

with

$$f_2(\theta) = \int_{\theta_1}^{\theta_s} \sin \theta (\lambda_2 + 12) d\theta \quad (4.5)$$

For the isothermal boundary condition, the local heat transfer coefficient can be defined as follows:

$$h(\theta) = -\frac{k_f \left. \frac{\partial T}{\partial \eta} \right|_{\eta=0}}{T_w - T_a} = \frac{3k_f}{2\delta_T} \quad (4.6)$$

Thus, the local heat transfer coefficients for both regions can be written as:

$$h_1(\theta) = \frac{3k_f}{2\delta_{T_1}} \quad \text{and} \quad h_2(\theta) = \frac{3k_f}{2\delta_{T_2}} \quad (4.7)$$

and the local Nusselt numbers for both the regions can be written as:

$$\frac{Nu_D(\theta)|_{isothermal}}{Re_D^{1/2} Pr^{1/3}} = \begin{cases} \frac{3}{2} \sqrt[3]{\frac{2(\lambda_1 + 12)^2 \sin^2 \theta}{45f_1(\theta)} \sqrt{\frac{\cos \theta}{\lambda_1}}} & \text{for Region I} \\ \frac{3}{2} \sqrt[3]{\frac{2\sin^2 \theta}{45f_3(\theta)} \sqrt{\frac{\cos \theta}{\lambda_2}}} & \text{for Region II} \end{cases} \quad (4.8)$$

These local Nusselt numbers are plotted in Fig. 4.3 for different Reynolds numbers using air as the fluid. It can be seen that the local heat transfer depends on the Reynolds

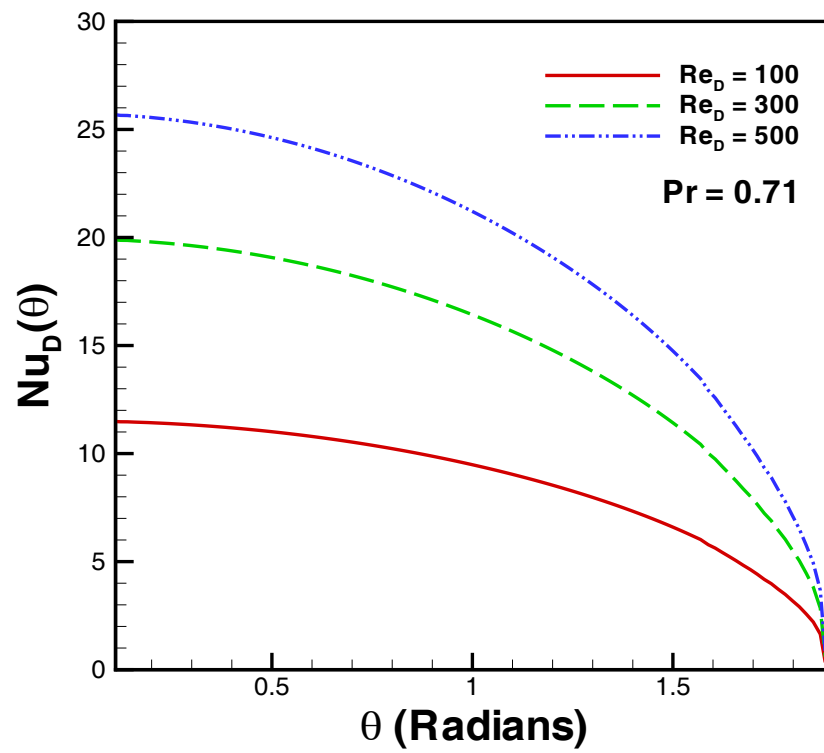


Figure 4.3: Local Heat Transfer Coefficients For Various Reynolds Numbers

number in the front region only and it approaches the same value close to the separation point. The average heat transfer coefficient is defined as

$$\begin{aligned}\bar{h} &= \frac{1}{\pi} \int_0^\pi h(\theta) d\theta \\ &= \frac{1}{\pi} \left\{ \int_0^{\theta_s} h(\theta) d\theta + \int_{\theta_s}^\pi h(\theta) d\theta \right\}\end{aligned}\quad (4.9)$$

It has been observed experimentally by many researchers that, at low Reynolds numbers up to $Re_D = 5000$, (according to Žukauskas and Žiugžda, 1985), there is no appreciable increase in the local heat transfer after separation point. However, at high Reynolds numbers, the local heat transfer increases from the separation point to the rear stagnation point but the effects of this increase on the average heat transfer are observed to be smaller. Hence, the average heat transfer coefficient can be written as:

$$\begin{aligned}\bar{h} &= \frac{1}{\pi} \int_0^{\theta_s} h(\theta) d\theta \\ &= \frac{1}{\pi} \left\{ \int_0^{\theta_1} h_1(\theta) d\theta + \int_{\theta_1}^{\theta_s} h_2(\theta) d\theta \right\}\end{aligned}\quad (4.10)$$

Using Eqs. (4.2) - (4.7), Eq. (4.10) can be solved for the average Nusselt number of an isothermal pin:

$$Nu_D|_{isothermal} = 0.5930 Re_D^{1/2} Pr^{1/3} \quad (4.11)$$

In Fig. 4.4, the dimensionless coefficients of heat transfer are plotted for air and water. As expected the heat transfer coefficients for water are higher than air.

4.2.2 Isoflux Boundary Condition

For the isoflux boundary condition, Eqs. (E-15) and (E-16) give the following dimensionless thermal boundary layer thicknesses:

$$\left(\frac{\delta_T(\theta)}{D}\right) Re_D^{1/2} Pr^{1/3} = \begin{cases} \sqrt[3]{\frac{4(\lambda_1 + 12) \sin \theta}{45 f_4(\theta)} \sqrt{\frac{\cos \theta}{\lambda_1}}} & \text{for Region I} \\ \sqrt[3]{\frac{4 \sin \theta}{45 f_6(\theta)} \sqrt{\frac{\cos \theta}{\lambda_2}}} & \text{for Region II} \end{cases} \quad (4.12)$$

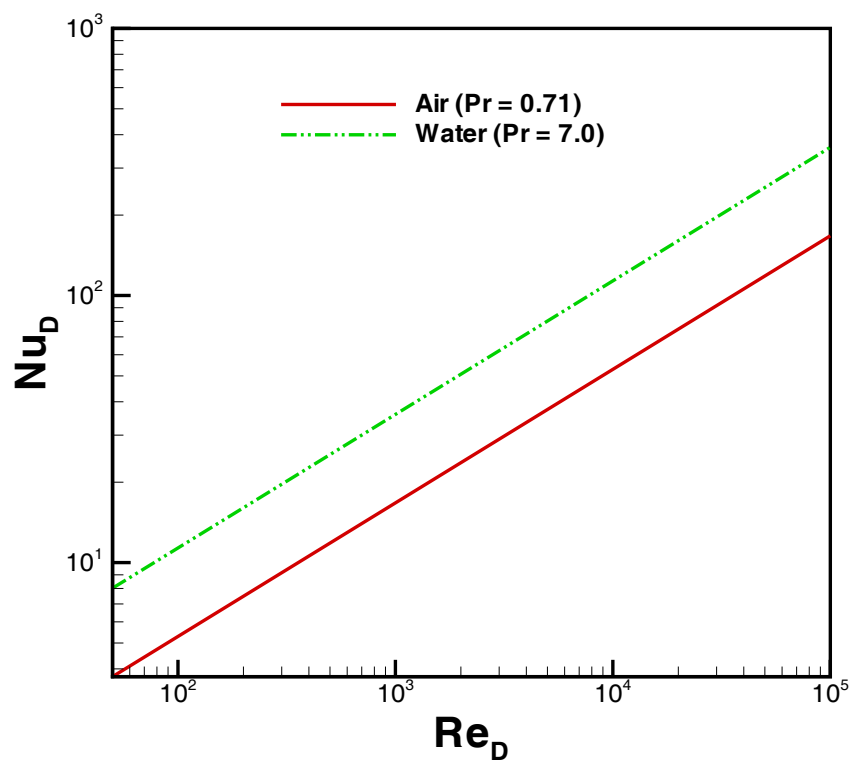


Figure 4.4: Average Heat Transfer Coefficients For Air and Water

where the functions are given by:

$$f_4(\theta) = \theta \quad (4.13)$$

$$f_5(\theta) = \theta - \pi/2 \quad (4.14)$$

$$f_6(\theta) = \frac{f_5(\theta)}{\lambda_2 + 12} + \frac{f_4(\theta)}{\lambda_1 + 12} \quad (4.15)$$

The local surface temperatures, for the two regions, can then be obtained from Eq. (C-6):

$$\Delta T_1(\theta) = \frac{2q\delta_{T_1}}{3k_f} \quad \text{and} \quad \Delta T_2(\theta) = \frac{2q\delta_{T_2}}{3k_f} \quad (4.16)$$

The local heat transfer coefficients can now be obtained from its definition as:

$$h_1(\theta) = \frac{q}{\Delta T_1(\theta)} = \frac{3k_f}{2\delta_{T_1}} \quad \text{and} \quad h_2(\theta) = \frac{q}{\Delta T_2(\theta)} = \frac{3k_f}{2\delta_{T_2}} \quad (4.17)$$

which give the local Nusselt numbers for the cross flow over an isoflux pin:

$$\frac{Nu_D(\theta)|_{isoflux}}{Re_D^{1/2} Pr^{1/3}} = \begin{cases} \frac{3}{2} \sqrt[3]{\frac{4(\lambda_1 + 12)\sin\theta}{45f_4(\theta)}} \sqrt{\frac{\cos\theta}{\lambda_1}} & \text{for Region I} \\ \frac{3}{2} \sqrt[3]{\frac{4\sin\theta}{45f_6(\theta)}} \sqrt{\frac{\cos\theta}{\lambda_2}} & \text{for Region II} \end{cases} \quad (4.18)$$

The comparison of local Nusselt numbers for the isothermal and isoflux boundary conditions is presented in Fig. 4.5. the isoflux boundary condition gives a higher heat transfer coefficient over the larger part of the circumference. On the front part of the pin (up to $\theta \approx 30^\circ$), there is no appreciable effect of boundary condition. In the flow in this region the heat transfer coefficients are insensitive to the boundary conditions on the surface.

Following the same procedure for the average heat transfer coefficient, as mentioned for isothermal pin, one can obtain the average Nusselt number for an isoflux pin as:

$$Nu_D|_{isoflux} = 0.6321 Re_D^{1/2} Pr^{1/3} \quad (4.19)$$

This Nusselt number is 6% greater than the average Nusselt number of an isothermal pin.

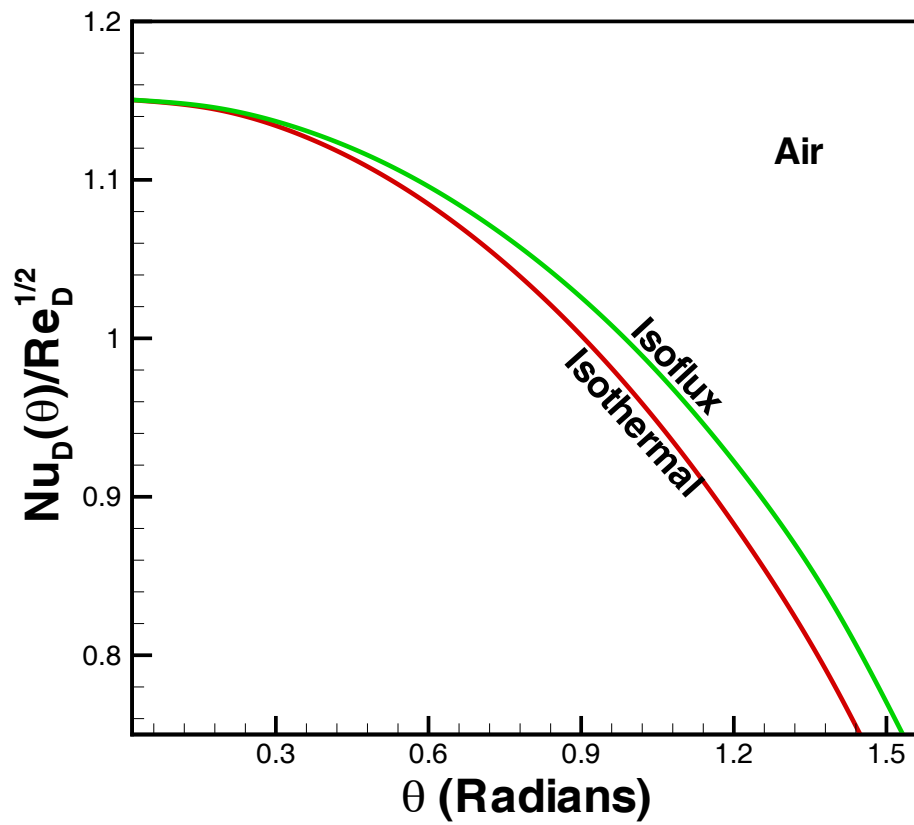


Figure 4.5: Local Nusselt Numbers for Different Thermal Boundary Conditions

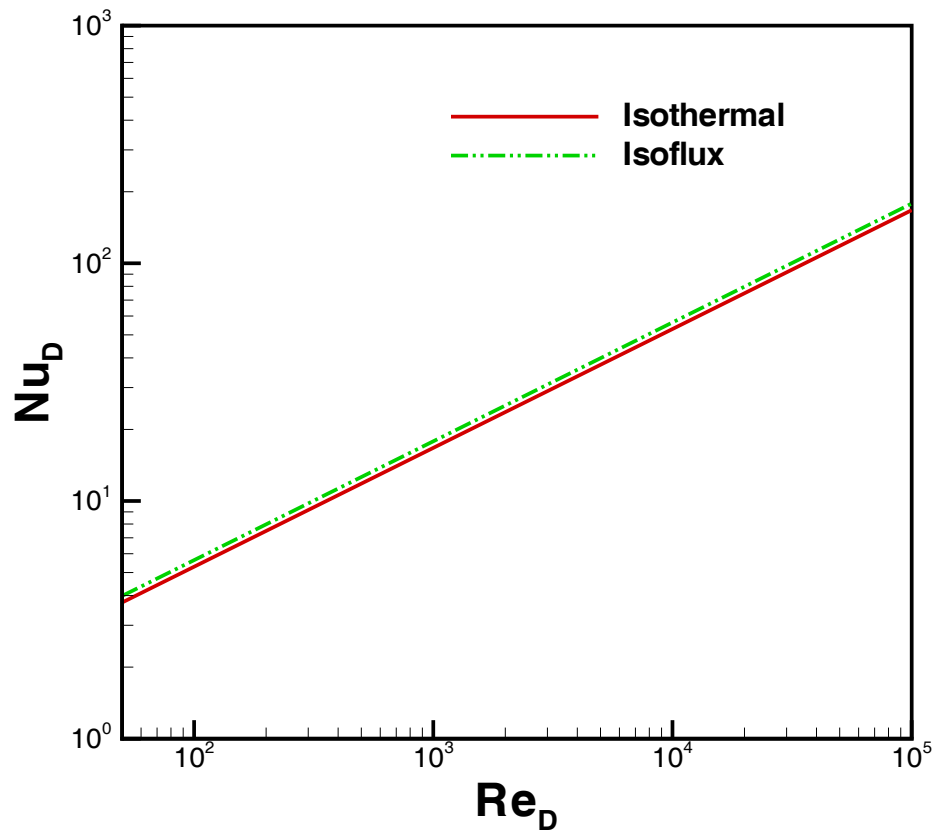


Figure 4.6: Average Nusselt Numbers for Different Thermal Boundary Conditions

Combining the results for both thermal boundary conditions, we have

$$\frac{Nu_D}{Re_D^{1/2} Pr^{1/3}} = \begin{cases} 0.5930 & \text{for UWT} \\ 0.6321 & \text{for UWF} \end{cases} \quad (4.20)$$

The average Nusselt numbers for isothermal and isoflux thermal boundary conditions are shown in Fig. 4.6. Air is used as a fluid to calculate heat transfer from a circular pin. It is clear from this figure that the isoflux boundary condition gives higher heat transfer for the whole range of Reynolds number.

4.3 Elliptical Pin-Fin in an Infinite Medium

Consider uniform flow of a Newtonian fluid past a fixed elliptical pin with a major axis of $2a$ and a minor axis of $2b$ (Fig. 3.6). The flow is assumed to be laminar, steady, and two dimensional. The approaching velocity of the air is U_{app} and the ambient temperature of the air is T_a . The surface temperature of the pin wall is assumed as T_w in case of the isothermal pin and the heat flux is q for the isoflux boundary condition. Using order-of-magnitude analysis (Appendix A), the energy equation in curvilinear coordinates (Fig. 3.6) can be written as:

$$u \frac{\partial T}{\partial s} + v \frac{\partial T}{\partial \eta} = \alpha \frac{\partial^2 T}{\partial \eta^2} \quad (4.21)$$

4.3.1 Isothermal Boundary Condition

Using Eq. (D-20) in Eqs. (E-11) and (E-12) and simplifying, thermal boundary layer thicknesses can be determined:

$$\left(\frac{\delta_T(\theta)}{\mathcal{L}}\right) \cdot Re_{\mathcal{L}}^{1/2} Pr^{1/3} = \sqrt{\frac{2.236}{(1+\epsilon)E(e)}} \begin{cases} \sqrt[3]{\frac{(1-e^2 \cos^2 \theta)^2 f_3(\theta)}{\epsilon(\lambda_1+12)^2 \sin^2 \theta}} \sqrt{\frac{\lambda_1}{\cos \theta}} & \text{for Region I} \\ \sqrt[3]{\frac{(1-e^2 \cos^2 \theta)^2 f_5(\theta)}{\epsilon \sin^2 \theta}} \sqrt{\frac{\lambda_2}{\cos \theta}} & \text{for Region II} \end{cases} \quad (4.22)$$

where the functions $f_3(\theta)$ and $f_5(\theta)$ are given by:

$$f_3(\theta) = \int_0^\theta \sin \theta (\lambda_1 + 12) d\theta \quad (4.23)$$

and

$$f_5(\theta) = \frac{f_3(\theta)}{\lambda_1 + 12} + \frac{f_4(\theta)}{\lambda_2 + 12} \quad (4.24)$$

with

$$f_4(\theta) = \int_{\theta_1}^{\theta_s} \sin \theta (\lambda_2 + 12) d\theta \quad (4.25)$$

Using the definition of the local heat transfer coefficient, given in Eq. (4.6), the local Nusselt numbers for an isothermal elliptical pin of arbitrary axis ratio ϵ can be written as:

$$\frac{Nu_{\mathcal{L}}(\theta)|_{isothermal}}{Re_{\mathcal{L}}^{1/2} Pr^{1/3}} = \frac{\sqrt{(1+\epsilon)E(e)}}{3.33} \begin{cases} \sqrt[3]{\frac{\epsilon(\lambda_1+12)^2 \sin^2 \theta}{(1-e^2 \cos^2 \theta)^2 f_3(\theta)}} \sqrt{\frac{\cos \theta}{\lambda_1}} & \text{for Region I} \\ \sqrt[3]{\frac{\epsilon \sin^2 \theta}{(1-e^2 \cos^2 \theta)^2 f_4(\theta)}} \sqrt{\frac{\cos \theta}{\lambda_2}} & \text{for Region II} \end{cases} \quad (4.26)$$

The average heat transfer coefficients are determined using Eq. (4.10) for different axis ratios and then correlated to obtain a single expression that can be used for a wide range of axis ratios, Reynolds, and Prandtl numbers. This expression is

$$\frac{Nu_{\mathcal{L}}|_{isothermal}}{Re_{\mathcal{L}}^{1/2} Pr^{1/3}} = 0.75 - 0.16 \exp(-0.018\epsilon^{-3.1}) \quad (4.27)$$

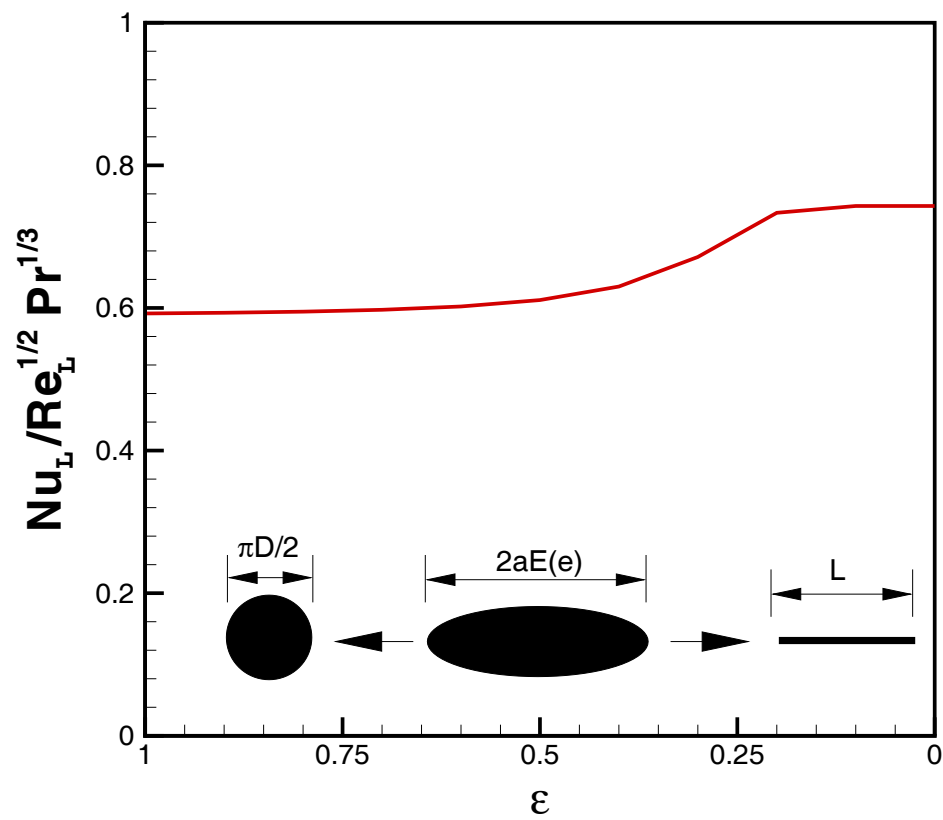


Figure 4.7: Variation of Average Nusselt Number with Axis Ratio for an Isothermal Elliptic Pin

The heat transfer parameter $\frac{Nu_{\mathcal{L}}|_{isothermal}}{Re_{\mathcal{L}}^{1/2} Pr^{1/3}}$ is plotted in Fig. 4.7 for different axis ratios of the elliptical pin. It can be seen that the heat transfer increases slowly with the axis ratio upto $\epsilon \simeq 0.1$ (flat plate), and then it becomes constant.

4.3.2 Isoflux Boundary Condition

Using again Eqs. (E-15) and (E-16), the thicknesses of the thermal boundary layer in both regions can be written as:

$$\frac{\delta_T(\theta)}{\mathcal{L}} = \frac{1}{Re_{\mathcal{L}}^{1/2} Pr^{1/3}} \sqrt{\frac{5\pi}{(1+\epsilon)E(e)}} \begin{cases} \sqrt[3]{\frac{(1-e^2 \cos^2 \theta)^{3/2} f_6(\theta)}{\epsilon(\lambda_1 + 12) \sin \theta}} \sqrt{\frac{\lambda_1}{\cos \theta}} & \text{for Region I} \\ \sqrt[3]{\frac{(1-e^2 \cos^2 \theta)^{3/2} f_8(\theta)}{\epsilon \sin \theta}} \sqrt{\frac{\lambda_2}{\cos \theta}} & \text{for Region II} \end{cases} \quad (4.28)$$

where the functions $f_6(\theta)$ and $f_8(\theta)$ are given by:

$$f_6(\theta) = \int_0^\theta \sqrt{1 - e^2 \cos^2 \theta} d\theta \quad (4.29)$$

and

$$f_8(\theta) = \frac{f_7(\theta)}{\lambda_1 + 12} + \frac{f_6(\theta)}{\lambda_2 + 12} \quad (4.30)$$

with

$$f_7(\theta) = \int_{\theta_1}^{\theta_s} \sqrt{1 - e^2 \cos^2 \theta} d\theta \quad (4.31)$$

Following Eqs. (4.6) and (4.7), one can determine the local Nusselt numbers for an elliptical pin of arbitrary axis ratio ϵ :

$$\frac{Nu_{\mathcal{L}}(\theta)|_{isoflux}}{Re_{\mathcal{L}}^{1/2} Pr^{1/3}} = \sqrt{\frac{(1+\epsilon)E(e)}{7}} \begin{cases} \sqrt[3]{\frac{\epsilon(\lambda_1 + 12) \sin \theta}{(1 - e^2 \cos^2 \theta)^{3/2} f_6(\theta)}} \sqrt{\frac{\cos \theta}{\lambda_1}} & \text{for Region I} \\ \sqrt[3]{\frac{\epsilon \sin \theta}{(1 - e^2 \cos^2 \theta)^{3/2} f_8(\theta)}} \sqrt{\frac{\cos \theta}{\lambda_2}} & \text{for Region II} \end{cases} \quad (4.32)$$

The comparison of local dimensionless heat transfer $Nu_{\mathcal{L}}(\theta)/Re_{\mathcal{L}}^{1/2}$ for both thermal boundary conditions is shown in Fig. 4.8 using air as the fluid. It can be seen again that there is no appreciable effect of the boundary condition in the front stagnation region. However, the isoflux boundary condition gives higher heat transfer over the remaining part of the elliptical pin. Here the values are compared for a specific axis ratio $\epsilon = 0.5$.

The average heat transfer coefficients are determined using Eqs. (4.10) and (4.11) for different axis ratios and then correlated to obtain a single expression that can be used for a wide range of axis ratios, Reynolds, and Prandtl numbers. This expression is

$$\frac{Nu_{\mathcal{L}}|_{isoflux}}{Re_{\mathcal{L}}^{1/2} Pr^{1/3}} = 0.91 - 0.31 \exp(-0.09\epsilon^{-1.79}) \quad (4.33)$$

Combining the results for both thermal boundary conditions, we have

$$\frac{Nu_{\mathcal{L}}}{Re_{\mathcal{L}}^{1/2} Pr^{1/3}} = \begin{cases} 0.75 - 0.16 \exp(-0.018\epsilon^{-3.1}) & \text{for UWT} \\ 0.91 - 0.31 \exp(-0.09\epsilon^{-1.79}) & \text{for UWF} \end{cases} \quad (4.34)$$

Equation (4.34) gives the dimensionless Nusselt numbers for elliptical pins of arbitrary axis ratio under isothermal and isoflux boundary conditions.

In the limiting cases, when $\epsilon = 1$ and $\mathcal{L} = D$, it represents the average Nusselt numbers for a circular pin:

$$\frac{Nu_D}{Re_D^{1/2} Pr^{1/3}} = \begin{cases} 0.5930 & \text{for UWT} \\ 0.6321 & \text{for UWF} \end{cases} \quad (4.35)$$

and when $\epsilon = 0$ and $\mathcal{L} = L$, it represents the average Nusselt number for a finite flat plate:

$$\frac{Nu_L}{Re_L^{1/2} Pr^{1/3}} = \begin{cases} 0.750 & \text{for UWT} \\ 0.912 & \text{for UWF} \end{cases} \quad (4.36)$$

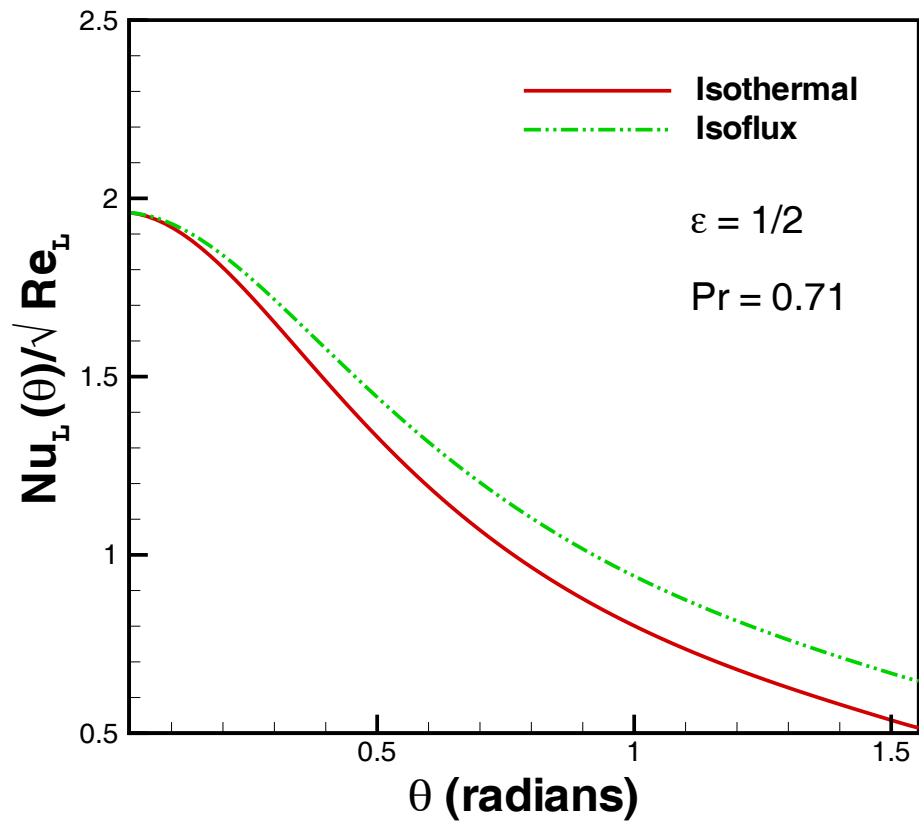


Figure 4.8: Comparison of Local Nusselt Numbers for Both Thermal Boundary Conditions

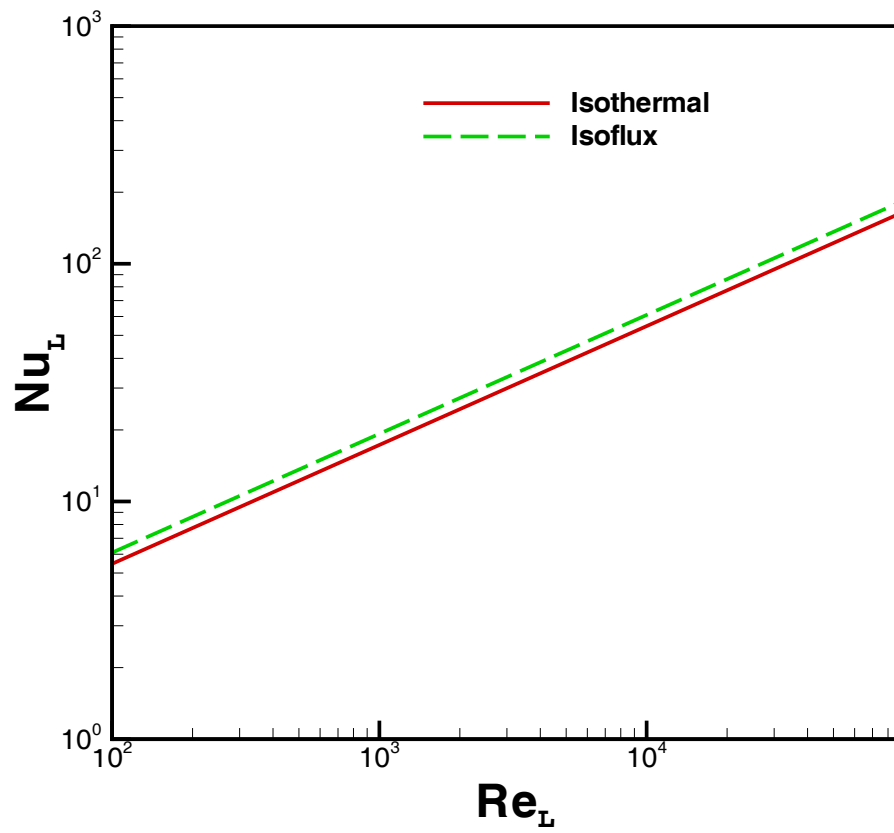


Figure 4.9: Comparison of Average Nusselt Numbers for Both Thermal Boundary Conditions

The comparison of average heat transfer coefficients of an elliptical pin ($\epsilon = 0.5$) for both thermal boundary conditions is shown in Fig. 4.9. It can be seen in this figure that the heat transfer from an isoflux pin is about 10% higher than isothermal pin. This difference decreases with the increase in axis ratio.

4.4 Circular Pin Confined Between Two Parallel Planes

A circular pin confined between two parallel planes is shown in Fig. 3.10. The approaching velocity of the fluid is U_{app} and the ambient temperature is assumed to be T_a . The surface temperature of the pin wall is T_w in the case of the isothermal pin and the heat flux is q for the isoflux boundary condition. For the same flow conditions, the energy equation in curvilinear coordinates, Eq. (4.1), can be used for both boundary conditions. The temperature distributions inside the boundary layer for both thermal boundary conditions are described in Appendix C, whereas the potential flow velocity outside the boundary layer is derived in Appendix D.

4.4.1 Isothermal Boundary Condition

Equations (E-11) and (E-12) can be solved separately in the two regions for the local thermal boundary layer thicknesses:

$$\left(\frac{\delta_T(\theta)}{D}\right) \cdot Re_D^{1/2} Pr^{1/3} = \begin{cases} \sqrt[3]{\frac{90f_1(\theta)}{(\lambda_1 + 12)^2 f^2(\theta)} \sqrt{\frac{\lambda_1}{2g(\theta)}}} & \text{for Region I} \\ \sqrt[3]{\frac{90f_3(\theta)}{f^2(\theta)} \sqrt{\frac{\lambda_2}{2g(\theta)}}} & \text{for Region II} \end{cases} \quad (4.37)$$

where $f(\theta)$ is given by Eq. (D-32), $g(\theta)$ is the first derivative of $f(\theta)$ with respect to θ , and the functions $f_1(\theta)$ and $f_3(\theta)$ are given by:

$$f_1(\theta) = \int_0^\theta f(\theta) (\lambda_1 + 12) d\theta \quad (4.38)$$

and

$$f_3(\theta) = \frac{f_1(\theta)}{(\lambda_1 + 12)^2} + \frac{f_2(\theta)}{(\lambda_2 + 12)^2} \quad (4.39)$$

with

$$f_2(\theta) = \int_{\theta_1}^{\theta_s} f(\theta)(\lambda_2 + 12)d\theta \quad (4.40)$$

Using the definitions of local heat transfer coefficients, given in Eqs. (4.6) and (4.7), the local Nusselt numbers can be written for a pin with arbitrary blockage ratio as follows:

$$\frac{Nu_D(\theta)|_{isothermal}}{Re_D^{1/2} Pr^{1/3}} = \frac{1}{3} \begin{cases} \sqrt[3]{\frac{(\lambda_1 + 12)^2 f^2(\theta)}{f_1(\theta)} \sqrt{\frac{2g(\theta)}{\lambda_1}}} & \text{for Region I} \\ \sqrt[3]{\frac{f^2(\theta)}{f_3(\theta)} \sqrt{\frac{2g(\theta)}{\lambda_2}}} & \text{for Region II} \end{cases} \quad (4.41)$$

The average heat transfer coefficients are determined using Eqs. (4.9) and (4.10) for different blockage ratios, defined as $b = D/S_T$, and then correlated to obtain a single expression that can be used for a wide range of blockage ratios, Reynolds, and Prandtl numbers. This expression is given by:

$$\frac{Nu_D|_{isothermal}}{Re_D^{1/2} Pr^{1/3}} = 0.843 - 0.25 \exp(-2.65b^{2.5}) \quad (4.42)$$

4.4.2 Isoflux Boundary Condition

Solving Eqs. (E-15) and (E-16) using the potential flow velocity, Eq. (D-33), the thermal boundary layer thicknesses for isoflux boundary condition can be written as:

$$\left(\frac{\delta_T(\theta)}{D}\right) \cdot Re_D^{1/2} Pr^{1/3} = \begin{cases} \sqrt[3]{\frac{45\theta}{(\lambda_1 + 12)f(\theta)} \sqrt{\frac{\lambda_1}{2g(\theta)}}} & \text{for Region I} \\ \sqrt[3]{\frac{45f_4(\theta)}{f(\theta)} \sqrt{\frac{\lambda_2}{2g(\theta)}}} & \text{for Region II} \end{cases} \quad (4.43)$$

where

$$f_4(\theta) = \frac{\theta}{\lambda_1 + 12} + \frac{\theta - \pi/2}{\lambda_2 + 12} \quad (4.44)$$

Following the definition of the local surface temperature, Eq. (4.16) and the local heat transfer coefficient, Eq. (4.17), Eq. (4.43) gives the local Nusselt numbers for the isoflux thermal boundary condition:

$$\frac{Nu_D(\theta)|_{isoflux}}{Re_D^{1/2} Pr^{1/3}} = 1.5 \begin{cases} \sqrt[3]{\frac{(\lambda_1 + 12)f(\theta)}{45\theta} \sqrt{\frac{2g(\theta)}{\lambda_1}}} & \text{for Region I} \\ \sqrt[3]{\frac{f(\theta)}{45f_4(\theta)} \sqrt{\frac{2g(\theta)}{\lambda_2}}} & \text{for Region II} \end{cases} \quad (4.45)$$

The average heat transfer coefficients are determined using Eq. (4.10) for different blockage ratios and then correlated to obtain a single expression:

$$\frac{Nu_D|_{isoflux}}{Re_D^{1/2} Pr^{1/3}} = 1.104 - 0.47 \exp(-1.54b^{2.77}) \quad (4.46)$$

Combining the results for both thermal boundary conditions, we have

$$\frac{Nu_D}{Re_D^{1/2} Pr^{1/3}} = \begin{cases} 0.843 - 0.25 \exp(-2.65b^{2.5}) & \text{for UWT} \\ 1.104 - 0.47 \exp(-1.54b^{2.77}) & \text{for UWF} \end{cases} \quad (4.47)$$

For infinite flows, when $b = 0$, Eq. (4.47) coincides with Eqs. (4.20) and (4.35). The effects of blockage ratio on heat transfer are shown in Figs. (4.10) and (4.11). Figure 4.10 shows that the heat transfer parameter decreases for both thermal boundary conditions with the blockage ratio. The only appreciable effect of both boundary conditions can be seen in the front stagnation region. As a result, the heat transfer from an isoflux pin will be higher than isothermal pin. Figure 4.11 shows that the average heat transfer decreases with blockage ratio and increases with the Reynolds number. They approach to the heat transfer values for an infinite circular pin when the blockage is zero.

4.5 Pin-Fin Heat Sinks

Heat sinks, used in microelectronics, usually consist of arrays of pin-fins in in-line or staggered arrangements. Both can work effectively depending on the surface one provides

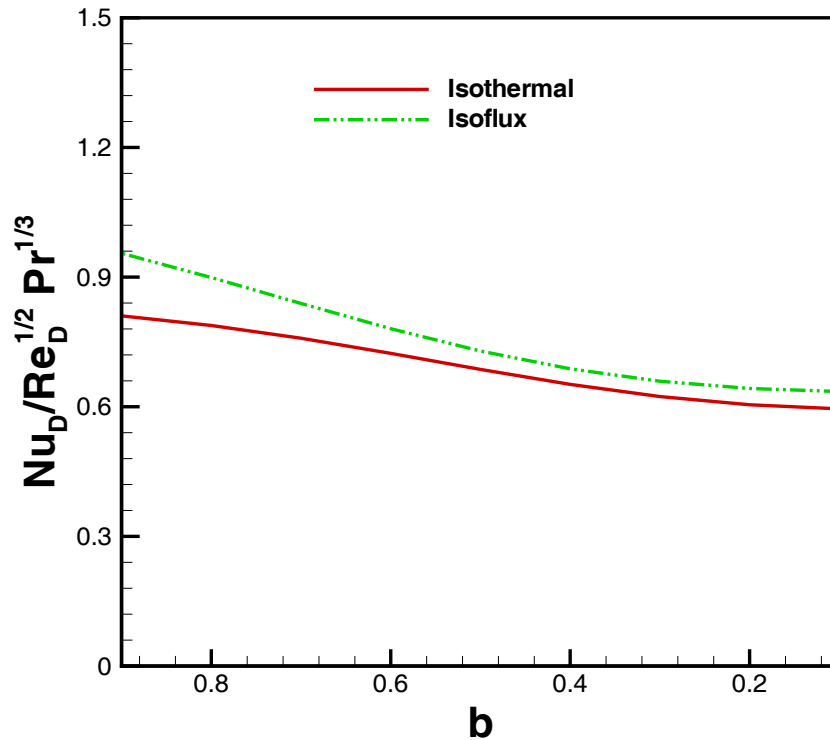


Figure 4.10: Effect of Blockage Ratio on Heat Transfer and Thermal Boundary Conditions

on the heat sink. Therefore, more surface area the more heat dissipated. The staggered arrangement of pin-fins increases turbulence around the pins, which increases the cooling rate significantly, see Fig. 4.12 for both arrangements.

The pins are attached to a common base of dimension $L \times W \times t_b$, and the geometry of the array is determined by the fin diameter D , pin height H , longitudinal spacing S_L , and transverse spacing S_T (Fig. 3-13). In this section, the average heat transfer coefficient will be determined first for the pin-fin arrays and then for the base plate alone. Finally, the overall average heat transfer coefficient will be determined for the whole system.

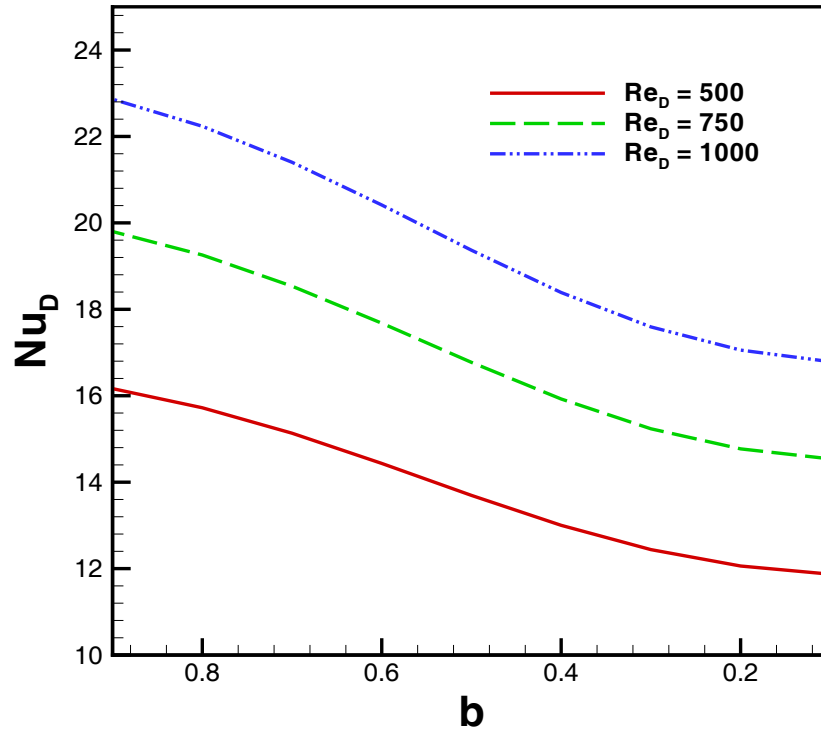
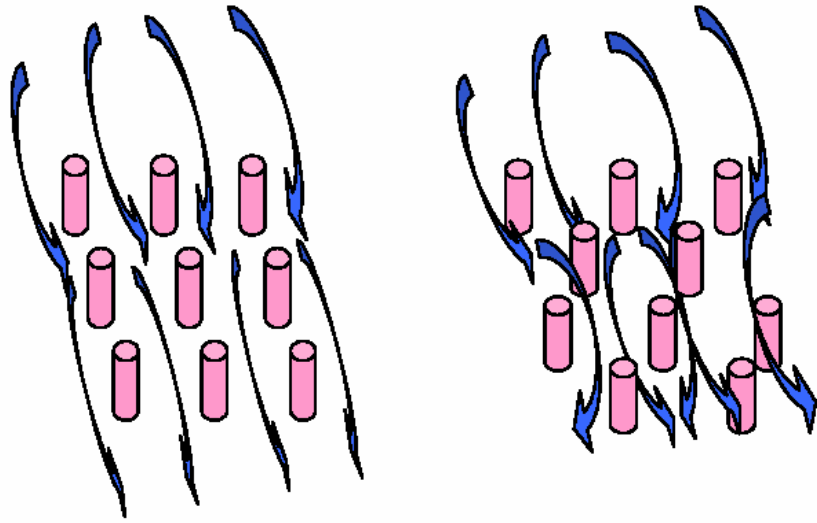


Figure 4.11: Effect of Blockage Ratio and Reynolds Number on Average Nusselt Numbers

4.5.1 Pin-Fin Arrays

Average heat transfer coefficients for pin-fin arrays can be determined by choosing a control volume as shown in Fig. 3.16 under isothermal or isoflux thermal boundary condition.



A)

B)

Figure 4.12: A) Aligned Pins with Fluid Flow B) Staggered Pins with Fluid Flow

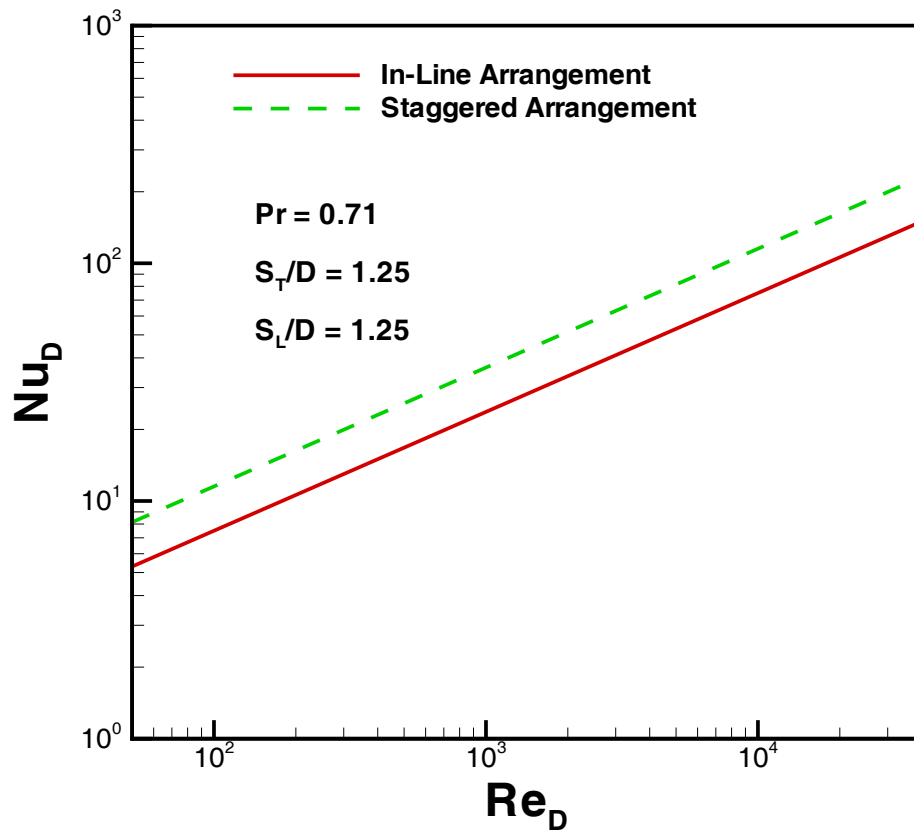


Figure 4.13: Comparison of Both Arrangements for 1.25×1.25

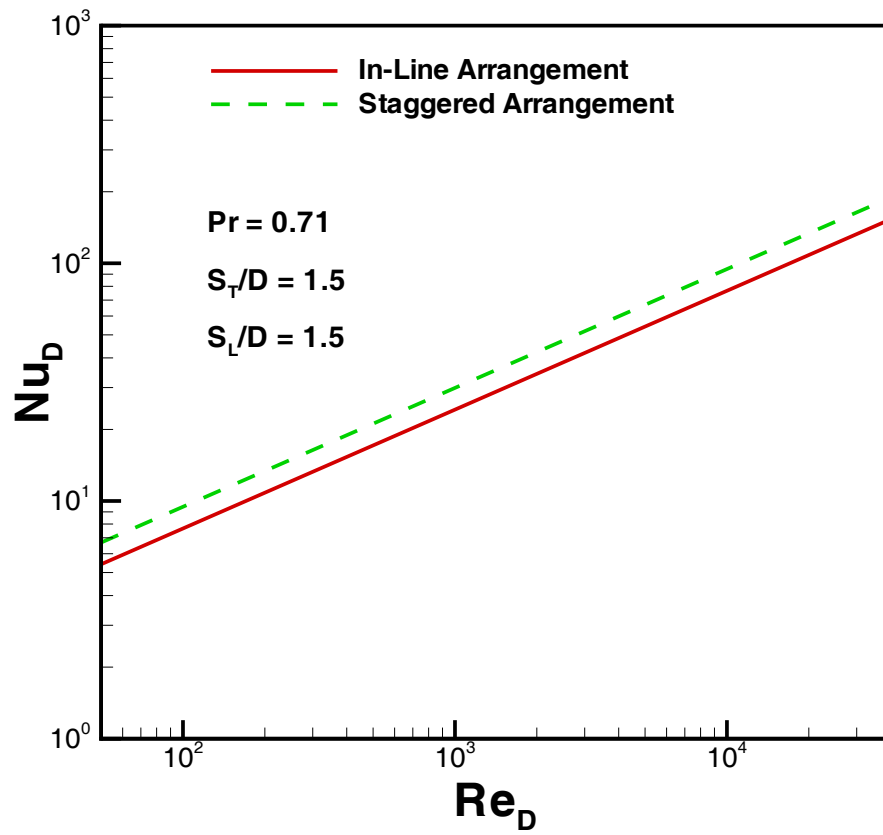


Figure 4.14: Comparison of Both Arrangements for 1.5×1.5

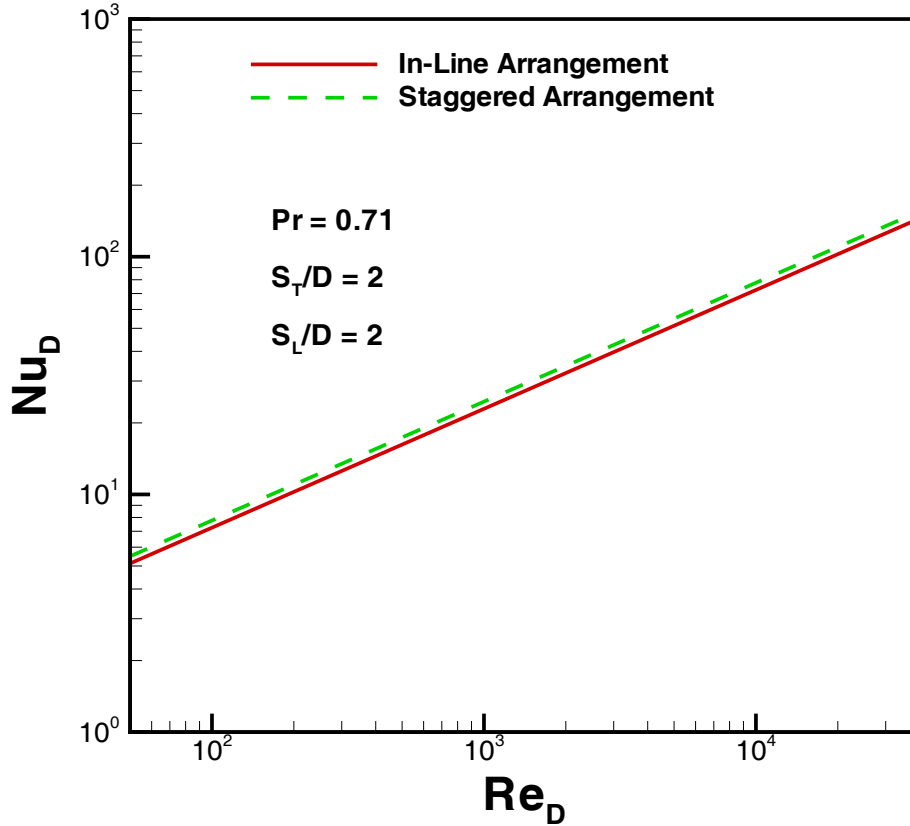


Figure 4.15: Comparison of Both Arrangements for 2×2

The hydrodynamic and thermal boundary conditions for this control volume are described in Appendix B. The potential flow velocities for in-line and staggered arrangements are derived in Appendix D, where $f(\theta)$ for in-line arrangement is given by Eq. (C-45) and for the staggered arrangement it is given by Eq. (C-52). Equation 4.1 can be solved for the control volume in the same manner as in Section 3 for a circular pin between parallel planes. The thermal boundary layer thicknesses for both boundary conditions can be determined by using Eqs. (4.37) and (4.43), whereas local Nusselt numbers are determined using Eqs. (4.41) and (4.45) respectively. Using the definition, average heat

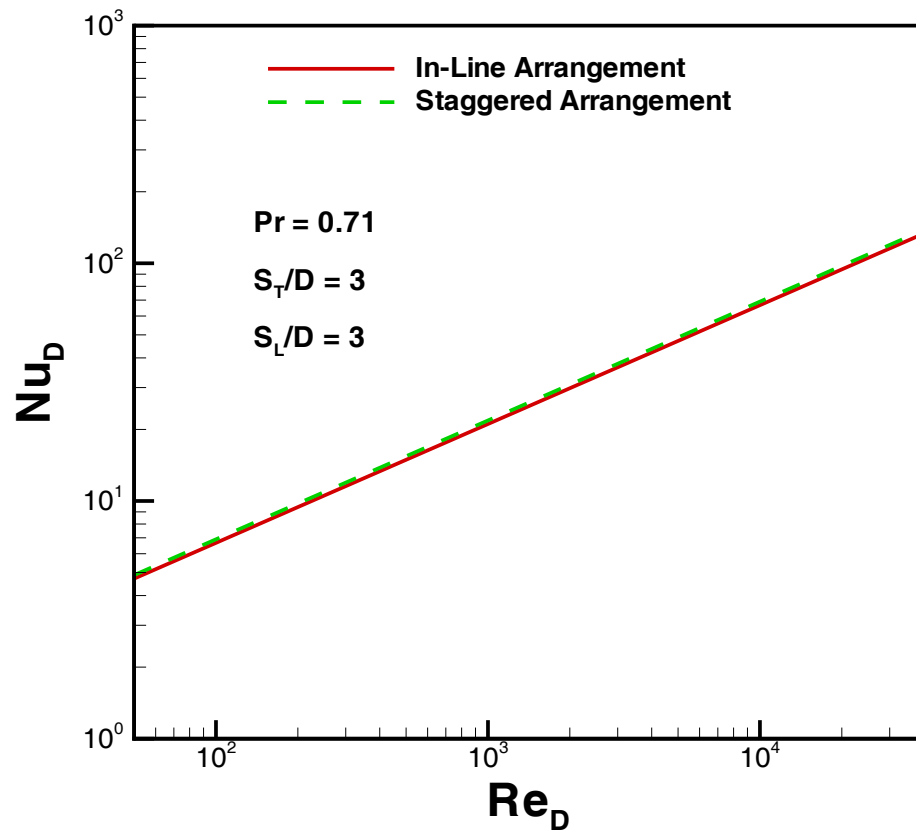


Figure 4.16: Comparison of Both Arrangements for 3×3

transfer coefficients are determined for both arrangements for different longitudinal and transverse pitches and a single correlation is obtained for both arrangements:

$$Nu_{Dfin} = \frac{h_{fin}D}{k_f} = C_1 Re_D^{1/2} Pr^{1/3} \quad (4.48)$$

where C_1 is a constant which depends upon the longitudinal and transverse pitches, arrangement of the pins, and thermal boundary conditions. For isothermal boundary condition, it is given by:

$$C_1 = \begin{cases} \frac{[0.25 + \exp(-0.55\mathcal{S}_L)]\mathcal{S}_T^{0.785}\mathcal{S}_L^{0.212}}{(\mathcal{S}_T - 1)^{0.5}} & \text{for In-Line Arrangement} \\ \frac{0.61\mathcal{S}_T^{0.591}\mathcal{S}_L^{0.053}}{(\mathcal{S}_T - 1)^{0.5}[1 - 2\exp(-1.09\mathcal{S}_L)]} & \text{for Staggered Arrangement} \end{cases} \quad (4.49)$$

The dimensionless heat transfer coefficient Nu_D is plotted versus Re_D in Figs. 4.13 - 4.16 for both arrangements (in-line and staggered) with various transverse and longitudinal pitches. It can be seen that the staggered arrangement gives higher heat transfer than the in-line arrangement and this difference decreases as the transverse and longitudinal pitches increase.

As the pitches increase, the difference between heat transfer values in the two arrangements diminishes, which shows that for larger pitches, say 3×3 , there is no appreciable effect of the arrangement. Both arrangements give almost the same heat transfer. The effects of longitudinal and transverse pitches on heat transfer in in-line arrangement are shown in Fig. 4.17.

It is clear that the lower pitches give higher heat transfer but as they increase, heat transfer approaches to a circular pin in an infinite medium. The effects of transverse pitch on heat transfer in staggered arrangement can be seen clearly in Fig. 4.18. In this case, the longitudinal pitch is kept constant.

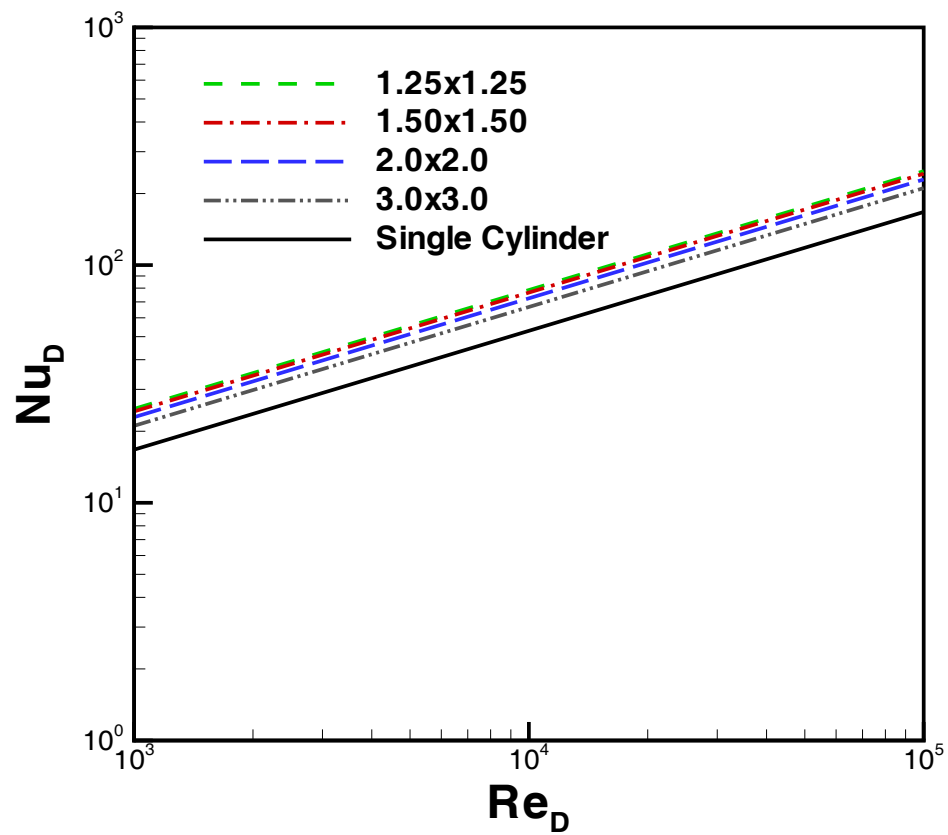


Figure 4.17: Effect of Pitches on Heat Transfer in In-Line Arrangement

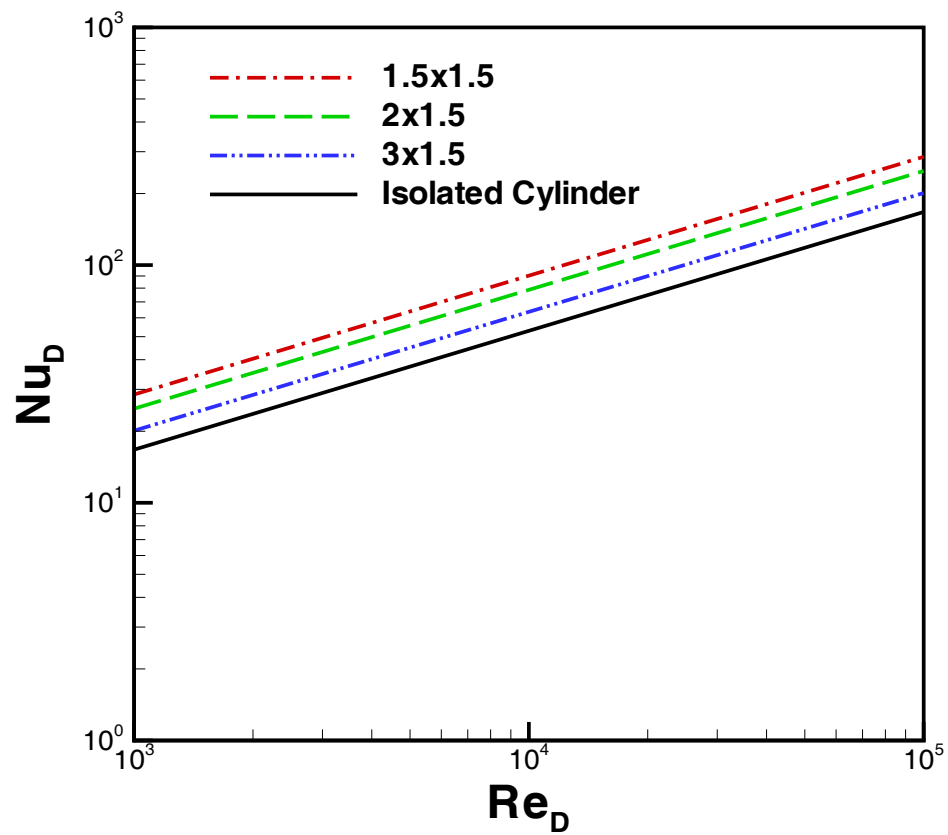


Figure 4.18: Effect of Transverse Pitch on Heat Transfer in Staggered Arrangement

4.5.2 Base Plate

The average heat transfer coefficient for the base plate, h_b , can be determined by considering it as a finite plate. It has been shown in section 2 that the dimensionless heat transfer coefficient for a finite plate, under isothermal boundary condition, can be written as:

$$Nu_L = \frac{h_b L}{k_f} = 0.75 Re_L^{1/2} Pr^{1/3} \quad (4.50)$$

where L is the length of the base plate in the streamwise direction.

4.6 Model Verification

4.6.1 Single Circular Pin in an Infinite Flow

The results of average heat transfer from a single isothermal pin are shown in Fig. 4.19, where they are compared with the correlations of Churchill and Bernstein (1977), Žukauskas (1972), and of Hilpert (1933). It shows that the present results are up to 8% higher than Churchill and Bernstein (1977), 15% higher than Žukauskas (1972), and 12% higher than Hilpert (1933) in the range $40 < Re_D < 1 \times 10^4$. Average Nusselt numbers for the isoflux boundary condition are compared in Fig. 4.20 with the experimental/numerical results. The present heat transfer values are found to be 11% higher than the numerical values of Krall and Eckert (1973) and 7% higher Chun and Boehm (1989) and 24% lower than the experimental values of Sarma and Sukhatme (1977). The reason behind the higher heat transfer values might be due to the approximate method and the assumed velocity and temperature profiles inside the boundary layers.

4.6.2 Single Elliptical Pin in an Infinite Flow

The results of heat transfer from a single infinite isothermal elliptical pin of axis ratio 1 : 2 are shown in Fig. 4.21, where they are compared with the experimental results of

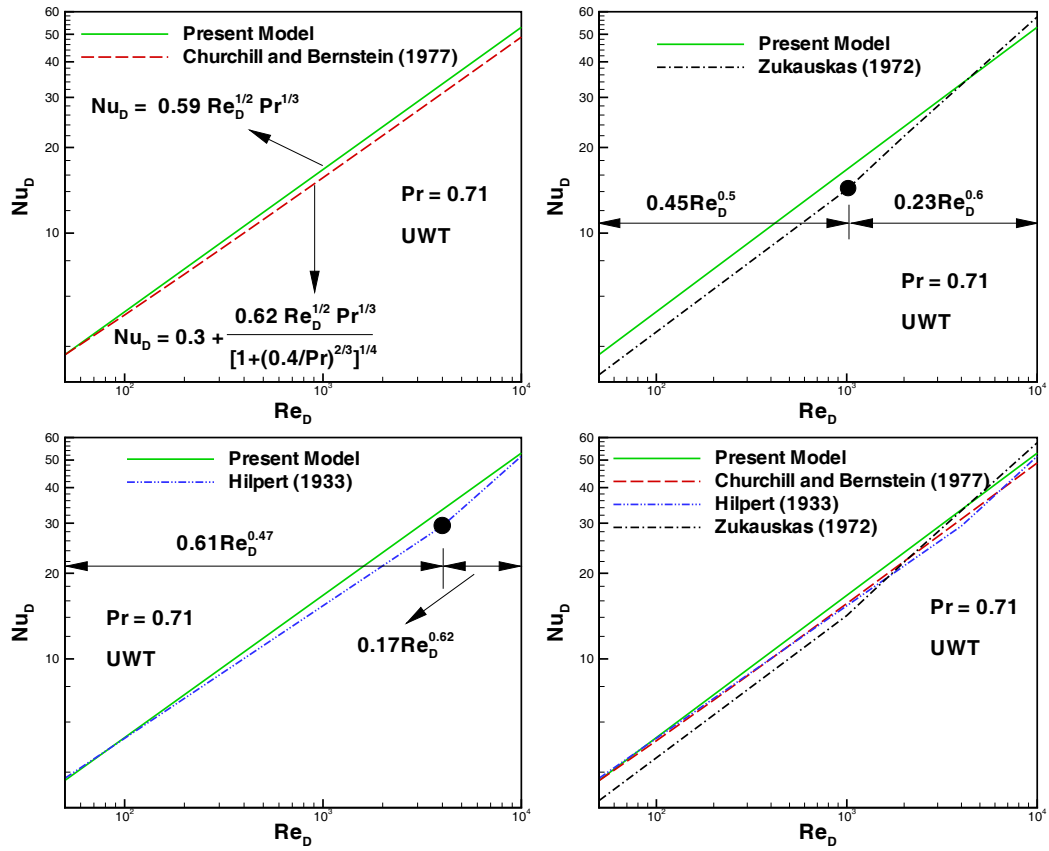


Figure 4.19: Variation of Average Nusselt Number with Reynolds Number for Isothermal Circular Pin

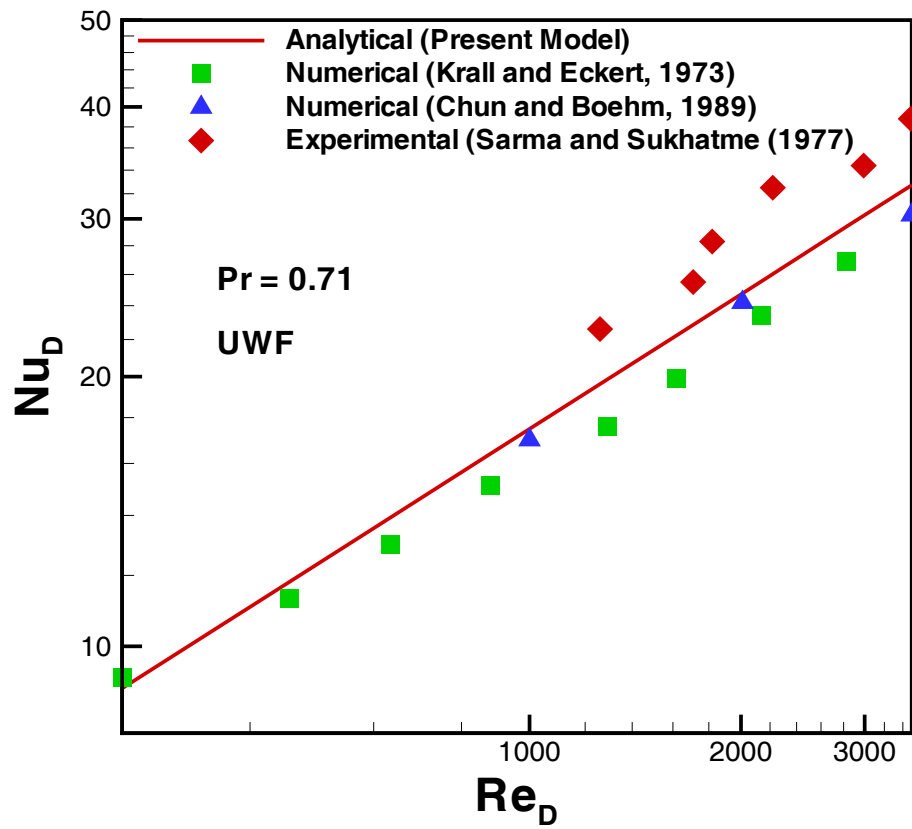


Figure 4.20: Variation of Average Nusselt Number with Reynolds Number for Isoflux Circular Pin

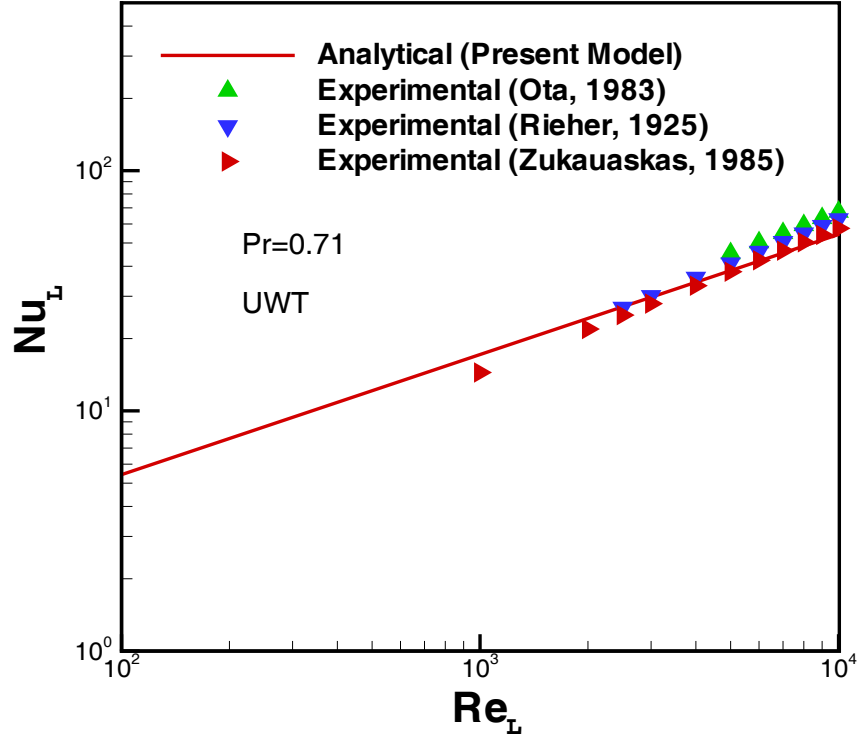


Figure 4.21: Variation of Average Nusselt Number with Reynolds Number for Isothermal Elliptic Pin With $\epsilon = 0.5$

Rieher (1925), Ota et al. (1983) and Žukauskas and Žiugžda (1985). Although the Rieher configuration was claimed as obscure by Ota et al. (1983), it shows good agreement with the present results. The results of Ota et al. (1983) and Žukauskas and Žiugžda (1985) also show very good agreement up to $Re_L = 4 \times 10^4$.

Beyond this range, the reason of discrepancy in the results is the same as explained above. Similar results for the same axis ratio can be observed for the isoflux boundary condition in Fig. 4.22. Here they show good agreement with Žukauskas and Žiugžda (1985). No other data could be found in the literature for isoflux boundary condition.

Fig. 4.23 shows the variation of the average heat transfer coefficients with the Reynolds number for an isothermal elliptical pin of axis ratio 0.33. The experimental results of Ota et al. (1984) are found to be in good agreement up to $Re_D = 40000$. This discrepancy can be observed again for higher Reynolds numbers due to the blockage and free stream turbulence effects present in the experiments. Furthermore, Ota et al. calculated their average values by graphical integration which could introduce errors. The variation of the average heat transfer coefficients with the axis ratios is shown in Fig. 4.24. It is clear that the average heat transfer coefficients increase with the increase in axis ratio upto $\epsilon = 0.01$ and then become constant for finite flat plate. These results are compared with Ota et al. (1984) for the same Reynolds numbers. Good agreement could be observed in the results at lower Reynolds number.

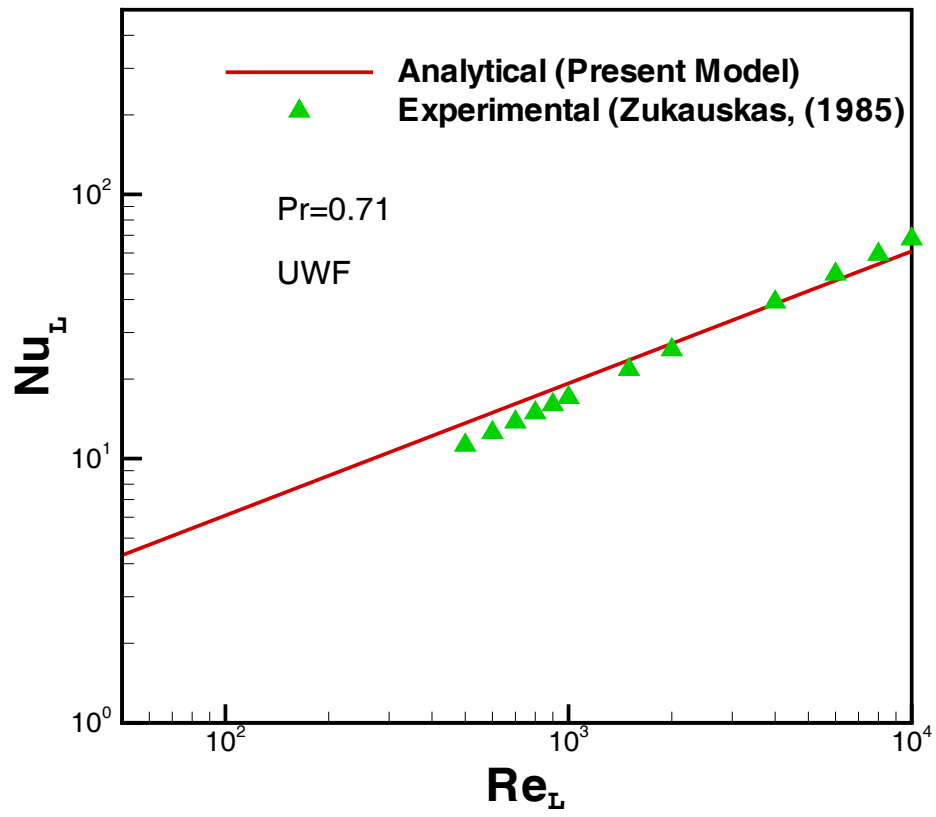


Figure 4.22: Variation of Average Nusselt Number with Reynolds Number for Isoflux Elliptic Pin With $\epsilon = 0.5$

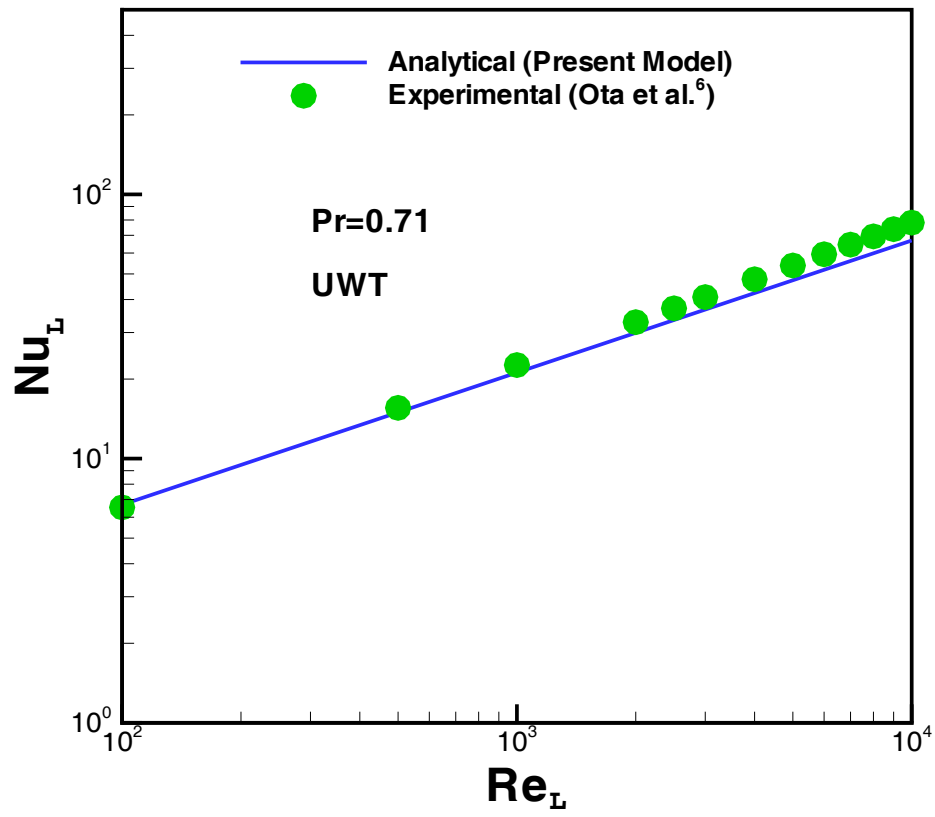


Figure 4.23: Variation of Average Nusselt Number with Reynolds Number for Isothermal Elliptic Pin

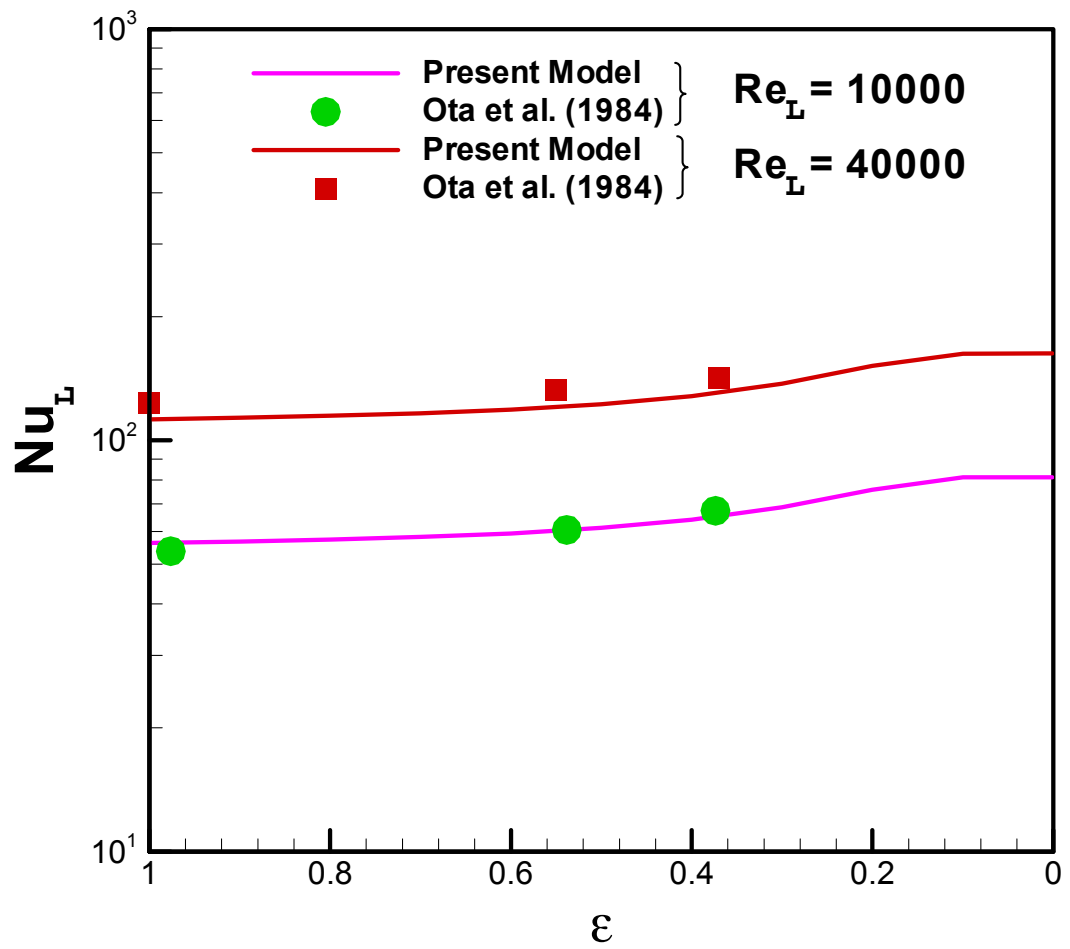


Figure 4.24: Variation of Average Nusselt Number with Axis Ratio for an Isothermal Elliptic Pin

4.6.3 Circular Pin Between Parallel Planes

The comparison of local Nusselt Numbers for the isothermal and isoflux boundary conditions for a given blockage ratio is shown in Fig. 4.25. The results are compared for water with $Pr = 7.8$ and blockage ratio $b = 0.4$. The isoflux boundary condition gives a higher heat transfer coefficient over the larger part of the circumference. On the front part of the pin (up to $\theta \approx 40^\circ$), there is no appreciable effect of boundary condition. Higher heat transfer coefficients have also been observed experimentally by Perkins and Leppert (1964) for the same blockage ratio with the isoflux boundary condition.

The results of average heat transfer from a single isoflux pin are shown in Figs. 4.26 and 4.27 for different blockage ratios, where they are compared with the experimental and numerical data of Hattori and Takahashi (1993) and Yamamoto and Hattori (1996). These figures show that the present results are in very good agreement with the previous experimental/ numerical work for a given range of Reynolds numbers.

The average Nusselt numbers for the isothermal pin for a given blockage ratio are compared in Fig. 4.28 with the experimental results of Niggenschmidt (1975) (reported by Hausen, 1983) and Hausen (1983). The average Nu_D values are found to be in a good agreement with both empirical results. However, both previous results are found to be higher at high Reynolds number due to free stream turbulence.

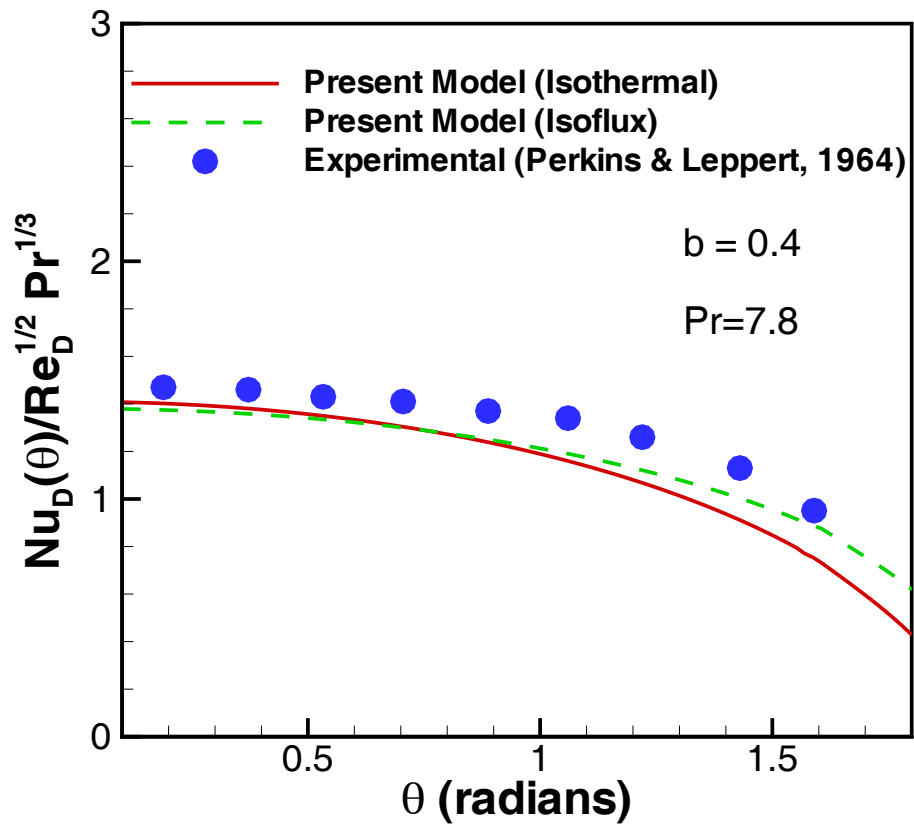


Figure 4.25: Local Nusselt Numbers for Different Thermal Boundary Conditions

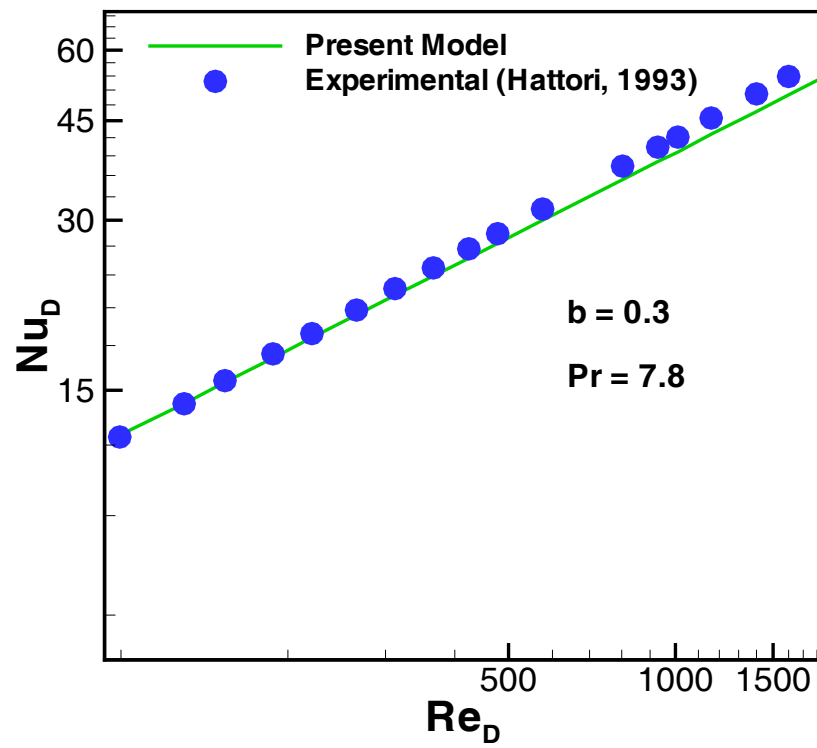


Figure 4.26: Average Nusselt Numbers for Isoflux Boundary Condition for Water

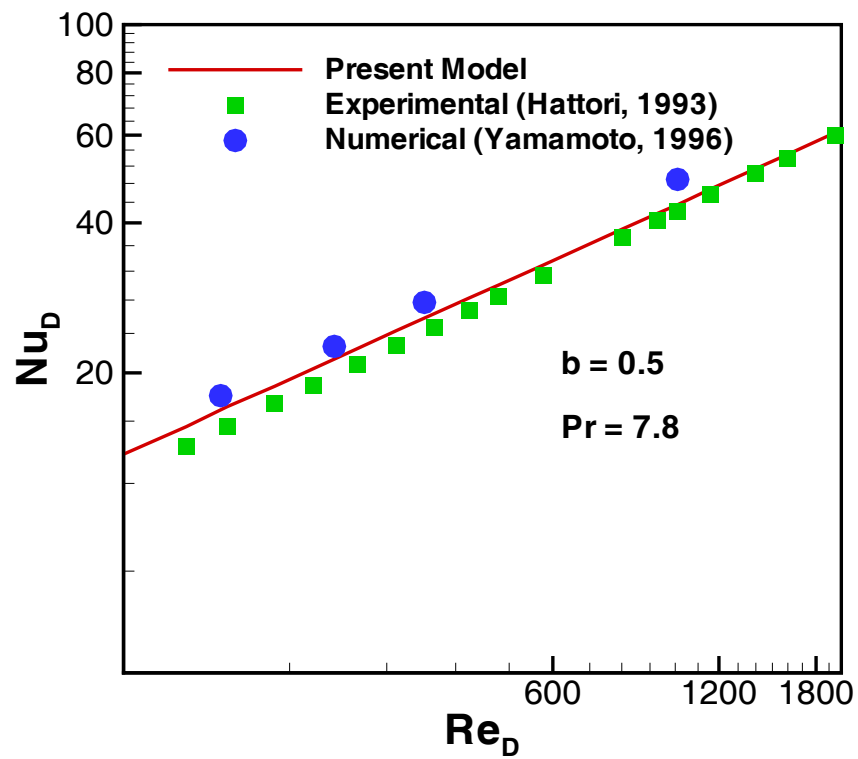


Figure 4.27: Average Nusselt Numbers for Isoflux Pin

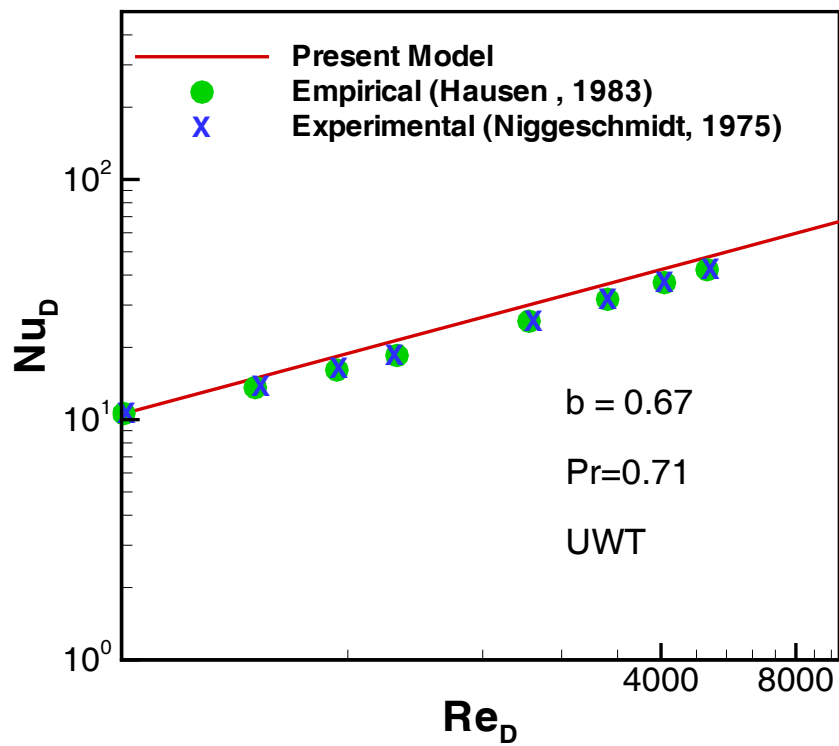


Figure 4.28: Effect of Blockage Ratio on Average Nusselt Numbers

4.6.4 Pin-Fin Arrays

Present heat transfer values are compared with Grimison (1937) for in-line arrangements in Figs. 4.29 - 4.31. Good agreement can be observed for all transverse and longitudinal pitches. A similar type of comparison is presented for different staggered arrangements in Figs. 4.32 - 4.34.

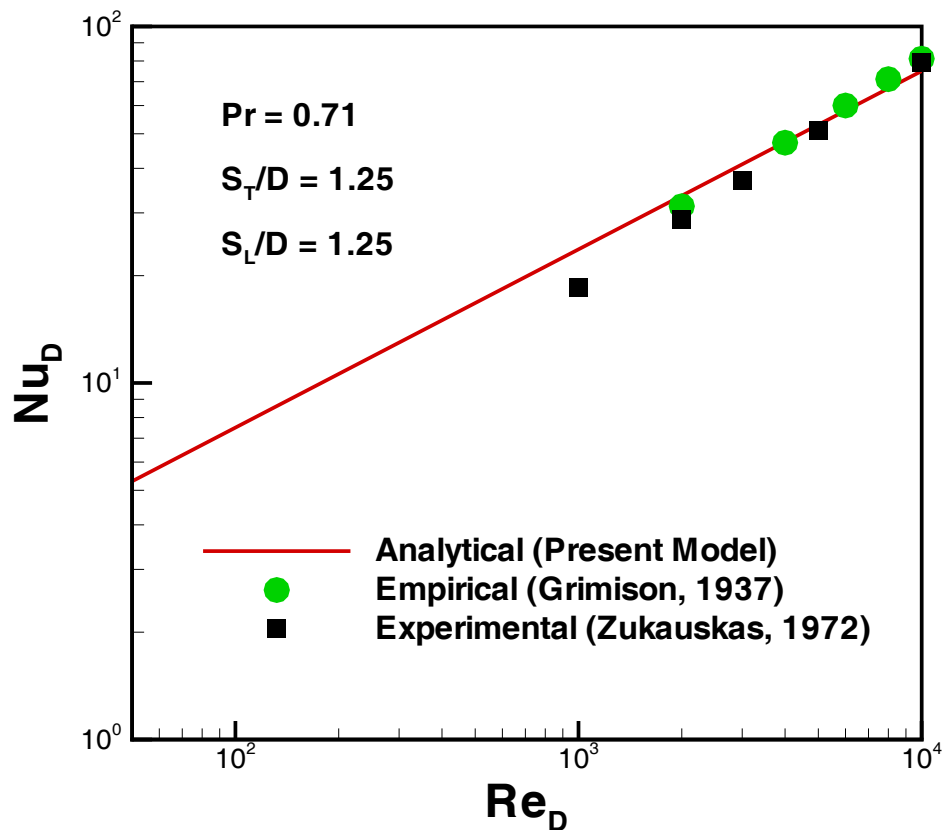


Figure 4.29: Average Nusselt Numbers for In-Line Arrangement 1.25×1.25

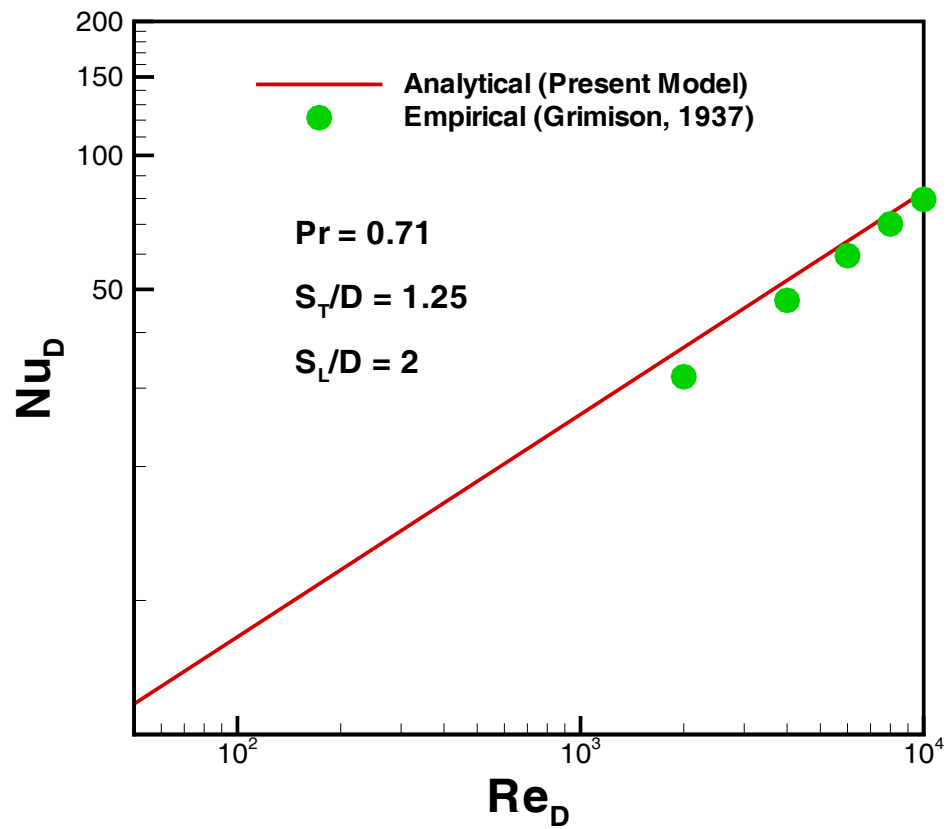


Figure 4.30: Average Nusselt Numbers for In-Line Arrangement 1.25×2

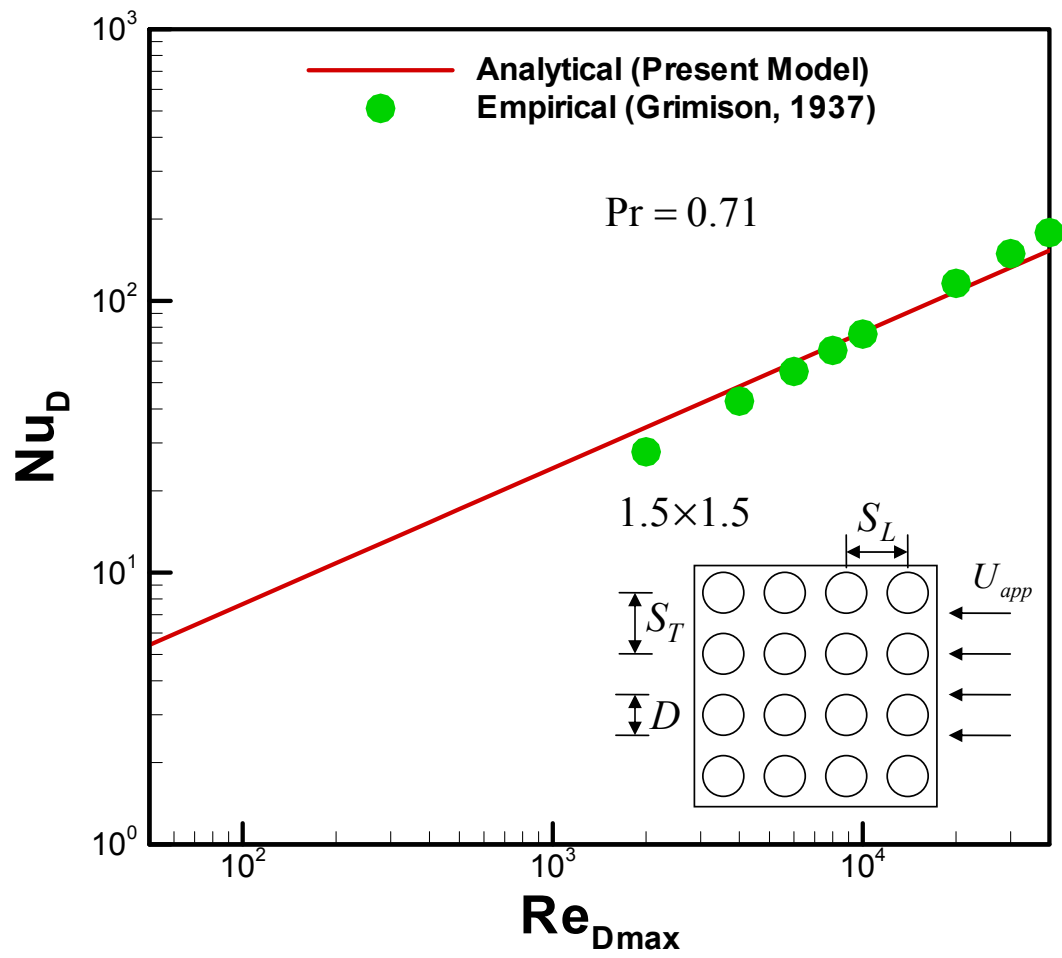


Figure 4.31: Average Nusselt Numbers for In-Line Arrangement 1.5×1.5

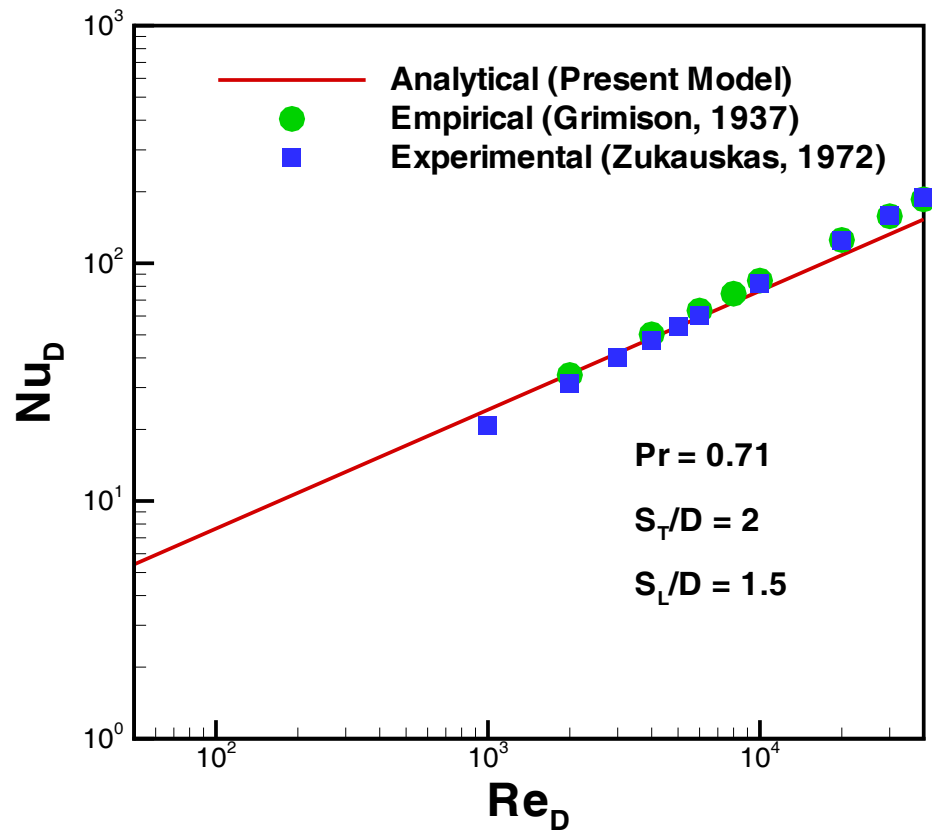


Figure 4.32: Average Nusselt Numbers for Staggered Arrangement 2×1.5

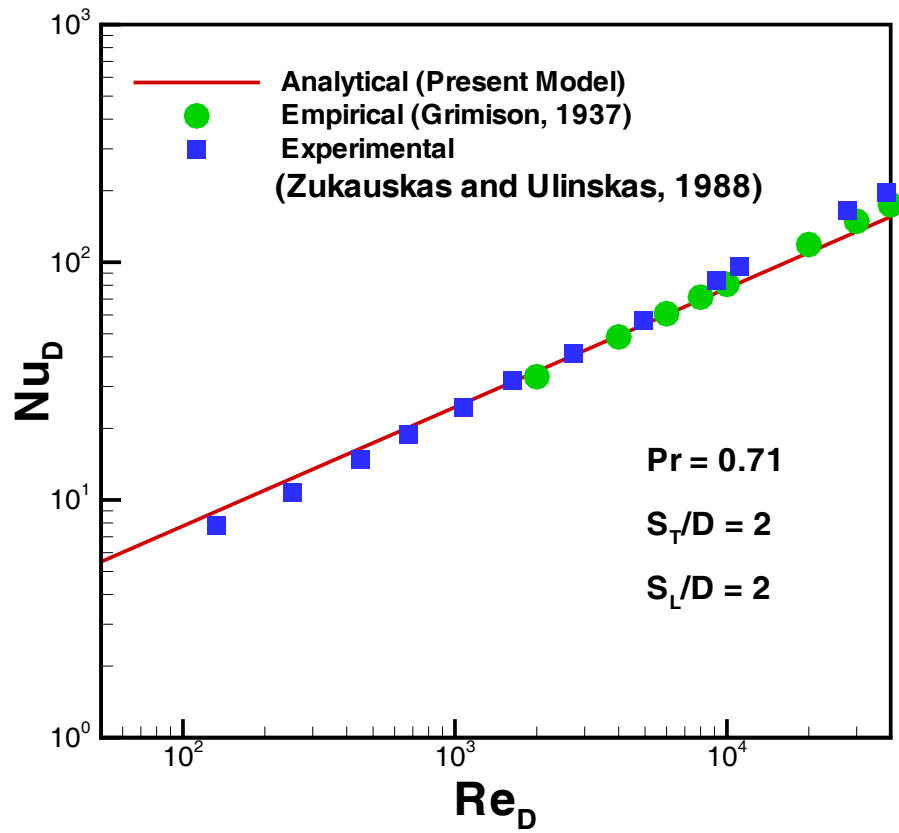


Figure 4.33: Average Nusselt Numbers for Staggered Arrangement 2×2

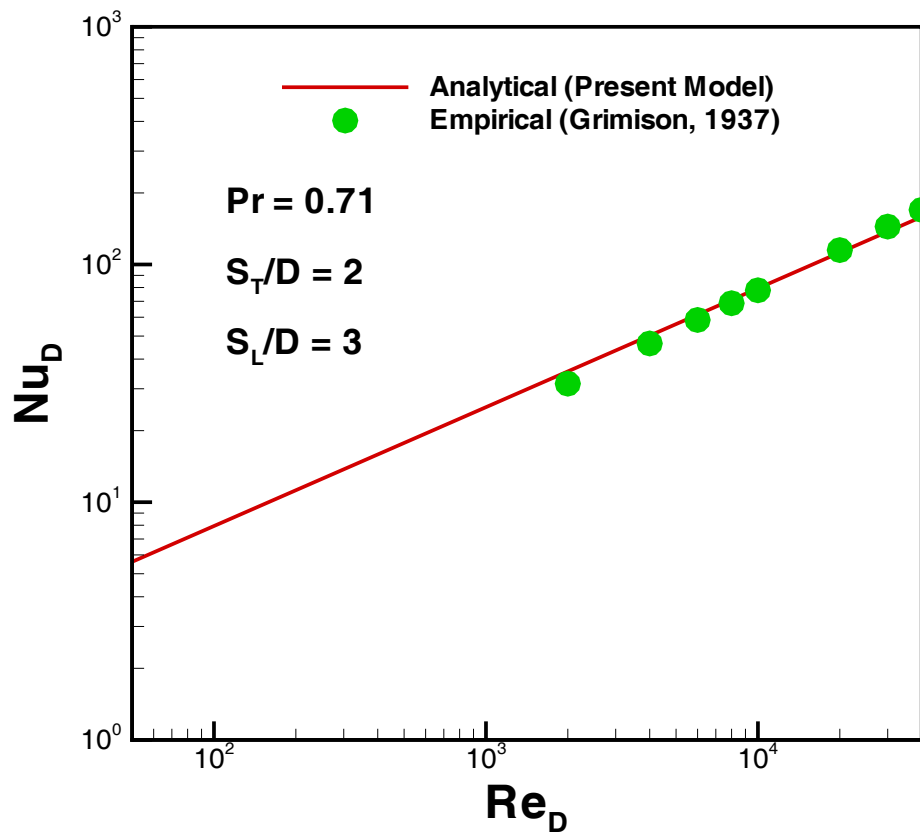


Figure 4.34: Average Nusselt Numbers for Staggered Arrangement 2×3

4.7 Summary

An integral approach is employed to investigate the heat transfer from pins with and without blockage. A third order temperature profile is used in the thermal boundary layer to solve the energy integral equation for both isothermal and isoflux boundary conditions. The same approach was applied to aligned and staggered pin-fin arrays. Closed form solutions are obtained for the heat transfer from the single pins and pin-fin arrays in terms of axis ratio, blockage ratio, transverse and longitudinal pitches, Reynolds, and Prandtl numbers. The results for both thermal boundary conditions are found to be in a good agreement with experimental/numerical data for all cases. It is observed that the average heat transfer coefficients are higher for elliptical pins. They range from circular pin to a plate-fin. The effects of the axis ratio of the elliptical pin upon average heat transfer are also observed and compared for the two extremes with experimental/numerical values obtained from the open literature. It was found that the average heat transfer coefficients depend upon the Reynolds number as well as the axis ratio or blockage ratio for single pins. In the case of pin-fin arrays, the staggered arrangement gives higher heat transfer rates than the in-line arrangement. These models will be used in the next chapters to determine the thermal performance of the individual pins and pin-fin arrays.

Chapter 5

Numerical Validation

5.1 Introduction

The purpose of this chapter is to validate the analytical results of a single circular pin and pin-fin heat sinks. Separate CFD models are created for all cases using ICEPACK 3.2.12, which uses the finite volume method. The basic program structure used by ICEPAK consists of five steps as shown in Fig. 7.1.

5.2 Single Circular Cylinder in an Infinite Flow

5.2.1 Problem Description

The problem (Fig. 7.2) involves a baseplate and a circular cylinder cooled by forced convection. The diameter of the cylinder is $3mm$ and the height is $30mm$. It is positioned on the surface of a $0.25m \times 0.356m$ vertical baseplate at the center of a cabinet. The heat source, attached on the back of the baseplate, dissipates power at the rate of 10 W . Three fans are used to force air over the cylinder. Each fan has a mass flow rate based on

the velocity calculated from the specified Reynolds number. The average heat transfer coefficient is to be determined which will be compared with analytical results.

Five numerical simulations are performed for $Re_D = 200, 400, 600, 800, 1000$. Air inlet velocity U_{app} is calculated for each simulation. Based on this velocity, the total air mass flow rate is determined which will be divided into three mass flow rates, one for each fan. As shown in Fig. 1, each simulation comprises the following five steps:

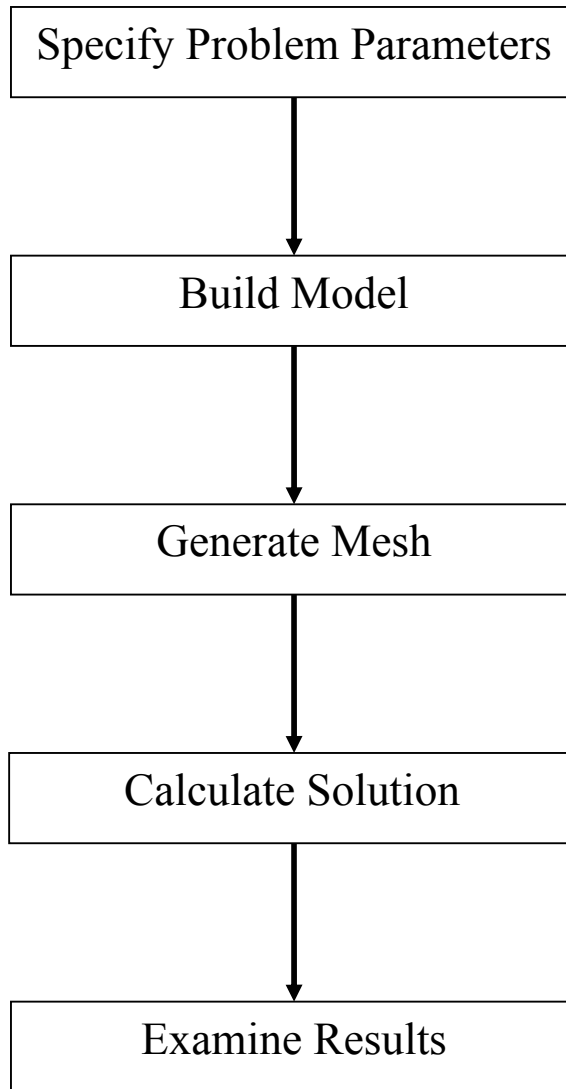


Figure 5.1: Flow Chart for Numerical Simulations

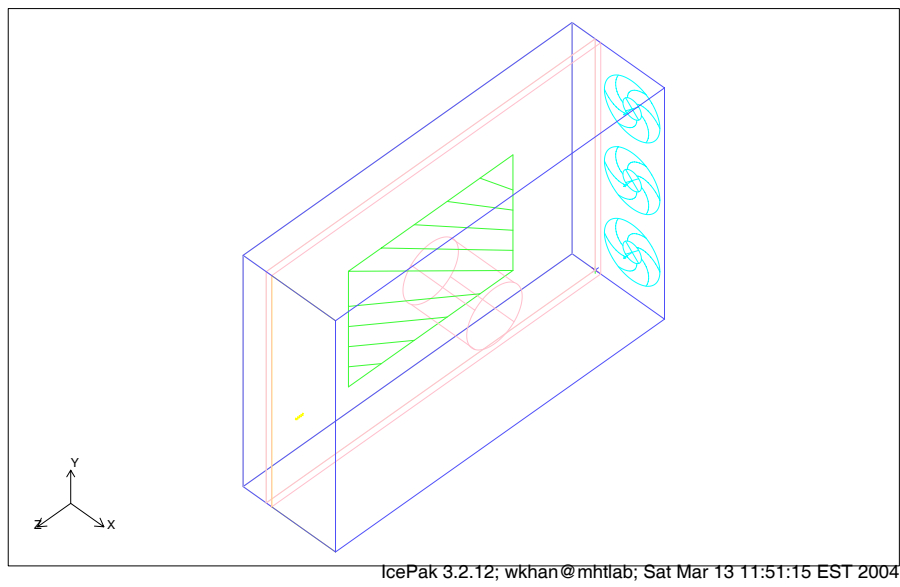


Figure 5.2: Model for Flow Over Circular Cylinder

5.2.2 Specifying Problem Parameters

The following parameters are specified for the problem:

1. steady and laminar flow
2. flow (velocity and pressure) and temperature
3. natural convection ignored
4. radiation ignored ambient temperature of $20^{\circ}C$
5. fluid is air and solid is extruded aluminum
6. ambient temperature and no flow for initial conditions

5.2.3 Building the Model

When a new job is started in ICEPAK, it automatically creates a 3D rectangular cabinet with the dimension $1 \times 1 \times 1$ and displays the cabinet in the graphics window. Following steps are used to build the complete model for the problem:

1. resize and reposition the cabinet
2. create baseplate and edit its dimensions
3. create the free opening on the cylinder side of the base plate and edit its dimensions
4. create first fan and specify geometry, type (fixed flow), and mass flow rate
5. make two more copies of this fan by specifying Y offset
6. model a heat source and specify its geometry and total heat
7. create a circular cylinder, specify its radius, height and the coordinates of the center point

8. model the housing for the cylinder by creating walls and specify heat transfer coefficients for each wall
9. check the model to be sure that there are no problems
10. generate parameter summary for all modeling objects

5.2.4 Generating the Mesh

In ICEPAK, the mesh generator is completely automatic, and generates body-fitted grids with O-grids automatically inserted. Fig. 3 shows mesh generated for the model. However, when control over the mesh is desired, it can be obtained in a number of ways. The maximum size of elements in each direction can be specified, along with the maximum height of an element away from an object. If further control is desired, a number of parameters can be given for each object that controls the nature of the mesh around it. Following steps are used to generate fine mesh:

1. specify the grid type and generate a coarse mesh
2. examine the coarse mesh on a cross-section of the model
3. generate a finer mesh and check the quality with respect to aspect ratio, face alignment, and element volume
4. change mesh parameters if the element aspect ratio or the face alignment is less than 0.15 or if the element volume is on the order of 10^{-12} or lower and check the quality of the mesh again

The finer mesh obtained is shown in Fig. 7.3.

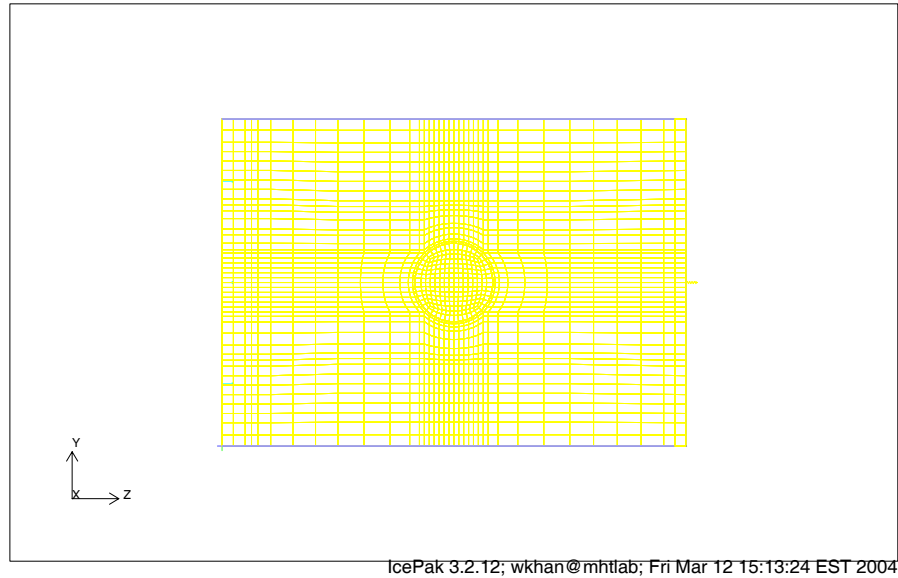
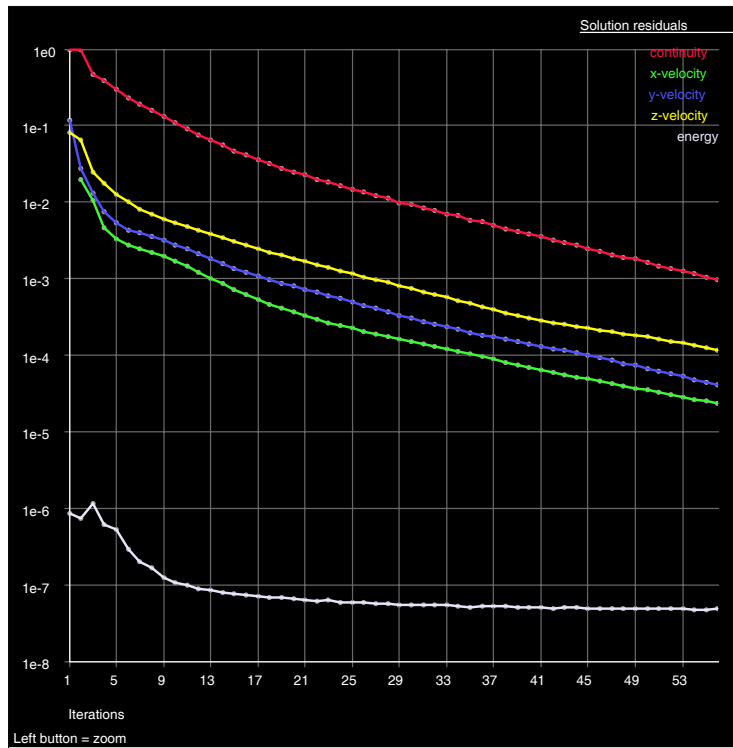


Figure 5.3: Mesh on YZ-Plane

5.2.5 Calculating the Solution

Setting up and running the flow solver, in ICEPAK, is also quite simple. In general, the default parameters which are computed by ICEPAK for the solution are adequate, and, just like for mesh generation, a single button click is enough to perform the simulation. Convergence graph (Fig. 7.4) shows how the solution is progressing as a function of time. The continuity residual is not quite converged, but since it has leveled off very close to the $1e^{-3}$ tolerance and the others are well below the convergence tolerance, it can be considered that the solution is effectively converged.



IcePak 3.2.12; wkhan@mhtlab; Fri Mar 12 15:13:24 EST 2004

Figure 5.4: Residuals

5.2.6 Examining the Results

Once the solution is finished, a variety of tools are available in ICEPAK to examine the results, e.g. graphical displays of data (velocity vectors, temperature and pressure contours), XY plots (convergence, history, and variation) and reports. Reports for average heat transfer coefficients are presented in Table 7.1

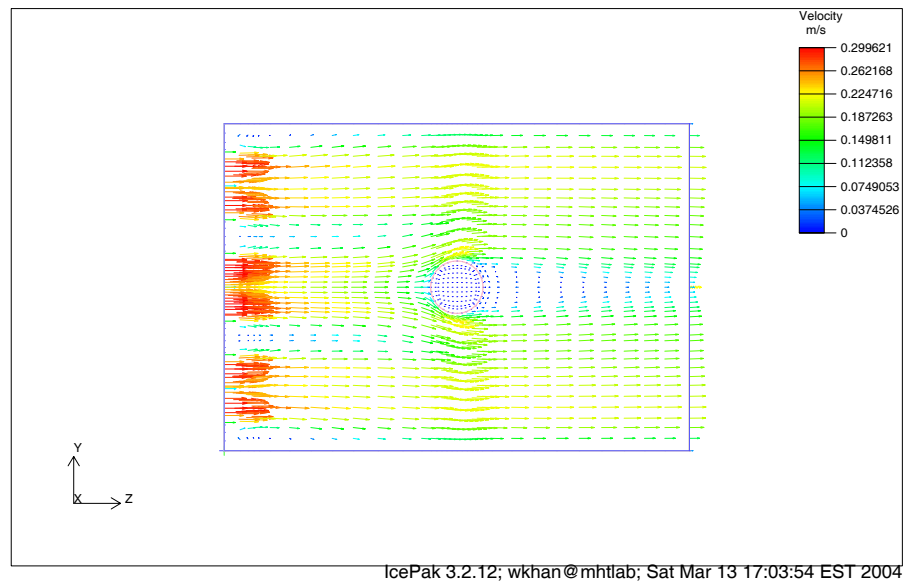


Figure 5.5: Velocity Vectors on the Cylinder Side of the Enclosure

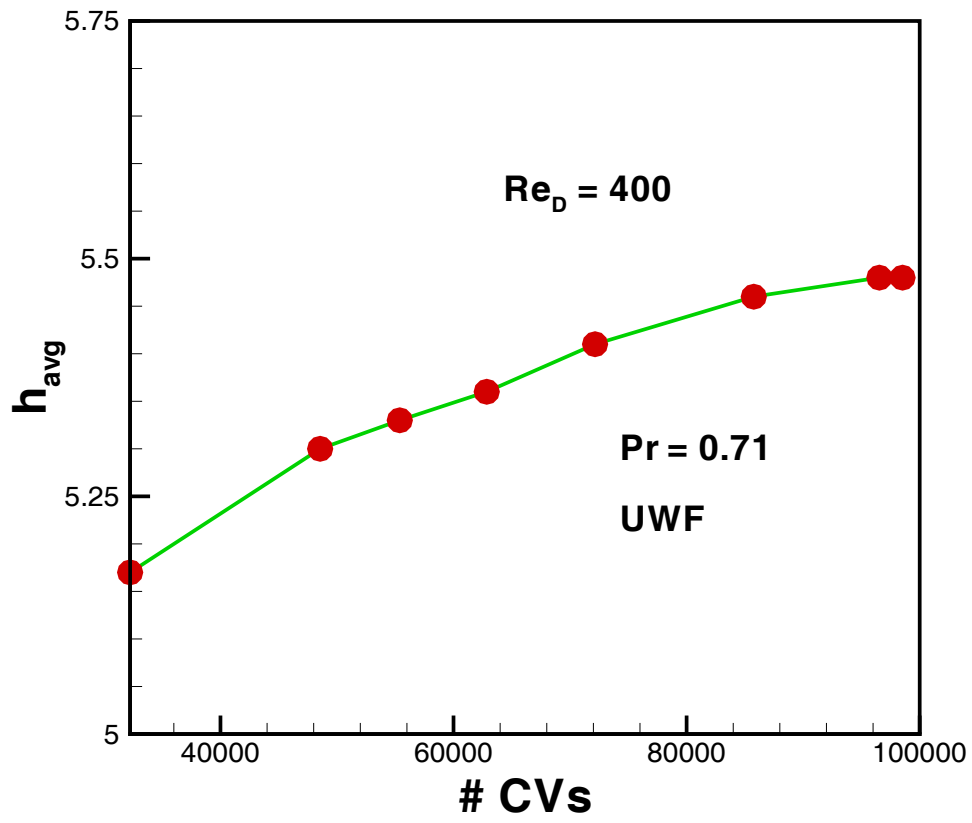


Figure 5.6: Grid Convergence for Circular Cylinder ($Re_D = 400$)

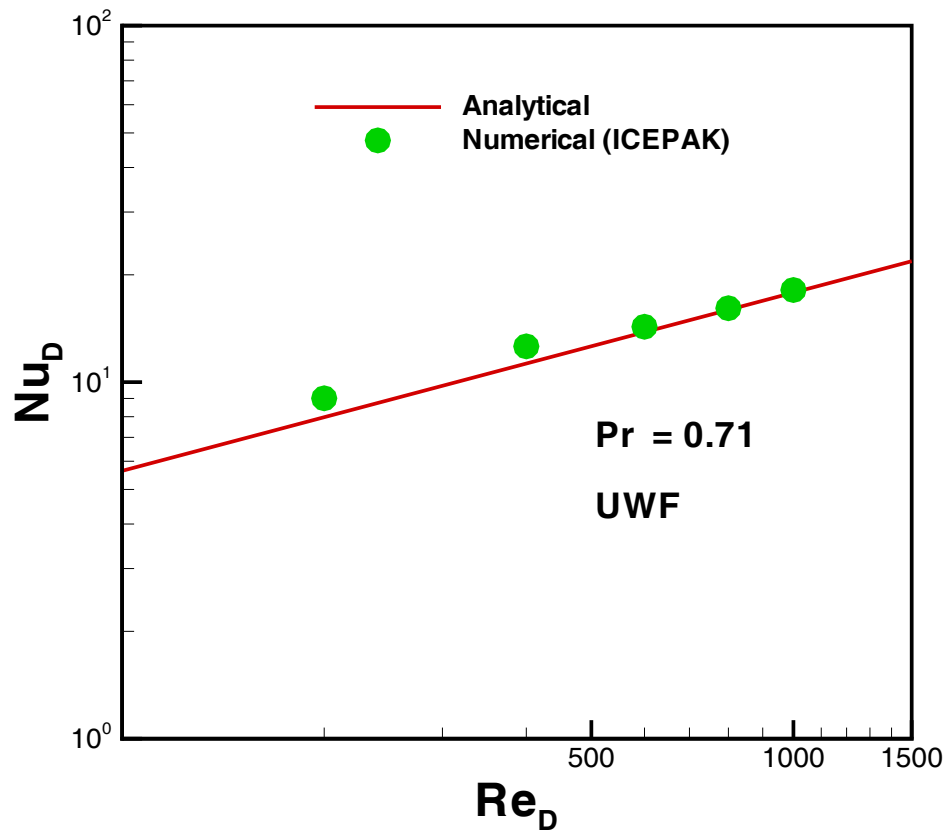


Figure 5.7: Variation of Average Heat Transfer Coefficients with Reynolds Numbers

Table 5.1: Results of Average Heat Transfer Coefficients for Circular Cylinder

Re_D	Numerical Results			Analytical Results	% Difference
	CVs	h_{avg}	Nu_D	Nu_D	
200	32248	3.57	8.20	10.52	2.89
	48554	3.65	8.390		5.02
	55388	3.78	8.68		8.28
	62849	3.84	8.82		9.71
	72146	3.88	8.91		10.65
	85764	3.9	8.96		11.10
	96540	3.92	9.01		11.56
	98532	3.92	9.01		11.56
	400	32248	5.17		11.88
48554		5.30	12.18	7.42	
55388		5.33	12.25	7.94	
62849		5.36	12.32	8.46	
72146		5.41	12.44	9.30	
85764		5.46	12.55	10.13	
96540		5.48	12.60	10.46	
98532		5.48	12.60	10.46	
600	32248	4.89	11.24	13.81	-22.85
	48554	5.79	13.31		-3.75
	55388	5.88	13.51		-2.17
	62849	5.92	13.61		-1.48
	72146	6.03	13.86		0.38
	85764	6.11	14.04		1.68
	96540	6.21	14.28		3.26
	98532	6.22	14.25		3.45

Table 7.1 (cont'd): Results of Average Heat Transfer Coefficients for Circular Cylinder

Re_D	Numerical Results			Analytical Results	% Difference		
	CVs	h_{avg}	Nu_D	Nu_D			
800	32248	6.12	14.07	15.95	-13.37		
	48554	6.5	14.94		-6.74		
	55388	6.69	15.38		-3.71		
	62849	6.73	15.47		-3.09		
	72146	6.79	15.61		-2.18		
	85764	6.88	15.81		-0.85		
	96540	7.01	16.10		0.88		
	98532	7.01	16.10		1.02		
	1000	32248	6.06		13.93	17.83	-27.99
		48554	6.55		15.06		-18.41
55388		7.1	16.32	-9.24			
62849		7.35	16.90	-5.52			
72146		7.52	17.29	-3.14			
85764		7.63	17.54	-1.65			
96540		7.88	18.12	1.57			
98532		7.89	18.13	1.70			

5.3 Pin-Fin Heat Sinks

5.3.1 Problem Description

The model consists of a forced-convection-cooled pin-fin heat sink composed of a baseplate, a heat source at the center of the baseplate, and 49 pins uniformly spaced in in-line (7×7) as shown in Fig. 7.8.

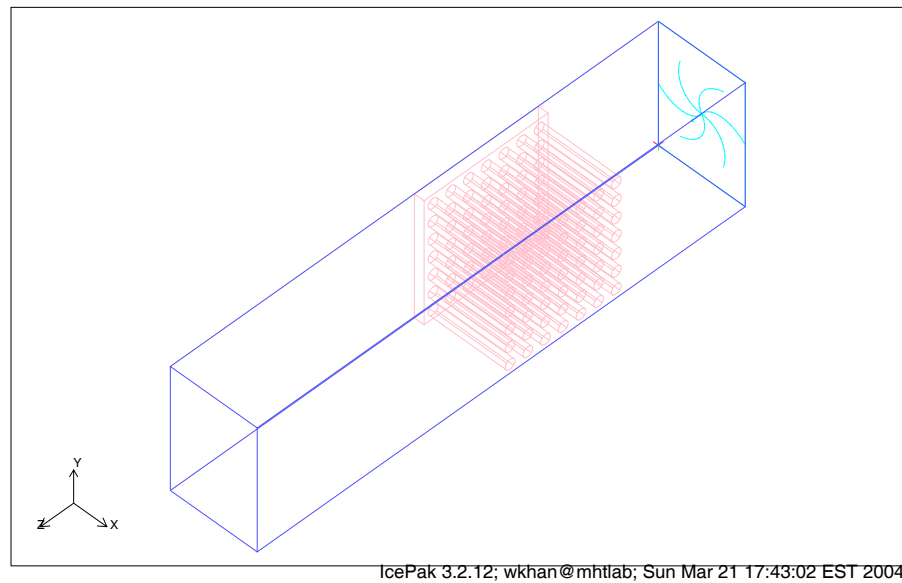


Figure 5.8: Numerical Model for In-Line Pin-Fin Heat Sink

The diameter of each pin is 2mm and the height is 15.8mm . The longitudinal and transverse pitches are 3.63mm each. The heat source, attached on the back of the baseplate, dissipates power at the rate of 10 W . Mass flow rate is specified based on the velocity calculated from the assumed Reynolds number. The average heat transfer coefficient is to be determined for the heat sink, which will be compared with analytical results.

Numerical simulations are performed in the same five steps as described above in

section 7.1.

5.3.2 Specifying Problem Parameters

Same parameters are specified as described in section 7.2.1.

5.3.3 Building the Model

In building the model, after resizing and repositioning the cabinet, a detailed heat sink macro is added in the model. In ICEPAK, detailed heat sink macros are available to model pin-fin heat sinks. They consist of a conducting solid block for the heat sink base and solid blocks for the pin-fins. The conducting solid block models heat transfer from the fins through the base of the heat sink to the heat source connected to the base. In order to add a detailed heat sink macro to the model, following steps are used:

1. specify the heat sink type, i.e. cylindrical pin
2. specify the position and size of the baseplate of the detailed heat sink
3. specify the thickness of the base plate
4. specify the radius and height of the pins
5. specify the number of pins
6. specify the arrangement of pins, i.e. in-line or staggered
7. specify the material for the pins and the baseplate

After the heat sink has been created and positioned in the model, create opening, source, fan and the wall in the same way as described in section 7.1. The specifications used in the detailed heat sink macro are presented in Table 7.2.

Table 5.2: Dimensions Used to Determine Performance of Heat Sinks

Quantity	Dimension
Footprint (mm^2)	25.4×25.4
Source Dimensions (mm^2)	18.0×18.0
Baseplate Thickness (mm)	2
Pin Diameter (mm)	2
Overall Height of Heat Sink(mm)	12
Number of Pins (In-Line)	7×7
Approach Velocity (m/s)	1
Thermal Conductivity of Solid ($W/m \cdot K$)	237
Thermal Conductivity of Air ($W/m \cdot K$)	0.026
Density of Air (kg/m^3)	1.1614
Specific Heat of Air ($J/kg \cdot K$)	1007
Kinematic Viscosity (m^2/s)	1.58×10^{-5}
Prandtl Number (Air)	0.71
Heat Load (W)	10
Ambient Temperature ($^{\circ}C$)	27

5.3.4 Generating the Mesh

For generating the mesh, follow the same steps as described in section 7.2.3. After generating the finer mesh, grid-independent solution is obtained and the results are examined in the same way as described in sections 7.2.4 and 7.2.5. The velocity vectors are shown in Fig. 7.9.

The results of average heat transfer coefficients for in-line pin-fin heat sink, shown in Fig. 7.8, are presented in Table 7.3 and are compared with analytical model in Fig. 7.10. It can be seen that both results are in good agreement.

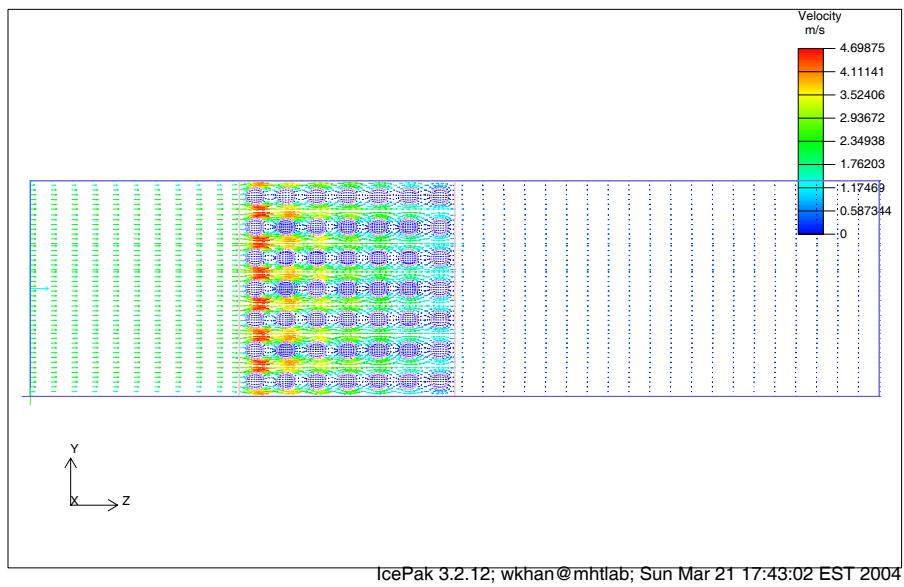


Figure 5.9: Velocity Vectors in In-Line Pin-Fin Heat Sink

Table 5.3: Results of Average Heat Transfer Coefficients for In-Line Pin-Fin Heat Sink

Re_D	Numerical Results			Analytical Results	% Difference
	CVs	h_{avg}	Nu_D	Nu_D	
300	65020	180.45	13.83	14.15	-2.33
	97523	189.32	14.51		2.46
	125356	195.68	14.99		5.63
	155384	200.32	15.35		7.82
	179353	205.16	15.72		9.99
500	65020	198.35	15.20	17.61	-15.86
	97523	220.61	16.90		-4.17
	125356	228.65	17.52		-0.51
	155384	234.89	18.00		2.16
	179353	235.61	18.05		2.46
700	65020	202.36	15.51	20.26	-30.65
	97523	243.64	18.67		-8.52
	125356	250.63	19.21		-5.49
	155384	268.88	20.60		1.67
	179353	272.69	20.90		3.04

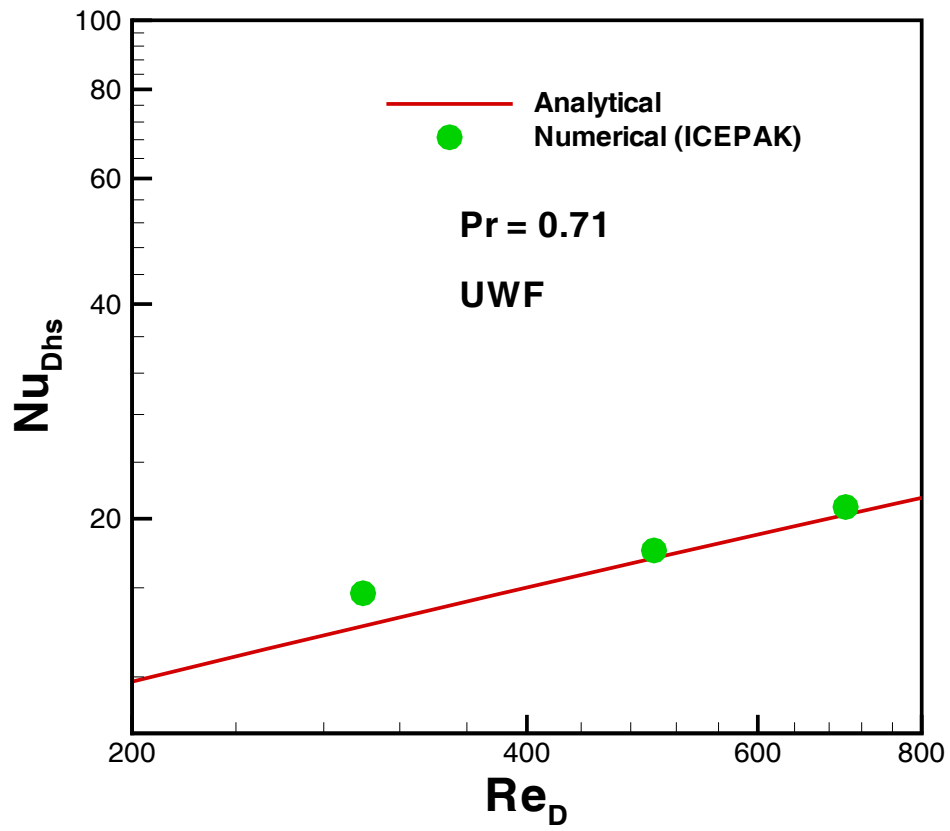


Figure 5.10: Comparison of Average Heat Transfer Coefficients for In-Line Pin-Fin Heat Sink

Chapter 6

Heat Sink Analysis

6.1 Introduction

Heat sinks are the most common thermal management hardware in use in microelectronics. They improve the thermal control of electronic components, assemblies, and modules by enhancing their surface area through the use of fins. Applications utilizing pin-fin heat sinks for cooling have increased significantly during the last few decades, especially in microelectronics. Fluid flow and heat transfer models for single pins (circular and elliptical), and pin-fin arrays have been developed in the previous chapters. In this chapter, those models will be used to analyze the performance of a heat sink. The procedure for the analysis of heat sinks involves:

1. The determination of total thermal heat sink resistance
2. The determination of total pressure drop (hydraulic resistance) across the heat sink
3. The determination of parametric behavior of the heat sink

A flow chart for the calculation of system resistance, which comprises thermal and hydraulic resistance, is shown in Fig. 5.1.

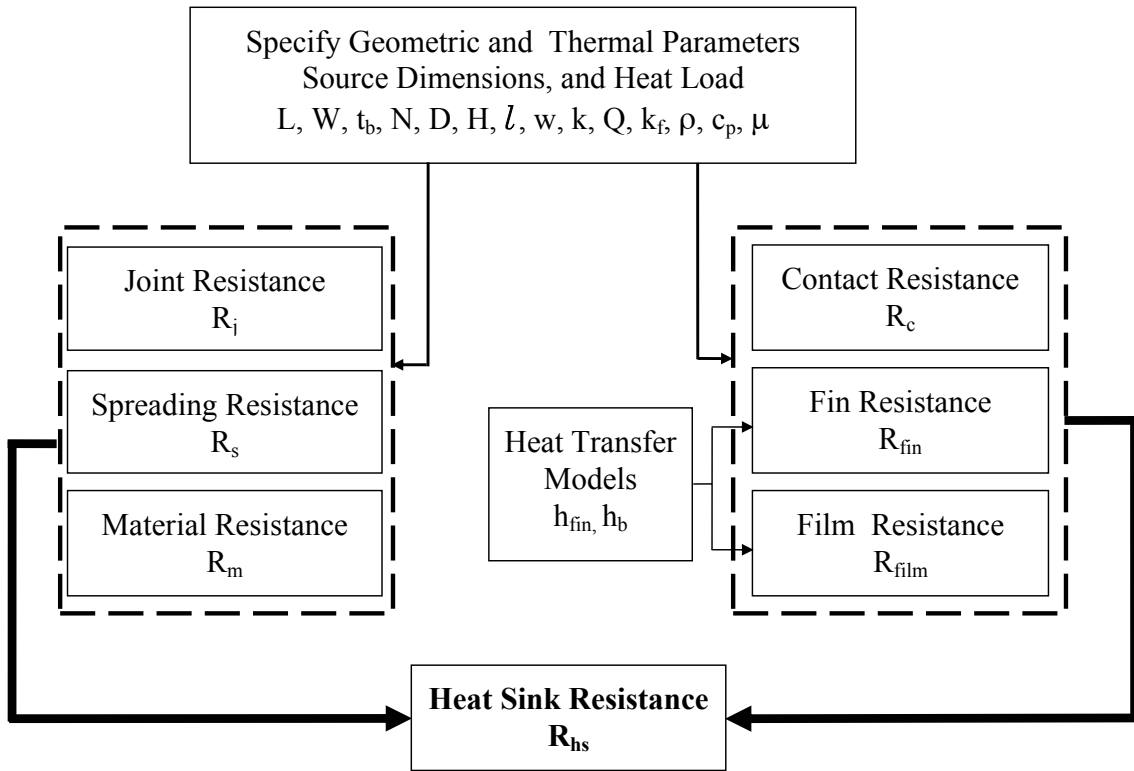


Figure 6.1: Flow Chart for System Resistance

6.2 Heat Sink Model

The geometry of an in-line pin-fin heat sink is shown in Figs. 5.2 and 5.3. The dimensions of the baseplate are $L \times W \times t_b$, where L is the length in the downstream direction, W is the width, and t_b is the thickness. Each pin fin has diameter D and height H . The longitudinal and transverse pitches are S_L and S_T respectively. The approach velocity of the air is U_{app} . The direction of the flow is parallel to the x -axis. The bottom surface ($y = 0$) is kept at constant temperature \bar{T}_b and the top surface ($y = H$) is insulated. The average wall temperature of the pin surface is $\bar{T}_w(x)$. The heat source is idealized as a constant heat flux boundary condition at the bottom surface of the baseplate. The mean temperature of the heat source is \bar{T}_s . It is assumed that the heat sink is fully shrouded and the heat source is situated at the center of the baseplate. In Fig. 5.3 it is shown unshrouded and inverted for convenience. It is assumed that the fluid temperature is averaged over the height of the heat sink, with $\bar{T}_f = \bar{T}_f(x)$, so the fluid temperature $\bar{T}_f(x)$ is the bulk mean fluid temperature. Fully developed heat and fluid flow are assumed in the analysis, and the thermophysical properties are taken to be temperature independent. In designing a heat sink, the size and the heat load are the usual constraints.

The boundary conditions for the heat sink under consideration can be specified as follows. For the hydrodynamic boundary conditions, the velocity is zero at all boundaries of the pins except the channel inlet and outlet. A uniform velocity U_{app} is applied at the channel inlet:

$$u = U_{app}, \quad v = 0, \quad w = 0 \Big|_{x=0, 0 \leq y \leq H, 0 \leq z \leq W} \quad (6.1)$$

For the thermal boundary conditions, adiabatic boundary conditions are applied to all the boundaries except the heat sink baseplate, where a constant heat flux is assumed. At the channel inlet, the fluid temperature is equal to the ambient temperature, that is

$$T = T_a \Big|_{x=0, 0 \leq y \leq H, 0 \leq z \leq W} \quad (6.2)$$

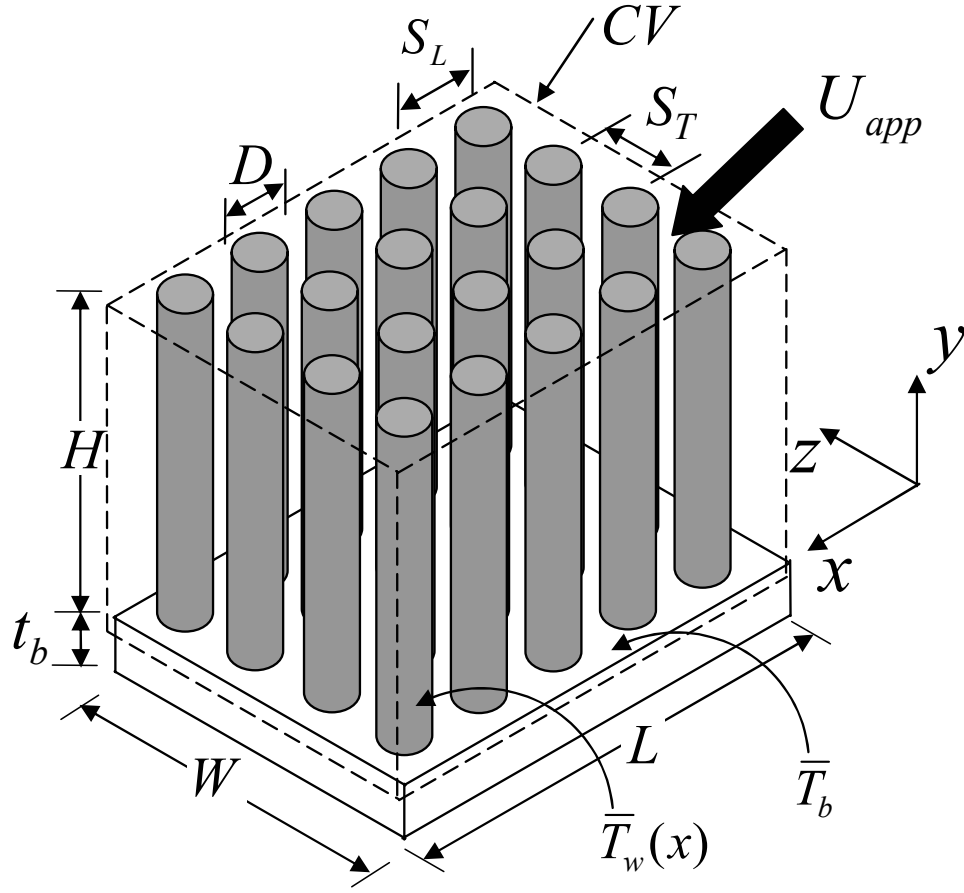


Figure 6.2: Control Volume for Pin-Fin Heat Sink

whereas, at the exit,

$$T = T_0|_{x=L, 0 \leq y \leq H, 0 \leq z \leq W} \quad (6.3)$$

The total rate of heat transfer by convection from the pin-fins and the exposed (unfinned) surface of the baseplate can be written as:

$$Q = [N(hA\eta)_{fin} + (hA)_b] \theta_b \quad (6.4)$$

where $\theta_b = \bar{T}_b - T_a$ is the temperature difference between the baseplate and the ambient, and the geometry can be defined as:

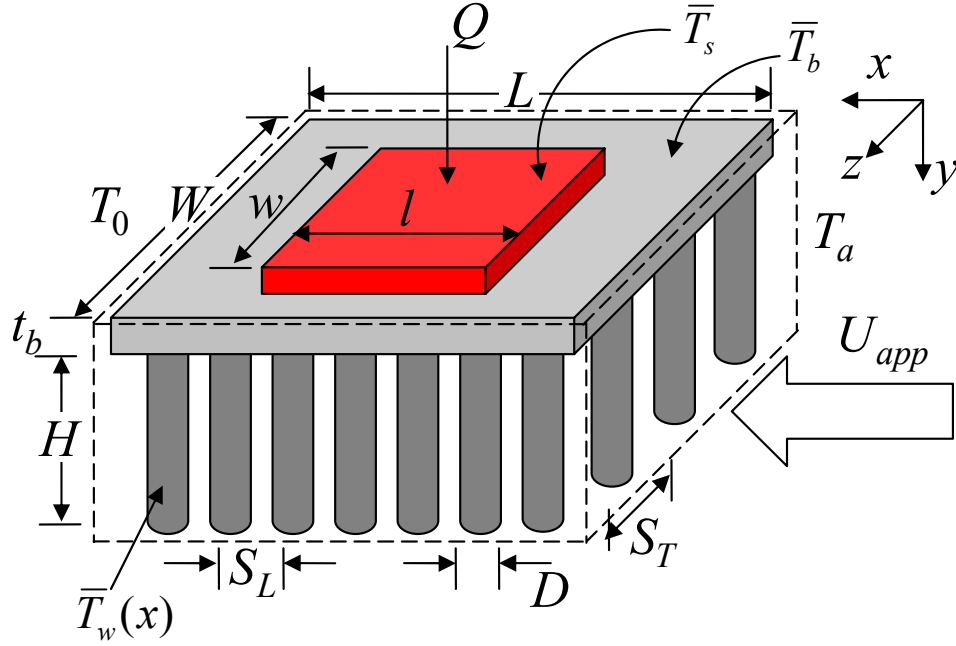


Figure 6.3: Geometry of Pin-Fin Heat Sink

$$A_{fin} = \pi DH, \quad A_b = A - N \frac{\pi D^2}{4}, \quad A = LW,$$

$$L = N_L S_L, \quad W = N_T S_T, \quad N = N_L N_T$$

The heat transfer coefficients h_b and h_{fin} for the baseplate and the fins can be determined from Eqs. (4-36) and (4-48):

$$h_b = 0.75 \frac{k_f/D}{\sqrt{N_L S_L}} Re_D^{1/2} Pr^{1/3} \quad (6.5)$$

$$h_{fin} = C_1 \frac{k_f}{D} Re_D^{1/2} Pr^{1/3} \quad (6.6)$$

where C_1 is a constant depending on the geometry of the heat sink and it can be determined from Eq. (4-49):

$$C_1 = \begin{cases} \frac{[0.2 + \exp(-0.55 S_T)] S_T^{0.785} S_L^{0.212}}{(S_T - 1)^{0.5}} & \text{for In-Line arrangement} \\ \frac{0.61 S_T^{0.591} S_L^{0.053}}{(S_T - 1)^{0.5} [1 - 2 \exp(-1.09 S_T)]} & \text{for Staggered arrangement} \end{cases} \quad (6.7)$$

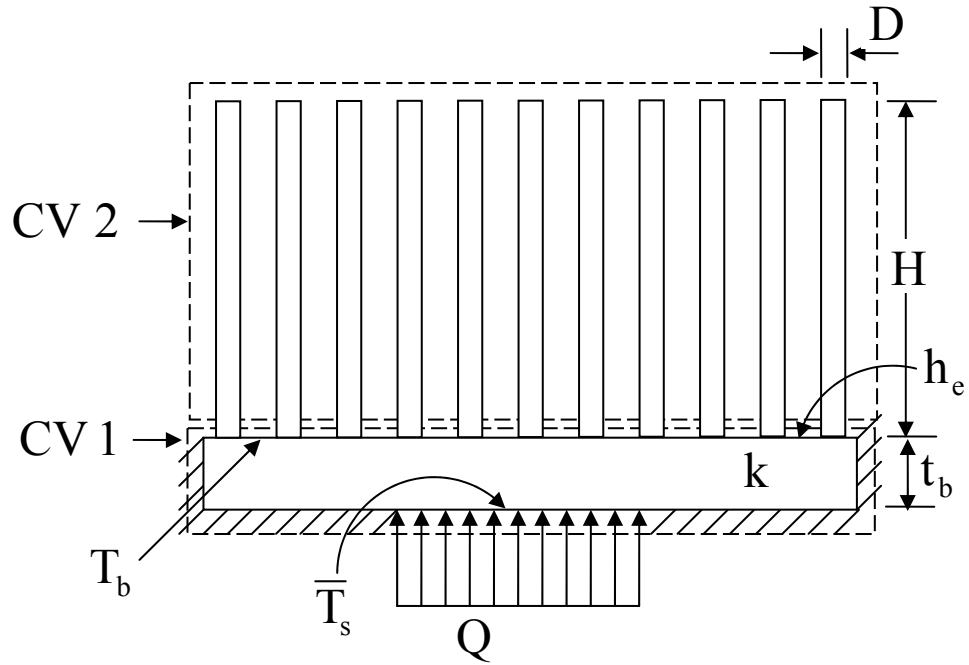


Figure 6.4: Control Volumes for Energy Balances

The efficiency of the fin η_{fin} with constant convective heat transfer coefficient and an insulated tip is:

$$\eta_{fin} = \frac{\tanh(mH)}{mH} \quad (6.8)$$

with the fin parameter $m = \sqrt{\frac{4h_{fin}}{kD}}$.

6.2.1 Overall Heat Transfer Coefficient for Heat Sink

If the base temperature of the heat sink, \bar{T}_b is averaged and assumed to be constant, the energy balance for the control volume CV 2 (Fig. 5.5) is

$$Q = NQ_{fin} + Q_b \quad (6.9)$$

where

$$Q = h_{avg} A_{hs} \theta_b \quad (6.10)$$

$$Q_{fin} = (Ah\eta)_{fin} \theta_b \quad (6.11)$$

$$Q_b = (\overline{hA})_b \theta_b \quad (6.12)$$

and $A_{hs} = A_{fin} + \left(A - N \frac{\pi D^2}{4} \right)$ is the total surface area of the heat sink. Combining Eqs. (5.10) - (5.12), and using Eqs. (5.5)-(5.8), Eq. (5.9) can be solved for the average heat transfer coefficient of the heat sink:

$$h_{avg} = C_2 \frac{k_f}{D} Re_D^{1/2} Pr^{1/3} \quad (6.13)$$

where C_2 is a constant and for both pin-fin arrangements, it can be written as:

$$C_2 = \frac{\left[C_1 \pi \gamma \eta_{fin} + \frac{0.75}{\sqrt{N_L S_L}} \left(S_T S_L - \frac{\pi}{4} \right) \right]}{\pi(\gamma - 1/4) + S_T S_L} \quad (6.14)$$

and $\gamma = H/D$ is called the aspect ratio of the fin. Thus the dimensionless heat transfer coefficient for the heat sink may be expressed as

$$(Nu_D)_{hs} = \frac{h_{avg} D}{k_f} = C_2 Re_D^{1/2} Pr^{1/3} \quad (6.15)$$

6.2.2 Temperature Distribution

The following equation for temperature distribution along the pin fin with an adiabatic tip can be found in any heat transfer text book (e.g. Incropera and DeWitt, 2002, and Holman, 1990):

$$T_w(x, y) = T_f(x) + \left[\overline{T}_b - T_f(x) \right] \frac{\cosh m(H - y)}{\cosh(mH)} \quad (6.16)$$

which gives the average fin temperature:

$$\begin{aligned} \overline{T}_w(x) &= \frac{1}{H} \int_0^H T(x, y) dy \\ &= T_f(x) + (\overline{T}_b - T_f(x)) \eta_{fin} \end{aligned} \quad (6.17)$$

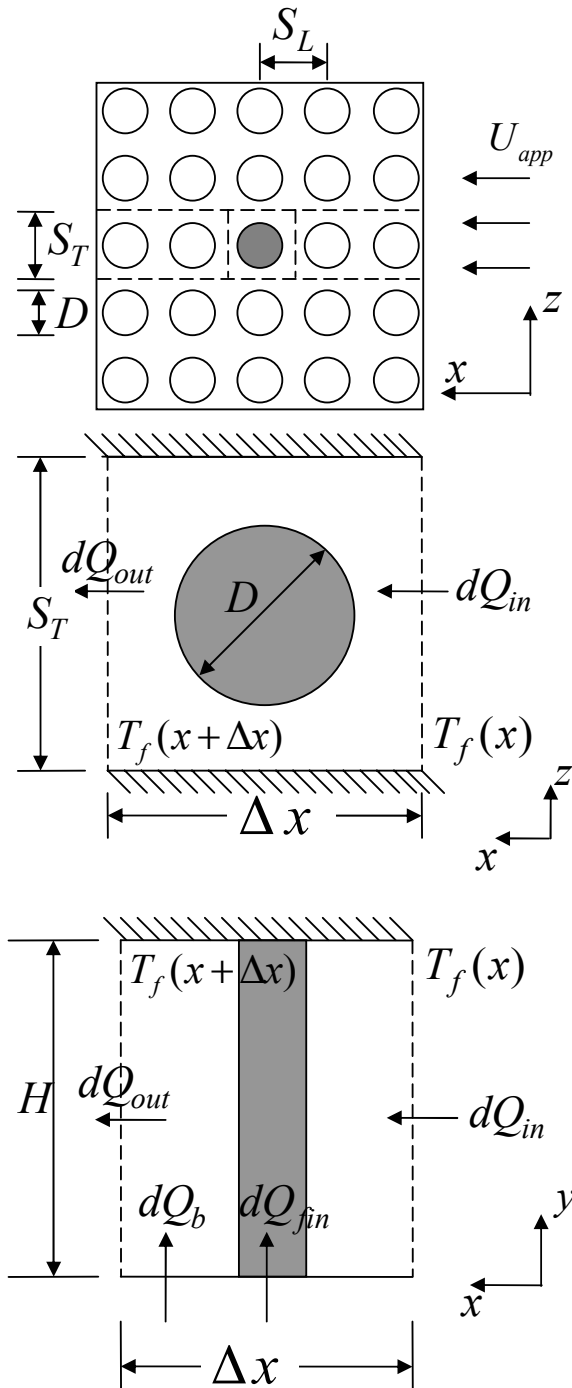


Figure 6.5: Control Volume for Analysis of Pin-Fin Heat Sinks

An energy balance for the control volume of length Δx (Fig. 5.5) gives

$$\dot{m}c_p[T_f(x + \Delta x) - T_f(x)] = dQ \quad (6.18)$$

where \dot{m} is the mass flow rate of air through the control volume and dQ ($\equiv dQ_{fin} + dQ_b$) is the total heat flow coming from the fin and the exposed (unfinned) surface of the baseplate in the control volume and they are given by:

$$\dot{m} = \rho U_{app} S_T H \quad (6.19)$$

$$dQ = h_{avg}(S_T \cdot dx)[\bar{T}_b - T_f(x)] \quad (6.20)$$

Using h_{avg} from Eq. (5.13) and combining Eqs. (5.19) and (5.20), Eq. (5.18) can be simplified to give an ordinary differential equation for the mean fluid temperature $T_f(x)$.

$$\frac{dT_f(x)}{\bar{T}_b - T_f(x)} = \frac{C_2}{Re_D^{1/2} Pr^{2/3}} \cdot \left(\frac{L}{H}\right) \cdot \frac{dx}{L} \quad (6.21)$$

where C_2 is given by Eq. (5.14). Integrating Eq. (5.21), and using the boundary condition, $T_f(x) = T_a$ at $x = 0$, the mean fluid temperature can be written as

$$T_f(x) = \bar{T}_b - (\bar{T}_b - T_a) \exp\left[-\frac{C_2 N_L S_L}{\gamma Re_D^{1/2} Pr^{2/3}} \cdot \frac{x}{L}\right] \quad (6.22)$$

Therefore, the average fluid temperature inside the heat sink is

$$\begin{aligned} \bar{T}_f &= \frac{1}{L} \int_0^L T_f(x) dx \\ &= \bar{T}_b - (\bar{T}_b - T_a) \left[\frac{\gamma Re_D^{1/2} Pr^{2/3}}{C_2 N_L S_L} \right] \cdot \left[1 - \exp\left(-\frac{C_2 N_L S_L}{\gamma Re_D^{1/2} Pr^{2/3}}\right) \right] \end{aligned} \quad (6.23)$$

The air temperature leaving the heat sink can be determined from Eq. (5.22):

$$T_O = T_f(x)|_{x=L} = \bar{T}_b - (\bar{T}_b - T_a) \cdot \exp\left(-\frac{C_2 N_L S_L}{\gamma Re_D^{1/2} Pr^{2/3}}\right) \quad (6.24)$$

6.3 Performance of Heat Sinks

The overall performance of a pin-fin heat sink depends upon the total thermal resistance of the system and the total pressure drop. This performance is a strong function of the operating environment. Accurate knowledge of the fluid flow and temperature distribution in the heat sink is necessary to calculate the heat sink performance.

6.3.1 Heat Sink Resistance

The thermal performance of a pin-fin heat sink depends upon the total thermal resistance of the system from a heat source on one side of the baseplate and a cooling medium on the other side. This thermal resistance is defined as (Fig. 5.6):

$$R_{th} = \frac{\theta_s}{Q} \quad (6.25)$$

where $\theta_s = T_s - T_a$. The total thermal resistance of the system can also be written as the sum of the two main resistances, R_b and R_{hs} (Fig. 5.6):

$$R_{th} = R_b + R_{hs} \quad (6.26)$$

where

$$R_b = R_j + R_s + R_m \quad (6.27)$$

$$R_{hs} = \frac{1}{\frac{N}{R_c + R_{fin}} + \frac{1}{R_{film}}} \quad (6.28)$$

with

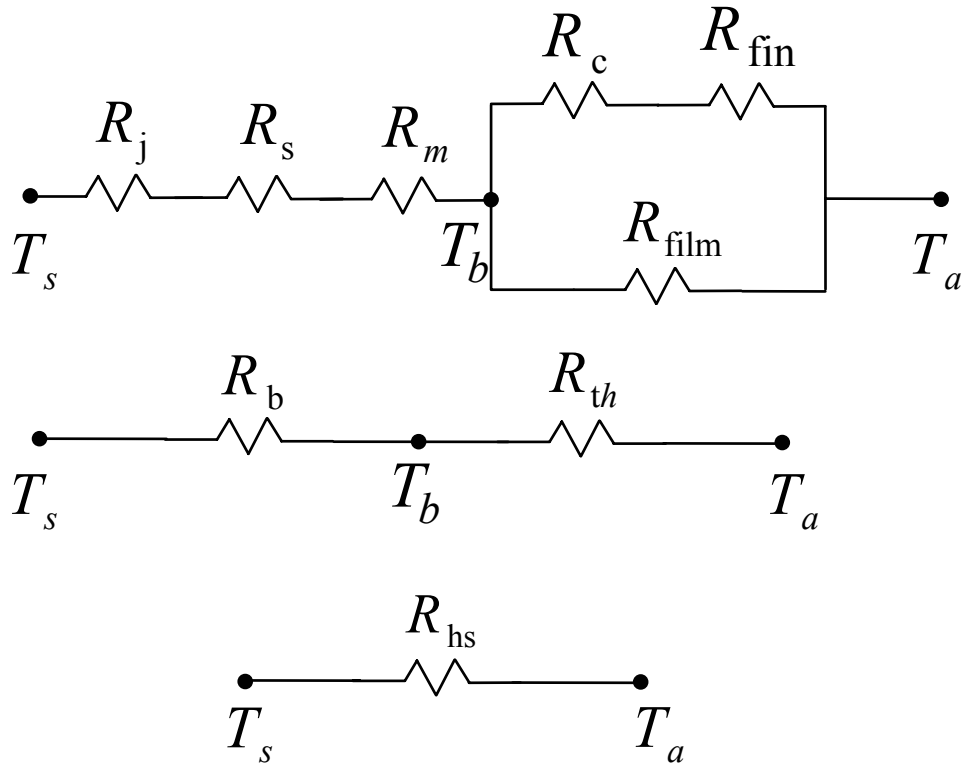


Figure 6.6: Thermal Resistance Network for a Heat Sink

- R_j = joint resistance between the source and the baseplate,
- R_s = spreading resistance in the baseplate,
- R_m = material resistance of the baseplate,
- R_c = contact resistance between fins and the baseplate,
- R_{fin} = overall resistance of a fin,
- R_{film} = thermal resistance of exposed (unfinned) surface of the baseplate,
- R_b = total resistance of baseplate, and
- R_{hs} = total resistance of fluid side of heat sink.

These resistances are shown in Fig. 5.6 and will be discussed in detail.

1. Thermal Joint Resistance - R_j

Due to surface irregularities at the interface between the source and the baseplate, only a fraction of the total apparent area is in contact (Fig. 5.7). As a result, a temperature drop occurs which depends on the thermal resistance of the contacting interface. Thermal joint resistance at the interfaces is a function of several geometric, physical and thermal parameters such as surface roughness and waviness, surface microhardness, thermal conductivity of the contacting solids, including layers, coatings and films, properties of any interstitial materials and the contact pressure. Interstitial substances, such as, gases, greases, oils, liquids, etc. which completely fill the gaps formed between contacting asperities can perfectly wet interfacial surfaces, producing interfaces which have relatively high contact conductances. Thin conductive layers, in the range of $1 - 50 \mu m$ thickness, when vapor deposited on contacting surfaces can decrease joint resistance by at least an order of magnitude. As an alternative to deposited layers, interstitial metallic foils made of aluminum, copper, indium, lead, tin, etc. can be placed between contacting rough surfaces to significantly decrease the joint resistance. Many researchers including Yovanovich (1982), Yovanovich et al. (1981, 1982), Savija et al. (2002), Bahrami et al. (2003, 2004) have presented analytical and empirical models for calculating the thermal joint resistance under different conditions. Yovanovich (1981) established the following correlation for conforming rough surfaces when interstitial fluids such as greases and gases are present in the gap:

$$R_j = \left\{ \left[1.25 k_s \frac{m}{\sigma} \left(\frac{P}{H_c} \right)^{0.95} + \frac{k_g}{Y + M} \right] A_a \right\}^{-1} \quad (6.29)$$

where k_s is the harmonic mean thermal conductivity for the two solids with thermal conductivities, k_1 and k_2 ,

$$k_s = \frac{2k_1k_2}{k_1 + k_2} \quad (6.30)$$

The effective rms surface roughness σ of the two materials with roughnesses σ_1 and σ_2 ,

$$\sigma = \sqrt{\sigma_1^2 + \sigma_2^2} \quad (6.31)$$

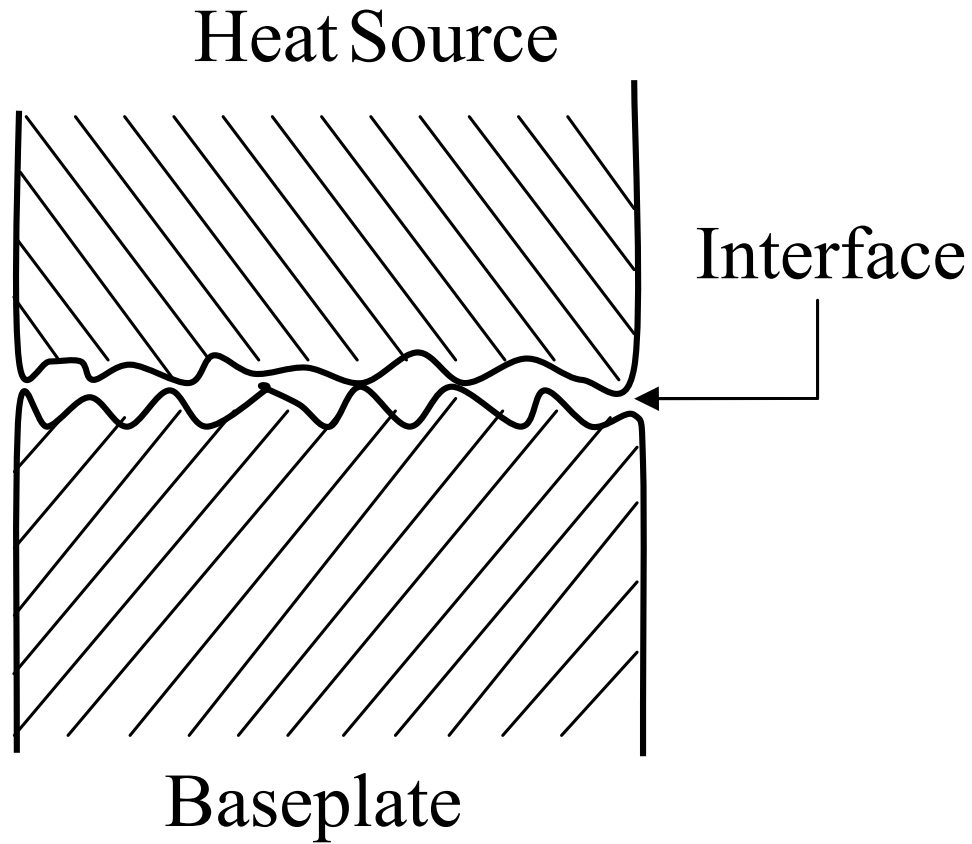


Figure 6.7: Interface Between Heat Source and Baseplate

The effective absolute surface slope m composed of the individual slopes of the two materials, m_1 and m_2 ,

$$m = \sqrt{m_1^2 + m_2^2} \quad (6.32)$$

The contact pressure is P and H_c is the surface microhardness of the softer of the two contacting solids. The microhardness is in general complex because it depends on several geometric and physical parameters, such as the Vickers microhardness correlation coefficients. The surface asperity slopes are frequently not given. In that case, Antonetti et al. (1991) proposed a correlation equation for the mean

absolute asperity slope:

$$m = 0.125(\sigma \times 10^6)^{0.402} \quad (6.33)$$

which was developed for the surface roughness range $0.216\mu m \leq \sigma < 9.6\mu m$. Antonetti and Yovanovich (1984) proposed a simple correlation for the effective gap thickness Y :

$$Y = 1.53\sigma \left(\frac{P}{H_c} \right)^{-0.097} \quad (6.34)$$

for the relative contact pressure range $10^{-5} < P/H_c < 2 \times 10^{-2}$. The gas parameter M is:

$$M = \alpha\beta\Lambda \quad (6.35)$$

with $\alpha = 2.4$ for air and clean metals, $\beta = 1.7$ for air and other diatomic gases, and $\Lambda = 0.06\mu m$ for air at atmospheric pressure and $15^\circ C$. For relatively smooth surfaces, Yovanovich (1981) proposed that the ratio m/σ can be taken equal to 0.111 to 0.20 *microns*⁻¹.

Yovanovich et al. (1997) used the aforementioned model to calculate the joint resistance at the interface formed by an aluminum 6063-T5 aluminum heat sink and an Al_2O_3 alumina package. The thermal conductivities of these materials are $201W/m \cdot K$ and $20.9W/m \cdot K$ respectively. The microhardness of the aluminum alloy $H_c = 1094MPa$, and based on surface roughness for flycut aluminum of $\sigma_1 = 0.4\mu m$ and a surface roughness for ground alumina of $\sigma_2 = 1.3\mu m$ were used to compute contact parameters. The specific thermal joint resistances are plotted for air ($k_g = 0.026W/m \cdot K$) and grease ($k_g = 0.2W/m \cdot K$) in Fig. 5.8 against the nominal contact pressure over the pressure range $0.007 \leq P(MPa) \leq 0.35$. It can be seen that for grease, the contact resistance is much smaller than the bare interface with air. The calculated values of the contact resistance for grease are an order of magnitude smaller than the contact resistance of a bare joint.

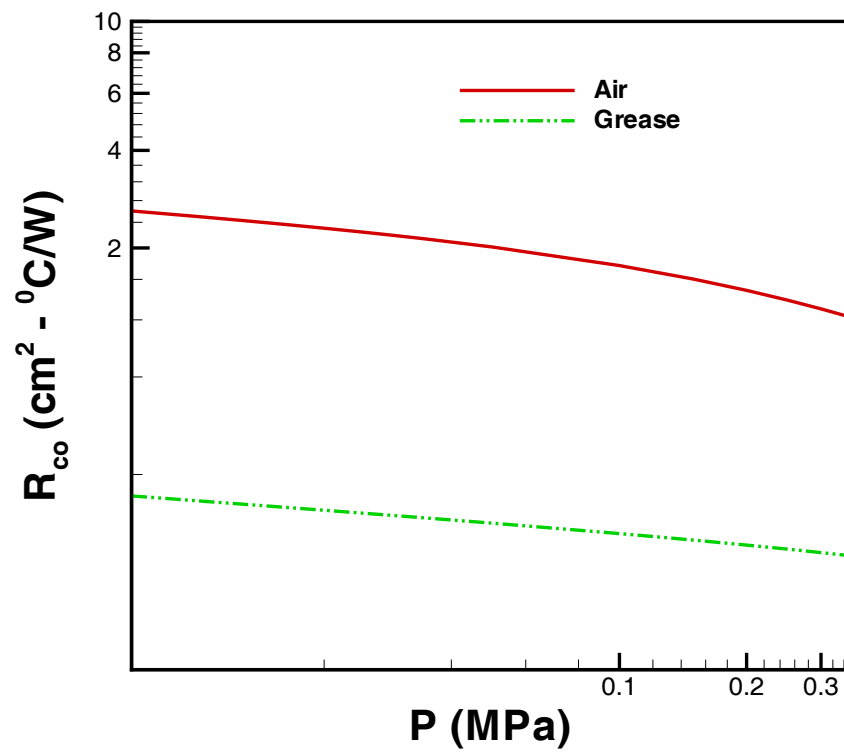


Figure 6.8: Interface Contact Resistance of Aluminum Heat Sink-Ceramic Package

2. Spreading Resistance - R_s

Thermal spreading resistance occurs when heat flow spreads from a surface-mounted heat source into a conducting solid (baseplate, in the case of a heat sink). Figure 5.4 shows a planar rectangular heat source situated on the bottom surface of the baseplate having thickness t_b and thermal conductivity k . The baseplate is cooled along the top surface through a uniform film coefficient h_e , which can be determined by the energy balance in CV 1 (Fig. 5.4):

$$Q = Q_b + Q_{fins} \quad (6.36)$$

where

$$Q = h_e A \theta_b \quad (6.37)$$

$$Q_b = (hA)_b \theta_b \quad (6.38)$$

$$Q_{fins} = (h\eta A)_{fins} \theta_b \quad (6.39)$$

with $\theta = \bar{T}_b - T_a$, and

$$A = LW, \quad A_b = LW - N\frac{\pi}{4}D^2, \quad A_{fins} = N\pi DH$$

Combining Eqs. (5.37) - (5.39), Eq. (5.36) can be solved for the uniform effective film coefficient h_e :

$$h_e = \frac{k_f/D}{\mathcal{S}_T \mathcal{S}_L} \left\{ \pi C_1 \gamma \eta_{fin} + \frac{0.75(\mathcal{S}_T \mathcal{S}_L - \pi)}{\sqrt{N_L \mathcal{S}_L}} \right\} \cdot Re_D^{1/2} Pr^{1/3} \quad (6.40)$$

The heat source area can be rectangular having dimensions $l \times w$. The lateral boundaries of the baseplate are adiabatic. Many models exist for spreading resistance subject to various imposed boundary conditions. In this study, only two models will be investigated to determine the spreading resistance. The first full

model is given by Yovanovich et al. (1999):

$$R_s = \frac{8}{LWk} \left\{ \frac{1}{l^2} \sum_{m=1}^{\infty} \frac{\sin^2\left(\frac{l\delta}{2}\right)}{\delta^3} \phi_m(\delta) + \frac{1}{w^2} \sum_{n=1}^{\infty} \frac{\sin^2\left(\frac{w\lambda}{2}\right)}{\lambda^3} \phi_n(\lambda) + \frac{8}{l^2 w^2} \sum_{m=1}^{\infty} \sum_{n=1}^{\infty} \frac{\sin^2\left(\frac{l\delta}{2}\right) \sin^2\left(\frac{w\lambda}{2}\right)}{\delta^2 \lambda^2 \beta} \phi_{m,n}(\beta) \right\} \quad (6.41)$$

where the eigenvalues δ_m , λ_n , and $\beta_{m,n}$ are given by:

$$\delta_m = \frac{2m\pi}{L}, \quad \lambda_n = \frac{2n\pi}{W}, \quad \beta_{m,n} = \sqrt{\delta_m^2 + \lambda_n^2}$$

The contributions of the baseplate thickness t_b , thermal conductivity k , and the uniform conductance h_e to the spreading resistance are determined by means of the general expression:

$$\phi(\zeta) = \frac{(e^{2\zeta t_b} + 1)\zeta + (1 - e^{2\zeta t_b})h_e/k}{(e^{2\zeta t_b} - 1)\zeta + (1 + e^{2\zeta t_b})h_e/k} \quad (6.42)$$

In all summations $\phi(\zeta)$ is evaluated in each series using $\zeta = \delta_m$, λ_n , and $\beta_{m,n}$ as defined above.

The second model, which is an approximate model for calculating spreading resistance, is given by Song et al. (1994). It is the solution to a single circular source of uniform flux on a circular substrate of uniform thickness. However, modifications can be made for a rectangular heat source and heat sinks. According to this model:

$$R_s = \frac{\Psi}{\sqrt{\pi} k a} \quad (6.43)$$

where Ψ is the dimensionless spreading resistance and includes the bulk material resistance, R_m , which is normally estimated as $\frac{t_b}{k A_b}$. This dimensionless spreading resistance is given by:

$$\Psi = \frac{\epsilon \tau}{\sqrt{\pi}} + \frac{1}{2} (1 - \epsilon)^{3/2} \phi_c \quad (6.44)$$

where

$$\phi_c = \frac{\tanh(\lambda_c \tau) + \frac{\lambda_c}{Bi}}{1 + \frac{\lambda_c}{Bi} \tanh(\lambda_c \tau)} \quad (6.45)$$

with

$$\begin{aligned} \lambda_c &= \pi + \frac{1}{\sqrt{\pi} \epsilon}, & a &= \sqrt{\frac{A_s}{\pi}}, & b &= \sqrt{\frac{A_b}{\pi}} \\ \epsilon &= \frac{a}{b}, & \tau &= \frac{t_b}{b}, & Bi &= \frac{1}{R_{fin} \pi b k} \end{aligned}$$

where R_{fin} depends upon the uniform heat transfer coefficient h_e .

3. Material Resistance - R_m

This resistance depends upon the thickness, t_b , and the area of the baseplate, A , and can be written as:

$$R_m = \frac{t_b}{kA} \quad (6.46)$$

4. Contact Resistance - R_c

When the pin-fins are machined as an integral part of the baseplate, there is no contact resistance at their base. But, more commonly, pin-fins are manufactured separately and are attached to the baseplate by a metallurgical or adhesive joint or are forced into slots machined on the baseplate. In such cases, there is a thermal contact resistance, R_c , which may adversely influence overall thermal performance of the heat sink. This resistance depends upon the thermal conductance of the material, h_c , and the contact area of the fins, A_c , and can be written as:

$$R_c = \frac{1}{(hA)_c} \quad (6.47)$$

5. Fin Resistance - R_{fin}

The thermal resistance of the fin, R_{fin} , is a function of fin efficiency, η_{fin} , the surface

area of the fin, A_{fin} , and the convection heat transfer coefficient, h_{fin} . Conduction and convection heat transfer are taken into consideration when analyzing the thermal contact resistance of the fin. Heat is carried out through the fin by conduction and dissipated to the surrounding ambient air by convection. The overall resistance of the fin can be written as:

$$R_{fin} = \frac{1}{(hA\eta)_{fin}} \quad (6.48)$$

where h_{fin} and η_{fin} can be determined from Eqs. (5.6) and (5.8) respectively.

6. Film Resistance - R_{film}

Heat is also convected from the exposed (unfinned) surface of the baseplate, which can be written as:

$$Q_b = h_b A_b \theta_b \quad (6.49)$$

where the heat transfer coefficient for the exposed surface of the baseplate, h_b , can be determined from Eq. (5.5) and the area of the exposed surface of the baseplate can be written as:

$$A_b = A - N \frac{\pi D^2}{4} \quad (6.50)$$

with $A = LW$, the total area of the baseplate and $N = N_T N_L$, the total number of pin-fins. Recalling the definition of the thermal resistance, Eq. (5.25) can be used to define an expression for the thermal resistance of the exposed surface of the baseplate, i.e.,

$$R_{film} = \frac{1}{h_b \left(A - N \frac{\pi D^2}{4} \right)} \quad (6.51)$$

6.3.2 Total Heat Sink Pressure Drop

In heat sinks, the pressure drop is important because of its association to the power required to move the fluid across the fin arrays. This pressure drop across the heat sink is also known as the hydraulic resistance of the system. It affects the overall performance of

the heat sink. Higher hydraulic resistance causes less airflow through the heat sink channel, attaining a lower convection heat transfer rate between the fins and the surrounding air and increasing fin thermal resistance. The actual volumetric flow rate can be found from the fan performance curve with a given total heat sink pressure drop. This point along the fan curve is called the system operating point. The dimensionless pressure drop, Eq. (4-65), is valid for a single isolated pin/cylinder, however, for a heat sink, the total pressure drop should also include the abrupt contraction and the abrupt expansion effects of the heat sink. This is shown in Fig. F.3. (Appendix F) and is given by

$$\Delta P_{tot} = \Delta P_{1-a} + \Delta P_{a-b} + \Delta P_{b-2} \quad (6.52)$$

where ΔP_{1-a} is the pressure drop due to the irreversible free expansion that always follows the abrupt contraction, ΔP_{a-b} is the pressure loss due to core friction, and ΔP_{b-2} is the pressure loss associated with the irreversible free expansion and momentum changes following an abrupt expansion. These pressure drops can be written as:

$$\Delta P_{1-a} = k_c \cdot \frac{\rho U_{max}^2}{2} \quad (6.53)$$

$$\Delta P_{b-2} = k_e \cdot \frac{\rho U_{max}^2}{2} \quad (6.54)$$

$$\Delta P_{a-b} = f N_L \cdot \frac{\rho U_{max}^2}{2} \quad (6.55)$$

where k_c and k_e are the abrupt contraction and abrupt expansion coefficients respectively, f is the friction factor, and N_L is the number of pins in the longitudinal direction. The coefficients of abrupt contraction and expansion have been established graphically by Kays (1950) for a number of geometries. The following correlations are derived from those graphs:

$$k_c = -0.0311\sigma^2 - .3722\sigma + 1.0676 \quad (6.56)$$

$$k_e = 0.9301\sigma^2 - 2.5746\sigma + 0.973 \quad (6.57)$$

with

$$\sigma = \frac{\mathcal{S}_T - 1}{\mathcal{S}_T} \quad (6.58)$$

Žukauskas and Ulinskas (1983) collected data, from a variety of sources, about friction factors for the flow in-line and staggered arrangements having many rows and plotted them in the form Eu/K_1 versus Re_D , where K_1 is a parameter accounting for geometry. They fitted these plots by inverse power series relationships and recommended several correlations depending on the value of \mathcal{S}_L and on the Reynolds number range. They also fitted and recommended correlations for the correction factors for the pressure drop with small number of rows. This author combined all the recommended correlations for pressure drop and their correction factors separately and developed single correlations for the friction factors and correction factors for each arrangement. These correlations can be used for any pitch and Reynolds number in the laminar flow range. They are

$$f = \begin{cases} K_1 [0.233 + 45.78/(\mathcal{S}_T - 1)^{1.1} Re_D] & \text{for In-Line arrays} \\ K_1 [378.6/\mathcal{S}_T^{13.1/\mathcal{S}_T}] / Re_D^{0.68/\mathcal{S}_T^{1.29}} & \text{for Staggered arrays} \end{cases} \quad (6.59)$$

where K_1 is a correction factor depending upon the flow geometry and arrangement of the pins. It is given by:

$$K_1 = \begin{cases} 1.009 \left(\frac{\mathcal{S}_T - 1}{\mathcal{S}_L - 1} \right)^{1.09/Re_D^{0.0553}} & \text{for In-Line arrays} \\ 1.175(\mathcal{S}_L/\mathcal{S}_T Re_D^{0.3124}) + 0.5 Re_D^{0.0807} & \text{for Staggered arrays} \end{cases} \quad (6.60)$$

The mean velocity in the minimum free cross section between two rows, U_{max} , is used as a reference velocity in the calculations of fluid flow and heat transfer for both types of arrangements, and is given by:

$$U_{max} = max \left\{ \frac{\mathcal{S}_T}{\mathcal{S}_T - 1} U_{app}, \frac{\mathcal{S}_T}{\mathcal{S}_D - 1} U_{app} \right\} \quad (6.61)$$

where U_{app} is the approach velocity, \mathcal{S}_L , and \mathcal{S}_T are the dimensionless longitudinal and transverse pitches, and $\mathcal{S}_D = \sqrt{\mathcal{S}_L^2 + (\mathcal{S}_T/2)^2}$ is the dimensionless diagonal pitch in case of staggered arrangement.

6.4 Case Studies and Discussion

The dimensions given in Table 5.1 are used as the default case to determine the performance parameters for both in-line and staggered pin-fin heat sinks.

Table 6.1: Dimensions Used to Determine Performance of Heat Sinks

Quantity	Dimension
Footprint (mm^2)	25.4×25.4
Source Dimensions (mm^2)	18.0×18.0
Baseplate Thickness (mm)	2
Pin Diameter (mm)	2
Overall Height of Heat Sink(mm)	12
Number of Pins (In-Line)	7×7
Number of Pins (Staggered)	8×6
Approach Velocity (m/s)	1
Thermal Conductivity of Solid ($W/m \cdot K$)	237
Thermal Conductivity of Air ($W/m \cdot K$)	0.026
Density of Air (kg/m^3)	1.1614
Specific Heat of Air ($J/kg \cdot K$)	1007
Kinematic Viscosity (m^2/s)	1.58×10^{-5}
Prandtl Number (Air)	0.71
Heat Load (W)	10
Ambient Temperature ($^{\circ}C$)	27

Table 6.2: Performance Parameters for In-Line and Staggered Heat Sinks

Quantity	In-Line	Staggered
Contact Resistance ($^{\circ}C/W$)	0.112×10^{-14}	0.114×10^{-14}
Material Resistance ($^{\circ}C/W$)	0.0133	0.0133
Fin Resistance ($^{\circ}C/W$)	264.51	260.84
Film Resistance ($^{\circ}C/W$)	64.75	64.54
Fins Resistance ($^{\circ}C/W$)	4.98	5.012
Spreading Resistance-Song Model ($^{\circ}C/W$)	0.125	0.136
Spreading Resistance-Yovanovich Model ($^{\circ}C/W$)	0.121	0.139
Heat Sink Resistance ($^{\circ}C/W$)	5.12	5.04
Average Heat Transfer Coefficient ($W/m^2 \cdot K$)	109.14	110.0
Efficiency of Heat Sink (%)	97.95	97.7
Friction Factor (m^2/s)	0.565	1.24
Pressure Drop (N/m^2)	8.18	15.62
Average Fluid Temperature ($^{\circ}C$)	74.44	72.87
Average Baseplate Temperature ($^{\circ}C$)	76.82	77.12
Air Temperature Leaving Heat Sink ($^{\circ}C$)	43.76	40.5

The air properties are evaluated at the ambient temperature. The results obtained for both in-line and staggered arrangements are shown in Table 5.2. It is important to note that for spreading resistance, two different models were used, but the approximate model of Song et al. (1994) give values only 0.4% lower than the full model of Yovanovich et al. (1999). Due to this very small difference, Song's model will be used in all calculations. It is also clear from Table 5.2 that the in-line arrangement gives higher heat sink resistance and lower pressure drop than the staggered arrangement. As a result, the average heat transfer coefficient and the fan power requirement are lower for the in-line arrangement. Figure 5.9 shows the temperature profiles through the heat sink for both arrangements. The baseplate is kept at constant temperature \bar{T}_b . It is clear that there is no appreciable effect of pin-fin arrangements on the temperature up to first half length of heat sink. However, the temperature increases slowly for the in-line arrangement close to the exit. The temperature differences at the inlet and exit, for both arrangements can be written as:

$$\Delta T_1 = \bar{T}_b - T_a \quad (6.62)$$

$$\Delta T_2 = \bar{T}_b - T_0 \quad (6.63)$$

The variation of air temperature at the exit versus number of pins in the transverse row is shown in Fig. 5.10. For small number of pins, there is no appreciable difference in T_0 for the two arrangements, but this difference increases slightly with the number of pins. Figure 5.11 shows the variation of T_0 versus pin-fin height H . It is clear that the temperature T_0 is higher for low profile heat sinks and it decreases with increase in pin height for both arrangements. It is important to note that there is no appreciable effect of pin arrangements on T_0 for the given height.

The parametric behavior, corresponding to a chosen variable with all others unchanged, is also investigated. The thermal resistance and the total pressure drop for the heat sink assembly are plotted as functions of the number of fins, fin diameter, and approach velocity in Figs. 5.12-5.15 for both in-line and staggered arrangements. Figure

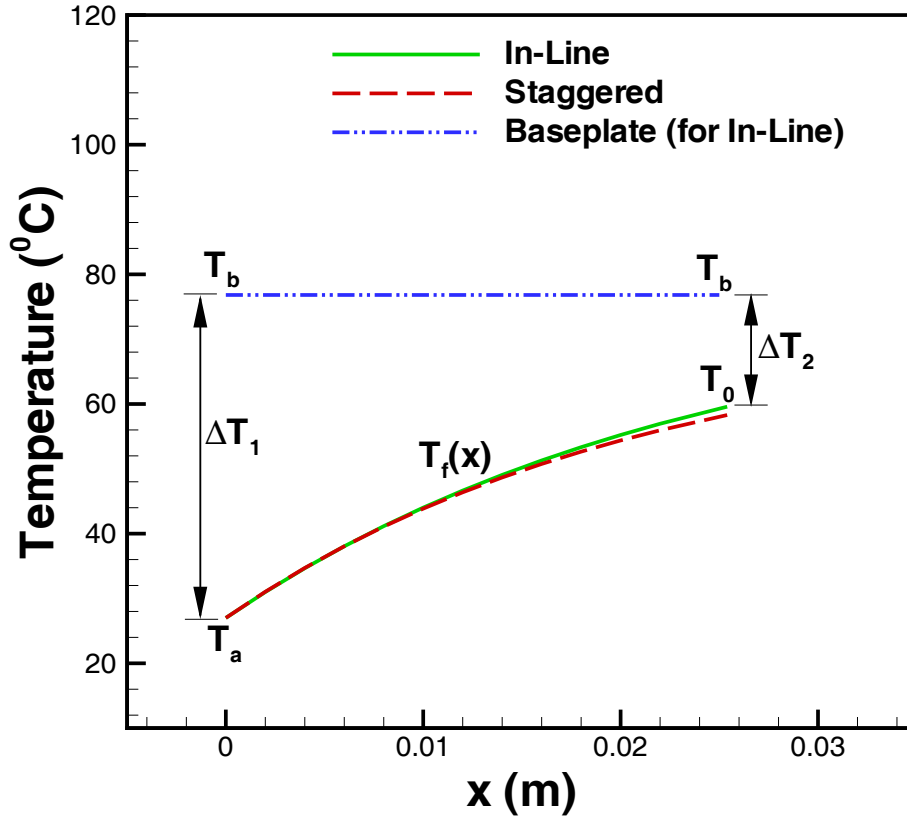


Figure 6.9: Temperature Distribution of Fluid in Heat Sink

5.12 shows the existence of an optimum number of fins N_T for both arrangements. As the number of fins increases, the heat sink resistance decreases and the pressure drop increases. The intersections of both performance curves gives the optimum condition for both arrangements. No appreciable effect of pin arrangements on the number of pins could be found upto the optimum number of pins. However, after optimum point the difference in ΔP between the two arrangements increases with the number of pins.

Figure 5.13 gives the optimum diameter of the pin-fin for each arrangement. It shows that smaller diameter pin-fins give better performance for the staggered arrangement than for the in-line arrangement. As the diameter of the pin-fin increases, thermal resistance

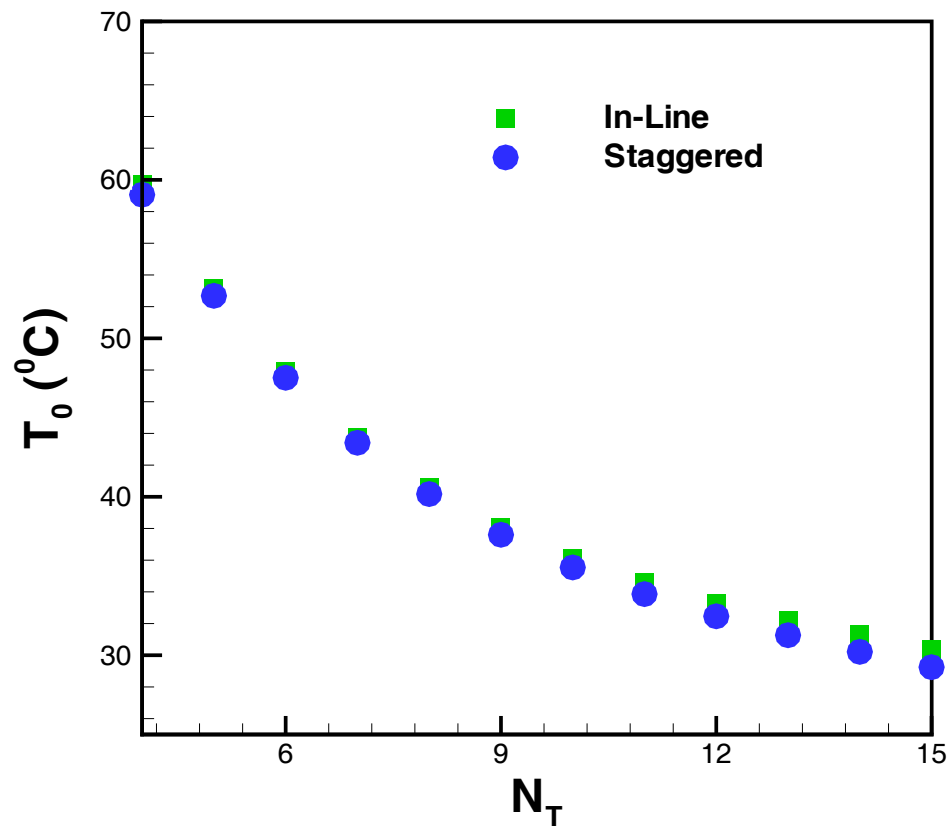


Figure 6.10: Temperature of Air Leaving Heat Sink versus N_T

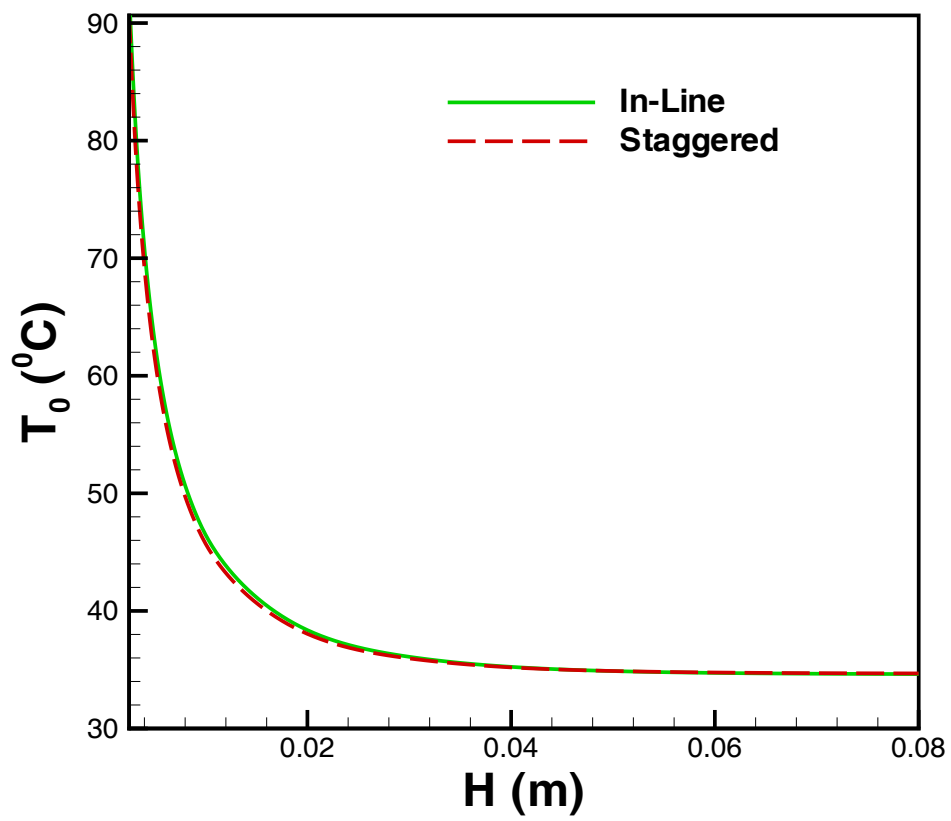


Figure 6.11: Temperature of Air Leaving Heat Sink versus H

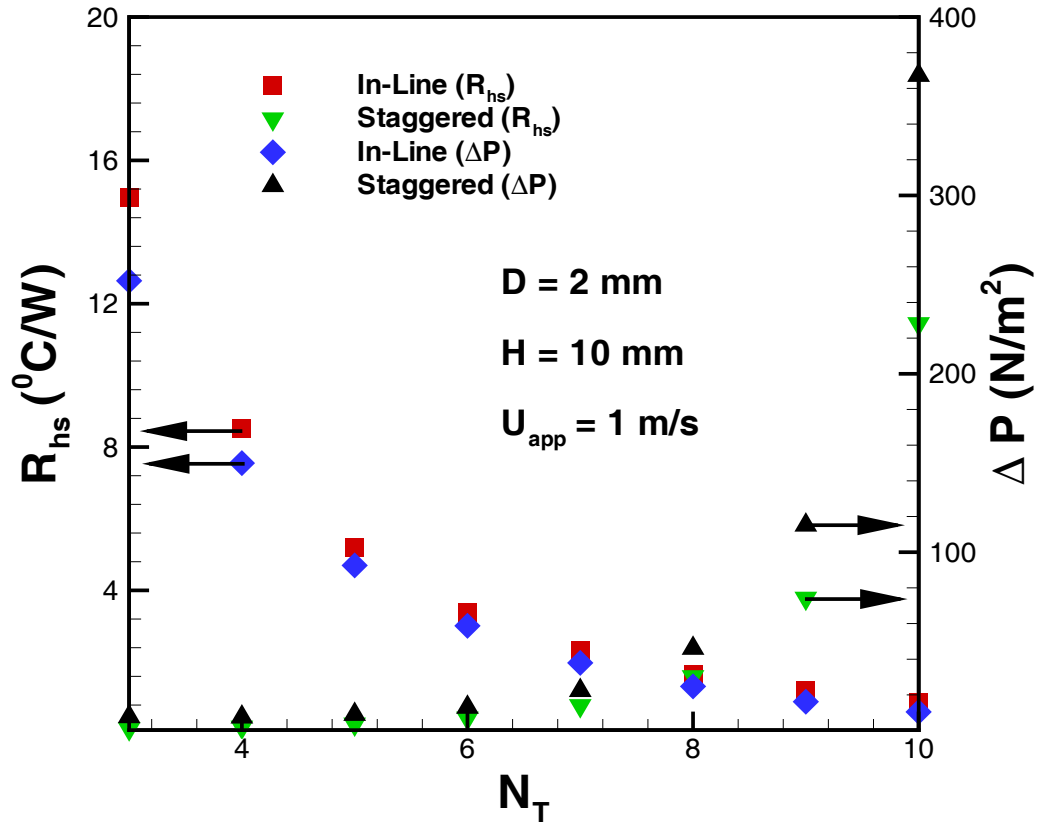


Figure 6.12: Performance of PFHS as Function of Number of Fins

decreases and pressure drop increases. This is because the larger pin diameter creates a larger area for heat to flow through and thus, decrease the thermal resistance. The difference between pressure drops is negligible for the small pin diameters, however, it increases with the pin diameters. Figure 5.14 shows the same performance behavior as a function of approach velocity. It shows that low approach velocities are preferable in the staggered arrangement, whereas for better performance in the in-line arrangement higher velocities are preferred.

The same dimensions of the heat sinks are used to determine the thermal performance of the heat sink for a range of thermal conductivities, which includes representative prop-

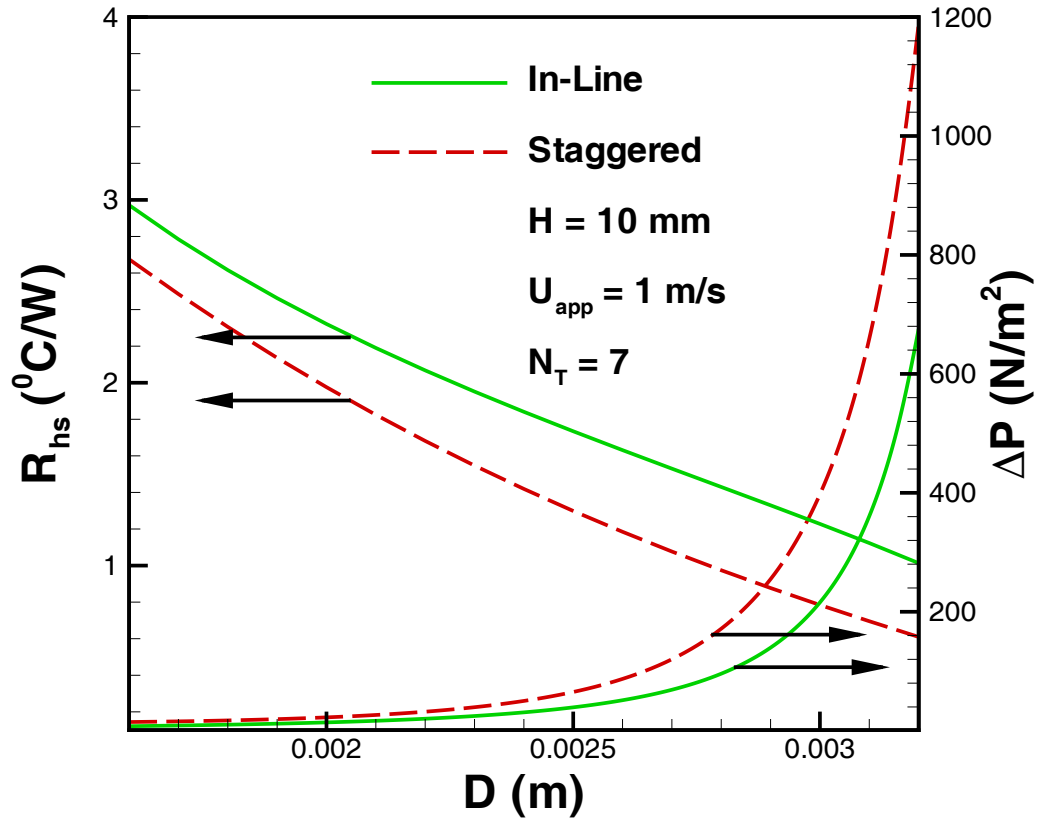


Figure 6.13: Performance of PFHS as Function of Pin Diameter

erties for a variety of materials from plastic composites to copper. Results are presented in Fig. 5.15. It is interesting to note that the thermal performance of in-line pin-fin heat sinks is higher than the staggered pin-fin heat sinks for the same material. Furthermore, aluminum is the best material for any type of arrangement.

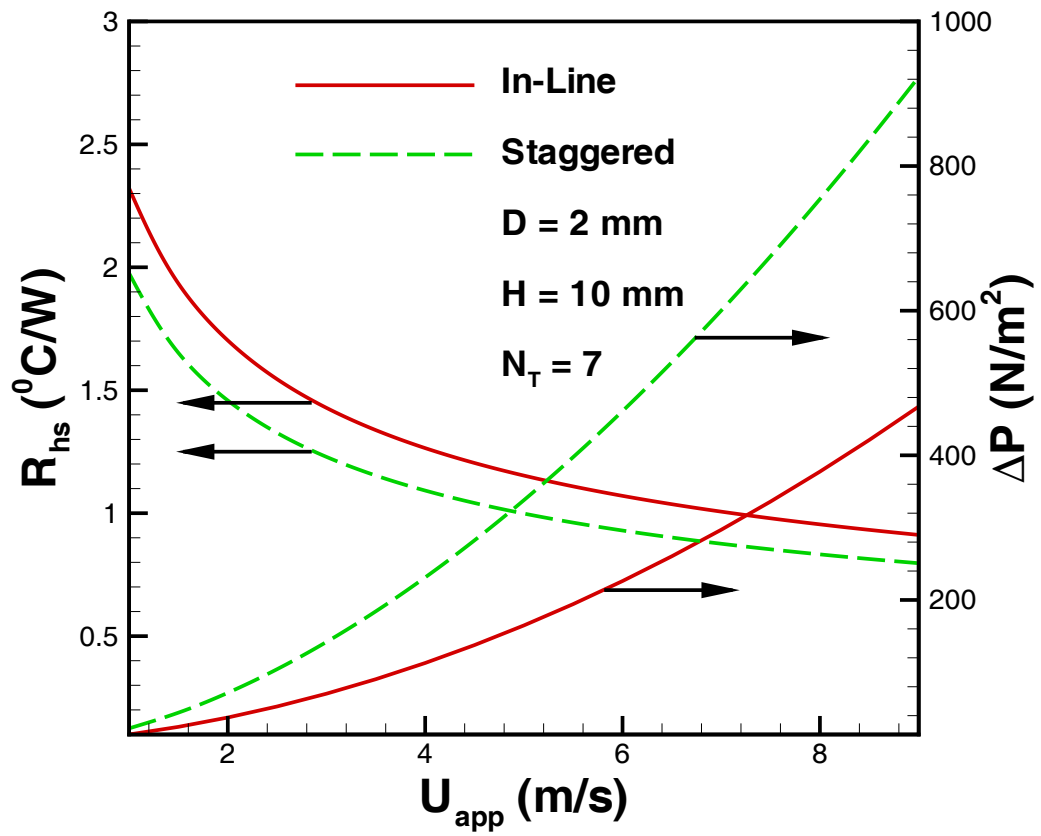


Figure 6.14: Performance of PFHS as Function of Approach Velocity

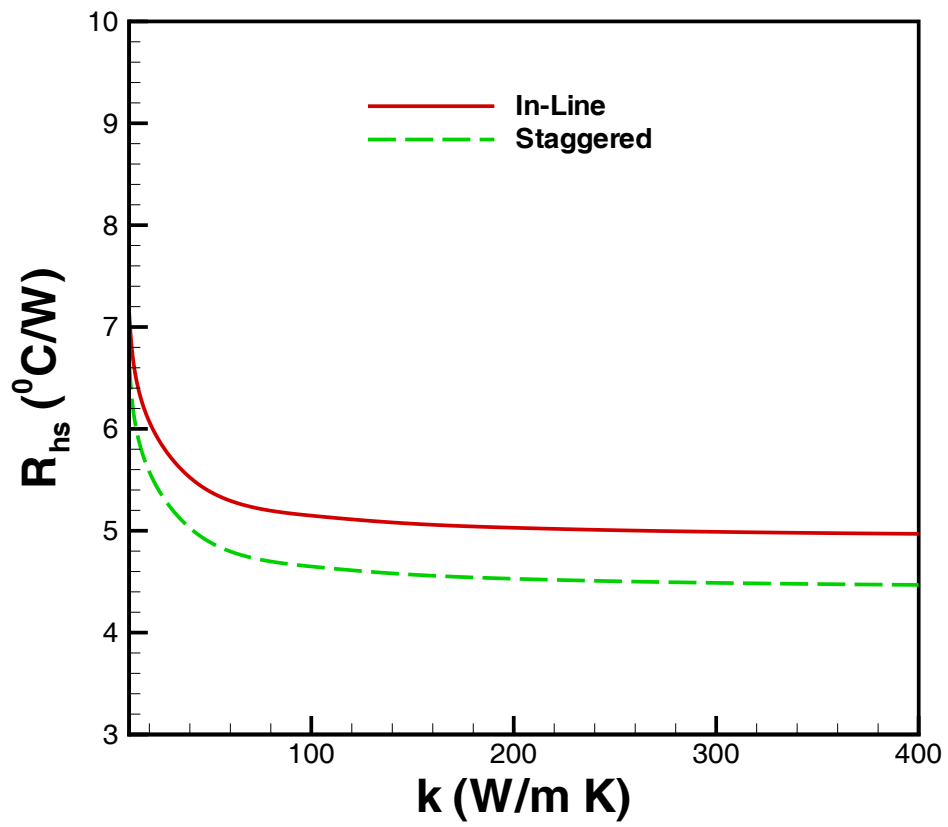


Figure 6.15: Performance of PFHS as Function of Thermal Conductivity

6.5 Summary

Energy balances and thermal circuit concepts are employed to develop models for thermal and hydraulic resistances of the heat sink. The analyses of in-line and staggered pin-fin heat sinks are performed by using parametric variation of total heat sink resistance. It is observed that the thermal resistance decreases whereas pressure drop increases for each design variable which gives optimum value of that variable. The effect of thermal conductivity is also observed in both arrangements. It is shown that the average heat transfer coefficient and the pressure drop are lower for the in-line pin-fin heat sink. Also the air temperature at the exit T_0 is found to be higher for low profile heat sinks for both arrangements. No appreciable effect of pin arrangements on T_0 could be found for the given height. Furthermore, smaller diameter pin-fins and low approach velocities give better performance for the staggered arrangement than for the in-line arrangement.

Chapter 7

Optimization

7.1 Introduction

A heat sink that cools adequately fulfills only a part of the objective. Optimizing the design creates the best available heat sink solution for the application and benefits the overall system design. Several independent variables like baseplate dimensions L , W , t_b , heat source dimensions l , w , heat load Q , pin-fin dimensions D , H , N , pin-fin arrangements in-line or staggered, material properties k , and fluid properties ν , ρ , k_f , μ can be modified to improve heat sink performance with respect to the selected design criteria. A larger heat sink surface area $L \times W$, for example, will improve cooling, but may increase the cost. Increasing the baseplate thickness t_b distributes heat more uniformly to the fins if the package is smaller than the heat sink, but increases weight. The interface material can have a significant affect on assembly costs as well as on thermal resistance. Thicker fins provide more structural integrity and may be easier to manufacture, but increase the weight for a given thermal resistance. In the context of entire electronic system, pressure drop ΔP across the heat sink may be another area to investigate more thoroughly. If the pressure drop is too great, airflow may bypass the heat sink or total system airflow may be reduced.

In Chapter 5, we noticed that the overall performance of a heat sink depend on the total heat sink resistance and the pressure drop across the heat sink. However, the point of intersection of both performances (thermal and hydraulic) gives roughly the optimum point corresponding to single parameter optimization. While single parameter optimization can provide an optimized design condition when all other design parameters are predetermined, there is no guarantee that this “optimized” result will hold when other design parameters are unconstrained.

It is important to note that within the context of the optimization methods, only one criterion or performance measure can be used to define the optimum. It is not possible to find a solution that, say, simultaneously minimizes heat sink resistance and the pressure drop or hydraulic resistance of the system. In this chapter, a unique measure will be explored to optimize the overall performance of pin-fin heat sinks.

7.2 Optimization

The general procedure for solving optimization problems consists of the following five steps:

1. Make a list of all independent variables and select constraints and design variables.
2. Determine the criterion for optimization.
3. Develop a mathematical model for optimization that relates all the variables.
4. Formulate the problem and include both equality and inequality constraints.
5. Apply a suitable optimization technique to the mathematical statement of the problem.
6. Check the answers for min or max and examine the sensitivity of the result.

7.2.1 Selection of Independent Variables

The first step in solving optimization problems is the selection of independent variables that are adequate to characterize the possible candidate designs or operating conditions of the heat sink. Several factors are considered in selecting the independent variables. However, a good rule is to include only those variables that have a significant impact on the heat sink performance criterion. For a heat sink, the independent variables are: baseplate length (L) in the flow direction, baseplate width (W), baseplate thickness (t_b), pin-fin diameter (D), pin-fin height (H), pin density (N), heat source dimensions ($\ell \times w$), heat load (Q) or chip temperature (T_c), approach velocity (U_{app}), and ambient temperature (T_a). Usually several of these variables are specified by the manufacturer or the designer and they include: baseplate length (L), baseplate width (W), heat source dimensions ($\ell \times w$), heat load (Q) or chip temperature (T_c), and ambient temperature (T_a). Therefore, in this study the design variables include pin-fin diameter (D), pin-fin height (H), pin density (N), approach velocity (U_{app}) and arrangements (in-line or staggered) that are to be optimized.

7.2.2 Performance Criterion

The performance criterion for the optimization of pin-fin heat sinks can be determined by using the following possible objective functions:

1. Minimum chip temperature
2. Minimum pressure drop
3. Minimum size
4. Minimum heat sink mass or weight
5. Minimum cost

The continuing increase of power densities in microelectronics and the simultaneous drive to reduce the size and weight of electronic products have led to the increased importance of thermal management issues in this industry. The temperature at the junction of an electronics package (chip temperature) has become the limiting factor determining the lifetime of the package. Besides this fact, the basic goal of a heat sink is to transfer maximum heat from the heat source which can be achieved by decreasing the chip temperature. For a given heat load Q and ambient temperature T_a , the chip temperature depends on the total heat sink resistance.

$$T_c = QR_{hs} + T_a \quad (7.1)$$

So, in order to reduce the chip temperature, we need to decrease the thermal resistance of the heat sink, which is given by:

$$R_{hs} = \frac{1}{h_{avg}A_{hs}} \quad (7.2)$$

where h_{avg} is the average heat transfer coefficient of the heat sink and A_{hs} is the total heat sink surface area. Equation (7.2) shows that the heat sink resistance can be decreased by increasing h_{avg} and/or by increasing A_{hs} . For a given fluid and approach velocity, h_{avg} depends on the geometry of the heat sink in a complex manner (Eq. 6.13) and, in that case, increasing h_{avg} may or may not be practical. The alternative is to increase the surface area of the heat sink by attaching pins to the baseplate, which increases the pressure drop (or hydraulic resistance) across the heat sink. The higher pressure drop causes the less air flow through the heat sink and increases the fin thermal resistance. So, in order to transfer maximum heat from the chip, we need to decrease the thermal resistance of the heat sink as well as to decrease the pressure drop across the heat sink. It was observed, in Chapter 5, that the total heat sink resistance decreases continuously and at the same time pressure drop or hydraulic resistance of the system increases corresponding to the design variables pin diameter D , pin density N , and approach velocity U_{app} . It was not possible to find the minimum values for both of them at the same time. In an optimal heat sink, there is a trade-off between heat sink resistance and the pressure drop.

Entropy generation rate is a unique criterion that combines both heat sink resistance and the pressure drop. It can be obtained by combining mass, force, energy, and entropy balances across the heat sink. It is a function of all system parameters considered in this study. By minimizing entropy generation rate with respect to each design variable, we can optimize the overall performance of the heat sink. It has been proven to be a suitable method to optimize the design variables of the heat sink by reducing both thermal and hydraulic resistances to a minimum, according to the physical constraints imposed on the system.

7.2.3 Model Development

In this step, EGM models will be developed for optimizing the overall performance associated with:

1. single pin-fin of arbitrary cross section (rectangular, square, circular and elliptical), and
2. in-line and staggered cylindrical pin-fin heat sinks.

A general expression for the entropy generation rate for each case is obtained by using the conservation equations for mass and energy with entropy balance (Appendix F). The formulation for the dimensionless entropy generation rate is developed in terms of dimensionless variables.

EGM Model for Optimization of Fin Geometry

Consider a fin of arbitrary constant cross section which is immersed in a uniform stream of air with velocity U_{app} and ambient temperature T_a . The fin is assumed to be isothermal at temperature T_w (Fig. 3.2). Following Bejan (1996), the entropy generation rate for a

single fin can be written as (Appendix F):

$$\dot{S}_{gen} = \frac{Q^2 R_{tot}}{T_a T_b} + \frac{F_D U_{app}}{T_a} \quad (7.3)$$

This expression shows that the entropy generation rate depends on the total thermal resistance R_{tot} of the system and the drag force F_D , provided that the heat load and ambient conditions are specified. The total thermal resistance for a fin of arbitrary cross section can be written as

$$R_{tot} = \frac{1}{\frac{1}{R_c + R_{fin}} + \frac{1}{R_{film}}} \quad (7.4)$$

with

$$R_c = \frac{1}{(hA)_c} \quad (7.5)$$

$$R_{fin} = \frac{1}{(hA\eta)_{fin}} \quad (7.6)$$

$$R_{film} = \frac{1}{(hA)_b} \quad (7.7)$$

where A_{fin} is the surface area of the fin, A_b is the area of the unfinned surface of the baseplate, A_c is the contact area of the fin, η_{fin} is the efficiency of the fin defined by Eq. (6.8), h_c is the thermal contact conductance, and h_{fin} and h_b are the average heat transfer coefficients for the fin and the unfinned surface of the baseplate (Eq. 4.34) which depend upon the characteristic length of the surface (\mathcal{L}), the approach velocity (U_{app}) as well as the physical properties of the fluid (ρ, μ, c_p, k_f), the functional relationship for the average dimensionless heat transfer coefficient can be written as:

$$Nu_{\mathcal{L}} = f(Re_{\mathcal{L}}, Pr) \quad (7.8)$$

So, the average Nusselt number for the selected geometries (Chapter 4) can be written as:

$$Nu_{\mathcal{L}} = C_1 Re_{\mathcal{L}}^n Pr^{1/3} \quad (7.9)$$

where C_1 is a constant depending upon the geometry of the fin, and n is the index (see Table 7.1). The constant C_1 and the index n are taken from Chapter 4 for the circular, elliptical and plate fins, whereas, for the square pin-fin they are taken from Jakob (1949). The drag force for the fin of arbitrary cross section can be written as:

$$F_D = C_D \left(\frac{1}{2} \rho U_{app}^2 \right) A_p \quad (7.10)$$

where A_p is the frontal area and C_D is the drag coefficient given by:

$$C_D = \frac{C_2}{\sqrt{Re_{\mathcal{L}}}} + C_3 + \frac{C_4}{Re_{\mathcal{L}}} \quad (7.11)$$

where C_2 , C_3 , and C_4 are the constants depending upon the geometry. These constants are taken from Chapter 3 for the circular, elliptical plate fins and presented in Table 7.1. The constants for the square geometry are taken from Jakob (1949).

Combining Eqs. (7.7)-(7.11), Eq. (7.6) can be written in dimensionless form as follows:

$$\begin{aligned} N_s &= \frac{\dot{S}_{gen}}{(Q^2 U_{app} / k \nu T_a^2)} \\ &= \frac{(T_a / T_b)}{k_{eq} Re_{\mathcal{L}}} \left[\frac{1}{\sqrt{C_5 Nu_{\mathcal{L}} / k_{eq} \tanh(\gamma \sqrt{C_6 Nu_{\mathcal{L}} k_{eq}})}} + \frac{1}{C_7 Nu_{\mathcal{L}}} \right] + \\ &\qquad\qquad\qquad \frac{1}{2} C_D B \gamma Re_{\mathcal{L}}^2 \end{aligned} \quad (7.12)$$

where $B = \rho \nu^3 k T_a / Q^2$ is a fixed dimensionless duty parameter that accounts for the importance of fluid friction irreversibility relative to heat transfer irreversibility. The duty parameter B is fixed as soon as the fluid, fin material, and the base heat transfer rate are specified. The greater the base heat transfer rate, the smaller will be the fluid friction irreversibility. The constants C_5 , C_6 , and C_7 in Eq. (7.12) depend on the geometry of the fin and are given by:

$$C_5 = \frac{P A_c}{\mathcal{L}^3}, \quad C_6 = \frac{P \mathcal{L}}{A_c}, \quad \text{and} \quad C_7 = L^* W^* - A_c^*$$

where $L^* = L / \mathcal{L}$ and $W^* = W / \mathcal{L}$ are the dimensionless length and width of the baseplate.

Table 7.1: Parameters for Different Geometries of Pin-Fins

Parameters	Geometry			
	Plate	Circular	Square	Elliptical
\mathcal{L}	L	d	s	$2a$
A_c	tL	$\pi d^2/4$	s^2	πab
A_p	LH	dH	sH	$2aH$
P	$2(L+t)$	πd	$4s$	$4aE(e)$
C_1	0.75	0.593	0.102	$0.75 - 0.16 \exp(-0.018\epsilon^{-3.1})$
C_2	1.357	5.781	0	$1.353 + 4.43\epsilon^{1.35}$
C_3	0	1.152	2	$1.1526\epsilon^{0.95}$
C_4	0	1.26	0	$1.26\epsilon^{0.95}$
C_5	$2\epsilon_1(1 + \epsilon_1)$	$\pi^2/4$	4	$\pi^4 \epsilon / 16E^2(e)$
C_6	$2(1 + \epsilon_1)/\epsilon_1$	4	4	$16E^2(e)/\pi^2 \epsilon$
n	1/2	1/2	0.675	1/2

The values of these constants for the selected geometries are given in Table 7.1.

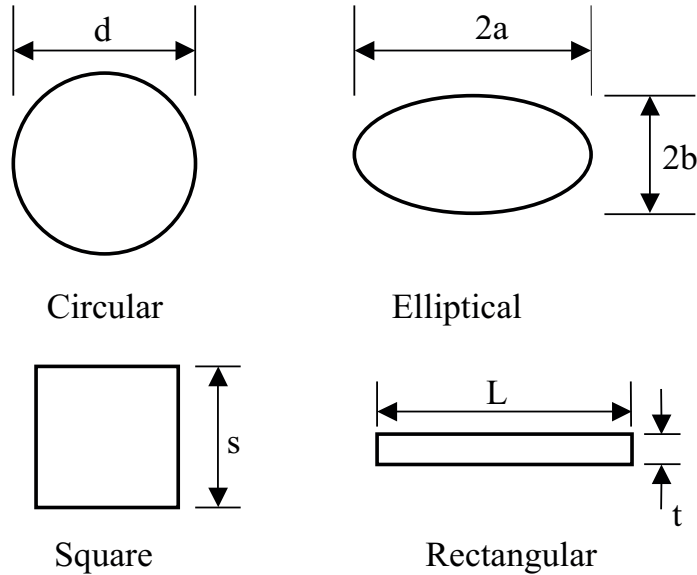


Figure 7.1: Cross Sections of Selected Geometries

Equation (7.12) shows that, for any given fin geometry, heat duty and a stream of constant thermophysical property fluid, the total dimensionless entropy generation rate will be a function of Reynolds number which in turn depends on the characteristic length \mathcal{L} and the approach velocity, U_{app} .

The cross sections for rectangular plate fin (RPF), circular pin fin (CPF), square pin fin (SPF), and elliptical pin fin (EPF) are shown in Fig. 7.1 and a summary of different parameters for the selected geometries is given in Table 7.1.

EGM Model for Optimization of Pin-Fin Heat Sinks

Following Bejan (1996) and applying the laws of conservation of mass and energy with entropy balance for a fluid flowing across a shrouded heat sink (Fig. 7.2), one can obtain an expression for the entropy generation rate:

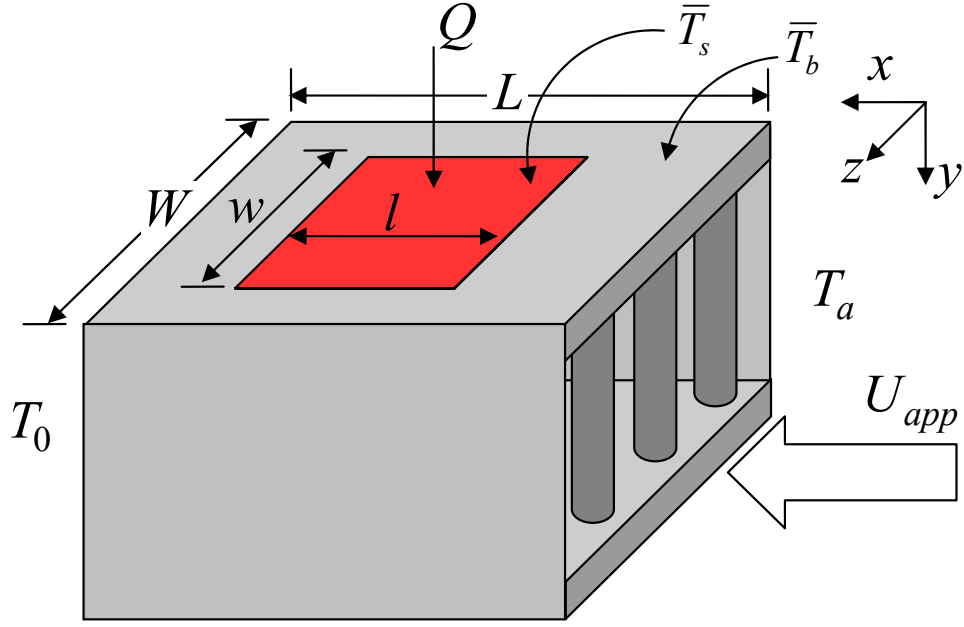


Figure 7.2: Shrouded Heat Sink

$$\dot{S}_{gen} = \left(\frac{Q^2}{T_a T_b} \right) R_{hs} + \frac{\dot{m} \Delta P}{\rho T_a} \quad (7.13)$$

where the thermal resistance of the heat sink R_{hs} can be determined from Eq. (6.28) and the total pressure drop across the heat sink can be determined from Eq. (6.52). The mass flow rate through the pins is given by:

$$\dot{m} = \rho U_{app} N_T \mathcal{S}_T H D \quad (7.14)$$

Using Eqs. (7.14), (6.26), and (6.52), Eq. (13) can be simplified to give the dimensionless entropy generation rate (Appendix F):

$$N_s = \frac{\dot{S}_{gen}}{(Q^2 U_{app} / k \nu T_a^2)} = \frac{C_8}{Re_D} + \frac{1}{2} C_{10} B \gamma Re_D^2 \quad (7.15)$$

where

$$C_8 = \frac{T_a}{T_b} \left[\frac{\Psi}{\sqrt{\epsilon_2 N \mathcal{S}_L \mathcal{S}_T}} + \frac{1}{C_9 (k_f/k) Re_D^{1/2} Pr^{1/3}} \right] \quad (7.16)$$

$$C_{10} = N_T \frac{\mathcal{S}_T^3}{(\mathcal{S}_T - 1)^2} (f N_L + k_c + k_e) \quad (7.17)$$

$$C_9 = N \left\{ \pi C_1 \gamma \eta_{fin} + \frac{0.75}{\sqrt{N_L \mathcal{S}_L}} \left(\mathcal{S}_T \mathcal{S}_L - \frac{\pi}{4} \right) \right\} \quad (7.18)$$

with ϵ_2 as the percentage of the area covered by the source on the baseplate and the constant C_1 is given by Eq. (4.49).

7.2.4 Problem Formulation

$f(x_i, P_i)$ represents the entropy generation rate that is to be minimized subject to equality constraints $g_j(x_i, P_i) = 0$ and inequality constraints $l_k(x_i, P_i) \geq 0$. In this case, the values of L, W, l, w, T_a , and Q are fixed as follows:

$$L = 25.4(\text{mm}) \quad (7.19)$$

$$W = 25.4(\text{mm}) \quad (7.20)$$

$$l = 18.0(\text{mm}) \quad (7.21)$$

$$w = 18.0(\text{mm}) \quad (7.22)$$

$$T_a = 300(^{\circ}K) \quad (7.23)$$

$$Q = 10(W) \quad (7.24)$$

The complete mathematical formulation of the optimization problem may be written in the following form:

$$\text{minimize } f(x_i, P_i) = \dot{S}_{gen}(x_i, P_i) \quad (7.25)$$

subject to the equality constraints:

$$g_j(x_i, P_i) = 0, \quad j = 1, 2, \dots, m \quad (7.26)$$

and inequality constraints

$$l_j(x_i, P_i) \geq 0, \quad j = m + 1, \dots, p \quad (7.27)$$

where x_i denotes the vector of the design variables $(x_1, x_2, x_3, \dots, x_n)^T$, P_i denotes the vector of the parameters $(P_1, P_2, P_3, \dots, P_n)^T$, and g_j and l_j are the imposed equality and inequality constraints. The design variables x_i are:

$$x_i = [D, H, N, U_{app}]$$

In this study, thermal conductivity of the material k is considered as the parameter P_i .

Equality constraints include all model equations and are given by:

$$C_8 = \frac{T_a}{T_b} \left[\frac{\Psi}{\sqrt{\epsilon_2 N S_L S_T}} + \frac{1}{C_9 (k_f/k) Re_D^{1/2} Pr^{1/3}} \right] \quad (7.28)$$

$$C_{10} = N_T \frac{S_T^3}{(S_T - 1)^2} (f N_L + k_c + k_e) \quad (7.29)$$

$$C_9 = N \left\{ \pi C_1 \gamma \eta_{fin} + \frac{0.75}{\sqrt{N_L S_L}} \left(S_T S_L - \frac{\pi}{4} \right) \right\} \quad (7.30)$$

and inequality constraints are:

$$\eta_{fin} - 0.75 \geq 0 \quad (7.31)$$

$$Re_D - 1000 \leq 0 \quad (7.32)$$

$$H_{overall} - 12(mm) \leq 0 \quad (7.33)$$

$$1 \leq U_{app} (m/s) \leq 6 \quad (7.34)$$

$$1 \leq D(mm) \leq 3 \quad (7.35)$$

$$1.25 \leq \mathcal{S}_L \leq 3 \quad (7.36)$$

$$1.25 \leq \mathcal{S}_T \leq 3 \quad (7.37)$$

$$3 \leq \gamma \leq 8 \quad (7.38)$$

For the nonlinear problem, mentioned above, Edgar and Himmelblau (1988) and Reklaitis et al. (1983) defined a new objective function as:

$$L(x_1, \dots, x_n, \lambda_1, \dots, \lambda_p, \sigma_1, \dots, \sigma_{p-m}) = f(x_i) + \sum_{j=1}^m \lambda_j g_j(x_i) + \sum_{k=m+1}^p \lambda_k [l_k(x_i) - \sigma_k^2] \quad (7.39)$$

where λ_j are the Lagrange multipliers and σ_j are slack variables. The use of slack variables enables the Lagrangian multiplier method to be applied to problems with inequality constraints.

7.2.5 Optimization Technique

The optimization problem (Eq. 7.34) can be reduced to solving the system of equations defined by

$$\frac{\partial L}{\partial x_i} = 0 \quad i = 1, \dots, n \quad (7.40)$$

$$\frac{\partial L}{\partial \lambda_j} = 0 \quad j = 1, \dots, m \quad (7.41)$$

$$\frac{\partial L}{\partial \sigma_j} = 0 \quad k = 1, \dots, p - m \quad (7.42)$$

The above system may be solved using numerical methods such as multivariable Newton-Raphson method. This method has been described by Stoeker (1989) and applied to the constrained optimization of the entropy generation rate by Culham et. al (2001).

A simple procedure was coded in MAPLE 9, a symbolic mathematics software, which solves the system of N non-linear equations using the multivariable Newton-Raphson method. Given, the Lagrangian L , the solution vector $[x]$, initial guess $[x_0]$, and maximum

number of iterations N_{max} , the procedure systematically applies the Newton-Raphson method until the desired convergence criteria and/or maximum number of iterations is achieved. The method is quite robust provided an adequate initial guess is made.

7.2.6 Optimal Solution and Sensitivity

Finally, we must check to see x^* is a minimum and not a stationary point (or maximum) because the Lagrangian function itself exhibits a saddle point with respect to x , λ^* , and σ^* at the optimum. The necessary condition for x^* to be a local minimum of the problem, under consideration, is that the Hessian matrix of L should be positive semidefinite, i.e.

$$v^T \nabla^2 [L(x^*, \lambda^*, \sigma^*)] v \geq 0 \quad (7.43)$$

For a local minimum to be a global minimum, all the Eigen-values of the Hessian matrix should be ≥ 0 . The Lagrange method is quite helpful in analyzing parameter sensitivities in problems with multiple constraints. In a typical heat sink, a number of different materials (from composite plastics to copper) are used in manufacturing; these materials must meet certain specifications in terms of cost and weight as required by the customers.

The sensitivity of the objective function is expressed as $\partial L / \partial p_0$ where as the sensitivity of the location of the optimum is expressed as $\partial x_i / \partial p_0$, where p_0 is the model parameter. Generally, $\partial L / \partial p_0 \neq 0$, indicating that as one changes the parameters the value of the objective function changes, but $\partial x_i / \partial p_0 = 0$, indicating that the location of the optimum is not a function of the parameters.

7.3 Results and Discussion

7.3.1 Optimization

Fin Geometry

The quantities given in Table 7.2 are used as the default case to compare the performance each geometry selected in this study. The air properties are evaluated at the ambient temperature.

The comparison of the performance of the selected geometries is shown in Figs. 7.3 - 7.6 on the basis of same perimeter. Figure 7.3 shows the variation of dimensionless entropy generation rate, N_s , with the approach velocity, U_{app} , for the selected geometries. The wetted surface area of each geometry, and the ambient temperature, T_a , are kept constant. As the approach velocity increases, the dimensionless entropy generation rate decreases for each geometry up to a certain velocity and then increases. The square pin-fin (SPF) gives the highest entropy generation rate for the entire range of the approach velocities. It should be noted that each geometry has its own optimum for N_s which moves from square geometry to the flat plate. Besides SPF, for low approach velocities, the choice of geometry moves from RPF to EPF and for higher velocities it moves from CPF to RPF. An optimal approach velocity U_{app} exists for all geometries which moves from SPF to RPF.

The effects of the axis ratio on the dimensionless total entropy generation rate for the selected geometries, are shown in Fig. 7.4. As expected, no effect of the axis ratio could be observed on N_s for the plate, circular, and square fin geometries, however, for elliptical geometry, it decreases from $\epsilon = 1$ (circular geometry) to $\epsilon = 0.01$ (flat plate). Under the same conditions of approach velocity and ambient temperature, the entropy generation rate for the square geometry is the highest, whereas, for the plate geometry, it is the lowest. Again, the square geometry is the worst choice.

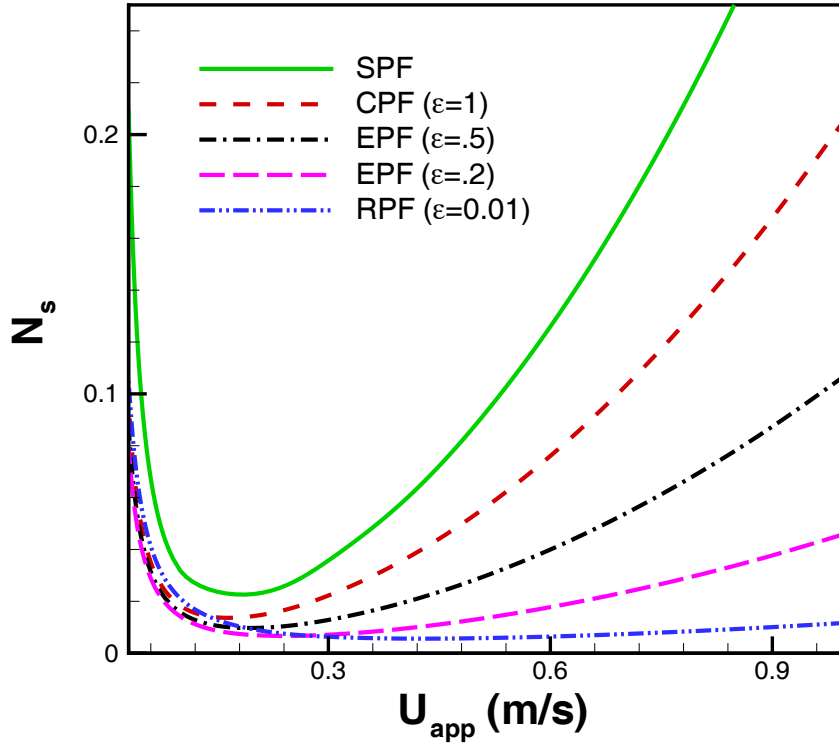


Figure 7.3: Dimensionless Entropy Generation Rate vs Approach Velocity

The effects of the aspect ratio on the dimensionless entropy generation rate for different geometries is shown in Fig. 7.5. Again, each geometry has its own optimum point for the minimum entropy generation rate which moves down from the square geometry to the plate fin. It is observed that, for smaller aspect ratios, the circular geometry gives better results from the point of view of minimum entropy generation rate but the choice of geometry moves with the aspect ratio. The dimensionless total entropy generation rate, N_s , includes the contributions due to heat transfer and viscous friction. As the approach velocity is increased, the contribution due to heat transfer, N_{sh} , decreases and that of viscous friction, N_{sf} , increases for each of the geometry considered. This behavior is shown in Fig. 7.6 for the circular geometry.

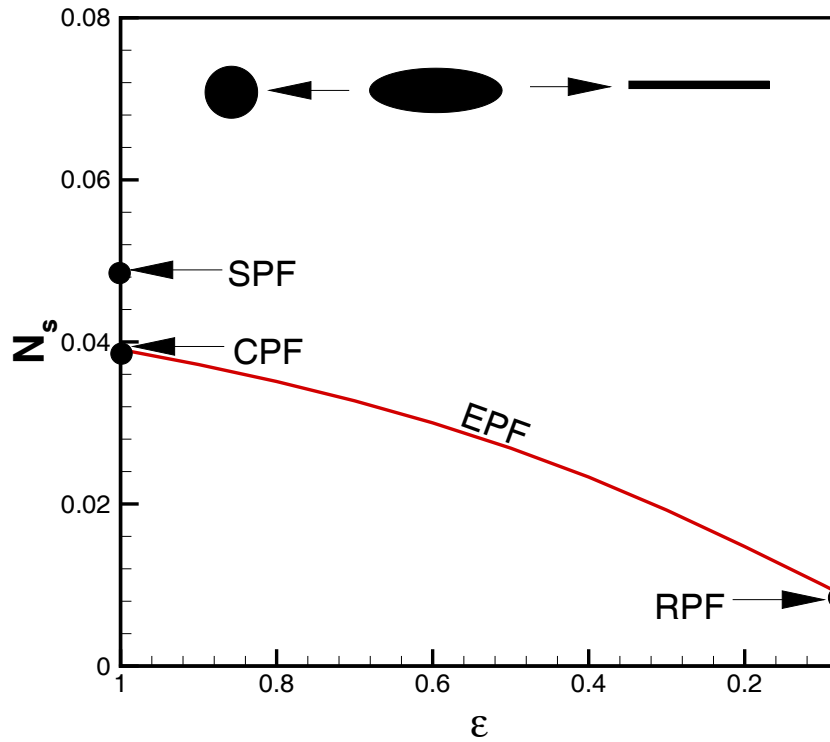


Figure 7.4: Effect of Axis Ratio on Dimensionless Entropy Generation Rate

The effect of the perimeter on the dimensionless total entropy generation rate is shown in Fig. 7.7. It is clear that the square geometry is again the worst choice from the point of view of entropy generation rate for the entire range of perimeters. The optimum dimensionless entropy generation rate $(N_s)_{opt}$ decreases with the increase in perimeter from SPF to RPF.

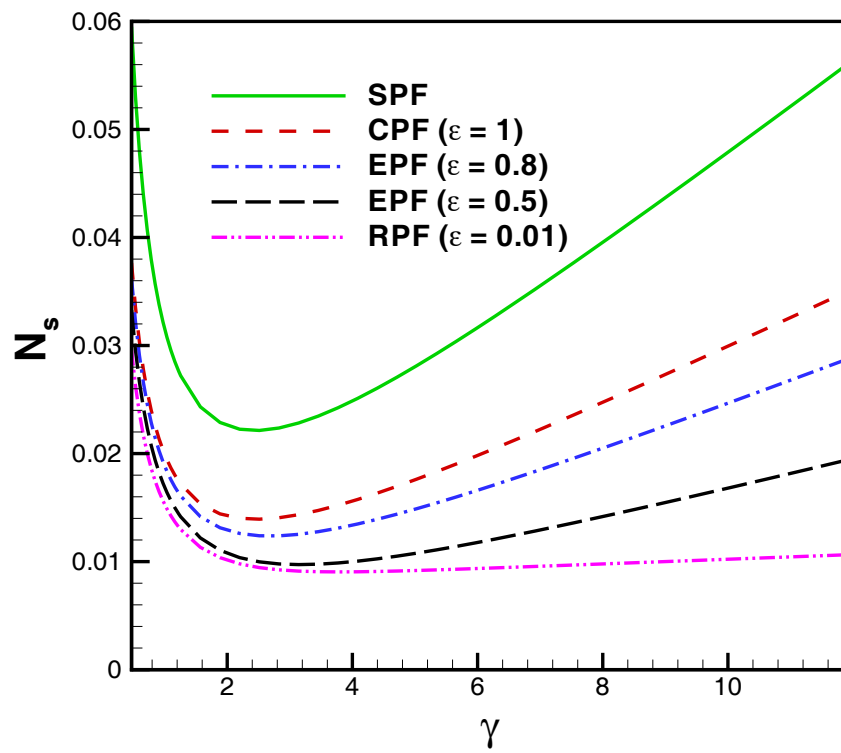


Figure 7.5: Effect of Aspect Ratio on Dimensionless Entropy Generation Rate

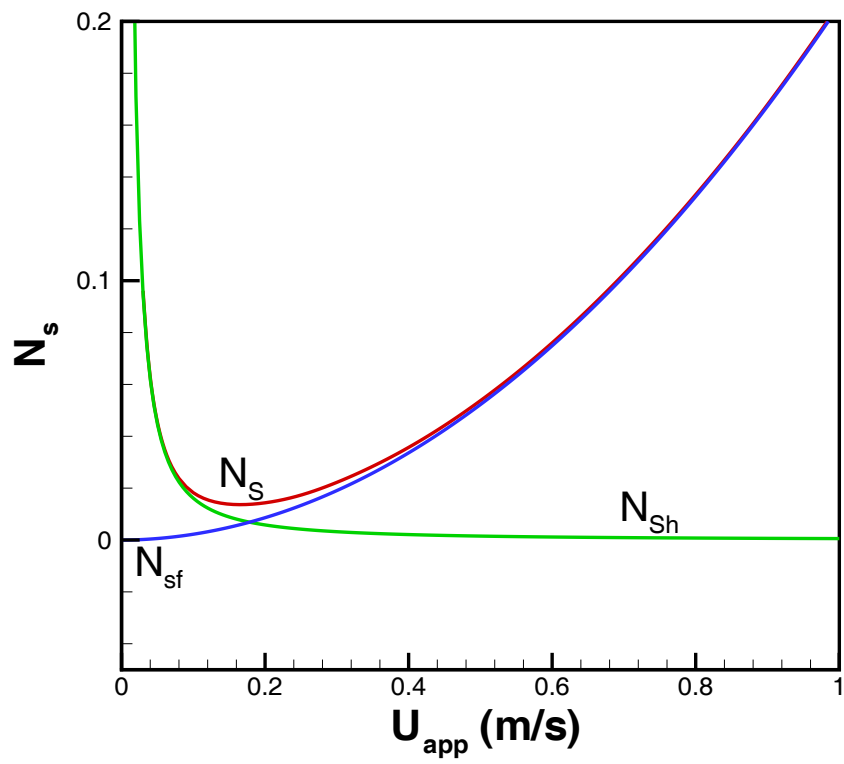


Figure 7.6: Effect of Approach Velocity on Heat Transfer and Friction Irreversibilities

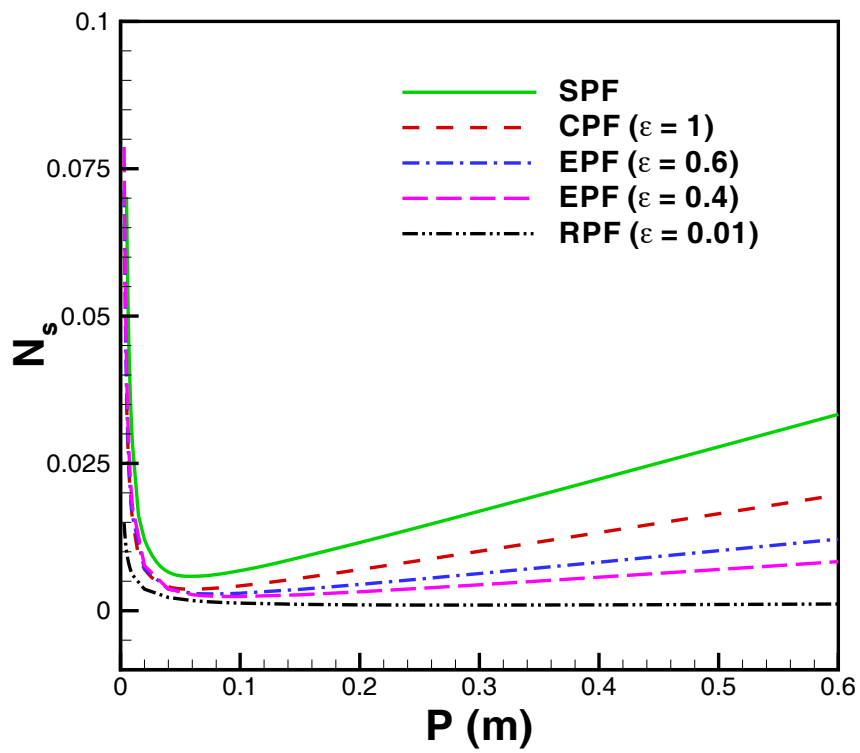


Figure 7.7: Effect of Perimeter on Dimensionless Entropy Generation Rate

Table 7.2: Quantities Used to Determine Performance of Pin-Fin Geometry

Quantity	Dimension
Perimeter (m)	0.015
Height (m)	0.05
Approach Velocity (m/s)	1
Thermal Conductivity of Solid ($W/m \cdot K$)	237
Thermal Conductivity of Air ($W/m \cdot K$)	0.026
Density of Air (kg/m^3)	1.1614
Specific Heat of Air ($J/kg \cdot K$)	1007
Kinematic Viscosity (m^2/s)	1.58×10^{-5}
Prandtl Number (Air)	0.71
Heat Load (W)	10
Ambient Temperature ($^{\circ}C$)	27

Pin-Fin Heat Sinks

For optimization, the objective is to select the “best” heat sink to fit the 25.4×25.4 mm foot print but not to exceed a maximum overall height of 12 mm. The maximum height restriction is selected to represent a typical board pitch found in communications systems. It is also assumed that a total heat dissipation of 10 W is applied at the center of the baseplate which has a uniform thickness of 2 mm (Fig. 7.8). The area of the source is 50% of the total area of the baseplate. The ambient temperature is fixed at 27°C and the problem is solved for the two extreme thermal conductivities 25 and $400 \text{ W/m}\cdot\text{K}$ (enhanced plastics and copper including pure aluminum with $k = 237 \text{ W/m}\cdot\text{K}$).

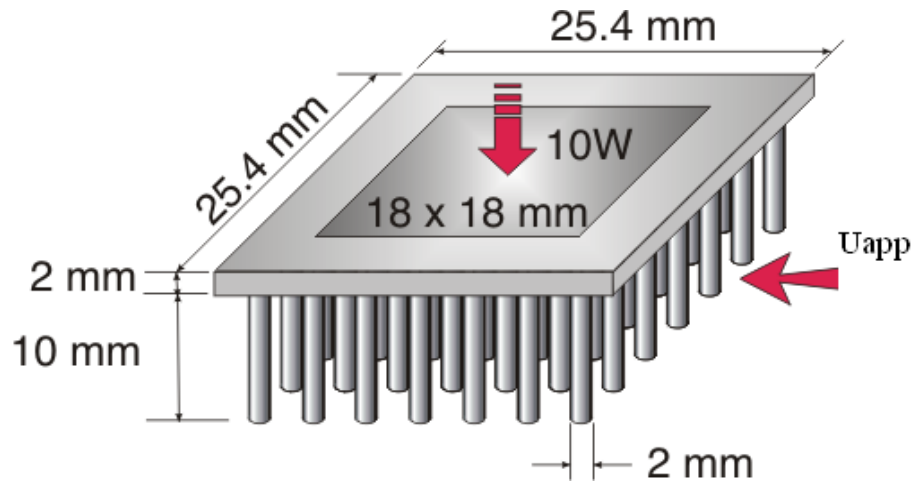


Figure 7.8: Selected Pin-Fin Heat Sink for Optimization

Parametric variations include the pin diameter, D , pin height, H , approach velocity, U_{app} , and the total number of pins, N . Using the same dimensions as given in the previous chapter (Table 6.3) as the default dimensions, three cases are examined by determining the dimensionless entropy generation rate N_s that leads to overall optimized performance where both heat transfer and viscous effects are considered.

In the first case, each variable is optimized for the selected materials (plastics, alu-

minum, and copper). Figures 7.9 -7.12 show the variation of dimensionless entropy generation rate for each design variable for in-line pin-fin heat sinks. The effect of pin diameter on the dimensionless entropy generation rate N_s for the three materials is shown in Fig. 7.9.

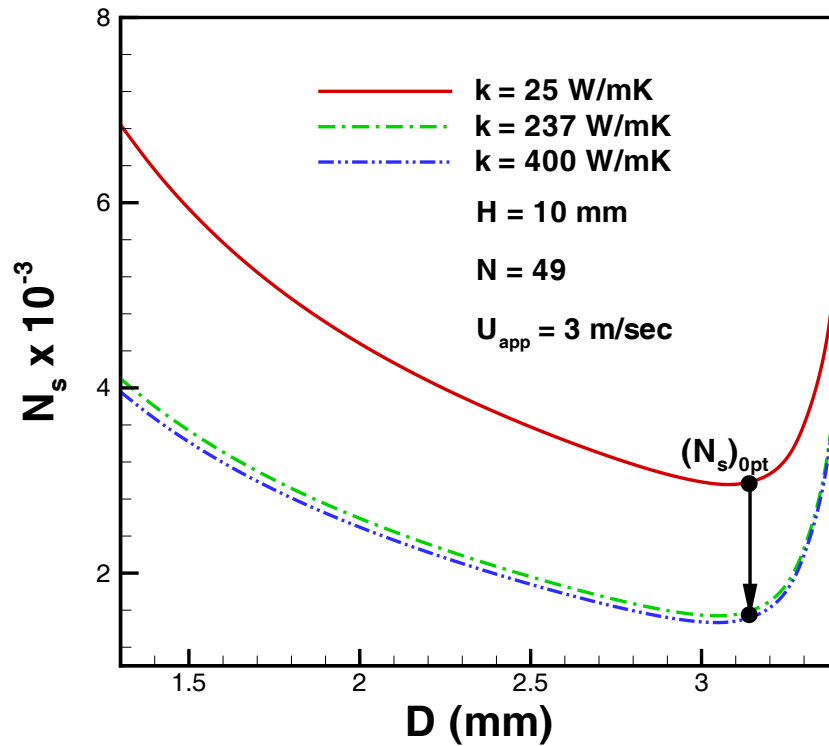


Figure 7.9: Effect of Pin Diameter on Dimensionless Entropy Generation Rate

The optimum dimensionless entropy generation rate moves down as the thermal conductivity of the material increases. Under the same operating conditions, the copper fin gives the best performance. If weight of the heat sink is a constraint, then aluminum fin would be preferable. However, the optimum diameter for all the three cases is the almost the same. Figure 7.10 shows that N_s decreases upto the optimum point and then increases with the pin height. The optimum N_s decreases with the increase in the thermal

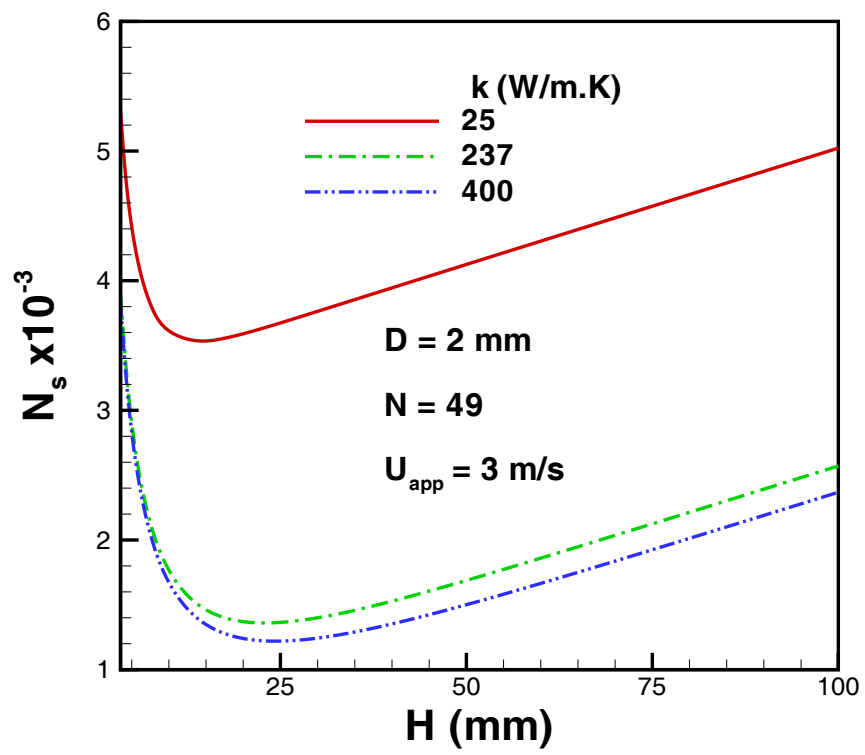


Figure 7.10: Effect of Pin Height on Dimensionless Entropy Generation Rate

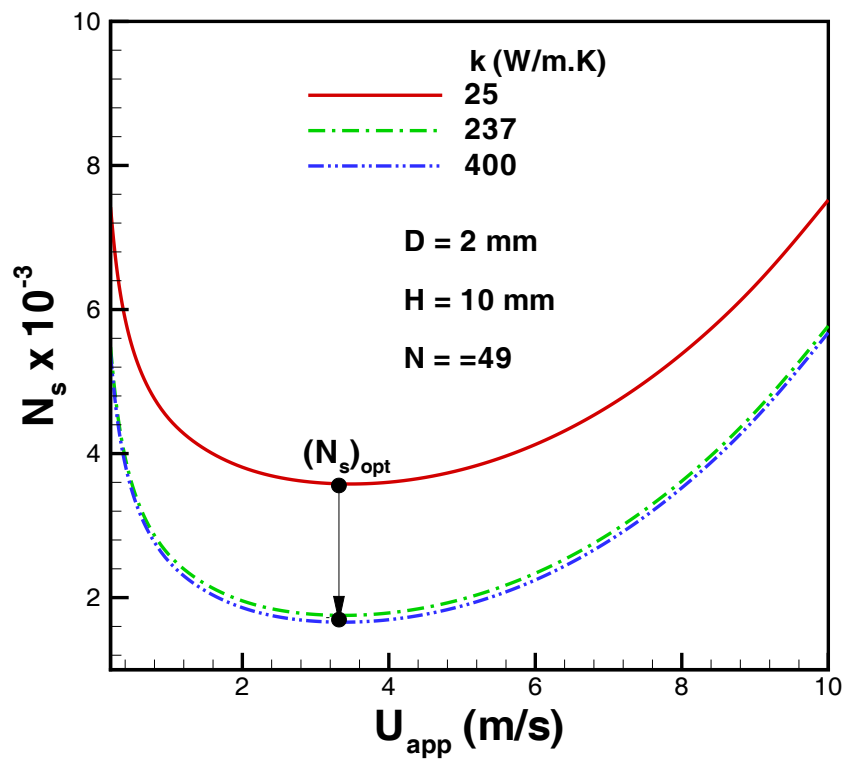


Figure 7.11: Effect of Approach Velocity on Dimensionless Entropy Generation Rate

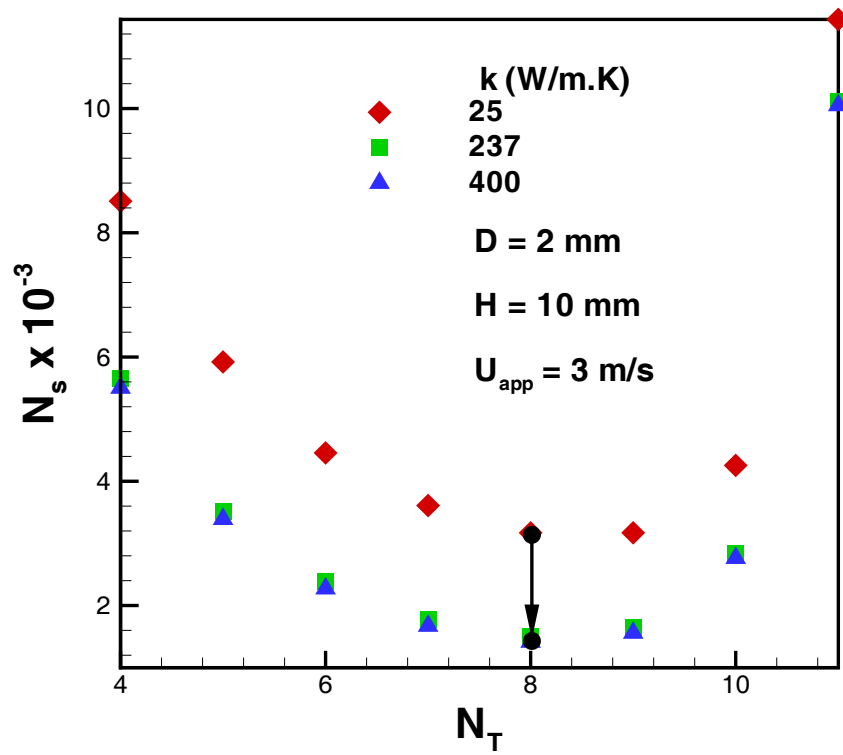


Figure 7.12: Effect of Number of Pins on Dimensionless Entropy Generation Rate

conductivity of the material. In this case the pin diameter, pin density and the approach velocity are kept constant. The optimum pin height also increases with the thermal conductivity of the material. The variation of N_s with optimum approach velocity U_{app} for each material is shown in Fig. 7.11. The optimum N_s moves down again with thermal conductivity of the material which shows the best performance of copper fins for the same approach velocity. It also shows that the optimum approach velocity is the same for all materials under the same operating conditions. Figure 7.12 shows the effects of the number of pins on the dimensionless entropy generation rate for the selected materials. For each material, the same optimum number of pins exist, however the entropy generation rate decreases with the increase in thermal conductivity for the same number of pins and under the same conditions.

Table 7.3: Dimensions Used to Determine Performance of Heat Sinks

Quantity	Dimension
Footprint (mm^2)	25.4×25.4
Source Dimensions (mm^2)	18.0×18.0
Baseplate Thickness (mm)	2
Pin Diameter (mm)	2
Overall Height of Heat Sink(mm)	12
Number of Pins (In-Line)	7×7
Number of Pins (Staggered)	8×6
Approach Velocity (m/s)	1
Thermal Conductivity of Solid ($W/m \cdot K$)	237
Thermal Conductivity of Air ($W/m \cdot K$)	0.026
Density of Air (kg/m^3)	1.1614
Specific Heat of Air ($J/kg \cdot K$)	1007
Kinematic Viscosity (m^2/s)	1.58×10^{-5}
Prandtl Number (Air)	0.71
Heat Load (W)	10
Ambient Temperature ($^{\circ}C$)	27

The second case was a multivariable optimization where two design variables were allowed to be free. Due to the same behavior of dimensionless entropy generation rate for both in-line and staggered arrangements, selected in this study, only the results for the in-line pin-fin heat sinks are shown in Figs. 7.13 - 7.21. Figure 7.13 shows the variation of dimensionless entropy generation rate corresponding to approach velocity and different pin diameters. The optimum approach velocity can be determined for each pin diameter.

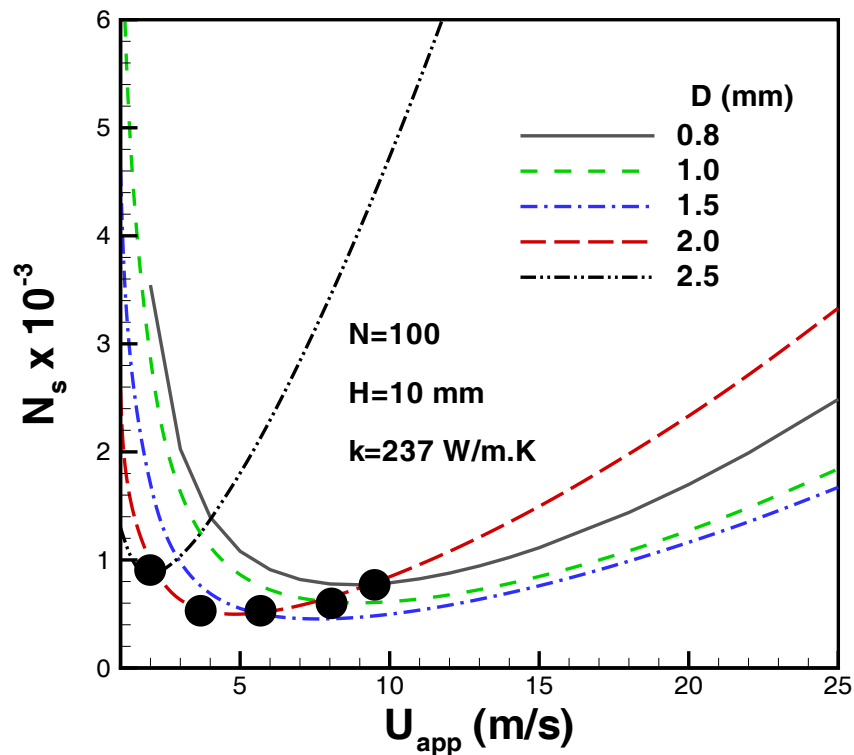


Figure 7.13: Dimensionless Entropy Generation Rate as Function of Pin Diameter and Approach Velocity

It is clear that the optimum N_s first decreases and then increases with the decrease in the approach velocity under the same conditions. It shows that the optimum pin diameter can be determined corresponding to the optimum approach velocity for the

same conditions. In Fig. 7.14, the N_s is plotted versus number of transverse rows for different pin diameters. Again the optimum N_s first decreases and then increases with the decrease in the N_T under the same conditions, showing the optimum pin diameter corresponding to the optimum N_T . The variation of dimensionless entropy generation rate with Re_D for characteristic values of the so called duty parameter B is shown in Fig. 7.15. It can be seen that the optimum Reynolds number increases with the decrease in B . Figure 7.16 shows that the optimum aspect ratio decreases with the increase in Reynolds number. It means that more slender pins will be required for high Reynolds number. The dependence of dimensionless entropy generation rate on the aspect ratio is also shown in Fig. 7.17 for different materials. As the thermal conductivity of the material increases, the optimum aspect ratio of the fin decreases which shows that more slender pin will be required for copper fin than a composite plastic fin.

Figure 7.18 shows the effect of pin diameter and number of pins on the entropy generation rate. The optimum diameter exists for each number of pins which decreases with the increase in the number of pins. It shows that high pin density is the best choice with reference to the lowest entropy generation rate. The optimum height corresponding to each pin diameter is shown in Fig. 7.19. It is clear that the entropy generation rate decreases with the height and then increases, again showing the optimum height corresponding to optimum diameter for the given conditions. Figure 7.20 shows the variation of entropy generation rate with the approach velocity and pin height. For low profile heat sinks, the entropy generation rate is highest corresponding to a approach velocity. The optimum approach velocity decreases with the increase in pin height. The variation in N_s versus number of pins is shown in Fig. 7.21 for three different approach velocities. As expected, the optimum entropy generation rate decreases with the increase in approach velocity.

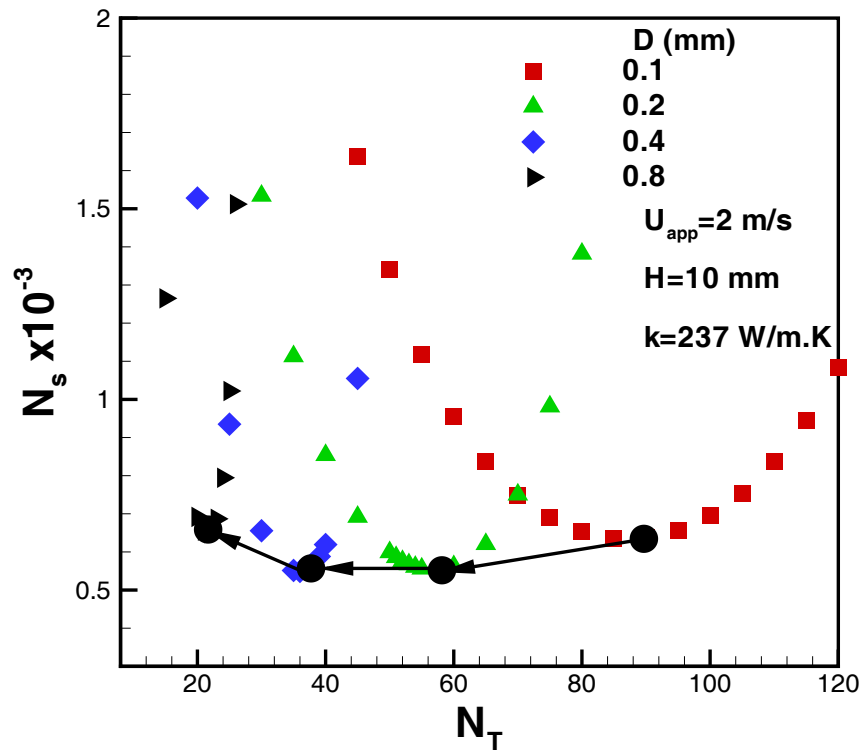


Figure 7.14: Dimensionless Entropy Generation Rate as Function of Pin Diameter and Number of Pins in Transverse Direction

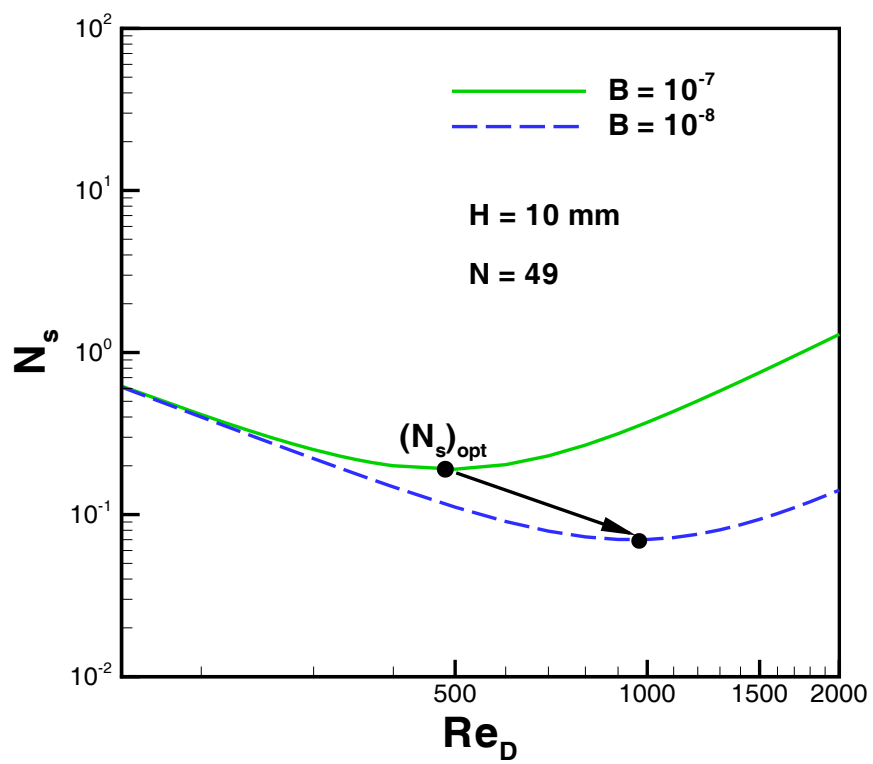


Figure 7.15: Dimensionless Entropy Generation Rate as Function of Reynolds Number

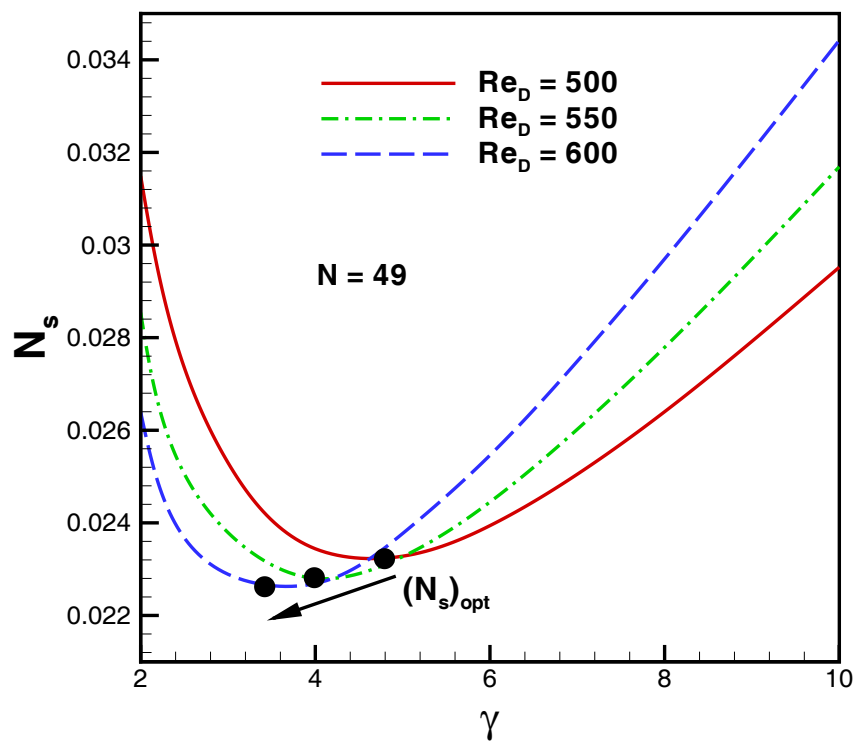


Figure 7.16: Dimensionless Entropy Generation Rate as Function of Aspect Ratio and Reynolds Number

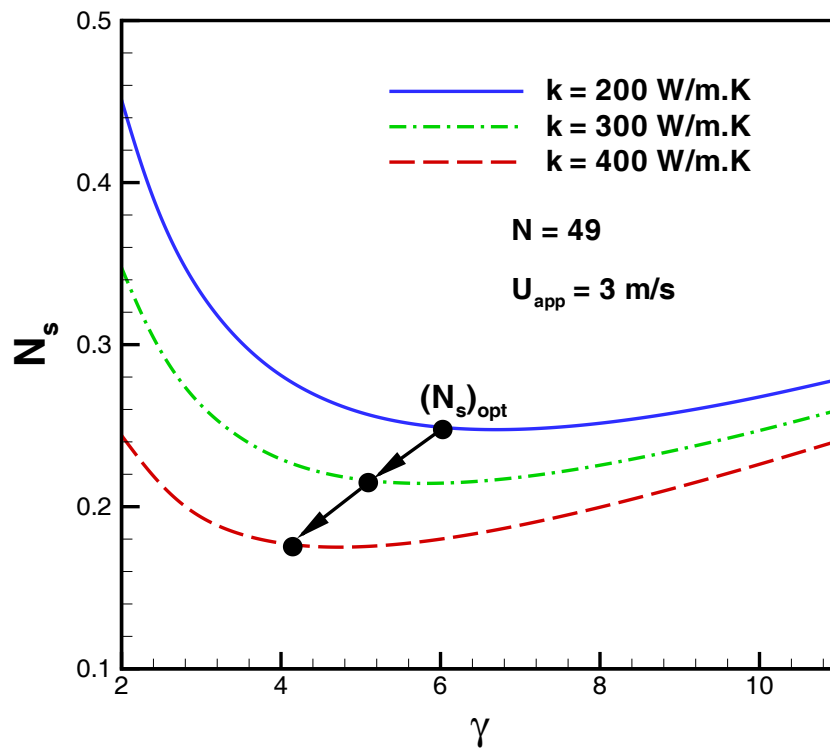


Figure 7.17: Dimensionless Entropy Generation Rate as Function of Aspect Ratio and Thermal Conductivity of Material

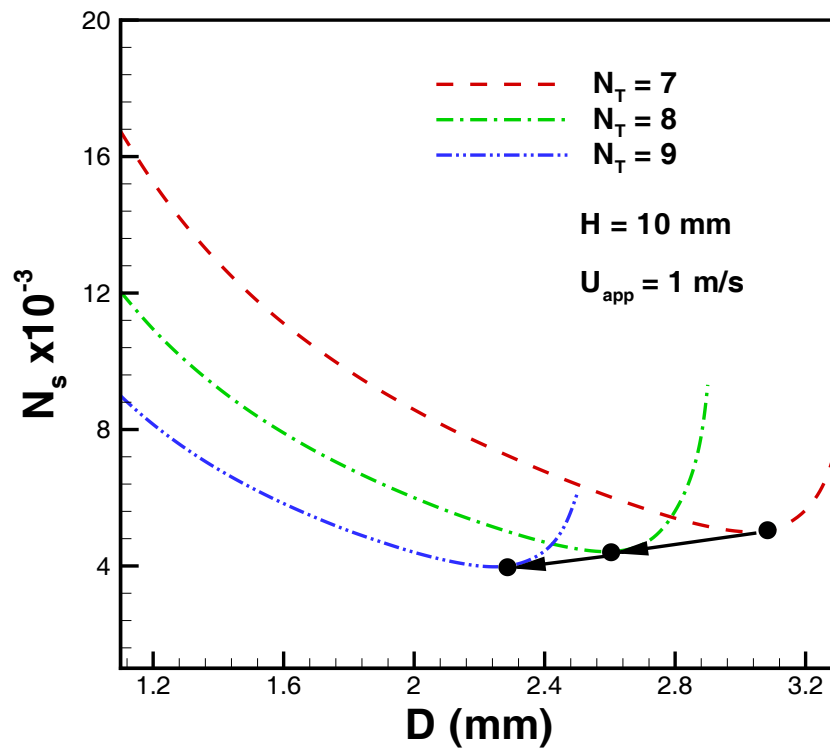


Figure 7.18: Effect of Pin Diameter and Number of Pins on Dimensionless Entropy Generation Rate

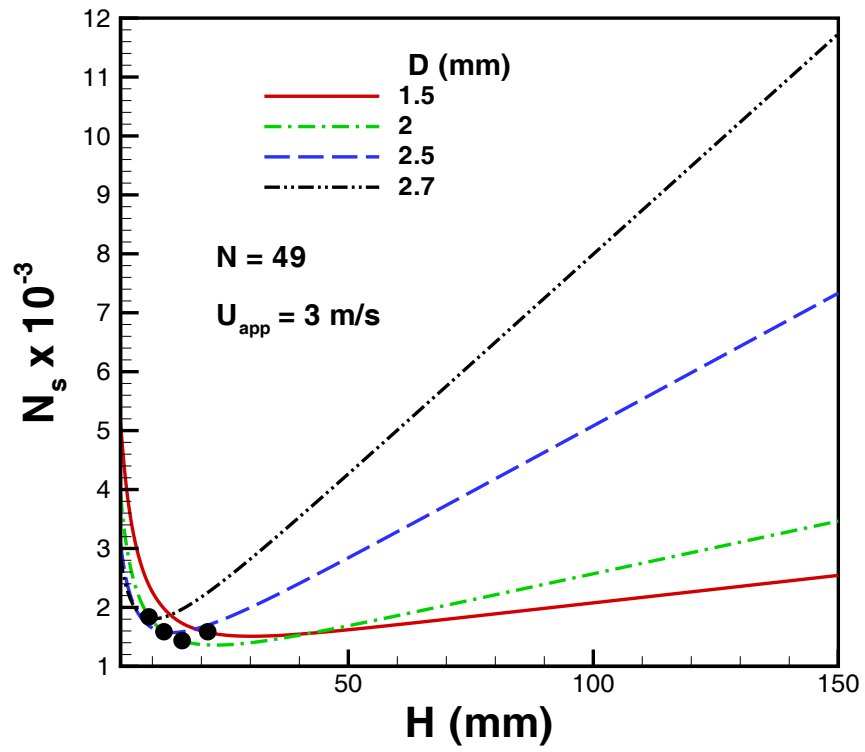


Figure 7.19: Effect of Pin Height and Diameter on Dimensionless Entropy Generation Rate

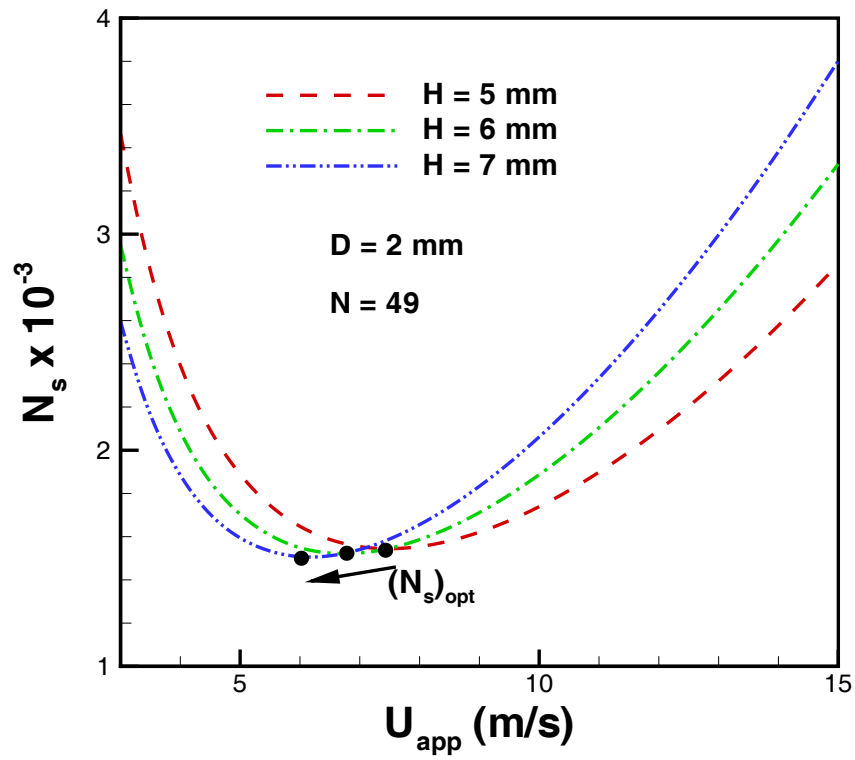


Figure 7.20: Effect of Approach Velocity and Pin Height on Dimensionless Entropy Generation Rate

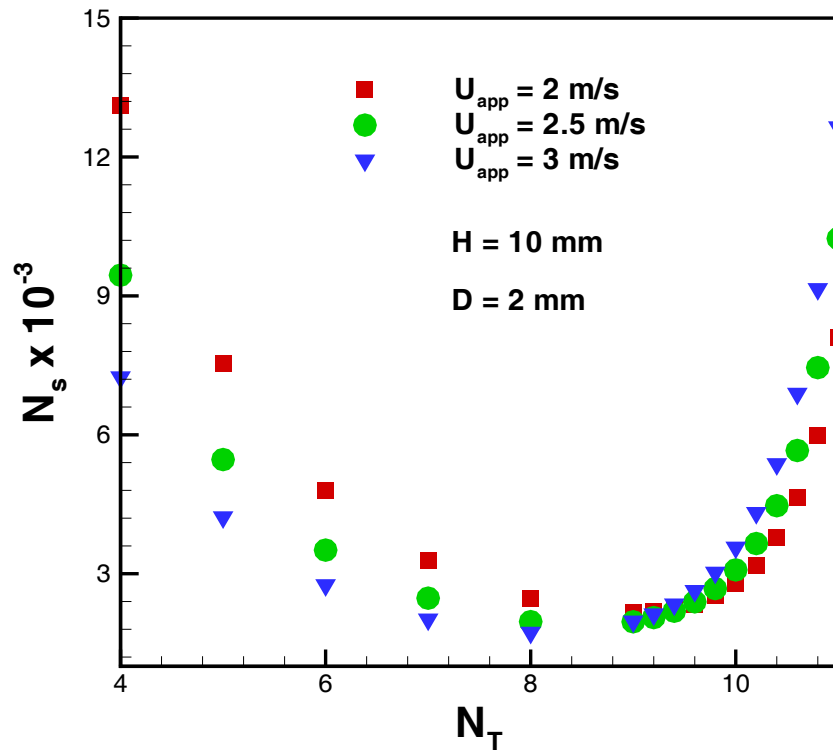


Figure 7.21: Effect of Approach Velocity and Number of Pins on Dimensionless Entropy Generation Rate

The comparisons of the results of optimization for the in-line and staggered arrangements are depicted in Figs. 7.22 - 7.25. Figure 7.22 shows the optimum diameter for both arrangements. It is clear that the staggered arrangement gives the lowest entropy generation rate. The smaller pins are preferred in staggered arrangement than in-line. The in-line arrangement requires higher pin height than staggered one. This is shown in Fig. 7.23, where the results are compared for both arrangements under the same conditions. The optimum approach velocity for both arrangements is shown in Fig. 7.24 for the same conditions. It is clear that the optimum approach velocity is higher for in-line arrangement for almost the same number of pins. Figure 7.25 gives the optimum number of pins for both arrangements. For the same approach velocity and same aspect ratio, same number of pins are required in both arrangements for overall better performance.

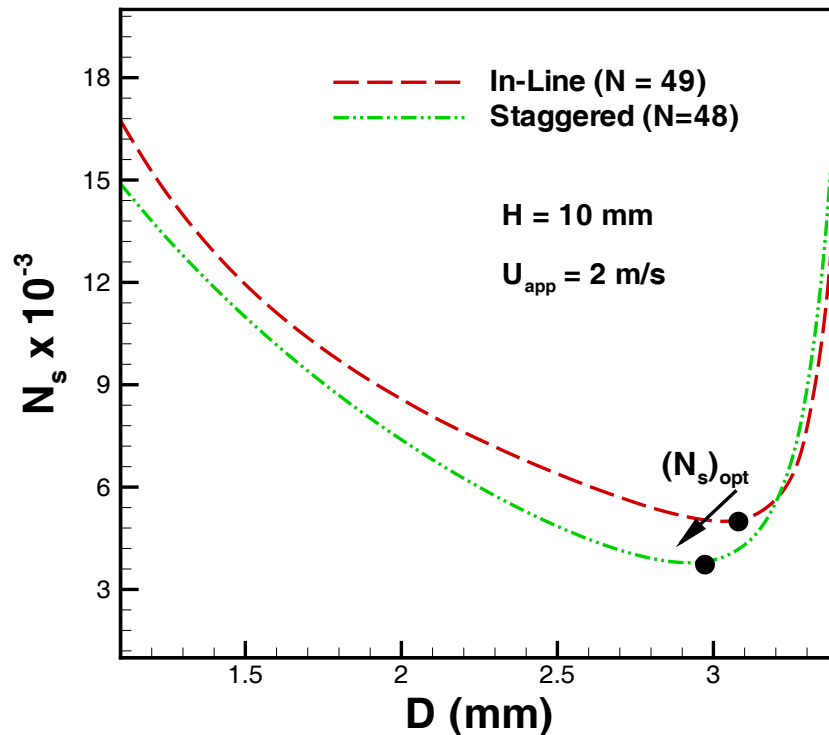


Figure 7.22: Comparison of In-Line and Staggered Arrangements for Optimum Diameter

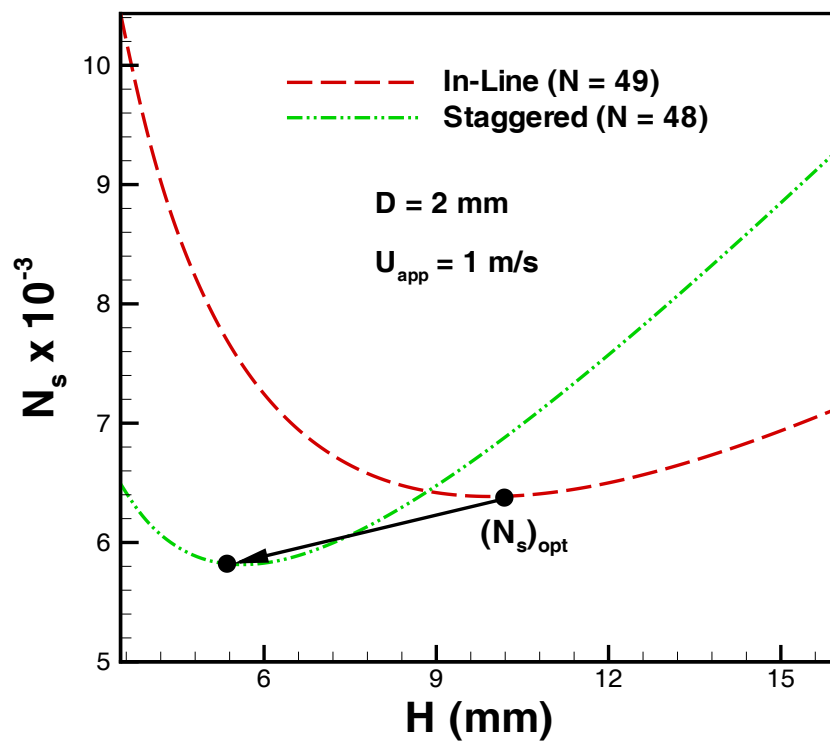


Figure 7.23: Comparison of In-Line and Staggered Both Arrangements for Optimum Height

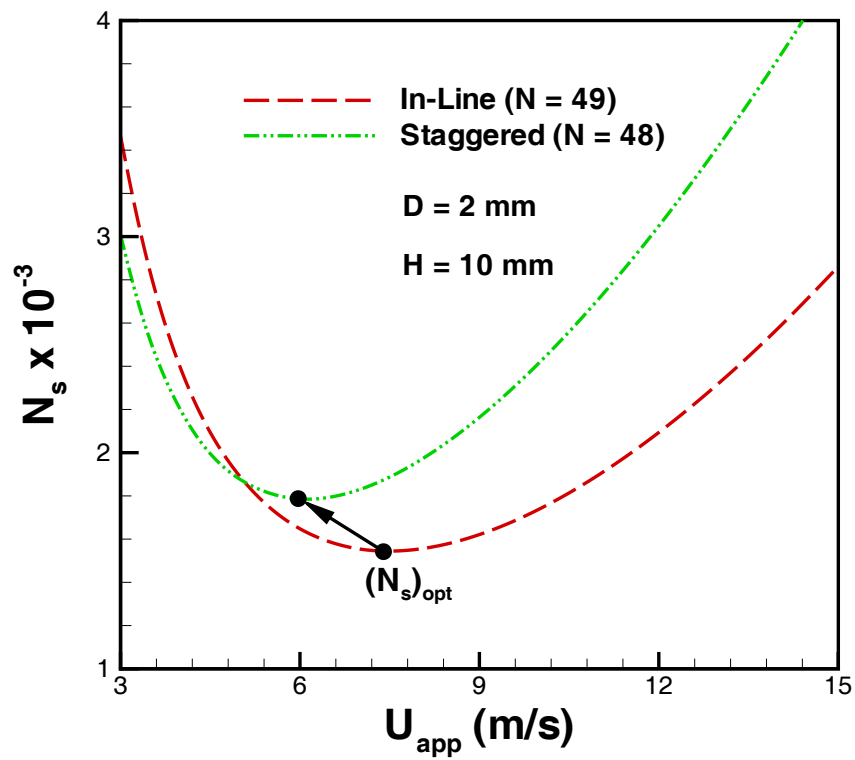


Figure 7.24: Comparison of In-Line and Staggered Arrangements for Optimum Approach Velocity

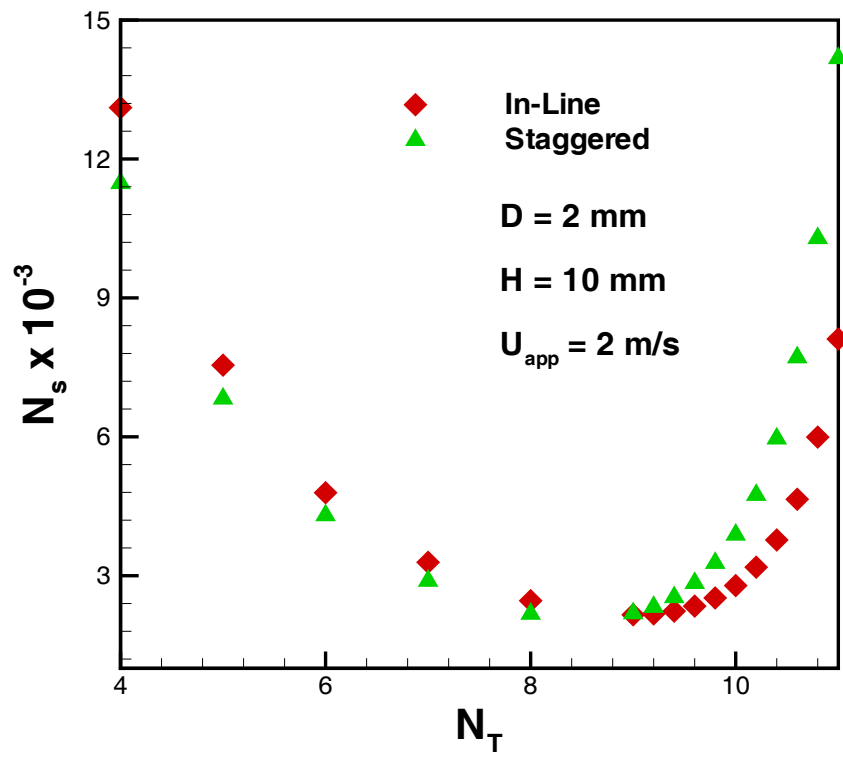


Figure 7.25: Comparison of In-Line and Staggered Arrangements for Optimum Number of Pins

The problem is then re-analyzed as multivariable optimization with three design variables D , U_{app} , and H as the free variables. These results are shown in Table 7.4 and 7.5 for in-line and staggered arrangements. It is clear that for the same material, R_{hs} and N_s are lower for high pin density in both arrangements. However, pressure drop is higher in each case. In each arrangement, high thermal conductivity with high pin density gives the best overall performance. It can be seen that of both arrangements, staggered arrangement gives the highest performance when the thermal conductivity as well as the pin density is high. The main disadvantage of in-line arrangement is that it requires higher approach velocity than the staggered arrangement.

Table 7.4: Results For Optimization of Three Parameters for In-Line Arrangement

k W/mK	N	Optimized Design Variables			Performance Criteria		
		D mm	U_{app} m/s	H mm	N_s $\times 10^{-3}$	R_{hs} $^{\circ}K/W$	ΔP Pa
25	6×6	2.0	4.0	7.0	1.87	2.56	60.1
	9×9	1.0	4.0	6.0	1.56	2.12	73.1
237	6×6	2.0	4.0	10.0	0.74	1.81	39.2
	9×9	1.0	4.0	7.0	0.61	1.60	57.71
400	6×6	2.0	4.0	10.0	0.60	1.77	38.5
	9×9	1.0	3.7	8.0	0.49	1.44	49.3

In Table 7.6, the results of optimization of four parameters are shown for both arrangements. Again, for the same material, R_{hs} and N_s are lower for high pin density in both arrangements, and pressure drop is higher in each case.

Table 7.5: Results For Optimization of Three Parameters for Staggered Arrangement

k W/mK	N	Optimized Design Variables			Performance Criteria		
		D mm	U_{app} m/s	H mm	N_s $\times 10^{-3}$	R_{hs} $^{\circ}K/W$	ΔP Pa
25	7×5	3.0	3.33	6.0	1.43	2.62	89.4
	10×8	2.0	2.51	6.0	1.19	1.97	97.6
237	7×5	3.0	2.4	10.0	0.64	1.65	49.16
	10×8	2.0	1.92	9.0	0.48	1.24	58.54
400	7×5	3.0	2.4	10.0	0.59	1.62	48.77
	10×8	2.0	1.77	10.0	0.36	1.12	50.88

Table 7.6: Results For Optimization of Four Parameters

In-Line Arrangement

k	Optimized Design Variables				N_s	R_{hs}	ΔP
W/mK	D (mm)	H (mm)	U (m/s)	$N_T \times N_L$	$\times 10^{-3}$	$^{\circ}K/W$	Pa
25	1.0	6.0	4.0	9×9	2.0	2.08	75.0
237	1.0	6.0	3.4	11×11	1.0	1.27	60.8

Staggered Arrangement

k	Optimized Design Variables				N_s	R_{hs}	ΔP
W/mK	D (mm)	H (mm)	U (m/s)	$N_T \times N_L$	$\times 10^{-3}$	$^{\circ}K/W$	Pa
25	2.0	6.0	2.75	8×8	2.0	2.21	125.5
237	1.0	8.0	1.54	12×12	0.92	0.94	76.95

7.3.2 Sensitivity Analysis

Objective Function

It can be seen in Figs. 7.9 - 7.12 that the objective function, dimensionless entropy generation rate, N_s is changing for each of the selected material. Also, if the design variables pin diameter D , pin height H , pin density N , and the approach velocity U_{app} are considered as the parameters, then from Figs. 7.19 - 7.23 it can be concluded that the objective function depends on these parameters as well as on the type of arrangement. It shows that the objective function is sensitive to each parameter as well as to the type of arrangement and the relation $\partial f/\partial p_0 \neq 0$ is true for each parameter and arrangement.

Location of Optimum

Figures 7.9 - 7.12 show that the location of the optimum points $D(\text{opt})$, $H(\text{opt})$, $U_{app}(\text{opt})$, $N_T(\text{opt})$ does not depend on the thermal conductivity of the material k , which is the main parameter in this study. The optimum values of the design variables are the same for each material. Thus $\partial x_i/\partial p_0 = 0$ for each design variable.

7.4 Summary

Different fin geometries having the same wetted surface area are compared from the point of view of entropy generation rate. Optimum dimensionless entropy generation rate exists for each geometry corresponding to approach velocity, perimeter, and the aspect ratio. No optimum dimensionless entropy generation rate exists for the axis ratio of the elliptical geometry when the approach velocity is taken as the parameter or vice versa. The square geometry is found to be the worst choice. Whereas, the circular geometry appears as the best from the point of view of the dimensionless total entropy generation rate for low

approach velocities and small perimeters. The plate fin gives the best results from the point of view of total entropy generation rate for higher approach velocities and large surface areas. The elliptical geometry is the next most favorable geometry from the point of view of total entropy generation rate for higher approach velocities and with low axis ratios. It offers higher heat transfer coefficients and lower drag force as the axis ratio is decreased and the approach velocity is increased. The elliptical geometry could perform better than circular geometry at medium approach velocities for larger surface areas and flat plate could outperform elliptical geometry at higher approach velocities for the same areas with high aspect ratios. However, for small surface areas and low velocities, flat plates are not a good selection from the point of view of entropy generation rate.

Parametric optimization is presented for determining optimum heat sink conditions given the simultaneous consideration of both heat transfer and viscous dissipation. The effects of pin diameter, approach velocity, pin density, pin height, and thermal conductivity of the material are examined with respect to their role in influencing optimum design conditions and the overall performance of the heat sink. It is demonstrated that the entropy generation rate is higher for in-line arrangement in all cases and it decreases with the increase in thermal conductivity of the material. While the heat sinks with high thermal conductivity and high pin density are superior to other heat sinks, a low conductivity heat sink also provides a viable alternative to those heat sinks.

It is shown that the objective function is sensitive to each parameter as well as to the type of arrangement, whereas the location of the design variables is not sensitive to the thermal conductivity of the material.

Chapter 8

Summary and Conclusions

A research study has been performed to develop models of fluid flow and heat transfer for the optimization of pin-fin heat sinks. The goals of the work were four fold: to develop analytical forced convection models capable of predicting fluid flow and heat transfer from single pins (circular and elliptical) and pin-fin arrays; to conduct a simplified heat sink analysis and determine heat sink performance; to develop an entropy generation minimization (EGM) model for the optimization of pin-fin heat sinks; and to conduct numerical validation using a CFD and heat transfer software package ICEPAK.

The first part of the study, modeling of fluid flow and heat transfer, was achieved in four steps. In each step, an integral approach of the boundary layer analysis was employed. The Von Karman-Pohlhausen method was used to solve the momentum integral equation, whereas the energy integral equation was solved for both isothermal and isoflux boundary conditions. A fourth order velocity profile in the hydrodynamic boundary layer and a third order temperature profile in the thermal boundary layer were used to study fluid flow and heat transfer characteristics.

In the first two steps, three general closed form correlations, one for drag coefficient and two for the heat transfer from circular and elliptical pins with isothermal and isoflux thermal boundary conditions, were developed. It was observed that the drag coefficients

were lower whereas the average heat transfer coefficients were higher for elliptical pins. The effects of the axis ratio of the elliptical cylinder upon drag and the average heat transfer coefficients were also observed and compared for the two extremes (circular cylinder and flat plate) with experimental/numerical values obtained from the open literature. It was found that the drag and the average heat transfer coefficients depend upon the Reynolds number as well as the axis ratio. In the third step, the effects of blockage on the fluid flow and heat transfer from a circular cylinder were investigated, and again three correlations were developed, one for the total drag coefficient, and two for the heat transfer under both isothermal and isoflux thermal boundary conditions. It was observed that the drag and the heat transfer coefficients decreased with the decrease in blockage ratio and finally, for zero blockage, they approached the values for an infinite circular cylinder. Both results showed good agreement with the experimental/numerical results for a wide range of laminar flow, Prandtl numbers, and for every possible blockage and axis ratios. In the last step, the closed form correlations for the drag and heat transfer coefficients were developed for the pin-fin arrays. The mean velocity in the minimum free cross section of the control volume was used as a reference velocity in the calculations of fluid flow and heat transfer for both types of arrangements. The potential flow velocity outside the boundary layer was obtained by using complex variable theory for both arrangements. It was found that the drag and heat transfer coefficients depend on the Reynolds number, longitudinal and transverse pitches. It was shown that the lower pitches give higher friction factors (or pressure drop) and heat transfer but as the pitches increase, both values approach a circular pin in an infinite medium. Furthermore, the staggered arrangement gives higher pressure drop and heat transfer rates than the in-line arrangement.

The second goal was achieved by analyzing the performance of a heat sink in terms of total thermal and hydraulic resistances. Fully developed heat and fluid flow were assumed in the analysis, and the thermophysical properties were taken to be temperature independent. It was observed that the thermal resistance decreases whereas pressure drop

increases for each design variable. This inverse relationship between thermal resistance and pressure drop with respect to each design variable provides an optimized condition where entropy is minimized with respect to that particular variable. It was shown that the average heat transfer coefficients, for the same material, were found to be lower in the in-line arrangement. The air temperature at the exit T_0 was found to be higher for low profile heat sinks in both arrangements. No appreciable effect of pin arrangements on T_0 could be found for the given height. Furthermore, smaller diameter pin-fins with low approach velocities give better performance for the staggered arrangement than for the in-line arrangement. The effect of thermal conductivity was also observed in both arrangements.

The third goal of this thesis was achieved by optimizing a pin-fin geometry and a pin-fin heat sink using an entropy generation minimization approach. For convenience, this part was divided into two sections. In the first section, the combined effect of the thermal resistance and the drag force (i.e. entropy generation rate) on overall thermal/fluid performance associated with different fin geometries, including, rectangular plate-fins as well as square, circular and elliptical pin-fins was examined. It was shown that an optimum dimensionless entropy generation rate exists for each geometry corresponding to approach velocity, wetted surface area, and the aspect ratio. No optimum dimensionless entropy generation rate could be found for the axis ratio of the elliptical geometry when the approach velocity was taken as the parameter or vice versa. The square geometry was found to be the worst from the point of view of the total entropy generation rate. Whereas, the circular geometry appears as the best from the point of view of the dimensionless total entropy generation rate for low approach velocities and small wetted surface areas. The optimization of a pin-fin heat sink was performed in the second section, where parametric optimization was presented for determining optimum heat sink conditions given the simultaneous consideration of both heat transfer and viscous dissipation. The effects of pin diameter, approach velocity, pin density, pin height, and thermal conductivity of the material were examined with respect to their role in influencing optimum design

conditions and the overall performance of the heat sink. It was demonstrated that the entropy generation rate is higher for in-line arrangement in all cases and it decreases with increase in thermal conductivity of the material. While the heat sinks with high thermal conductivity and high pin density are superior to other heat sinks, a low conductivity heat sink also provides a viable alternative to those heat sinks.

This work is the first of its kind to develop analytical models of fluid flow and heat transfer for the optimization of pin-fin heat sinks. A number of issues remain which need to be improved, particularly the assumed constant approach velocity. Ordinarily, the approach velocity, is a result of the balance between the fan capacity and the system pressure loss, and is not known a priori. However, once the model is developed, the approach velocity can be varied to produce the pressure drop versus flow velocity relationship for a given system which, in turn, can be used in conjunction with a particular fan curve to determine the operating condition of the system.

The second major unresolved issue involves the separation region. The heat transfer coefficients for single pins and pin-fin arrays were determined up to the separation point only, due to its analytical definition, which gives the pressure gradient values up to the separation point. That was acceptable for low Reynolds numbers (≤ 40000) but for high Reynolds numbers, the accuracy of heat transfer coefficients could be improved by conducting a separate analysis in the separation region.

The third major issue was about the constant thermophysical properties of fluid. Some fluids, like engine oil and transformer oil, show a great change in viscosity and Prandtl numbers for a small change in temperature. It is therefore, recommended that the effects of thermophysical properties on the average heat transfer coefficients should be investigated.

The heat transfer coefficients, for each geometry, were verified for incompressible and Newtonian fluids having $Pr \geq 0.7$. It is recommended that the work should be extended to compressible and/or non-Newtonian fluids used in many industries: petrochemical,

pharmaceutical, biochemical, and food. In order to get a more indepth understanding of the analysis and its associated approximations, the applicability of the method should be verified at various Prandtl numbers and extend to liquid metals having very low Prandtl numbers (≤ 0.01) which are used in the field of nuclear power.

References

1. Achenbach, E., "Total and Local Heat Transfer From a Smooth Circular Cylinder in Cross Flow at High Reynolds Number," *International Journal of Heat and Mass Transfer*, Vol. 18, pp. 1387-1396, 1975.
2. Aiba, S. and Yamazaki, Y., "An Experimental Investigation of Heat Transfer Around a Tube in a Bank," *ASME Journal of Heat Transfer*, Vol. 98, pp. 503-508, 1976.
3. Aiba, S., Ota, T., and Tsuchida, H., "Heat Transfer Tubes Closely Spaced in In-Line Bank," *International Journal of Heat and Mass Transfer*, Vol. 23, pp. 311-319, 1980.
4. Aiba, S., Tsuchida, H., and Ota, T., "Heat Transfer Around a Tube in a Bank," *Bulletin of the JSME*, Vol. 24, No.188, pp. 380-387, 1981.
5. Aiba, S., Tsuchida, H., and Ota, T., "Heat Transfer Around Tubes in In-Line Tube Banks," *Bulletin of the JSME*, Vol. 25, No.204, pp. 919-926, 1982.
6. Aiba, S., Tsuchida, H., and Ota, T., "Heat Transfer Around Tubes in Staggered Tube Banks," *Bulletin of the JSME*, Vol. 25, No.204, pp. 927-933, 1982.
7. Aiba, S., "Heat Transfer Around a Tube in In-Line Tube Banks Near a Plane Wall," *ASME Journal of Heat Transfer*, Vol. 112, pp. 933-938, 1990.
8. Akilba'yev, Zh. S., Isata'yev, S. I., Krashtalev, P. A., and Masle'yeva, N. V., "The Effect of Channel Blockage on the Local Heat Transfer Coefficient of a Uniformly Heated Cylinder," In *Problemy Teploenergetyki i Prikladnoi Teplofiziki*, Vol. 3, pp. 179-198, 1966.
9. Antonetti, V. W., Whittle, T. D., and Simons, R. E., "An Approximate Thermal Contact Conductance Correlation," *HTD-Vol. 170, Experimental/Numerical Heat Transfer in Combustion and Phase Change*, pp. 35-42, 1991.

10. Antonetti, V. W. and Yovanovich, M. M., "Thermal Contact Resistance in Micro-electronic Equipment," Thermal Management Concepts in Microelectronic Packaging from Component to System, ISHM Technical Monograph Series 6984-003, pp. 135-151, 1984.
11. Azar, K. and Mandrone, C. D., "Effect of Pin Fin Density of the Thermal Performance of Unshrouded Pin Fin Heat Sinks," ASME Journal of Electronic Packaging, Vol. 116, pp. 306-309, 1994.
12. Armstrong, J. and Winstanley, D., "A Review of Staggered Array Pin Fin Heat Transfer for Turbine Cooling Applications," ASME Journal of Turbomachinery, Vol. 110, pp. 94-103, 1988.
13. Babus'Haq, R. F., Akintunde, K. and Probert, S. D., "Thermal Performance of a Pin-Fin Assembly," Int. J. of Heat and Fluid Flow, Vol. 16, No. 1, pp. 50-55, 1995.
14. Bahrami, M., Culham, J. R., and Yovanovich, M. M., "Thermal Resistances of Gaseous Gap for Conforming Rough Contacts," AIAA Paper N0. 2004-0821, 42nd AIAA Aerospace Meeting and Exhibit, Jan 5-8, Reno, Nevada, 2004.
15. Bahrami, M., Culham, J. R., and Yovanovich, M. M., "A Scale Analysis Approach to Thermal Contact Resistance," Paper N0. IMECHE 2003-44283, ASME International Mechanical Engineering Congress and RDD Expo, November 16-21, Washington D. C., 2003.
16. Beale, S. B. and Spalding, D. B., "Numerical Study of Fluid Flow and Heat Transfer in Tube Banks With Stream-Wise Periodic Boundary Conditions," Transactions of the CSME, Vol. 22, No. 4A, pp. 397-416, 1998.
17. Beale, S. B. and Spalding, D. B., "A Numerical Study of Unsteady Fluid Flow in In-Line and Staggered Tube Banks," Journal of Fluids and Structures, Vol. 13, pp. 723-754, 1999.
18. Beale, S. B., "Fluid Flow and Heat Transfer in Tube Banks," Ph. D. Thesis, Imperial College, London, 1992.
19. Bejan, A., "Entropy Generation Minimization," CRC Press, New York, 1996.
20. Bejan, A. and Morega, A. M., "Optimal Arrays of Pin Fins and Plate Fins in Laminar Forced Convection," ASME Journal of Heat Transfer, Vol. 115, pp. 75-81, 1993.
21. Bejan, A., "The Optimal Spacing for Cylinders in Crossflow Forced Convection," ASME Journal of Heat Transfer, Vol. 117, pp. 767-770, 1995.

22. Bergelin, O. P., Davis, E. S., and Hull, H. L., "A Study of Three Tube Arrangements in Unbaffled Tubular Heat Exchangers," ASME Journal of Heat Transfer, Vol. 71, pp. 369-374, 1949.
23. Bergelin, O. P., Brown, G. A., Hull, H. L., and Sullivan, F. W., "Heat Transfer and Fluid Friction During Flow Across Banks of Tubes - III: A Study of Tube Spacing and Tube Size," ASME Journal of Heat Transfer, Vol. 72, pp. 881-888, 1950.
24. Bergelin, O. P., Brown, G. A., and Doberstein, S. C., "Heat Transfer and Fluid Friction During Flow Across Banks of Tubes - IV: A Study of the Transition Zone Between Viscous and Turbulent Flow," ASME Journal of Heat Transfer, Vol. 74, pp. 953-959, 1952.
25. Chang, P. K., "Separation of Flow," Pergamon Press, New York, 1970.
26. Chilton, T. H. and Genereaux, R. P., "Pressure Drop Across Tube Banks," Transactions of the American Institute of Chemical Engineers, Vol. 29, pp. 161-173, 1933.
27. Chun, W. and Boehm, R. F., "Calculation of Forced Flow and Heat Transfer Around a Cylinder in Cross Flow," Numerical Heat Transfer, Vol. 15, pp. 101-122, 1989.
28. Churchill, S. W., and Bernstein, M., "A Correlating Equation for Forced Convection from Gases and Liquids to a Circular Cylinder in Crossflow," ASME Journal of Heat Transfer, Vol. 99, No. 2, pp. 300-306, 1977.
29. Churchill, S. W., "Viscous Flows: The Practical Use of Theory," Butterworths Series in Chemical Engineering, London, 1988.
30. Colburn, A. P., "A Method of Correlating Forced Convection Heat Transfer Data And a Comparison With Fluid Friction," Transactions of the American Institute of Chemical Engineers, Vol. 29, pp. 174-210, 1933.
31. Culham, R. J. and Muzychka, Y. S., "Optimization of Plate Fin Heat Sinks Using Entropy Generation Minimization," IEEE Transactions on Components and Packaging Technologies, Vol. 24, No. 2, pp. 159-165, 2001.
32. Culham, R. J., Khan, W. A., Yovanovich, M. M., and Muzychka, Y. S., "The Influence of Material Properties And Spreading Resistance in the Thermal Design of Plate Fin Heat Sinks," Proceedings of NHTC'01, 35th National Heat Transfer Conference, June 10-12, Anaheim, California, pp. 240-246, 2001.
33. D'Alessio, S. J. D. and Dennis, S. C. R., "A Method of Domain Decomposition for Calculating the Steady Flow Past a Cylinder," Journal of Engineering Mathematics, Vol. 28, pp. 227-240, 1994a.

34. D'Allesio, S. J. D. and Dennis, S. C. R., "A Vorticity Model for Viscous Flow Past a Cylinder," *Computers and Fluids*, Vol. 23, pp. 279-293, 1994b.
35. D'Allesio, S. J. D. and Dennis, S. C. R., "Steady Laminar Forced Convection From an Elliptic Cylinder," *Journal of Engineering Mathematics*, Vol. 29, pp. 181-193, 1995.
36. D'Allesio, S. J. D., "Steady, Unsteady and Linear Stability of Flow Past an Elliptic Cylinder," *Canadian Applied Mathematics Quarterly*, Vol. 4, pp. 341-379, 1996.
37. Dennis, S. C. R. and Chang, G. Z., "Numerical Solutions for Steady Flow Past a Circular Cylinder at Reynolds Numbers Up to 100," *Journal of Fluid Mechanics*, Vol. 42, pp. 471, 1970.
38. Dennis, S. C. R. and Dunwoody J., "The Steady Flow of a Viscous Fluid Past a Flat Plate," *Journal of Fluid Mechanics*, Vol. 24, Part 3, pp. 577-595, 1966.
39. Dhaubhadel, M. N., Reddy, J. N., and Telionis, D. P., "Finite Element Analysis of Fluid Flow and Heat Transfer for Staggered Banks of Cylinders in Cross Flow," *International Journal for Numerical Methods in Fluids*, Vol. 7, pp. 1325-1342, 1987.
40. Drake, R. M., Sauer, F. M., and Schaaf, S. A., "Forced Convection Heat Transfer from Cylinders and Spheres in a Rarefied Gas," Technical Report No. HE-150-74 NACA, University of California, Institute of Engineering Research, Berkeley California, 1950.
41. Dvinsky, A., Bar-Cohen, A. and Strelets, M., "Thermofluid Analysis of Staggered and In-line Pin Fin Heat Sinks," *The Seventh Inter Society Conference on Thermal Phenomena*, Las Vegas, Nevada, USA, May 23 - 26, Vol. 1, pp. 157-164, 2000.
42. Dyban, E. P. and Epick, E. Ya., "Some Heat Transfer Features in the Air Flows of Intensified Turbulence," *Proceedings of 4th Heat Transfer Conference*, F. C. 5.7, Part 2, Paris-Versailles, 1970.
43. Eckert, E. R. G., "Die Berechnung des Wärmeüberganges in der laminaren Grenzschicht umströmter Körper," *VDI-Forschungsheft*, Vol. 416, pp. 1-26, 1942.
44. Eckert, E. R. G. and Soehngen, E., "Distribution of Heat-Transfer Coefficients Around Circular Cylinders in Crossflow at Reynolds Numbers from 20 to 500," *ASME Journal of Heat Transfer*, Vol. 74, pp. 343-347, 1952.
45. Edgar, T. F. and Himmelblau, D. M., "Optimization of Chemical Processes," McGraw-Hill Book Company, New York, 1988.

46. Flachsbart, O., "Winddruck auf Gasbehälter," Reports of the AVA in Göttingen, IVth Series, pp. 461-469, 1932.
47. Fujii, M. and Fujii, T., "A Numerical Analysis of Laminar Flow and Heat Transfer of Air in an In-Line Tube Bank," Numerical Heat Transfer, Vol. 7, pp. 89-102, 1984.
48. Gerrard, J., "The Three-Dimensional Structure of the Wake of a Circular Cylinder," Journal of Fluid Mechanics, Vol. 25, No. 1, pp. 60-81, 1966.
49. Giedt, W. H., "Investigation of Variation of Point Unit Heat-Transfer Coefficient Around a Cylinder Normal to an Air Stream," ASME Journal of Heat Transfer, Vol. 71, pp. 375-381, 1949.
50. Goldstein, S., Modern Developments in Fluid Dynamics, Vol. 2, Dover, New York, 1965.
51. Gram, A. J., Mackey, C. O., and Monroe, E. S., "Convection Heat Transfer and Pressure Drop of Air Flowing Across In-Line Tube Banks: Part II - Correlation of Data for Ten-Row-Deep Tube Banks," Transactions of ASME, Vol. 80, pp. 25-35, 1958.
52. Grimison, E. D., "Correlation and Utilization of New Data on Flow Resistance and Heat Transfer for Cross Flow of Gases over Tube Banks," Transactions of ASME, Vol. 59, pp. 583-594, 1937.
53. Gunter, A. Y. and Shaw, W. A., "A General Correlation of Friction Factors for Various Types of Surfaces in Crossflow," Transactions of ASME, Vol. 67, pp. 643-660, 1945.
54. Hattori, N. and Takahashi, T., "Heat Transfer from a Single Row of Circular Cylinders Placed in the Transverse Direction of Water Flow," Transactions of the Japan Society of Mechanical Engineers, Part B, Vol. 59, No. 568, pp. 4064-4068, 1993.
55. Hausen, H., "Heat Transfer in Counterflow, Parallel Flow and Cross Flow," McGraw-Hill, Inc, New York, 1983.
56. Hiemenz, K., "Die Grenzschicht an einem in den gleichförmigen Flüssigkeitsstrom eingetauchten geraden Kreiszyylinder," Dingler's Polytech J., Vol. 326, P. 326, 1911.
57. Hilpert, R., "Wärmeabgabe von geheizten Drahten und Röhren," Forsch. Geb. Ingenieurwes, Vol. 4, pp. 215-224, 1933.
58. Holstein, H. and Bohlen, T., "Ein einfaches Verfahren zur Berechnung Laminaren Reibungsschichten," die dem Nahenungsansatz von K. Pohlhausen genügen, Lilenthal Bericht 510, p. 5, 1950.

59. Hoge, E. C., "Experimental Investigation of Effects of Equipment Size on Convection Heat Transfer and Flow Resistance in Cross Flow of Gases Over Tube Banks" Transactions of ASME, Vol. 59, pp. 573-581, 1937.
60. Incropera, F. P., "Liquid Cooling of Electronic Devices By Single-Phase Convection," John Wiley & Sons, Inc., New York, 1999.
61. Incropera, F. P. and DeWitt, D. P., "Introduction to Heat Transfer," John Wiley & Sons, Inc., New York, 2000.
62. Jakob, M., "Heat Transfer and Flow Resistance in Cross Flow of Gases Over Tube Banks," ASME Journal of Heat Transfer, Vol. 60, pp. 384-386, 1938.
63. Jackson, C. P., "A Finite-Element Study of the Onset of Vortex Shedding in Flow Past Various Shaped Bodies," Journal of Fluid Mechanics, Vol. 182, pp. 23-45, 1987.
64. Janour, Z., "Resistance of a Plate in Parallel Flow at Low Reynolds Number," NACA TM No. 1316, 1951.
65. Jones, C. E. and Monroe, E. S., "Convection Heat Transfer and Pressure Drop of Air Flowing Across In-Line Tube Banks: Part I - Apparatus, Procedures, and Special Effects," ASME Journal of Heat Transfer, Vol. 80, pp. 18-24, 1958.
66. Jubran, B. A., Hamdan, M. A., and Abdullah, R. M., "Enhanced Heat Transfer, Missing Pin, and Optimization for Cylindrical Pin Fin Arrays," ASME Journal of Heat Transfer, Vol. 115, pp. 576-583, 1993.
67. Jung, H. H. and Maveety, J. G., "Pin Fin Heat Sink Modeling and Characterization," Sixteenth IEEE Semi-Therm Symposium, San Jose, CA USA, March 21 -23, pp. 260-265, 2000.
68. Kakac, S., Shah, R. K., and Aung, W., "Handbook of Single-Phase Convective Heat Transfer," John Wiley and Sons, New York, 1987.
69. Kays, W. M. and London, A. L., "Compact Heat Exchangers," McGraw Hill, New York, 1964.
70. Kestin, J. and Wood, R. T., "The Influence of Turbulence on Mass Transfer from Cylinders," Advances in Heat Transfer, Vol. 3, Academic Press, New York, pp. 1-32, 1971.
71. Khan, W. A., Culham, J. R., and Yovanovich, M. M., "Fluid Flow and Heat Transfer from a Pin-Fin: Analytical Approach," Paper No. AIAA 2003-163, 41st Aerospace Sciences Meeting and Exhibit, Reno, Nevada, January 2003.

72. Knudsen, J. G. and Katz, D. L., "Fluid Dynamics and Heat Transfer," McGraw-Hill Book Company, Inc., New York, 1958.
73. Kochin, N. E., Kibel, I. A., and Roze, N. V., Theoretical Hydromechanics, Interscience Publishers (translated from the 5th Russian Edition), 1964.
74. Kondjoyan, A. and Daudin, J. D., "Effects of Free Stream Turbulence Intensity on Heat and Mass Transfers at the Surface of a Circular Cylinder and an Elliptical Cylinder, Axis Ratio 4," International Journal of Heat and Mass Transfer, Vol. 38, No. 10, pp. 1735-1749, 1995.
75. Kondo, Y., Matsushima, H. and Komatsu, T., "Optimization of Pin-Fin Heat Sinks for Impingement Cooling of Electronic Packages," J. of Electronic Packaging, Vol. 122, September, pp. 240-246, 2000.
76. Kostic, Z. G. and Oka, S. N., "Fluid Flow and Heat Transfer with Two Cylinders in Cross Flow," Int. J. Heat Mass Transfer, Vol. 15, No. 2, pp. 279-299, 1978.
77. Krall, K. M. and Eckert, E. R. G., "Local Heat Transfer Around a Cylinder at Low Reynolds Number," ASME Journal of Heat Transfer, Vol. 95, No. 2, pp. 273-275, 1973.
78. Krall, K. M. and Eckert, E. R. G., "Heat Transfer to a Transverse Circular Cylinder at Low Reynolds Number Including Refraction Effects," Heat Transfer, Vol. 3, pp. 225-232, 1970.
79. Kuo, Y. H., "On the Flow of an Incompressible Viscous Fluid Past a Flat Plate at Moderate Reynolds Numbers," Journal of Mathematical Physics, Vol. 32, pp. 83-101, 1953.
80. Larson, E. D. and Sparrow, E. M., "Performance Comparisons Among Geometrically Different Pin-Fin Arrays Situated in an Oncoming Longitudinal Flow," Int. J. Heat Mass Transfer, Vol. 25, No. 5, pp. 723-725, 1993.
81. Launder, B. E. and Massey, T. H., "The Numerical Prediction of Viscous Flow and Heat Transfer in Tube Banks," ASME Journal of Heat Transfer, Vol. 100, No. 4, pp. 565-571, 1978.
82. Li, Q., Chen, Z., Flechtner, U., and Warnecke, H. J., "Heat Transfer and Pressure Drop Characteristics in Rectangular Channels with Elliptical Pin Fins," International Journal of Heat and Fluid Flow, Vol. 19, pp. 245-250, 1998.
83. Lin, W. W. and Lee, D. J., "Second-Law Analysis on a Pin Fin Array Under Crossflow," Int. J. Heat Mass Transfer, Vol. 40, No. 8, pp. 1937-1945, 1997.

84. Mandhani, V. K., Chhaabra, R. P., and Eswaran, V., "Forced Convection Heat Transfer in Tube Banks in Cross Flow," *Chemical Engineering Science*, Vol. 57, pp. 379-391, 2002.
85. Maudgal, V. K., and Sunderland, J. E., "Forced Convection Heat Transfer from Staggered Pin Fin Arrays," 31st National Heat Transfer Conference, Vol. 7, Houston, Texas, August 3-6, pp. 35-44, 1996.
86. Merk, H. J., "Rapid Calculations for Boundary Layer Transfer Using Wedge Solutions and Asymptotic Expansions," *Journal of Fluid Mechanics*, Vol. 5, pp. 460-480, 1959.
87. Metzger, D. E., Berry, R. A., and Bronson, J. P., "Developing Heat Transfer in Rectangular Ducts With Staggered Arrays of Short Pin Fins," *ASME Journal of Heat Transfer*, Vol. 104, pp. 700-706, 1982a.
88. Metzger, D. E., Fan, Z. X., and Shepard, W. B., "Pressure Loss and Heat Transfer Through Multiple Rows of Short pin Fins," *Heat Transfer 1982*, Vol. 3, Grigull et al. Editors, Hemisphere, Washington, pp. 137-142, 1982b.
89. Metzger, D. E., Fan, C. S., and Haley, S. W., "Effects of Pin Shape and Array Orientation on Heat Transfer and Pressure Loss in Pin Fin Arrays," *ASME Journal of Heat Transfer*, Vol. 106, pp. 252-257, 1984.
90. Milne-Thomson, L. M., "Theoretical Hydrodynamics," Macmillan & C Ltd, London, 1968.
91. Minakami, K. and Iwasaki, H., "Heat-Transfer Characteristics of Pin-Fins with In-Line Arrangement," *Heat Transfer - Japanese Research*, Vol. 23, No. 3, pp. 213-228, 1994.
92. Modi, V. J., Wiland, E., and Dikshit, A. K., "On the Fluid Dynamics of Elliptic Cylinders," *International Journal of Offshore and Polar Engineering*, Vol. 2, No. 4, pp. 267-280, 1992.
93. Moores, K. A., Joshi, Y. K., and Schiroky, G. K., "Thermal Characterization of a Liquid Cooled AISiC Base Plate with Integral Pin Fins," *IEEE Transactions on Components and Packaging Technologies*, Vol. 24, No. 2, pp. 213-219, 2001.
94. Morgan, V. T., "The Overall Convective Heat Transfer from Smooth Circular Cylinders," *Advances in Heat Transfer*, Vol. 11, Academic Press, New York, pp. 199-264, 1975.
95. Murray, D., "Comparison of Heat Transfer in Staggered and In-Line Tube Banks With Gas Particle Flow," *Experimental Thermal and Fluid Science*, Vol. 6, No. 2, pp. 177-185, 1993.

96. Nieuwstadt, F. and Keller, H. B., "Viscous Flow Past Circular Cylinders," *Computational Fluids*, Vol. 1, pp. 59, 1973.
97. Niggeschmidt, W., "Druckverlust und Wärmeübergang bei fluchtenden, versetzten und teilversetzten querangestromten Rohrbündeln," Dissertation Darmstadt, 1975.
98. Norris, R. H. and Spofford, W. A., "High Performance Fins for Heat Transfer," *Transactions of ASME*, Vol. 64, pp. 489-496, 1942.
99. Omohundro, G. A., Bergelin, and Colburn, A. P., "Heat Transfer and Fluid Friction During Flow Across Banks of Tubes," *ASME Journal of Heat Transfer*, Vol. 71, pp. 27-34, 1949.
100. Oosthuizen, P. H. and Naylor, D., "An Introduction to Convective Heat Transfer Analysis," McGraw-Hill, New York, 1999.
101. Ota, T., Aiba, S., Tsuruta, T., and Kaga, M., "Forced Convection Heat Transfer from an Elliptic Cylinder," *Bulletin of the JSME*, Vol. 26, No. 212, pp. 262 - 267, 1983.
102. Ota, T., Nishiyama, H., and Taoka, Y., "Heat Transfer and Flow Around an Elliptic Cylinder," *International Journal of Heat and Mass Transfer*, Vol. 27, No. 10, pp. 1771 - 1779, 1984.
103. Perkins, H. C. and Leppert, G., "Local Heat Transfer Coefficients on a Uniformly Heated Cylinder," *International Journal of Heat and Mass Transfer*, Vol. 7, pp. 143-158, 1964.
104. Pierson, O. L., "Experimental Investigation of the Influence of Tube Arrangement on Convection Heat Transfer and Flow Resistance in Cross Flow of Gases Over Tube Banks," *Transactions of ASME*, Vol. 59, pp. 563-572, 1937.
105. Pohlhausen, K., "Zur Näherungsweise Integration der Differential Gleichung der Laminaeren Reibungsschicht," *Zeitschrift für angewandte Mathematic und Mechanic*, Vol. 1, pp. 252-268, 1921.
106. Poulikakos, A. and Bejan, A., "Fin Geometry for Minimum Entropy Generation in Forced Convection," *ASME Journal of Heat Transfer*, Vol. 104, pp. 616-623, 1982.
107. Raithby, G. D. and Hollands, K. G. T., "Handbook of Heat Transfer," 3rd Edition, Chapter 4, McGraw-Hill, New York, 1998.
108. Reklaitis, G. V., Ravindran, A., and Ragsdell, K. M., "Engineering Optimization," John Wiley & Sons, Inc., New York, 1983.

109. Refai-Ahmed, G. and Yovanovich, M. M., "Analytical Method for Forced Convection from Flat Plates, Circular Cylinders, and Spheres," *Journal of Thermophysics and Heat Transfer*, Vol. 9, No. 3, pp. 516-523, 1995.
110. Refai-Ahmed, G. and Yovanovich, M. M., "Experimental Study of Forced Convection from Isothermal Circular and Square Cylinders, and Toroids," *ASME Journal of Heat Transfer*, Vol. 119, February, pp. 70-79, 1997.
111. Reiher, H., "Handbuch der Experimentalphysik," 9-1, p. 312, 1925.
112. Rizzi, M. et al., "Experimental Investigation of Pin Fin Heat Sink Effectiveness," *Proceedings of ASME NHTC'01, 35th National Heat Transfer Conference*, Anaheim, California, June 10-12, 2001.
113. Roshko, A., "Experiments on the Flow Past Circular Cylinders at Very High Reynolds Number," *Journal of Fluid Mechanics*, Vol. 10, No. 3, pp. 345-356, 1961.
114. Sadik, K. and Yaman, Y., "Convective Heat Transfer," 2nd ed., CRC Press, Florida, 1995.
115. Sarma, T. S. and Sukhatme, S. P., "Local Heat Transfer from a Horizontal Cylinder to Air in Cross Flow: Influence of Free Convection and Free Stream Turbulence," *International Journal of Heat and Mass Transfer*, Vol. 20, pp. 51-56, 1977.
116. Savija, I., Culham, J. R., Yovanovich, M. M., and Marotta, E. E., "Review of Thermal Conductance Models for Joints Incorporating Enhancement Materials," *AIAA Paper No. 2002-0494, 40th AIAA Aerospace Meeting and Exhibit*, Jan 7-10, Reno, Nevada, 2002.
117. Schlichting, H. and Ulrich, A., "Zur Berechnung des Umschlages Laminar-Turbulent," *Jb. dt. Luftfahrtforschung I*, pp: 8-35, 1942.
118. Schlichting, H., "Boundary Layer Theory," 7th Edition., McGraw-Hill, New York, 1979.
119. Schönauer, W., "Ein Differenzenverfahren zur Lösung der Grenzschichtgleichung für stationäre, laminare, inkompressible Strömung," *Ing.-Arch.*, Vol. 33, p. 173, 1964.
120. Schubauer, G. B., "Air Flow in a Separating Laminar Boundary Layer," T. R. No. 527, N. A. C. A., 1934.
121. Schubauer, G. B., "Air Flow in the Boundary Layer of an Elliptic Cylinder," T. R. No. 652, N. A. C. A., 1939.

122. Shaukatullah, H., Storr, W. R., Hansen, B. J., and Gaynes, M. A., "Design and Optimization of Pin Fin Heat Sinks for Low Velocity Applications," *IEEE Transactions on Components Packaging and Manufacturing Technology - Part A*, 1996, Vol. 19, No. 4, pp. 486-495, 1996.
123. Shou Guang Yao and Zhu DeShu, "Modified Solution and Thermal Optimum Analysis of Pin Fin Extended Surface," *Energy and Environment*, pp. 427-433, 1996.
124. Sieder, E. N. and Scott, Jr., N. A., "Fluid Friction at Parallel and Right Angles to Tubes and Tube Banks," *ASME Unpublished Paper*, No. 83, 1932.
125. Smith, M. C. and Kuethe, A. M., "Effects of Turbulence on Laminar Skin Friction and Heat Transfer," *Physics of Fluids*, Vol. 9, No. 12, pp. 2337-2344, 1966.
126. Song, S., Lee, S., and Au, V., "Closed-Form Equation for Thermal Constriction/Spreading Resistances with Variable resistance Boundary Condition," *IEPS Conference*, Atlanta, GA, Sept. 25-28, pp. 111-121, 1994.
127. Sparrow, E. M. and Larson, E. D., "Heat Transfer from Pin-Fins Situated in an Oncoming Longitudinal Flow which Turns to Crossflow," *Int. J. Heat Mass Transfer*, Vol. 25, No. 5, pp. 603-614.
128. Stanescu, G., Fowler, A. J. and Bejan, A., "The Optimal Spacing of Cylinders in Free-Stream Crossflow Forced Convection," *Int. J. Heat Mass Transfer*, Vol. 39, No. 2, pp. 311-317, 1996.
129. Stoeker, W. F., "Design of Thermal Systems," McGraw Hill, New York, 1989.
130. Streeter, V. L., "Fluid Dynamics," McGraw-Hill Book Company, Inc., New York, 1948.
131. Sucker, D. and Brauer, H., "Investigation of the Flow Around Transverse Cylinders," *Wärme-und Stoffübertragung*, Vol. 8, pp. 149-158, 1975.
132. Suh, Y. B., Somasundaram, S. and , Anand, N. K. "Remarks on the Potential Cross Flow Over Tube Banks," *Journal of Applied Mechanics*, Vol. 56, pp. 476-479, 1989.
133. Takami, H. and Keller, H. B., "Steady Two-Dimensional Viscous Flow of an Incompressible Fluid Past a Circular Cylinder," *Physics of Fluids*, Vol. 12, Suppl. II, pp. 1-51, 1969.
134. Tahat, M. A., Kodah, Z. H., Jarrah, B. A. and Probert, S. D., "Heat Transfer from Pin-Fin Arrays Experiencing Forced Convection," *Applied Energy*, Vol. 67, pp. 419-442, 2000.

135. Tahat, M. A., Babus'Haq, R. F., and Probert, S. D., "Forced Steady-State Convections from Pin Fin Arrays," *Applied Energy*, Vol. 48, pp. 335-351, 1994.
136. Theoclitus, G., "Heat Transfer and Flow-Friction Characteristics of Nine Pin-Fin Surfaces," *ASME Journal of Heat Transfer*, Vol. 88, pp. 385-390, 1966.
137. Vaitiekūnas, P. P., and Bulota, A. J. "Analysis of the Effect of Duct Blocking on Crossflow and Heat Transfer of a Cylinder," *Heat Transfer - Soviet Research*, Vol. 17, No. 4, pp. 79-86, 1985.
138. Van Dyke, M., "Perturbation Methods in Fluid Mechanics," Academic Press, New York, pp. 121-146, 1964.
139. Van Dyke, M., "An Album of Fluid Motion," The Parabolic Press, Stanford, California, pp. 20, 28, 1982.
140. Vanfossen, G. J., "Heat Transfer Coefficients for Staggered Arrays of Short Pin Fins," *ASME Journal of Engineering for Power*, Vol. 104, pp. 268-274, 1982.
141. Venezian, E. and Sage, B. H., "Thermal Transfer from a Small Wire in the Boundary Flow About a Cylinder," *Int. J. Heat Mass Transfer*, Vol. 5, pp. 225-237, 1961.
142. Von Karman, T., "Über Laminar Und Turbulente Reibung," *Zeitschrift für angewandte Mathematic Und Mechanic*, Vol. 1, pp. 233-252, 1921.
143. Wallis, R. P. and White, C. M., "Resistance to Flow Through Nests of Tubes," *Transactions of ASME*, Vol. 59, pp. 583-594, 1938.
144. Walz, A., "Ein neuer Ansatz für das Greschwindigkeitsprofil der laminaren Reibungsschicht," *Lilienthal-Bericht* 141, p. 8, 1941.
145. Wang, W. and Sangani, A. S., "Nusselt Number for Flow Perpendicular to Arrays of Cylinders in the Limit of Small Reynolds and Large Peclet Numbers," *Physics of Fluids*, Vol. 9, No. 6, pp. 1529-1539, 1997.
146. Wieselsberger, C., "New Data on The Laws of Fluid Resistance," *NACA TN No.* 84, 1921.
147. Wilson, A. S. and Bassiouny, M. K., "Modeling of Heat Transfer for Flow acrosss Tube Banks," *Chemical Engineering and Processing*, Vol. 39, pp. 1-14, 2000.
- 13 Wirtz, R. A., Sohal, R., and Wang, H., "Thermal Performance of Pin-Fin Fan-Sink Assemblies," *J. of Electronic Packaging*, Vol. 119, March, pp. 26-31, 1997.
148. Wung, T. S. and Chen, C. J., "Finite Analytic Solution of Convective Heat Transfer For Tube Arrays in Crossflow: Part I - Flow Field Analysis," *ASME Journal of Heat Transfer*, Vol. 111, August, pp. 633-640, 1989.

149. Wung, T. S. and Chen, C. J., "Finite Analytic Solution of Convective Heat Transfer For Tube Arrays in Crossflow: Part II - Heat Transfer Analysis," ASME Journal of Heat Transfer, Vol. 111, August, pp. 641-648, 1989.
150. Yamamoto, H. and Hattori, N., "Flow and Heat Transfer Around a Single Row of Circular Cylinders," Heat Transfer - Japanese Research, Vol. 25, No. 3, pp. 192-200, 1996.
151. Yovanovich, M. M., "New Contact and Gap Conductance Correlations for Conforming Rough Surfaces," Paper No. AIAA-81-1164, 16th AIAA Thermophysics Conference, Palo, Alto, California, June 23-25, 1981.
152. Yovanovich, M. M., "Thermal Contact Correlations," Progress in Aeronautics and Aerodynamics: Spacecraft Radiative Transfer and Temperature Control, in Horton, T. E. (editor), Vol. 83, pp. 83-95, 1982.
153. Yovanovich, M. M., Culham, J. R., and Teertstra, P., "Calculating Interface Resistances," Electronics Cooling, May, 1997.
154. Yovanovich, M. M. and Teertstra, P., "Laminar Forced Convection From Isothermal Rectangular Plates From Small to Large Reynolds Numbers," 7th AIAA/ASME Joint Thermophysics and Heat Transfer Conference, Albuquerque, June 15-18, 1998.
155. Zapach, T., Newhouse, T., Taylor, J., and Thomasing, P., "Experimental Verification of a Model for the Optimization of Pin Fin Heat Sinks," The Seventh Inter Society Conference on Thermal Phenomena, Las Vegas, Nevada, USA, May 23 - 26, Vol. 1, pp. 63-69, 2000.
156. Žukauskas, A., "Heat Transfer from Tubes in Crossflow," Advances in Heat Transfer, Vol. 8, pp. 93-160, 1972.
157. Žukauskas, A. and Ulinskas, R., "Heat Transfer in Tube Banks in Crossflow," Hemisphere, Washington, DC, 1988.
158. Žukauskas, A. and Žiugžda, J., Heat Transfer of a Cylinder in Crossflow, Hemisphere Publishing Corporation, New York, 1985.

Appendix A

Equations of Motion

The equations of motion for the steady-state, forced convection of an incompressible Newtonian, constant property fluid can be written as:

$$\nabla \cdot \vec{V} = 0 \quad (\text{A.1})$$

$$\vec{V} \cdot \nabla \vec{V} = -\frac{1}{\rho} \nabla P + \nu \nabla^2 \vec{V} \quad (\text{A.2})$$

$$\vec{V} \cdot \nabla T = \alpha \nabla^2 T \quad (\text{A.3})$$

where \vec{V} is the velocity vector, P is the pressure, T is the temperature, and ρ , ν and α are the density, kinematic viscosity and thermal diffusivity of the fluid, respectively.

A.1 Plane Polar Coordinates

In plane polar coordinates, these equations can be written as:

Continuity:

$$\frac{\partial u_r}{\partial r} + \frac{u_r}{r} + \frac{1}{r} \frac{\partial u_\theta}{\partial \theta} = 0 \quad (\text{A.4})$$

r - Momentum:

$$u_r \frac{\partial u_r}{\partial r} + \frac{u_\theta}{r} \frac{\partial u_r}{\partial \theta} - \frac{u_\theta^2}{r} = -\frac{1}{\rho} \frac{\partial P}{\partial r} + \nu \left\{ \frac{\partial^2 u_r}{\partial r^2} + \frac{1}{r} \frac{\partial u_r}{\partial r} - \frac{u_r}{r^2} + \frac{1}{r^2} \frac{\partial^2 u_r}{\partial \theta^2} - \frac{2}{r^2} \frac{\partial u_\theta}{\partial \theta} \right\} \quad (\text{A.5})$$

θ - Momentum:

$$u_r \frac{\partial u_\theta}{\partial r} + \frac{u_\theta}{r} \frac{\partial u_\theta}{\partial \theta} + \frac{u_r u_\theta}{r} = -\frac{1}{\rho r} \frac{\partial P}{\partial \theta} + \nu \left\{ \frac{\partial^2 u_\theta}{\partial r^2} + \frac{1}{r} \frac{\partial u_\theta}{\partial r} - \frac{u_\theta}{r^2} + \frac{1}{r^2} \frac{\partial^2 u_\theta}{\partial \theta^2} + \frac{2}{r^2} \frac{\partial u_r}{\partial \theta} \right\} \quad (\text{A.6})$$

Energy:

$$u_r \frac{\partial T}{\partial r} + \frac{u_\theta}{r} \frac{\partial T}{\partial \theta} = \alpha \left\{ \frac{\partial^2 T}{\partial r^2} + \frac{1}{r} \frac{\partial T}{\partial r} + \frac{1}{r^2} \frac{\partial^2 T}{\partial \theta^2} \right\} \quad (\text{A.7})$$

where u_r and u_θ are the velocity components in the radial and transverse directions, respectively. For a fixed pin, Bird et. al (1994) ignored the two terms, centrifugal force (u_θ^2/r) and the coriolis force ($u_r u_\theta/r$) found in the momentum equations, on physical grounds. The remaining terms can be simplified by the order-of-magnitude analysis. The orders of magnitude for different terms are given below:

$$\begin{array}{cccc} u_r \sim O(\delta) & u_\theta \sim O(1) & r \sim O(\delta) & r d\theta \sim O(1) \\ \\ \frac{\partial u_r}{\partial r} \sim O(1) & \frac{\partial u_r}{r \partial \theta} \sim O(\delta) & \frac{\partial^2 u_\theta}{r^2 \partial \theta^2} \sim O(1) & \frac{\partial u_r}{r^2 \partial \theta} \sim O(1) \\ \\ \frac{\partial^2 u_r}{\partial r^2} \sim O\left(\frac{1}{\delta}\right) & \frac{\partial u_r}{r \partial r} \sim O\left(\frac{1}{\delta}\right) & \frac{\partial u_\theta}{r^2 \partial \theta} \sim O\left(\frac{1}{\delta}\right) & \frac{u_r}{r^2} \sim O\left(\frac{1}{\delta}\right) \\ \\ \frac{\partial^2 u_\theta}{\partial r^2} \sim O\left(\frac{1}{\delta}\right)^2 & \frac{\partial u_\theta}{r \partial r} \sim O\left(\frac{1}{\delta}\right)^2 & \frac{\partial u_r}{r^2 \partial \theta} \sim O(1) & \frac{u_\theta}{r^2} \sim O\left(\frac{1}{\delta}\right)^2 \end{array}$$

A boundary layer equation must satisfy conditions everywhere within the boundary layer region and at the boundary layer edge as well. In the free stream the effect of viscosity is negligible, so we could drop the viscous terms of the θ -momentum equation.

$$\underbrace{u_r \frac{\partial u_\theta}{\partial r}}_{\delta \times \frac{1}{\delta} = 1} + \underbrace{\frac{u_\theta}{r} \frac{\partial u_\theta}{\partial \theta}}_{1 \times \frac{1}{1} = 1} = -\frac{1}{r} \frac{\partial p}{\partial \theta}$$

So, the order of magnitude of $\partial P/r\partial\theta$ is estimated as 1.

In the boundary layer, the viscous terms balance the inertia terms, therefore

$$\underbrace{u_r \frac{\partial u_\theta}{\partial r}}_{\delta \times \frac{1}{\delta} = 1} + \underbrace{\frac{u_\theta}{r} \frac{\partial u_\theta}{\partial \theta}}_{1 \times \frac{1}{1} = 1} = \underbrace{-\frac{1}{r} \frac{\partial P}{\partial \theta}}_1 + \frac{1}{Re_D} \left\{ \underbrace{\frac{\partial^2 u_\theta}{\partial r^2}}_{\frac{1}{\delta^2}} + \underbrace{\frac{1}{r} \frac{\partial u_\theta}{\partial r}}_{\frac{1}{\delta^2}} - \underbrace{\frac{u_\theta}{r^2}}_{\frac{1}{\delta^2}} + \underbrace{\frac{1}{r^2} \frac{\partial^2 u_\theta}{\partial \theta^2}}_1 + \underbrace{\frac{2}{r^2} \frac{\partial u_r}{\partial \theta}}_1 \right\}$$

$$\Rightarrow Re_D = O\left(\frac{1}{\delta^2}\right)$$

Repeating the foregoing analysis for the r-momentum and energy equations, we can write the orders of magnitude below the terms:

r-Momentum:

$$\underbrace{u_r \frac{\partial u_r}{\partial r}}_{\delta \times \frac{\delta}{\delta} = \delta} + \underbrace{\frac{u_\theta}{r} \frac{\partial u_r}{\partial \theta}}_{1 \times \frac{\delta}{1} = \delta} = \underbrace{-\frac{\partial P}{\partial r}}_{\delta^2} + \frac{1}{Re_D} \left\{ \underbrace{\frac{\partial^2 u_r}{\partial r^2}}_{\frac{1}{\delta}} + \underbrace{\frac{1}{r} \frac{\partial u_r}{\partial r}}_{\frac{1}{\delta}} - \underbrace{\frac{u_r}{r^2}}_{\frac{1}{\delta}} + \underbrace{\frac{1}{r^2} \frac{\partial^2 u_r}{\partial \theta^2}}_{\delta} - \underbrace{\frac{2}{r^2} \frac{\partial u_\theta}{\partial \theta}}_{\frac{1}{\delta}} \right\}$$

We conclude that the pressure gradient in the r-direction must be of order δ . In fact, the entire equation must be of order of δ . Comparing to the θ -component equation, which is of order 1, we can neglect the r component equation.

Energy:

$$\underbrace{u_r \frac{\partial \Theta}{\partial r}}_{\delta \times \frac{1}{\delta} = 1} + \underbrace{\frac{u_\theta}{r} \frac{\partial \Theta}{\partial \theta}}_{1 \times \frac{1}{1} = 1} = \frac{1}{Re_D Pr} \left\{ \underbrace{\frac{\partial^2 \Theta}{\partial r^2}}_{\delta^2} + \underbrace{\frac{1}{r} \frac{\partial \Theta}{\partial r}}_{\frac{1}{\delta^2}} + \underbrace{\frac{1}{r^2} \frac{\partial^2 \Theta}{\partial \theta^2}}_1 \right\}$$

Neglecting small terms, we can write the boundary-layer equations in polar coordinates as follows:

Continuity:

$$\frac{\partial u_r}{\partial r} + \frac{u_r}{r} + \frac{1}{r} \frac{\partial u_\theta}{\partial \theta} = 0 \quad (\text{A.8})$$

r - Momentum:

$$\frac{\partial P}{\partial r} = 0 \quad (\text{A.9})$$

θ - Momentum:

$$u_r \frac{\partial u_\theta}{\partial r} + \frac{u_\theta}{r} \frac{\partial u_\theta}{\partial \theta} = -\frac{1}{r} \frac{\partial P}{\partial \theta} + \frac{1}{Re_D} \left\{ \frac{\partial^2 u_\theta}{\partial r^2} + \frac{1}{r} \frac{\partial u_\theta}{\partial r} - \frac{u_\theta}{r^2} \right\} \quad (\text{A.10})$$

Energy:

$$u_r \frac{\partial \Theta}{\partial r} + \frac{u_\theta}{r} \frac{\partial \Theta}{\partial \theta} = \frac{1}{Re_D Pr} \left\{ \frac{\partial^2 \Theta}{\partial r^2} + \frac{1}{r} \frac{\partial \Theta}{\partial r} \right\} \quad (\text{A.11})$$

A.2 Curvilinear Coordinates

Equations (A.8)-(A.11) can be rewritten in a curvilinear system of coordinates in which s denotes distance along the curved surface of the circular pin measured from the forward stagnation point and η the distance normal to and measured from the surface (Fig. 3.2). In this system of coordinates, the velocity components u_r and u_θ are replaced by u and v in the local s - and η - directions whereas $r d\theta$ and dr are replaced by ds and $d\eta$ respectively. The s -component of velocity just outside the boundary layer is denoted by $U(s)$. So, the governing equations in this curvilinear system will be:

Continuity:

$$\frac{\partial u}{\partial s} + \frac{\partial v}{\partial \eta} + \frac{v}{r} = 0 \quad (\text{A.12})$$

s - Momentum:

$$u \frac{\partial u}{\partial s} + v \frac{\partial u}{\partial \eta} = -\frac{1}{\rho} \frac{\partial P}{\partial s} + \nu \left\{ \frac{\partial^2 u}{\partial s^2} + \frac{\partial^2 u}{\partial \eta^2} + \frac{1}{r} \frac{\partial u}{\partial \eta} - \frac{u}{r^2} + \frac{2}{r} \frac{\partial v}{\partial s} \right\} \quad (\text{A.13})$$

η - Momentum:

$$u \frac{\partial v}{\partial s} + v \frac{\partial v}{\partial \eta} = -\frac{1}{\rho} \frac{\partial P}{\partial \eta} + \nu \left\{ \frac{\partial^2 v}{\partial s^2} + \frac{\partial^2 v}{\partial \eta^2} + \frac{1}{r} \frac{\partial v}{\partial \eta} - \frac{v}{r^2} - \frac{2}{r} \frac{\partial u}{\partial s} \right\} \quad (\text{A.14})$$

Energy:

$$u \frac{\partial T}{\partial s} + v \frac{\partial T}{\partial \eta} = \alpha \left\{ \frac{\partial^2 T}{\partial s^2} + \frac{\partial^2 T}{\partial \eta^2} + \frac{1}{r} \frac{\partial T}{\partial \eta} \right\} \quad (\text{A.15})$$

Also Bernoulli's equation in differential form can be written as:

$$-\frac{1}{\rho} \frac{dP}{ds} = U \frac{dU}{ds} \quad (\text{A.16})$$

These equations can be nondimensionalized using the diameter of the pin D as the length scale, free stream velocity U_{app} as the velocity scale, ρU_{app}^2 as the scale for pressure, and

$T_w - T_a$ as the scale for $T - T_a$. Using these scales, the distances, velocities, and pressure are made dimensionless as follows:

$$s/D, \eta/D, r/D, u/U_{app}, v/U_{app}, U/U_{app}, P/\rho U_{app}^2$$

For simplicity, the symbols $s, \eta, r, u, v, U, p = P/\rho U_{app}^2$, and $\Theta = (T - T_a)/(T_w - T_a)$ will be used to denote the dimensionless quantities. These symbols with their new meaning are summarized as follows:

s = dimensionless distance along the curved surface

η = dimensionless normal distance from the pin surface

r = dimensionless radius of circular pin

u = s - component of velocity in the boundary layer

v = η - component of velocity in the boundary layer

U = potential flow velocity just outside the boundary layer

P = pressure in the boundary layer

Θ = non-dimensional temperature in the thermal boundary layer

Using these dimensionless quantities, equations (12)- (16) can be written as follows:
Continuity:

$$\frac{\partial u}{\partial s} + \frac{\partial v}{\partial \eta} + \frac{v}{r} = 0 \quad (\text{A.17})$$

s - Momentum:

$$u \frac{\partial u}{\partial s} + v \frac{\partial u}{\partial \eta} = -\frac{\partial P}{\partial s} + \frac{1}{Re_D} \left\{ \frac{\partial^2 u}{\partial s^2} + \frac{\partial^2 u}{\partial \eta^2} + \frac{1}{r} \frac{\partial u}{\partial \eta} - \frac{u}{r^2} + \frac{2}{r} \frac{\partial v}{\partial s} \right\} \quad (\text{A.18})$$

η - Momentum:

$$u \frac{\partial v}{\partial s} + v \frac{\partial v}{\partial \eta} = -\frac{\partial P}{\partial \eta} + \frac{1}{Re_D} \left\{ \frac{\partial^2 v}{\partial s^2} + \frac{\partial^2 v}{\partial \eta^2} + \frac{1}{r} \frac{\partial v}{\partial \eta} - \frac{v}{r^2} - \frac{2}{r} \frac{\partial u}{\partial s} \right\} \quad (\text{A.19})$$

Energy:

$$u \frac{\partial \Theta}{\partial s} + v \frac{\partial \Theta}{\partial \eta} = \frac{1}{Re_D Pr} \left\{ \frac{\partial^2 \Theta}{\partial s^2} + \frac{\partial^2 \Theta}{\partial \eta^2} + \frac{1}{r} \frac{\partial \Theta}{\partial \eta} \right\} \quad (\text{A.20})$$

Also Bernoulli's equation in differential form can be written as:

$$-\frac{dP}{ds} = U \frac{dU}{ds} \quad (\text{A.21})$$

These equations will be simplified by an order-of-magnitude analysis. The order of magnitude, increasing from a small quantity to a large quantity, are

$$\delta^2 \ll \delta \ll 1 \ll \frac{1}{\delta} \ll \frac{1}{\delta^2}$$

where δ is the hydrodynamic boundary layer thickness. Since Pr for air is close to unity, the thermal boundary layer thickness will be approximately the same as the hydrodynamic boundary layer thickness, i.e.

$$\delta_T \approx \delta$$

The orders of magnitude for different terms are given below: A boundary layer equation must satisfy conditions everywhere within the boundary layer region and at the boundary layer edge as well. In the free stream the effect of viscosity is negligible, so we could drop the viscous terms of the s -momentum equation.

$$\underbrace{u \frac{\partial u}{\partial s}}_{1 \times 1 = 1} + \underbrace{v \frac{\partial u}{\partial \eta}}_{\delta \times \frac{1}{\delta} = 1} = -\frac{\partial P}{\partial s}$$

So, the order of magnitude of $\partial P/\partial s$ is estimated as 1. In the boundary layer, the viscous terms balance the inertia terms, therefore,

$$\underbrace{u \frac{\partial u}{\partial s}}_{1 \times 1 = 1} + \underbrace{v \frac{\partial u}{\partial \eta}}_{\delta \times \frac{1}{\delta} = 1} = -\underbrace{\frac{\partial P}{\partial s}}_1 + \frac{1}{Re_D} \left\{ \underbrace{\frac{\partial^2 u}{\partial s^2}}_1 + \underbrace{\frac{\partial^2 u}{\partial \eta^2}}_{\frac{1}{\delta^2}} + \underbrace{\frac{1}{r} \frac{\partial u}{\partial \eta}}_{\frac{1}{\delta}} - \underbrace{\frac{u}{r^2}}_1 + \underbrace{\frac{2}{r} \frac{\partial v}{\partial s}}_{\delta} \right\}$$

$$\begin{aligned}
v &\sim O(\delta) & u &\sim O(1) & \eta &\sim O(\delta) & s &\sim O(1) \\
r &\sim O(1) & U &\sim O(1) & \frac{\partial u}{\partial s} &\sim O(1) & \frac{\partial U}{\partial s} &\sim O(1) \\
\frac{\partial p}{\partial s} &\sim O(1) & \frac{\partial u}{\partial \eta} &\sim O\left(\frac{1}{\delta}\right) & \frac{\partial^2 u}{\partial s^2} &\sim O(1) & \frac{\partial^2 u}{\partial \eta^2} &\sim O\left(\frac{1}{\delta^2}\right)
\end{aligned}$$

\Rightarrow

$$Re_D = O\left(\frac{1}{\delta^2}\right)$$

Now the orders of magnitude for the continuity, momentum and energy equations can be written as:

Continuity:

$$\underbrace{\frac{\partial u}{\partial s}}_1 + \underbrace{\frac{\partial v}{\partial \eta}}_1 + \underbrace{\frac{v}{r}}_\delta = 0$$

s - Momentum:

$$\underbrace{u \frac{\partial u}{\partial s}}_{1 \times \frac{1}{1} = 1} + \underbrace{v \frac{\partial u}{\partial \eta}}_{\delta \times \frac{1}{\delta} = 1} = -\underbrace{\frac{\partial P}{\partial s}}_1 + \underbrace{\frac{1}{Re_D}}_{\delta^2} \left\{ \underbrace{\frac{\partial^2 u}{\partial s^2}}_1 + \underbrace{\frac{\partial^2 u}{\partial \eta^2}}_{\frac{1}{\delta^2}} + \underbrace{\frac{1}{r} \frac{\partial u}{\partial \eta}}_{\frac{1}{\delta}} - \underbrace{\frac{u}{r^2}}_1 + \underbrace{\frac{2}{r} \frac{\partial v}{\partial s}}_\delta \right\}$$

η - Momentum:

$$\underbrace{u \frac{\partial v}{\partial s}}_{1 \times \delta = \delta} + \underbrace{v \frac{\partial v}{\partial \eta}}_{\delta \times 1 = \delta} = -\underbrace{\frac{\partial P}{\partial \eta}}_1 + \underbrace{\frac{1}{Re_D}}_{\delta^2} \left\{ \underbrace{\frac{\partial^2 v}{\partial s^2}}_\delta + \underbrace{\frac{\partial^2 v}{\partial \eta^2}}_{\frac{1}{\delta}} + \underbrace{\frac{1}{r} \frac{\partial v}{\partial \eta}}_{\frac{1}{\delta}} - \underbrace{\frac{v}{r^2}}_\delta - \underbrace{\frac{2}{r} \frac{\partial u}{\partial s}}_1 \right\}$$

Energy:

$$\underbrace{u \frac{\partial \Theta}{\partial s}}_{1 \times 1 = 1} + \underbrace{v \frac{\partial \Theta}{\partial \eta}}_{\delta \times \frac{1}{\delta} = 1} = \underbrace{\frac{1}{Re_D Pr}}_{\delta^2} \left\{ \underbrace{\frac{\partial^2 \Theta}{\partial s^2}}_1 + \underbrace{\frac{\partial^2 \Theta}{\partial \eta^2}}_{\frac{1}{\delta^2}} + \underbrace{\frac{1}{r} \frac{\partial \Theta}{\partial \eta}}_{1 \times \frac{1}{\delta} = \frac{1}{\delta}} \right\}$$

Bernoulli Equation:

$$-\frac{dP}{ds} = \underbrace{U \frac{dU}{ds}}_{1 \times 1 = 1} \quad (\text{A.22})$$

so, the pressure gradient dP/ds must be of order 1. Eliminating small terms, we can write nondimensionalized reduced equations in Cartesian coordinates as follows:

Continuity:

$$\frac{\partial u}{\partial s} + \frac{\partial v}{\partial \eta} = 0 \quad (\text{A.23})$$

s-Momentum:

$$u \frac{\partial u}{\partial s} + v \frac{\partial u}{\partial \eta} = -\frac{dP}{ds} + \frac{1}{Re_D} \frac{\partial^2 u}{\partial \eta^2} \quad (\text{A.24})$$

η -Momentum:

$$\frac{dP}{d\eta} = 0 \quad (\text{A.25})$$

Energy:

$$u \frac{\partial \Theta}{\partial s} + v \frac{\partial \Theta}{\partial \eta} = \frac{1}{Re_D Pr} \frac{\partial^2 \Theta}{\partial \eta^2} \quad (\text{A.26})$$

Bernoulli Equation:

$$-\frac{dP}{ds} = U \frac{dU}{ds} \quad (\text{A.27})$$

A.3 Elliptical Coordinates

Following the previous order of magnitude analysis, the equations of motion, Eqs. (A.1) - (A.3), in elliptical coordinates (η, θ) (see Fig. 3.2) for 2-D steady state, forced convection of an incompressible Newtonian, constant property fluid can be written as:

Continuity:

$$\frac{\partial(h_2 u_\eta)}{\partial \eta} + \frac{\partial(h_1 u_\theta)}{\partial \theta} = 0 \quad (\text{A.28})$$

θ -Momentum:

$$\frac{u_\eta}{h_1} \frac{\partial u_\theta}{\partial \eta} + \frac{u_\theta}{h_2} \frac{\partial u_\theta}{\partial \theta} = -\frac{1}{h_2} \frac{dP}{d\theta} + \frac{1}{Re_D} \frac{1}{h_1 h_2} \frac{\partial^2 u_\theta}{\partial \theta^2} \quad (\text{A.29})$$

Energy:

$$\frac{u_\eta}{h_1} \frac{\partial \Theta}{\partial \eta} + \frac{u_\theta}{h_2} \frac{\partial \Theta}{\partial \theta} = \frac{1}{Re_D Pr} \frac{1}{h_1 h_2} \frac{\partial^2 \Theta}{\partial \theta^2} \quad (\text{A.30})$$

where u_η and u_θ are the velocity components and h_1 and h_2 are the scale factors and are given by:

$$h_1 = h_2 = c \sqrt{\sinh^2 \eta + \sin^2 \theta} \quad (\text{A.31})$$

with $c = a \sqrt{1 - \epsilon^2}$ and $\epsilon = b/a$

Appendix B

Boundary Conditions

B.1 Hydrodynamic Boundary Conditions

A schematic of the velocity distribution in the viscous and non-viscous regions is shown in Fig. B.1. In plane polar coordinates, $u_r = 0$ and $u_\theta = 0$ at the pin surface, therefore, from Eq. A-10,

$$\frac{1}{R} \frac{\partial P}{\partial \theta} = \frac{1}{Re_D} \left\{ \frac{\partial^2 u_\theta}{\partial r^2} \right\}$$

At the edge of the boundary layer, $r = \delta + R$, the potential flow solution can be used, i.e.

$$u_\theta = \sin \theta \left(1 + \frac{R^2}{r^2} \right)$$

which gives

$$\frac{\partial u_\theta}{\partial r} = \sin \theta \left(-\frac{2R^2}{r^3} \right) < 0 \quad \text{and} \quad \frac{\partial^2 u_\theta}{\partial r^2} = \sin \theta \left(\frac{6R^2}{r^4} \right) > 0$$

whereas in the viscous region,

$$\frac{\partial u_\theta}{\partial r} > 0 \quad \text{and} \quad \frac{\partial^2 u_\theta}{\partial r^2} < 0$$

Thus at $r = \delta + R$,

$$\frac{\partial u_\theta}{\partial r} = 0 \quad \text{and} \quad \frac{\partial^2 u_\theta}{\partial r^2} = 0$$

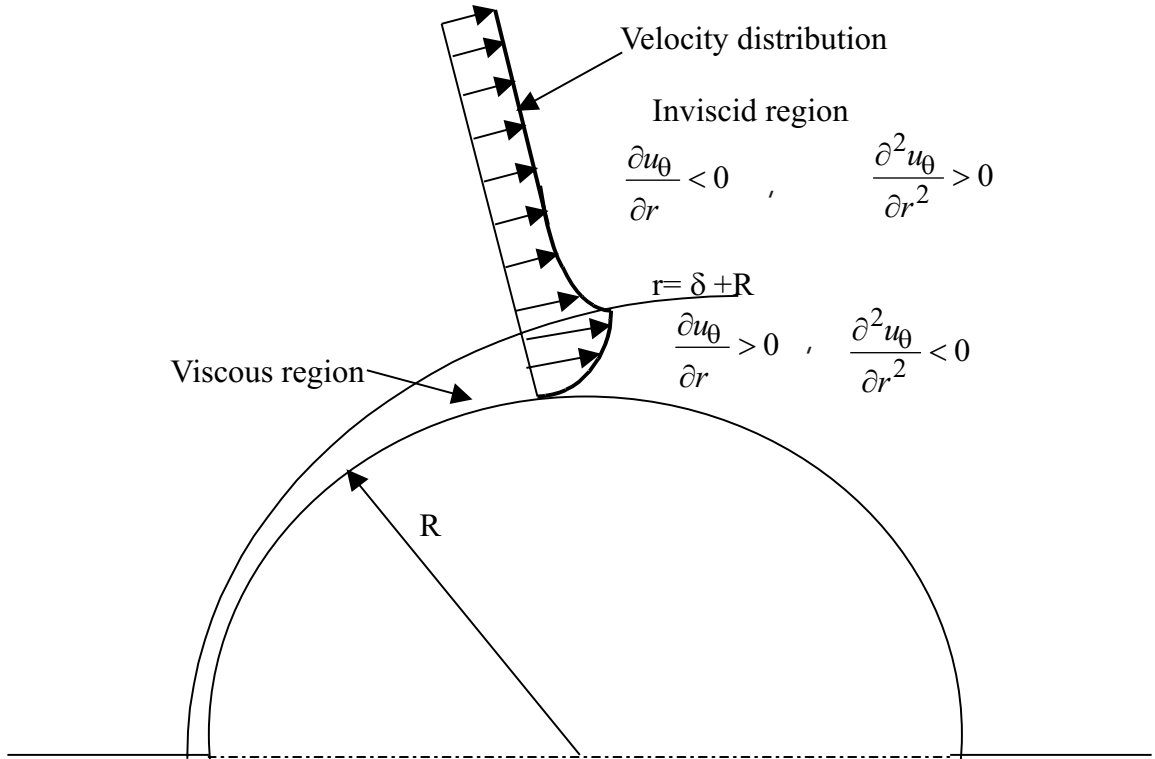


Figure B.1: Velocity Distribution in Viscous and Inviscid Regions

In Curvilinear coordinates, these boundary conditions can be written as:

At the pin surface, i.e., at $\eta = 0$:

$$u = 0 \quad \text{and} \quad \frac{\partial^2 u}{\partial \eta^2} = \frac{1}{\mu} \frac{\partial P}{\partial s} \quad (\text{B.1})$$

At the edge of the boundary layer, i.e., at $\eta = \delta(s)$:

$$u = U(s), \quad \frac{\partial u}{\partial \eta} = 0 \quad \text{and} \quad \frac{\partial^2 u}{\partial \eta^2} = 0 \quad (\text{B.2})$$

B.2 Thermal Boundary Conditions

The boundary conditions for the uniform wall temperature (UWT) and uniform wall flux (UWF) are:

$$\eta = 0, \left\{ \begin{array}{ll} T = T_w & \text{for UWT} \\ \frac{\partial T}{\partial \eta} = -\frac{q}{k_f} & \text{for UWF} \end{array} \right. \quad (\text{B.3})$$

$$\eta = 0, \quad \frac{\partial^2 T}{\partial \eta^2} = 0 \quad (\text{B.4})$$

$$\eta = \delta_T, \quad T = T_a \quad \text{and} \quad \frac{\partial T}{\partial \eta} = 0 \quad (\text{B.5})$$

B.3 Boundary Conditions for Control Volume

The following boundary conditions are specified for the control volume of Fig. 3.16:

1. On the curved surfaces of the pin-fins:

$$u = 0 \quad v = 0 \quad \text{and} \quad T = T_w$$

2. Along the top and bottom of the control volume and on the side-wall regions contained between pin-fins:

$$v = 0 \quad \tau_w = 0 \quad \text{and} \quad Q = 0$$

3. At large distances ahead of the heat sink (AP):

$$u = U_{app} \quad \text{and} \quad T = T_a$$

4. Well downstream of the heat sink (HI):

$$\frac{\partial u}{\partial x} = 0 \quad \frac{\partial v}{\partial x} = 0 \quad \text{and} \quad \frac{\partial T}{\partial x} = 0$$

Appendix C

Velocity and Temperature Distributions

C.1 Velocity Distribution

Assuming a thin boundary layer around the pin, the velocity distribution in the boundary layer can be approximated by a fourth order polynomial as suggested by Pohlhausen (1921):

$$\frac{u}{U(s)} = a\eta_H + b\eta_H^2 + c\eta_H^3 + d\eta_H^4 \quad (\text{C.1})$$

where $0 \leq \eta_H = \eta/\delta \leq 1$. Applying hydrodynamic boundary conditions (1) and (2), given in Appendix 2, we have:

$$a = 2 + \frac{\lambda}{6} \quad b = -\frac{\lambda}{2} \quad c = -2 + \frac{\lambda}{2} \quad d = 1 - \frac{\lambda}{6}$$

So, the velocity profile inside the boundary layer will be:

$$\frac{u}{U(s)} = (2\eta_H - 2\eta_H^3 + \eta_H^4) + \frac{\lambda}{6}(\eta_H - 3\eta_H^2 + 3\eta_H^3 - \eta_H^4) \quad (\text{C.2})$$

where λ is the pressure gradient parameter given by:

$$\lambda = \frac{\delta^2}{\nu} \frac{dU(s)}{ds} \quad (\text{C.3})$$

Schlichting (1979) drew velocity profiles for different values of λ and found that the parameter λ is restricted to the range $-12 \leq \lambda \leq 12$.

C.2 Temperature Distribution

To approximate the temperature profile in the thermal boundary layer, a third-degree polynomial is used in this study:

$$\frac{T - T_a}{T_w - T_a} = A + B\eta_T + C\eta_T^2 + D\eta_T^3 \quad (\text{C.4})$$

where $0 \leq \eta_T = \eta/\delta_T \leq 1$. Using isothermal boundary conditions, we get:

$$A = 1 \quad B = -\frac{3}{2} \quad C = 0 \quad D = \frac{1}{2}$$

So, the temperature profile for isothermal pin will be:

$$\frac{T - T_a}{T_w - T_a} = 1 - \frac{3}{2}\eta_T + \frac{1}{2}\eta_T^3 \quad (\text{C.5})$$

Whereas, isoflux boundary conditions will give the following temperature profile:

$$T - T_a = \frac{2q\delta_T}{3k_f} \left(1 - \frac{3}{2}\eta_T + \frac{1}{2}\eta_T^3 \right) \quad (\text{C.6})$$

where δ_T is the thermal boundary layer thickness.

Appendix D

Potential Flow Velocity

D.1 Circular Pin in Infinite Flow

Using circle theorem, Milne-Thomson (1960) gave the complex potential for a circular pin of radius R in a uniform flow (Fig. 3.2):

$$w(z) = U_{app} \left(z + \frac{R^2}{z} \right) \quad (\text{D.1})$$

which gives the stream and potential functions as follows:

$$\psi = U_{app} \left(r - \frac{R^2}{r} \right) \sin \theta \quad (\text{D.2})$$

and

$$\phi = U_{app} \left(r + \frac{R^2}{r} \right) \cos \theta \quad (\text{D.3})$$

The radial and transverse components of velocity at the surface of the pin can be defined as:

$$u_r = \frac{1}{r} \frac{\partial \psi}{\partial \theta} \Big|_{r=R} \quad \text{and} \quad u_\theta = - \frac{\partial \psi}{\partial r} \Big|_{r=R} \quad (\text{D.4})$$

which gives:

$$u_r = U_{app} \cos \theta \left(1 - \frac{R^2}{r^2} \right) \quad \text{and} \quad u_\theta = -U_{app} \sin \theta \left(1 + \frac{R^2}{r^2} \right) \quad (\text{D.5})$$

At the pin surface, $r = R$, therefore

$$u_r = 0 \quad \text{and} \quad u_\theta = -2U_{app} \sin \theta \quad (\text{D.6})$$

The resultant velocity along the pin surface will be:

$$U(\theta) = 2U_{app} \sin \theta \quad (\text{D.7})$$

D.2 Elliptical Pin in Infinite Flow

The mapping between Cartesian (x, y) and elliptic (η, θ) coordinates is given by:

$$x = c \cosh \eta \cos \theta \quad \text{and} \quad y = c \sinh \eta \sin \theta \quad (\text{D.8})$$

where c is the dimensional focal distance and is given by

$$c = a \sqrt{1 - \epsilon^2} \quad \text{with} \quad \epsilon = b/a$$

The surface of an ellipse is defined by $\eta = \eta_0$, so

$$\tanh \eta_0 = \epsilon \quad (\text{D.9})$$

The elliptic coordinate system gives the following metrics:

$$h_1 = h_2 = c \sqrt{\sinh^2 \eta \cos^2 \theta + \cosh^2 \eta \sin^2 \theta} = h(\text{say}) \quad (\text{D.10})$$

For the steady flow around an elliptic pin, Streeter (1948) gave the following complex potential:

$$w(z) = U_{app} b \sqrt{\frac{1+\epsilon}{1-\epsilon}} e^{-\zeta} + U_{app} c \cosh \zeta \quad (\text{D.11})$$

where $\zeta = \eta + i\theta$. Equation (D.11) can be separated into real and imaginary parts to obtain the following potential and stream functions:

$$\phi = U_{app} b \sqrt{\frac{1+\epsilon}{1-\epsilon}} e^{-\eta} \cos \theta + U_{app} c \cosh \eta \cos \theta \quad (\text{D.12})$$

$$\psi = -U_{app} b \sqrt{\frac{1+\epsilon}{1-\epsilon}} e^{-\eta} \sin \theta + U_{app} c \sinh \eta \sin \theta \quad (\text{D.13})$$

Using Eq. (D.4), the velocity components u_η and u_θ can be defined as:

$$u_\eta = -\frac{1}{h} \frac{\partial \phi}{\partial \eta} \Big|_{\eta=\eta_0} \quad \text{and} \quad u_\theta = \frac{1}{h} \frac{\partial \phi}{\partial \theta} \Big|_{\eta=\eta_0} \quad (\text{D.14})$$

which gives:

$$u_\eta = -\frac{U_{app} c \cos \theta}{h(1-\epsilon)} (\sinh \eta - \epsilon \cosh \eta) \quad (D.15)$$

and

$$u_\theta = -\frac{U_{app} c \sin \theta}{h(1-\epsilon)} (\cosh \eta - \epsilon \sinh \eta) \quad (D.16)$$

At the surface, $\eta = \eta_0$, the velocity components will be:

$$u_\eta = 0 \quad (D.17)$$

and

$$u_\theta = -\frac{U_{app} (1+\epsilon) \sin \theta}{\sqrt{1-\epsilon^2} \cos^2 \theta} \quad (D.18)$$

with

$$e = \sqrt{1-\epsilon^2} \quad (D.19)$$

The resultant velocity along the elliptic arc will be:

$$U(\theta) = \frac{U_{app} (1+\epsilon) \sin \theta}{\sqrt{1-\epsilon^2} \cos^2 \theta} \quad (D.20)$$

D.3 Circular Pin Between Two Parallel Planes

Streeter (1948) and Perkins and Leppert (1964) mentioned that, using the method of images, a pin confined between two parallel planes (Fig. 3.10) can be modeled as a system of infinite transverse row of doublets superimposed on a uniform flow field (Fig. D.1). For this system, the complex potential can be written as:

$$\begin{aligned} w(z) &= U_{app} z + \sum_{j=-\infty}^{\infty} \frac{\mu}{2\pi(z - ijS_T)} \\ &= U_{app} z + \frac{\mu}{2\pi} \sum_{j=-\infty}^{\infty} \frac{1}{z - ijS_T} \end{aligned} \quad (D.21)$$

where j is the number of doublets or pins and

$$\sum_{j=-\infty}^{\infty} \frac{1}{z - ijS_T} = \frac{\pi}{S_T} \coth \left(\frac{\pi z}{S_T} \right) \quad (D.22)$$

Therefore, the complex potential for a pin confined in a channel (Fig. 1) can be written as:

$$w(z) = U_{app} z + \frac{\mu}{2S_T} \coth \left(\frac{\pi z}{S_T} \right) \quad (D.23)$$

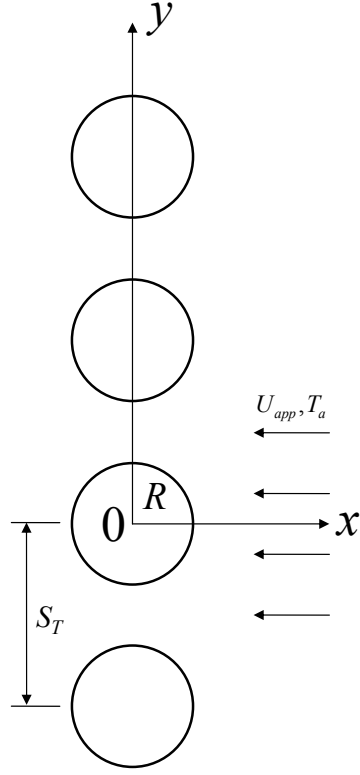


Figure D.1: Transverse Row of Doublets or Circular Pins

The complex velocity will be:

$$w'(z) = U_{app} - \frac{\mu\pi}{2S_T^2} \left\{ \frac{1}{\sinh^2\left(\frac{\pi z}{S_T}\right)} \right\} \quad (\text{D.24})$$

The stagnation points are $z = \pm R \Rightarrow w'(\pm R) = 0$. Therefore, Eq. (D.20) gives:

$$\frac{\mu}{2S_T} = \frac{U_{app}S_T}{\pi} \sinh^2\left(\frac{\pi R}{S_T}\right) \quad (\text{D.25})$$

Substituting this value in Eq. (D.19), the required complex potential will be:

$$w(z) = \phi + i\psi = U_{app} \left\{ z + C \coth\left(\frac{\pi z}{S_T}\right) \right\} \quad (\text{D.26})$$

where ϕ and ψ are the potential and stream functions and C is a constant given by:

$$C = \frac{S_T}{\pi} \sinh^2\left(\frac{\pi R}{S_T}\right) \quad (\text{D.27})$$

The stream function ψ in polar coordinates (r, θ) can be obtained from Eq. (D.22) as follows:

$$\psi = U_{app} \left\{ r \sin \theta - C \frac{\sin \left(\frac{2\pi r \sin \theta}{S_T} \right)}{\cosh \left(\frac{2\pi r \cos \theta}{S_T} \right) - \cos \left(\frac{2\pi r \sin \theta}{S_T} \right)} \right\} \quad (D.28)$$

The radial and transverse components of velocity at the surface of the pin can be written as:

$$u_r = -\frac{1}{r} \frac{\partial \psi}{\partial \theta} \Big|_{r=R} \quad \text{and} \quad u_\theta = \frac{\partial \psi}{\partial r} \Big|_{r=R} \quad (D.29)$$

which gives:

$$u_r = 0 \quad \text{and} \quad u_\theta = U_{app} f(\theta) \quad (D.30)$$

where

$$f(\theta) = \sin \theta - \left(\frac{2\pi C}{S_T} \right) \left\{ \frac{\cos \left(\frac{2\pi R \cos \theta}{S_T} \right) \sin \theta}{\cosh \left(\frac{2\pi R \cos \theta}{S_T} \right) - \cos \left(\frac{2\pi R \sin \theta}{S_T} \right)} + \sin \left(\frac{2\pi R \sin \theta}{S_T} \right) \right. \\ \left. \frac{\sinh \left(\frac{2\pi R \cos \theta}{S_T} \right) \cos \theta + \sin \theta \sin \left(\frac{2\pi R \sin \theta}{S_T} \right)}{\left[\cosh \left(\frac{2\pi R \cos \theta}{S_T} \right) - \cos \left(\frac{2\pi R \sin \theta}{S_T} \right) \right]^2} \right\} \quad (D.31)$$

Setting $C_1 = \frac{2\pi R}{S_T}$ and substituting the value of C , we get:

$$f(\theta) = \sin \theta - 2 \sinh^2 \left(\frac{C_1}{2} \right) \left\{ \frac{\cos(C_1 \cos \theta) \sin \theta}{\cosh(C_1 \cos \theta) - \cos(C_1 \sin \theta)} + \sin(C_1 \sin \theta) \right. \\ \left. \frac{\sinh(C_1 \cos \theta) \cos \theta + \sin \theta \sin(C_1 \sin \theta)}{[\cosh(C_1 \cos \theta) - \cos(C_1 \sin \theta)]^2} \right\} \quad (D.32)$$

The resultant potential flow velocity will be:

$$U = U_{app} f(\theta) \quad (D.33)$$

D.4 Cylindrical Pin-Fins in In-Line Arrangement

Following Suh et al. (1989), the complex potential for in-line arrays, subjected to uniform flow, can be written as:

$$\begin{aligned}
w(z) &= U_{app}z + \sum_{j,k=-\infty}^{\infty} \frac{\mu}{2\pi[(z - kS_L) - ijS_T]} \\
&= U_{app}z + \frac{\mu}{2\pi} \sum_{j,k=-\infty}^{\infty} \frac{1}{[(z - kS_L) - ijS_T]}
\end{aligned} \tag{D.34}$$

where j and k are the number of rows and columns. Using Eq. (D.22), the complex potential for in-line bank can be written as:

$$\begin{aligned}
w(z) &= U_{app}z + \frac{\mu}{2S_T} \sum_{k=-\infty}^{\infty} \coth \frac{\pi}{S_T}(z - kS_L) \\
&= U_{app}z + \frac{\mu}{2S_T} T(z)
\end{aligned} \tag{D.35}$$

where

$$T(z) = \sum_{k=-\infty}^{\infty} \coth \frac{\mu}{2S_T}(z - kS_L) \tag{D.36}$$

Using complex variable theory, Suh (1989) showed that

$$T(z) = \frac{S_T}{2S_L} \cot \frac{\pi z}{S_L} \tag{D.37}$$

Therefore, the complex potential will be

$$W(z) = U_{app}z + \frac{\mu}{4S_L} \cot \frac{\pi z}{S_L} \tag{D.38}$$

which gives the complex velocity $W'(z)$ as follows:

$$W'(z) = U_{app} - \frac{\mu}{4S_L} \frac{1}{\sin^2\left(\frac{\pi z}{S_L}\right)} \left(\frac{\pi}{S_L}\right) \tag{D.39}$$

At the surface of the pin, $W'(R) = 0$, $\Rightarrow \frac{\mu}{4S_L} = \frac{U_{app}S_L}{\pi} \sin^2\left(\frac{\pi R}{S_L}\right)$

Therefore the required potential flow function for in-line pin fins will be:

$$W(z) = \phi + i\psi = U_{app} \left\{ z + C \cot \left(\frac{\pi z}{S_L} \right) \right\} \tag{D.40}$$

where ϕ and ψ are the potential and stream functions and C is a constant, given by:

$$C = \frac{S_L}{\pi} \sin^2\left(\frac{\pi R}{S_L}\right) \tag{D.41}$$

It is interesting to note here that the potential flow field has no dependence on the transverse spacing, S_T for the infinite number of rows. The stream function ψ in polar coordinates (r, θ) can be obtained from Eq. (D.40) as:

$$\psi = U_{app} \left\{ r \sin \theta - C \frac{\sinh(C_1 r \sin \theta)}{\cosh(C_1 r \sin \theta) - \cos(C_1 r \cos \theta)} \right\} \quad (D.42)$$

where $C_1 = \frac{2\pi}{S_L}$ is a constant. The radial and transverse components of velocity at the surface of the pin can be written as:

$$u_r = -\frac{1}{r} \frac{\partial \psi}{\partial \theta} \Big|_{r=R} \quad \text{and} \quad u_\theta = \frac{\partial \psi}{\partial r} \Big|_{r=R} \quad (D.43)$$

which gives:

$$u_r = 0 \quad \text{and} \quad u_\theta = U_{app} f(\theta) \quad (D.44)$$

where

$$f(\theta) = \sin \theta - 2 \sin^2 \left(\frac{\pi D}{2S_L} \right) \left\{ \frac{\cosh \left(\frac{\pi D}{S_L} \sin \theta \right) \sin \theta}{\cosh \left(\frac{\pi D}{S_L} \sin \theta \right) - \cos \left(\frac{\pi D}{S_L} \cos \theta \right)} + \left[\frac{\sinh \left(\frac{\pi D}{S_L} \sin \theta \right) \sin \theta + \cos \theta \sin \left(\frac{\pi D}{S_L} \cos \theta \right)}{[\cosh \left(\frac{\pi D}{S_L} \sin \theta \right) - \cos \left(\frac{\pi D}{S_L} \cos \theta \right)]^2} \right] \right\} \quad (D.45)$$

The resultant potential flow velocity will be:

$$U = U_{app} f(\theta) \quad (D.46)$$

D.5 Cylindrical Pin-Fins in Staggered Arrangement

Following Suh et al. (1989), the complex potential for in-line arrays, subjected to uniform flow, can be written as:

$$W(z) = \phi + i\psi = U_{app} \left\{ z + C \left[\cot \left(\frac{\pi z}{2S_L} \right) + \cot \left(\frac{\pi [z - (S_L + iS_T)]}{2S_L} \right) \right] \right\} \quad (D.47)$$

where ϕ and ψ are the potential and stream functions and C is a constant, given by:

$$C = \frac{2S_L}{\pi} \sin^2 \left(\frac{\pi R}{2S_L} \right) \quad (D.48)$$

The stream function ψ in polar coordinates (r, θ) can be obtained from Eq. (D.47) as:

$$\psi = U_{app} \left\{ r \sin \theta - \frac{2S_L}{\pi} \sin^2 \left(\frac{\pi R}{2S_L} \right) \left[\frac{\sinh \left(\frac{\pi r \sin \theta}{S_L} \right)}{\cosh \left(\frac{\pi r \sin \theta}{S_L} \right) - \cos \left(\frac{\pi r \sin \theta}{S_L} \right)} \right] - \left[\frac{2S_L}{\pi} \sin^2 \left(\frac{\pi R}{2S_L} \right) \frac{\sinh \left(\frac{\pi(r \sin \theta - S_T)}{S_L} \right)}{\cosh \left(\frac{\pi(r \sin \theta - S_T)}{S_L} \right) - \cos \left(\frac{\pi(r \cos \theta - S_L)}{S_L} \right)} \right] \right\} \quad (D.49)$$

The radial and transverse components of velocity at the surface of the pin can be written as:

$$u_r = -\frac{1}{r} \frac{\partial \psi}{\partial \theta} \Big|_{r=R} \quad \text{and} \quad u_\theta = \frac{\partial \psi}{\partial r} \Big|_{r=R} \quad (D.50)$$

which gives:

$$u_r = 0 \quad \text{and} \quad u_\theta = U_{app} f(\theta) \quad (D.51)$$

where

$$f(\theta) = \sin \theta - 2 \sin^2 \left(\frac{\pi D}{4S_L} \right) \left\{ \frac{\cosh \left(\frac{\pi D \sin \theta}{2S_L} \right) \sin \theta}{\cosh \left(\frac{\pi D \sin \theta}{2S_L} \right) - \cos \left(\frac{\pi D \cos \theta}{2S_L} \right)} - \left[\frac{\sinh \left(\frac{\pi D \sin \theta}{2S_L} \right) \frac{\sinh \left(\frac{\pi D \sin \theta}{2S_L} \right) \sin \theta + \sin \left(\frac{\pi D \cos \theta}{2S_L} \right) \cos \theta}{\left[\cosh \left(\frac{\pi D \sin \theta}{2S_L} \right) - \cos \left(\frac{\pi D \cos \theta}{2S_L} \right) \right]^2} \right] + \frac{\cosh \left(\pi \frac{D \sin \theta - 2S_T}{2S_L} \right) \sin \theta}{\cosh \left(\pi \frac{D \sin \theta - 2S_T}{2S_L} \right) - \cos \left(\pi \frac{D \cos \theta - 2S_L}{2S_L} \right)} - \sinh \left(\pi \frac{D \sin \theta - 2S_T}{2S_L} \right) \left[\frac{\sinh \left(\pi \frac{D \sin \theta - 2S_T}{2S_L} \right) \sin \theta + \sin \left(\pi \frac{D \cos \theta - 2S_L}{2S_L} \right) \cos \theta}{\left[\cosh \left(\pi \frac{D \sin \theta - 2S_T}{2S_L} \right) - \cos \left(\pi \frac{D \cos \theta - 2S_L}{2S_L} \right) \right]^2} \right] \right\} \quad (D.52)$$

The resultant potential flow velocity will be:

$$U = U_{app} f(\theta) \quad (D.53)$$

Appendix E

Fluid Friction and Heat Transfer

E.1 Fluid Friction

The first parameter of interest in this study is fluid friction which manifests itself in the form of the drag force F_D , where F_D is the sum of the skin friction drag D_f and pressure drag D_p . Skin friction drag is due to viscous shear forces produced at the pin surface predominantly in those regions where the boundary layer is attached. The component of shear force in the flow direction is given by

$$D_f = \int_A \tau_w \sin \theta dA \quad (\text{E.1})$$

where τ_w is the shear stress along the pin wall. The friction drag coefficient can be defined as:

$$C_{Df} = \frac{D_f}{\left(\frac{1}{2}\rho U_{app}^2\right)A} = \frac{1}{A} \int_A C_f \sin \theta dA \quad (\text{E.2})$$

where A is the characteristic area of the pin and $C_f = \frac{\tau_w}{\frac{1}{2}\rho U_{app}^2}$ is the local skin friction coefficient. The shear stress can be determined from Newton's law of viscosity:

$$\tau_w = \mu \left. \frac{\partial u}{\partial \eta} \right|_{\eta=0} \quad (\text{E.3})$$

where

$$\left. \frac{\partial u}{\partial \eta} \right|_{\eta=0} = \frac{U(\theta)}{\delta} \left(2 + \frac{\lambda}{6}\right) \quad (\text{E.4})$$

where $U(\theta)$ is the potential flow velocity along the pin surface outside the boundary layer and δ is the hydrodynamic boundary layer thickness. In dimensionless form, shear stress can be written as:

$$C_f = \frac{\tau_w}{\frac{1}{2}\rho U_{app}^2} = \frac{2\nu U(\theta)}{U_{app}^2 \delta} \left(2 + \frac{\lambda}{6}\right) \quad (\text{E.5})$$

So, the friction drag coefficient will become:

$$C_{Df} = \frac{\nu}{3AU_{app}^2} \int_A \frac{U(\theta)(\lambda + 12) \sin\theta}{\delta} dA \quad (\text{E.6})$$

Pressure drag is due to the unbalanced pressure, ($\Delta P = P_1 - P_2$), which exists between the relatively high pressures on the upstream surfaces and the lower pressures on the downstream surfaces. The component of pressure force in the flow direction is given by

$$D_p = \int_A \Delta P \cos\theta dA \quad (\text{E.7})$$

It can be rewritten in terms of pressure drag coefficient as:

$$C_{Dp} = \frac{D_p}{\left(\frac{1}{2}\rho U_{app}^2\right) A} = \frac{1}{A} \int_A C_p \cos\theta dA \quad (\text{E.8})$$

where $C_p = \Delta P / \left(\frac{1}{2}\rho U_{app}^2\right)$ is the pressure coefficient.

E.2 Heat Transfer

The second parameter of interest in this study is the dimensionless average heat transfer coefficient for large Prandtl numbers. This parameter is determined by integrating energy equation, Eq. (A-26), from the pin surface to the thermal boundary layer edge.

E.2.1 Isothermal Boundary Condition

Assuming the presence of a thin thermal boundary layer δ_T along the pin surface, the energy integral equation for the isothermal boundary condition can be written as:

$$\frac{d}{ds} \int_0^{\delta_T} (T - T_\infty) u d\eta = -\alpha \left. \frac{\partial T}{\partial \eta} \right|_{\eta=0} \quad (\text{E.9})$$

Using velocity profile, Eq. (C-2), and temperature profile, Eq. (C-5) and assuming $\zeta = \delta_T/\delta < 1$, Eq. (21) can be integrated to give:

$$\delta_T \frac{d}{ds} [U(s)\delta_T\zeta(\lambda + 12)] = 90\alpha \quad (\text{E.10})$$

Multiplying both sides by $U(s)\zeta(\lambda + 12)$ and rewriting separately for the two regions (Fig. 3.2), we get:

$$\delta_T U(s)\zeta(\lambda_1 + 12) \frac{d}{ds} [U(s)\delta_T\zeta(\lambda_1 + 12)] = 90\alpha U(s)\zeta(\lambda_1 + 12) \quad (\text{E.11})$$

for the region I, and

$$\delta_T U(s)\zeta(\lambda_2 + 12) \frac{d}{ds} [U(s)\delta_T\zeta(\lambda_2 + 12)] = 90\alpha U(s)\zeta(\lambda_2 + 12) \quad (\text{E.12})$$

for the region II.

E.2.2 Isoflux Boundary Condition

For the isoflux boundary condition, the energy integral equation can be written as:

$$\frac{d}{ds} \int_0^{\delta_T} (T - T_\infty)u d\eta = \frac{q}{\rho c_p} \quad (\text{E.13})$$

Using velocity profile, Eq. (C-2), and temperature profile, Eq. (C-6) and assuming $\zeta = \delta_T/\delta < 1$ and constant heat flux and thermophysical properties, Eq. (25) can be integrated to give:

$$\frac{d}{ds} [U(s)\delta_T^2\zeta(\lambda + 12)] = 90\frac{\nu}{Pr} \quad (\text{E.14})$$

Rewriting Eq. (26) for the two regions in the same way as Eq. (22), we get:

$$\frac{d}{ds} [U(s)\delta_T^2\zeta(\lambda_1 + 12)] = 90\frac{\nu}{Pr} \quad (\text{E.15})$$

for region I, and

$$\frac{d}{ds} [U(s)\delta_T^2\zeta(\lambda_2 + 12)] = 90\frac{\nu}{Pr} \quad (\text{E.16})$$

for region II.

Appendix F

Entropy Generation Rate Model

The entropy generation rate model is based on the following assumptions:

1. The fin is nonisothermal with adiabatic tip.
2. The airflow is normal to the fin.
3. The flow is steady, laminar and two dimensional.
4. The radiation heat transfer is negligible.
5. The fluid is considered incompressible with constant properties.
6. There are no heat sources within the fin itself.
7. The baseplate is isothermal.

F.1 Model for Fin Geometry

The entropy generation model can be developed by considering the control volume CV as shown in Fig. F.1. This control volume includes a pin-fin and a baseplate. The side surfaces AEFB and BCJI and the top surface CJFE of this CV can be regarded as impermeable, adiabatic and shear free (no mass transfer and shear work transfer across these surfaces). The heat transfer rate over the boundary of the CV is \dot{Q} . The approach velocity of the air is U_{app} and the ambient temperature is T_a . The surface temperature of the pin wall is $T_w (> T_a)$. The bulk properties of air are represented by u_{in} , P_{in} , s_{in}

at the inlet and by u_{out} , P_{out} , s_{out} at the outlet respectively. Fluid friction is represented by F_D , which is the sum of the friction drag and pressure drag. The irreversibility of this system is due to heat transfer across the nonzero temperature difference $T_b - T_a$ and to frictional drag.

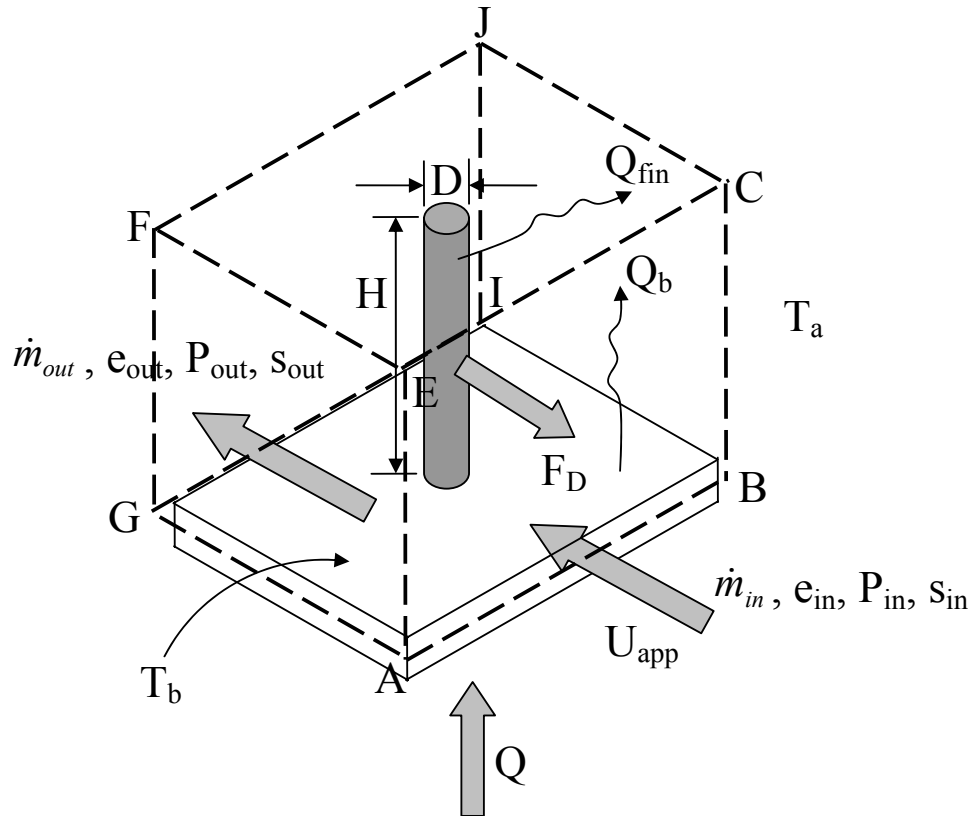


Figure F.1: Control Volume for Calculating \dot{S}_{gen} for Single Circular Pin

The mass rate balance for the CV, shown in Fig. F.1, gives

$$\frac{dm_{cv}}{dt} = \dot{m}_{in} - \dot{m}_{out} \quad (\text{F.1})$$

For steady state, it reduces to

$$\dot{m}_{in} = \dot{m}_{out} = \dot{m} \quad (\text{F.2})$$

First law of thermodynamics for the same CV can be written as

$$\frac{dE_{cv}}{dt} = \mathcal{Q} - \dot{W}_{cv} + \dot{m}_{in}(e_{in} + P_{in}v_{in}) - \dot{m}_{out}(e_{out} + P_{out}v_{out}) \quad (\text{F.3})$$

- $\frac{dE_{cv}}{dt}$ = time rate of change of energy within CV,
 \mathcal{Q} = heat transfer rate over the boundaries of CV,
 \dot{W}_{cv} = energy transfer by work across the boundaries of CV,
 e_{in}, e_{out} = specific energies at the inlet and exit of CV,
 P_{in}, P_{out} = pressure at the inlet and exit of CV,
 v_{in}, v_{out} = specific volume of fluid at the inlet and exit of CV,

For steady state, $\frac{dE_{cv}}{dt} = 0$. The specific energy e is the sum of specific internal, kinetic, and potential energies. Due to continuity and same elevation of the CV, $V_{in} = V_{out}$ and $z_{in} = z_{out}$, so the kinetic and potential energy terms will drop out. Therefore, $e_{in} = u_{in}$ and $e_{out} = u_{out}$. The only work is flow work at the inlet and exit of the CV, so the term \dot{W}_{cv} also drops out. Thus the energy rate balance reduces to:

$$\mathcal{Q} = \dot{m}[\underbrace{(u_{out} + P_{out}v_{out})}_{h_{out}} - \underbrace{(u_{in} + P_{in}v_{in})}_{h_{in}}] \quad (\text{F.4})$$

The combination of specific internal and flow energies is defined as specific enthalpy; therefore, the energy rate balance reduces further to:

$$\mathcal{Q} = \dot{m}(h_{out} - h_{in}) \quad (\text{F.5})$$

From the second law of thermodynamics

$$\frac{dS_{cv}}{dt} = \dot{m}(s_{in} - s_{out}) + \frac{\mathcal{Q}_{fin}}{T_b} + \frac{\mathcal{Q}_b}{T_b} + \dot{S}_{gen} \quad (\text{F.6})$$

For steady state, $\frac{dS_{cv}}{dt} = 0$, and the total heat transferred from the baseplate $\mathcal{Q} = \mathcal{Q}_{fin} + \mathcal{Q}_b$, so the entropy rate balance reduces to

$$\dot{S}_{gen} = \dot{m}(s_{out} - s_{in}) - \frac{\mathcal{Q}}{T_b} \quad (\text{F.7})$$

where T_b represents the baseplate absolute temperature. From a force balance, the total drag force can be written as

$$F_D = -(P_{out} - P_{in})A \quad (\text{F.8})$$

where A is the free stream cross-sectional area. The mass flow rate is given by:

$$\dot{m} = \rho A U_{app} \quad (\text{F.9})$$

where ρ is the density of the fluid at the ambient temperature. Gibb's equation [$dh = Tds + (1/\rho)dP$] can be written as:

$$h_{out} - h_{in} = T_a(s_{out} - s_{in}) + \frac{1}{\rho}(P_{out} - P_{in}) \quad (\text{F.10})$$

Combining Eqs. (F.2 - F.10), the entropy generation rate can be written as:

$$\dot{S}_{gen} = \dot{Q} \left[\frac{1}{T_a} - \frac{1}{T_b} \right] + \frac{F_D U_{app}}{T_a} \quad (\text{F.11})$$

Rearranging the terms and writing $\theta_b = T_b - T_a$, we have

$$\dot{S}_{gen} = \frac{\dot{Q} \theta_b}{T_a T_b} + \frac{F_D U_{app}}{T_a} \quad (\text{F.12})$$

As $\theta_b = \dot{Q} R_{tot}$, the entropy generation rate can be written as:

$$\dot{S}_{gen} = \frac{\dot{Q}^2 R_{tot}}{T_a T_b} + \frac{F_D U_{app}}{T_a} \quad (\text{F.13})$$

This expression describes the entropy generation rate model completely and it shows that the entropy generation rate depends on the total thermal resistance R_{tot} and the drag force, provided that the heat load and ambient conditions are specified. The total resistance R_{tot} is developed in Chapter 5 as R_{hs} and can be obtained from Eq. (5.48):

$$R_{tot} = \frac{1}{\frac{1}{R_c + R_{fin}} + \frac{1}{R_{film}}} \quad (\text{F.14})$$

where

$$R_c = \frac{1}{(hA)_c} \quad (\text{F.15})$$

$$R_{fin} = \frac{1}{(hA\eta)_{fin}} \quad (\text{F.16})$$

$$R_{film} = \frac{1}{h_b \left(LW - \frac{\pi D^2}{4} \right)} \quad (\text{F.17})$$

The drag force is described in Appendix E and is written as the sum of the skin friction drag and the pressure drag:

$$F_D = D_f + D_p \quad (\text{F.18})$$

In dimensionless form, it can be written as:

$$C_D = C_{Df} + C_{Dp} \quad (\text{F.19})$$

where C_{Df} and C_{Dp} are the friction and pressure drag coefficients and are obtained in Chapter 3 (Eqs. 3.25, 3.29, and 3.30 for circular cylinder)

F.2 Model for Pin-Fin Heat Sinks

The control volume for the in-line pin-fin heat sink is shown in Fig. F.2. This control volume includes all pin-fins and the baseplate. Again the side surfaces and the top surface of this control volume can be regarded as impermeable, adiabatic and shear free (no mass transfer and shear work transfer across these surfaces). The heat transfer rate over the boundary of the control volume is \mathcal{Q} . The approach velocity of the air is U_{app} and the ambient temperature is T_a . The temperature of the baseplate is T_b . The properties of air are represented by e_{in} , P_{in} , s_{in} at the inlet and by e_{out} , P_{out} , s_{out} at the outlet respectively. The irreversibility of this system is also due to heat transfer across the nonzero temperature difference $T_b - T_a$ and to the total pressure drop across the heat sink.

The mass, energy, and entropy balances, Eqs. (F.1 - F.7), are also valid for the control volume, whereas Eq. (F.8) is true only for a single pin-fin. So, combining Eqs. (F.1 - F.7) and (F.9 - F.10), we get:

$$\dot{S}_{gen} = \left(\frac{\mathcal{Q}^2}{T_a T_b} \right) R_{hs} + \frac{\dot{m} \Delta P}{\rho T_a} \quad (\text{F.20})$$

where the thermal resistance of the heat sink R_{hs} can be determined from Eq. (5.28) and the total pressure drop across the heat sink can be determined from Eq. (5.52). For a heat sink, the total pressure drop should also include the abrupt contraction and the abrupt expansion effects of the heat sink. This is shown in Fig. F.3. and is given by

$$\Delta P_{tot} = \Delta P_{1-a} + \Delta P_{a-b} + \Delta P_{b-2} \quad (\text{F.21})$$

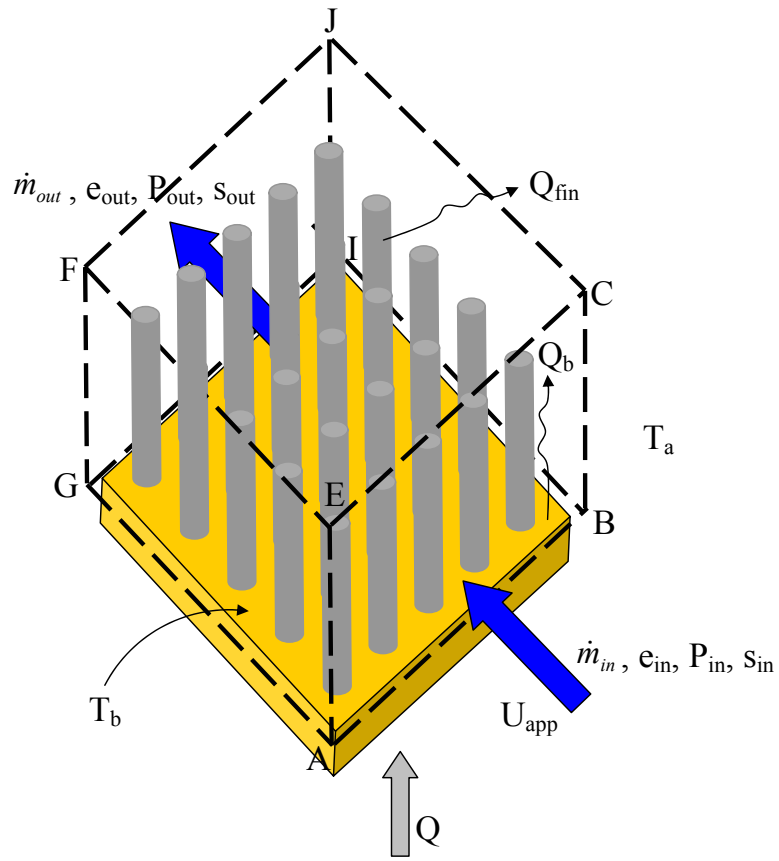


Figure F.2: Control Volume for Calculating \dot{S}_{gen} for Pin-Fin Heat Sink

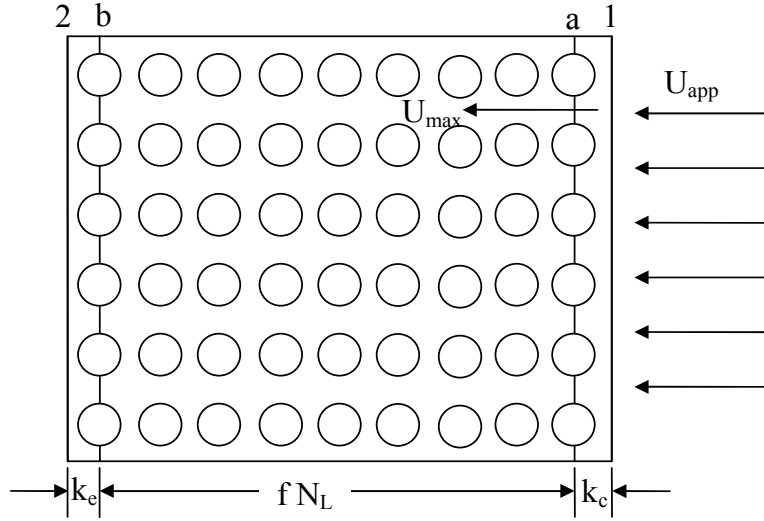


Figure F.3: Dimensionless Pressure Drop Components

where ΔP_{1-a} is the pressure drop due to the irreversible free expansion that always follows the abrupt contraction, ΔP_{a-b} is the pressure loss due to core friction, and ΔP_{b-2} is the pressure loss associated with the irreversible free expansion and momentum changes following an abrupt expansion. These pressure drops can be written as:

$$\Delta P_{1-a} = k_c \cdot \frac{\rho U_{max}^2}{2} \quad (F.22)$$

$$\Delta P_{b-2} = k_e \cdot \frac{\rho U_{max}^2}{2} \quad (F.23)$$

$$\Delta P_{a-b} = f N_L \cdot \frac{\rho U_{max}^2}{2} \quad (F.24)$$

where k_c and k_e are the abrupt contraction and abrupt expansion coefficients respectively, f is the friction factor, and N_L is the number of pins in the longitudinal direction. The coefficients of abrupt contraction and expansion have been established graphically by Kays (1950) for a number of geometries. The mass flow rate through the pins is given by:

$$\dot{m} = \rho U_{app} N_T S_T H D \quad (F.25)$$

The mean velocity in the minimum free cross section between two rows, U_{max} , is used as a reference velocity in the calculations of fluid flow and heat transfer for both types of arrangements, and is given by:

$$U_{max} = \max \left\{ \frac{S_T}{S_T - 1} U_{app}, \frac{S_T}{S_D - 1} U_{app} \right\} \quad (F.26)$$

where U_{app} is the approach velocity, \mathcal{S}_L and \mathcal{S}_T are the dimensionless longitudinal and transverse pitches, and $\mathcal{S}_D = \sqrt{\mathcal{S}_L^2 + (\mathcal{S}_T/2)^2}$ is the dimensionless diagonal pitch in case of the staggered arrangement. Fluid friction factors will be obtained from Chapter 3. The temperature difference, $\theta_b = \mathcal{Q}R_{hs}$, for a heat sink is described in Chapter 5 (Eq. 5.28) and can be written as:

$$R_{hs} = \frac{1}{\frac{N}{R_c + R_{fin}} + \frac{1}{R_{film}}} \quad (\text{F.27})$$

where

$$R_{film} = \frac{1}{h_b \left(LW - N \frac{\pi D^2}{4} \right)} \quad (\text{F.28})$$

F.3 Optimization Code

```
restart:
Newton-Raphson Solver for Systems of Non-Linear Equations
Optimize:=proc(F,X,Xo,Nmax,Nvar)
local neq, delta, eqs, sols, eq, f, i, k, l, S, converge:
global Xs:
neq:=nops(X);
delta:=[seq(Xc[i],i=1..neq)];
Xs:=Xo;
converge:=100:
for i from 1 to neq do
f[i]:=diff(F,X[i]);
eq[i]:=value(sum(Diff(f[i],X[j])*delta[j],j=1..neq)=f[i]):
od;
S:=evalf(subs(seq(X[i]=Xs[i], i=1..neq),F)):
for k from 1 to Nmax while converge > 0.0001 do
printf("%2d ",k);
for l from 1 to Nvar do
printf("%8.5f +%8.5f I ", Re(Xs[l]), Im(Xs[l]));
od;
printf("%8.5f +%8.5f I ",Re(S), Im(S));
printf("%8.5f",converge );
printf(" n");
eqs:=evalf(subs(seq(X[i] = Xs[i], i=1..neq),seq(eq[i], i=1..neq))):
sols:=fsolve(eqs,seq(delta[i], i=1..neq)):
Xs:=subs(sols,[seq(Xs[i]-Xc[i], i=1..neq)]):
converge:=sqrt(subs(sols, add((delta[i]/Xs[i])2, i=1..Nvar)/Nvar)):
S:=evalf(subs(seq(X[i]=Xs[i], i=1..neq),F)):
od;
Xs:=evalf(Xs,5):
end:
```

Appendix G

Boundary-Layer Parameters

Table G.1: Boundary-Layer Parameters For a Circular Pin

θ^0	λ	$\frac{\delta_2}{D}\sqrt{Re_D}$	$\frac{\delta}{D}\sqrt{Re_D}$	$C_f\sqrt{Re_D}$	θ^0	λ	$\frac{\delta_2}{D}\sqrt{Re_D}$	$\frac{\delta}{D}\sqrt{Re_D}$	$C_f\sqrt{Re_D}$
0	7.24	0.01958	1.346	0.00166	31	6.788	0.02191	1.407	4.586
1	7.239	0.01959	1.346	0.1664	32	6.757	0.02208	1.412	4.699
2	7.238	0.01959	1.346	0.3326	33	6.725	0.02225	1.416	4.801
3	7.235	0.0196	1.346	0.4987	34	6.69	0.02243	1.42	4.908
4	7.231	0.01962	1.346	0.6646	35	6.654	0.02262	1.425	5.005
5	7.229	0.01964	1.347	0.8293	36	6.619	0.02282	1.43	5.103
6	7.224	0.01966	1.348	0.9943	37	6.579	0.02302	1.435	5.197
7	7.217	0.01969	1.348	1.159	38	6.54	0.02323	1.44	5.279
8	7.212	0.01973	1.35	1.319	39	6.498	0.02346	1.446	5.371
9	7.204	0.01977	1.35	1.484	40	6.455	0.02369	1.452	5.447
10	7.194	0.01981	1.352	1.644	41	6.411	0.02392	1.458	5.52
11	7.187	0.01986	1.353	1.804	42	6.364	0.02417	1.463	5.595
12	7.176	0.01991	1.354	1.964	43	6.316	0.02443	1.47	5.665
13	7.165	0.01997	1.356	2.119	44	6.266	0.0247	1.476	5.731
14	7.153	0.02003	1.358	2.274	45	6.215	0.02498	1.482	5.794
15	7.14	0.0201	1.36	2.427	46	6.161	0.02527	1.489	5.849
16	7.126	0.02017	1.362	2.581	47	6.106	0.02557	1.496	5.903
17	7.111	0.02025	1.364	2.731	48	6.049	0.02588	1.504	5.949
18	7.095	0.02033	1.366	2.878	49	5.988	0.02621	1.51	5.993
19	7.077	0.02042	1.368	3.027	50	5.926	0.02655	1.518	6.033
20	7.059	0.02051	1.37	3.173	51	5.863	0.0269	1.526	6.065
21	7.04	0.02061	1.373	3.313	52	5.796	0.02726	1.534	6.1
22	7.021	0.02071	1.376	3.454	53	5.729	0.02764	1.542	6.116
23	7	0.02082	1.379	3.587	54	5.658	0.02804	1.552	6.134
24	6.976	0.02093	1.382	3.724	55	5.584	0.02845	1.56	6.156
25	6.954	0.02106	1.385	3.855	56	5.508	0.02887	1.57	6.162
26	6.929	0.02118	1.388	3.983	57	5.43	0.02931	1.579	6.176
27	6.903	0.02132	1.392	4.112	58	5.344	0.02978	1.588	6.172
28	6.878	0.02146	1.396	4.235	59	5.259	0.03025	1.598	6.173
29	6.849	0.0216	1.399	4.355	60	5.174	0.03075	1.608	6.166
30	6.819	0.02175	1.403	4.47	61	5.082	0.03127	1.62	6.158

Table G.1 (cont'd): Boundary-Layer Parameters For a Circular Pin

θ^0	λ	$\frac{\delta_2}{D}\sqrt{Re_D}$	$\frac{\delta}{D}\sqrt{Re_D}$	$C_f\sqrt{Re_D}$	θ^0	λ	$\frac{\delta_2}{D}\sqrt{Re_D}$	$\frac{\delta}{D}\sqrt{Re_D}$	$C_f\sqrt{Re_D}$
62	4.987	0.0318	1.63	6.137	86	1.145	0.0553	2.025	4.316
63	4.89	0.0324	1.642	6.11	87	0.8800	0.057	2.05	4.182
64	4.786	0.0330	1.652	6.085	88	0.6017	0.0588	2.076	4.044
65	4.679	0.0336	1.665	6.057	89	0.3088	0.0607	2.103	3.901
66	4.566	0.0342	1.676	6.022	90	0.0316	0.0625	2.128	3.769
67	4.456	0.0349	1.688	5.984	91	-0.3259	0.0648	2.161	3.601
68	4.349	0.0356	1.704	5.925	92	-0.6704	0.0670	2.191	3.444
69	4.212	0.0363	1.714	5.885	93	-1.035	0.0694	2.224	3.282
70	4.086	0.0370	1.728	5.829	94	-1.422	0.0719	2.258	3.116
71	3.961	0.0378	1.744	5.769	95	-1.834	0.0745	2.294	2.943
72	3.823	0.0386	1.76	5.697	96	-2.273	0.0774	2.332	2.766
73	3.675	0.0395	1.772	5.637	97	-2.742	0.0804	2.372	2.583
74	3.524	0.0404	1.79	5.557	98	-3.245	0.0836	2.414	2.394
75	3.373	0.0413	1.805	5.483	99	-3.787	0.0870	2.46	2.198
76	3.213	0.0423	1.824	5.393	100	-4.372	0.0906	2.509	1.996
77	3.051	0.04337	1.842	5.305	101	-5.009	0.0945	2.562	1.786
78	2.87	0.0444	1.856	5.221	102	-5.706	0.09865	2.619	1.567
79	2.694	0.0456	1.88	5.113	103	-6.475	0.1031	2.683	1.338
80	2.494	0.0468	1.895	5.022	104	-7.334	0.1078	2.753	1.096
81	2.294	0.0480	1.915	4.916	105	-8.308	0.1129	2.833	0.839
82	2.085	0.0494	1.935	4.805	106	-9.439	0.1184	2.926	0.561
83	1.866	0.0507	1.957	4.69	107	-10.8	0.1243	3.039	0.251
84	1.637	0.0521	1.979	4.57	107.7	-12	0.1288	3.14	.001
85	1.397	0.0536	2.002	4.445					

Table G.2: Boundary-Layer Parameters For an Elliptical Pin With $\epsilon = 1/2$

θ^0	λ	$\frac{\delta_2}{D}\sqrt{Re_D}$	$\frac{\delta}{D}\sqrt{Re_D}$	$C_f\sqrt{Re_D}$	θ^0	λ	$\frac{\delta_2}{D}\sqrt{Re_D}$	$\frac{\delta}{D}\sqrt{Re_D}$	$C_f\sqrt{Re_D}$
0	7.23905	0.08080	0.77670	0.01898	29	4.64215	0.12494	1.13400	3.12362
1	7.23343	0.08085	0.77716	0.18962	30	4.53879	0.12766	1.15652	3.13916
2	7.21648	0.08103	0.77855	0.37818	31	4.43732	0.13044	1.17949	3.15115
3	7.18849	0.08133	0.78087	0.56462	32	4.33776	0.13328	1.20289	3.15986
4	7.14983	0.08175	0.78412	0.74793	33	4.24014	0.13615	1.22671	3.16555
5	7.10101	0.08229	0.78828	0.92717	34	4.14446	0.13908	1.25092	3.16845
6	7.04264	0.08294	0.79337	1.10148	35	4.05072	0.14205	1.27551	3.16879
7	6.97542	0.08371	0.79938	1.27007	36	3.95891	0.14506	1.30046	3.16677
8	6.90009	0.08459	0.80629	1.43226	37	3.86899	0.14811	1.32575	3.16259
9	6.81745	0.08558	0.81410	1.58748	38	3.78094	0.15120	1.35136	3.15642
10	6.72833	0.08668	0.82281	1.73526	39	3.69473	0.15432	1.37728	3.14844
11	6.63351	0.08789	0.83239	1.87525	40	3.61030	0.15748	1.40349	3.13878
12	6.53379	0.08921	0.84284	2.00719	41	3.52761	0.16067	1.42998	3.12759
13	6.42994	0.09062	0.85414	2.13095	42	3.44662	0.16389	1.45673	3.11499
14	6.32267	0.09214	0.86628	2.24645	43	3.36725	0.16714	1.48373	3.10111
15	6.21266	0.09375	0.87924	2.35373	44	3.28946	0.17042	1.51096	3.08604
16	6.10053	0.09546	0.89299	2.45288	45	3.21319	0.17372	1.53842	3.64378
17	5.98684	0.09726	0.90751	2.54407	46	3.13836	0.17705	1.56608	3.05274
18	5.87213	0.09915	0.92279	2.62752	47	3.06492	0.18041	1.59395	3.03468
19	5.75684	0.10112	0.93881	2.70348	48	2.99280	0.18378	1.62200	3.01577
20	5.64140	0.10318	0.95553	2.77225	49	2.92192	0.18718	1.65022	2.99608
21	5.52616	0.10532	0.97293	2.83416	50	2.85223	0.19060	1.67862	2.97568
22	5.41146	0.10753	0.99100	2.88954	51	2.78364	0.19404	1.70716	2.95462
23	5.29756	0.10982	1.00971	2.93873	52	2.71609	0.19749	1.73586	3.82987
24	5.18471	0.11217	1.02903	2.98209	53	2.64950	0.20097	1.76469	2.91068
25	5.07311	0.11460	1.04893	3.01998	54	2.58380	0.20446	1.79365	2.88790
26	4.96292	0.11709	1.06941	3.05275	55	2.51891	0.20797	1.82274	2.86462
27	4.85430	0.11965	1.09043	3.08072	56	2.45476	0.21149	1.85193	2.84087
28	4.74734	0.12226	1.11197	3.10424	57	2.39126	0.21502	1.88124	2.81669

Table G.2 (cont'd): Boundary-Layer Parameters For an Elliptical Pin With $\epsilon = 1/2$

θ^0	λ	$\frac{\delta_2}{D}\sqrt{Re_D}$	$\frac{\delta}{D}\sqrt{Re_D}$	$C_f\sqrt{Re_D}$	θ^0	λ	$\frac{\delta_2}{D}\sqrt{Re_D}$	$\frac{\delta}{D}\sqrt{Re_D}$	$C_f\sqrt{Re_D}$
57	2.39126	0.21502	1.88124	2.81669	90	-0.01092	0.33922	2.88770	1.82275
58	2.32834	0.21858	1.91064	2.79209	91	-0.11136	0.34287	2.91613	1.78958
59	2.26593	0.22214	1.94014	2.76710	92	-0.22787	0.34695	2.94786	1.75216
60	2.20392	0.22572	1.96973	2.74173	93	-0.34995	0.35107	2.97976	1.71413
61	2.14225	0.22931	1.99939	2.71601	94	-0.47806	0.35522	3.01183	1.67544
62	2.08083	0.23291	2.02914	2.68994	95	-0.61268	0.35941	3.04410	1.63606
63	2.01957	0.23652	2.05896	2.66355	96	-0.75437	0.36364	3.07659	1.59596
64	1.95837	0.24014	2.08884	2.63683	97	-0.90369	0.36792	3.10934	1.55508
65	1.89716	0.24378	2.11879	2.60979	98	-1.06130	0.37224	3.14236	1.51340
66	1.83583	0.24743	2.14880	2.58245	99	-1.22790	0.37662	3.17571	1.47086
67	1.77429	0.25108	2.17886	2.55480	100	-1.40427	0.38105	3.20941	1.42741
68	1.71244	0.25475	2.20898	2.52686	101	-1.59126	0.38554	3.24352	1.38300
69	1.65017	0.25843	2.23915	2.49861	102	-1.78981	0.39010	3.27809	1.33755
70	1.58738	0.26212	2.26937	2.47006	103	-2.00099	0.39472	3.31318	1.29101
71	1.52395	0.26582	2.29964	2.44122	104	-2.22597	0.39942	3.34886	1.24329
72	1.45977	0.26953	2.32995	2.41207	105	-2.46607	0.40419	3.38523	1.19432
73	1.39471	0.27325	2.36030	2.38261	106	-2.72278	0.40906	3.42237	1.14400
74	1.32865	0.27699	2.39070	2.35285	107	-2.99781	0.41401	3.46041	1.09222
75	1.26146	0.28073	2.42115	2.32277	108	-3.29307	0.41906	3.49949	1.03886
76	1.19299	0.28449	2.45163	2.29237	109	-3.61082	0.42422	3.53978	0.98380
77	1.12310	0.28826	2.48217	2.26163	110	-3.95363	0.42950	3.58149	0.92686
78	1.05163	0.29204	2.51274	2.23056	111	-4.32457	0.43489	3.62485	0.86787
79	0.97842	0.29584	2.54337	2.19913	112	-4.72726	0.44042	3.67019	0.80662
80	0.90330	0.29966	2.57404	2.16735	113	-5.16608	0.44609	3.71790	0.74283
81	0.82608	0.30348	2.60477	2.13519	114	-5.64643	0.45192	3.76848	0.67620
82	0.74657	0.30733	2.63555	2.10265	115	-6.17506	0.45791	3.82258	0.60632
83	0.73485	0.31119	2.80386	1.97916	116	-6.76068	0.46409	3.88108	0.53269
84	0.57984	0.31507	2.69731	2.03634	117	-7.41489	0.47045	3.94521	0.45462
85	0.49215	0.31897	2.72829	2.00255	118	-8.15380	0.47703	4.01674	0.37118
86	0.40127	0.32289	2.75935	1.96830	119	-9.00115	0.48383	4.09838	0.28097
87	0.30691	0.32684	2.79050	1.93359	120	-9.99491	0.49088	4.19466	0.18174
88	0.20879	0.33081	2.82174	1.89838	121	-11.99902	0.50229	4.39499	0.00008
89	0.01087	0.33842	2.88139	1.83005					

Table G.3: Boundary-Layer Parameters For an Elliptic Pin with $\epsilon = 1/3$

θ^0	λ	$\frac{\delta_2}{D}\sqrt{Re_D}$	$\frac{\delta}{D}\sqrt{Re_D}$	$C_f\sqrt{Re_D}$	θ^0	λ	$\frac{\delta_2}{D}\sqrt{Re_D}$	$\frac{\delta}{D}\sqrt{Re_D}$	$C_f\sqrt{Re_D}$
0	7.23892	0.05207	0.50059	0.02428	33	2.35726	0.14930	1.30564	2.22624
1	7.22105	0.05220	0.50154	0.24215	34	2.27615	0.15361	1.34179	2.20943
2	7.16769	0.05256	0.50440	0.48015	35	2.19861	0.15794	1.37815	2.19246
3	7.08124	0.05318	0.50916	0.71010	36	2.12445	0.16229	1.41469	2.17538
4	6.96513	0.05403	0.51581	0.92857	37	2.05348	0.16665	1.45140	2.15825
5	6.82355	0.05511	0.52433	1.13280	38	1.98552	0.17104	1.48825	2.14110
6	6.66102	0.05642	0.53470	1.32076	39	1.92038	0.17543	1.52523	2.12395
7	6.48213	0.05795	0.54687	1.49117	40	1.85792	0.17984	1.56232	2.10684
8	6.29118	0.05969	0.56079	1.64346	41	1.79798	0.18427	1.59951	2.08978
9	6.09204	0.06163	0.57640	1.77770	42	1.74040	0.18870	1.63678	2.07278
10	5.88809	0.06376	0.59363	1.89442	43	1.68505	0.19313	1.67412	2.05586
11	5.68218	0.06607	0.61241	1.99458	44	1.63179	0.19758	1.71150	2.42020
12	5.47666	0.06855	0.63266	2.07936	45	1.58050	0.20202	1.74893	2.02227
13	5.27338	0.07120	0.65429	2.15010	46	1.53107	0.20647	1.78639	2.00560
14	5.07382	0.07399	0.67722	2.20820	47	1.48337	0.21093	1.82387	1.98902
15	4.87909	0.07692	0.70137	2.25507	48	1.43730	0.21538	1.86135	1.97254
16	4.68999	0.07999	0.72666	2.29205	49	1.39275	0.21983	1.89883	1.95614
17	4.50711	0.08317	0.75301	2.32041	50	1.34964	0.22428	1.93630	1.93982
18	4.33080	0.08647	0.78036	2.34130	51	1.30786	0.22873	1.97375	2.77058
19	4.16128	0.08988	0.80862	2.35578	52	1.26733	0.23318	2.01117	1.90741
20	3.99864	0.09338	0.83774	2.36478	53	1.22796	0.23762	2.04856	1.89132
21	3.84285	0.09697	0.86764	2.36911	54	1.18967	0.24206	2.08589	1.87529
22	3.69384	0.10065	0.89827	2.36951	55	1.11602	0.25091	2.16041	1.84340
23	3.55145	0.10440	0.92958	2.36660	56	1.08051	0.25533	2.19757	1.82753
24	3.41550	0.10823	0.96150	2.36092	57	1.04578	0.25974	2.23466	1.81170
25	3.16203	0.11607	1.02703	2.34303	58	1.01176	0.26414	2.27167	1.79591
26	3.04402	0.12007	1.06054	2.33155	59	0.97839	0.26853	2.30860	1.78014
27	2.93149	0.12413	1.09450	2.31878	60	0.94560	0.27292	2.34544	1.76439
30	2.62422	0.13656	1.19867	2.27496	61	0.91333	0.27729	2.38218	1.74866
31	2.53108	0.14078	1.23405	2.25910	62	0.88151	0.28165	2.41883	1.73294
32	2.44217	0.14503	1.26972	2.24282	63	0.85009	0.28601	2.45538	1.71722

Table G.3 (cont'd): Boundary-Layer Parameters For an Elliptic Pin with $\epsilon = 1/3$

θ^0	λ	$\frac{\delta_2}{D} \sqrt{Re_D}$	$\frac{\delta}{D} \sqrt{Re_D}$	$C_f \sqrt{Re_D}$	θ^0	λ	$\frac{\delta_2}{D} \sqrt{Re_D}$	$\frac{\delta}{D} \sqrt{Re_D}$	$C_f \sqrt{Re_D}$
64	0.81899	0.29035	2.49182	1.70149	98	-0.43395	0.42279	3.58602	1.15634
65	0.78817	0.29467	2.52814	1.68576	99	-0.50120	0.42677	3.61786	1.13654
66	0.75756	0.29899	2.56435	1.67000	100	-0.57219	0.43076	3.64957	1.11644
67	0.72709	0.30330	2.60045	1.65423	101	-0.64722	0.43474	3.68117	1.09604
68	0.69672	0.30759	2.63642	1.63842	102	-0.72665	0.43873	3.71267	1.07531
69	0.66637	0.31187	2.67226	1.62258	103	-0.81085	0.44272	3.74407	1.05424
70	0.63599	0.31614	2.70798	1.60669	104	-0.90023	0.44672	3.77539	1.03281
71	0.60551	0.32039	2.74356	1.59076	105	-0.99523	0.45072	3.80663	1.01099
72	0.57486	0.32463	2.77901	1.57477	106	-1.09636	0.45474	3.83782	0.98876
73	0.54399	0.32886	2.81433	1.55872	107	-1.20415	0.45876	3.86897	0.96610
74	0.51282	0.33307	2.84950	1.54260	108	-1.31919	0.46280	3.90009	0.94297
75	0.48129	0.33728	2.88454	1.52640	109	-1.44215	0.46686	3.93121	0.91935
76	0.44931	0.34146	2.91943	1.51013	110	-1.57376	0.47094	3.96237	0.89520
77	0.41682	0.34564	2.95417	1.49377	111	-1.71482	0.47504	3.99358	0.87049
78	0.38374	0.34980	2.98877	1.47731	112	-1.86624	0.47917	4.02489	0.84517
79	0.34998	0.35395	3.02322	1.46076	113	-2.02901	0.48333	4.05633	0.81920
80	0.31547	0.35808	3.05752	1.44410	114	-2.20428	0.48752	4.08798	0.79254
81	0.30865	0.36221	3.24539	1.36288	115	-2.39329	0.49175	4.11987	0.76512
82	0.24379	0.36632	3.12567	1.41042	116	-2.59749	0.49603	4.15210	0.73688
83	0.20643	0.37041	3.15952	1.39339	117	-2.81849	0.50036	4.18475	0.70776
84	0.16792	0.37450	3.19322	1.37623	118	-3.05816	0.50474	4.21793	0.67768
85	0.12815	0.37857	3.22677	1.35892	119	-3.31862	0.50918	4.25178	0.64655
86	0.08699	0.38264	3.26016	1.34146	120	-3.60234	0.51370	4.28645	0.61426
87	0.04432	0.38669	3.29340	1.32383	121	-3.91220	0.51828	4.32216	0.58071
88	0.00451	0.39033	3.32319	1.30783	122	-4.25159	0.52296	4.35917	0.54575
89	-0.04612	0.39476	3.35944	1.28807	123	-4.62457	0.52772	4.39779	0.50922
90	-0.09418	0.39879	3.39223	1.26990	124	-5.03603	0.53259	4.43846	0.47094
91	-0.14437	0.40280	3.42488	1.25154	125	-5.49200	0.53757	4.48171	0.43066
92	-0.19686	0.40681	3.45739	1.23297	126	-6.00007	0.54268	4.52828	0.38809
93	-0.25184	0.41081	3.48975	1.21418	127	-6.57002	0.54792	4.57918	0.34286
94	-0.30953	0.41481	3.52197	1.19515	128	-7.21489	0.55332	4.63582	0.29448
95	-0.37015	0.41880	3.55406	1.17588	129	-7.95283	0.55889	4.70030	0.24226
96	-0.3805	0.41890	3.55406	1.17588	130	-8.81070	0.56464	4.77590	0.18521
97	-0.39034	0.42880	3.55406	1.17588	131	-9.83172	0.57060	4.86822	0.12170
					132	-11.99775	0.58047	5.07898	0.00012

Table G.4: Boundary-Layer Parameters For an Elliptical Pin With $\epsilon = 1/4$

θ^0	λ	$\frac{\delta_2}{D} \sqrt{Re_D}$	$\frac{\delta}{D} \sqrt{Re_D}$	$C_f \sqrt{Re_D}$	θ^0	λ	$\frac{\delta_2}{D} \sqrt{Re_D}$	$\frac{\delta}{D} \sqrt{Re_D}$	$C_f \sqrt{Re_D}$
0	7.23884	0.04425	0.42543	0.02717	38	1.58804	0.17333	1.50063	1.91916
1	7.21258	0.04441	0.42661	0.27058	39	1.53073	0.17802	1.54017	1.90332
2	7.13469	0.04487	0.43018	0.53441	40	1.47613	0.18271	1.57978	1.88766
3	7.01013	0.04563	0.43613	0.78534	41	1.42406	0.18742	1.61943	1.87220
4	6.84577	0.04669	0.44443	1.01831	42	1.37435	0.19212	1.65911	1.85693
5	6.64957	0.04803	0.45505	1.22969	43	1.32685	0.19683	1.69882	1.84184
6	6.42966	0.04965	0.46792	1.41733	44	1.28141	0.20154	1.73853	1.82692
7	6.19359	0.05152	0.48296	1.58047	45	1.23791	0.20624	1.77824	2.15095
8	5.94795	0.05364	0.50009	1.71953	46	1.19621	0.21095	1.81794	1.79759
9	5.69821	0.05599	0.51918	1.83581	47	1.15621	0.21565	1.85761	1.78316
10	5.44872	0.05856	0.54013	1.93118	48	1.11777	0.22035	1.89725	1.76887
11	5.20282	0.06133	0.56281	2.00783	49	1.08081	0.22504	1.93685	1.75472
12	4.96297	0.06428	0.58709	2.06807	50	1.04523	0.22972	1.97639	1.74069
13	4.73092	0.06741	0.61286	2.11416	51	1.01093	0.23440	2.01587	1.72677
14	4.50784	0.07069	0.63999	2.14823	52	0.97782	0.23907	2.05529	2.52562
15	4.29444	0.07411	0.66838	2.17219	53	0.94583	0.24373	2.09463	1.69925
16	4.09109	0.07767	0.69793	2.18777	54	0.91487	0.24838	2.13389	1.68563
17	3.89789	0.08135	0.72852	2.19644	55	0.88487	0.25303	2.17306	1.67209
18	3.71475	0.08514	0.76008	2.19946	56	0.85576	0.25766	2.21213	1.65863
19	3.54145	0.08902	0.79252	2.19791	57	0.82748	0.26227	2.25110	1.64522
20	3.37766	0.09300	0.82576	2.19268	58	0.79995	0.26688	2.28997	1.63188
21	3.22300	0.09707	0.85973	2.18452	59	0.77312	0.27147	2.32872	1.61858
22	3.07705	0.10121	0.89435	2.17405	60	0.74694	0.27605	2.36735	1.60532
23	2.93935	0.10541	0.92958	2.16178	61	0.72133	0.28062	2.40586	1.59209
24	2.80946	0.10968	0.96535	2.14810	62	0.69625	0.28517	2.44425	1.57889
25	2.68692	0.11400	1.00161	2.13337	63	0.67164	0.28971	2.48250	1.56572
26	2.57130	0.11838	1.03832	2.11785	64	0.64746	0.29423	2.52061	1.55255
27	2.46217	0.12280	1.07543	2.10177	65	0.62365	0.29873	2.55858	1.53939
28	2.35912	0.12726	1.11290	2.08530	66	0.60015	0.30322	2.59641	1.52623
29	2.26177	0.13176	1.15070	2.06857	67	0.57693	0.30770	2.63408	1.51307
30	2.16975	0.13629	1.18878	2.05171	68	0.55394	0.31215	2.67161	1.49989
31	2.08271	0.14085	1.22713	2.03480	69	0.53112	0.31659	2.70898	1.48670
32	2.00033	0.14543	1.26571	2.01791	70	0.50842	0.32101	2.74619	1.47349
33	1.92230	0.15004	1.30449	2.00110	71	0.48581	0.32542	2.78323	1.46024
34	1.84834	0.15467	1.34345	1.98439	72	0.46323	0.32980	2.82011	1.44696
35	1.77817	0.15931	1.38256	1.96782	73	0.44063	0.33417	2.85683	1.43365
36	1.71155	0.16397	1.42181	1.95142	74	0.41797	0.33852	2.89337	1.42029
37	1.64825	0.16864	1.46117	1.93520	75	0.39519	0.34285	2.92973	1.40688

Table G.4 (cont'd): Boundary-Layer Parameters For an Elliptical Pin With $\epsilon = 1/4$

θ^0	λ	$\frac{\delta_2}{D}\sqrt{Re_D}$	$\frac{\delta}{D}\sqrt{Re_D}$	$C_f\sqrt{Re_D}$	θ^0	λ	$\frac{\delta_2}{D}\sqrt{Re_D}$	$\frac{\delta}{D}\sqrt{Re_D}$	$C_f\sqrt{Re_D}$
76	0.37225	0.34716	2.96592	1.39342	107	-0.86091	0.47236	3.99323	0.91835
77	0.34908	0.35146	3.00193	1.37989	108	-0.94288	0.47621	4.02342	0.89979
78	0.32564	0.35573	3.03776	1.36631	109	-1.03044	0.48007	4.05346	0.88089
79	0.30187	0.35999	3.07340	1.35265	110	-1.12410	0.48392	4.08338	0.86162
80	0.27772	0.36423	3.10886	1.33892	111	-1.22444	0.48779	4.11319	0.84198
81	0.25311	0.36845	3.14414	1.32511	112	-1.33206	0.49166	4.14290	0.82192
82	0.22800	0.37265	3.17922	1.31122	113	-1.44766	0.49554	4.17254	0.80142
83	0.22245	0.37683	3.37031	1.23916	114	-1.57200	0.49943	4.20212	0.78046
84	0.17597	0.38099	3.24881	1.28316	115	-1.70594	0.50334	4.23167	0.75899
85	0.14892	0.38513	3.28332	1.26898	116	-1.85044	0.50726	4.26124	0.73699
86	0.12107	0.38926	3.31763	1.25470	117	-2.00655	0.51121	4.29086	0.71440
87	0.09234	0.39337	3.35175	1.24031	118	-2.17550	0.51519	4.32057	0.69118
88	0.06265	0.39746	3.38567	1.22580	119	-2.35864	0.51920	4.35045	0.66728
89	0.03190	0.40153	3.41939	1.21117	120	-2.55751	0.52324	4.38057	0.64265
90	0.00325	0.40518	3.44958	1.19790	121	-2.77390	0.52732	4.41100	0.61721
91	-0.03316	0.40962	3.48625	1.18152	122	-3.00980	0.53146	4.44188	0.59090
92	-0.06770	0.41364	3.51937	1.16649	123	-3.26757	0.53564	4.47332	0.56362
93	-0.10372	0.41764	3.55231	1.15131	124	-3.54992	0.53988	4.50551	0.53528
94	-0.14137	0.42163	3.58504	1.13598	125	-3.86004	0.54420	4.53866	0.50576
95	-0.18078	0.42560	3.61757	1.12048	126	-3.86795	0.54858	4.57519	0.51619
96	-0.22211	0.42956	3.64991	1.10481	127	-4.57944	0.55306	4.60901	0.44265
97	-0.26551	0.43350	3.68205	1.08896	128	-4.99879	0.55762	4.64704	0.40871
98	-0.31116	0.43743	3.71400	1.07293	129	-5.46661	0.56230	4.68773	0.37288
99	-0.35925	0.44135	3.74576	1.05669	130	-5.99157	0.56709	4.73192	0.33486
100	-0.40998	0.44525	3.77732	1.04025	131	-6.58501	0.57201	4.78077	0.29428
101	-0.46359	0.44915	3.80870	1.02359	132	-7.26225	0.57708	4.83597	0.25064
102	-0.52032	0.45303	3.83989	1.00671	133	-8.04504	0.58232	4.90006	0.20321
103	-0.58043	0.45691	3.87090	0.98958	134	-8.96638	0.58774	4.97718	0.15094
104	-0.64421	0.46078	3.90173	0.97219	135	-10.08160	0.59336	5.07471	0.09202
105	-0.71198	0.46464	3.93239	0.95454	136	-11.49997	0.59921	5.20819	0.02296
106	-0.78409	0.46850	3.96289	0.93660	137	-11.99956	0.60095	5.25832	0.00002

Table G.5: Boundary-Layer Parameters For a Circular Pin Between Parallel Planes for $b=0.8$

θ^0	λ	$\frac{\delta_2}{D}\sqrt{Re_D}$	$\frac{\delta}{D}\sqrt{Re_D}$	$C_f\sqrt{Re_D}$	θ^0	λ	$\frac{\delta_2}{D}\sqrt{Re_D}$	$\frac{\delta}{D}\sqrt{Re_D}$	$C_f\sqrt{Re_D}$
0	7.2391	0.1151	1.1065	0.01337	30	7.14272	0.11698	1.12184	3.87803
1	7.23893	0.1151	1.10652	0.13373	31	7.14005	0.11708	1.12269	4.00028
2	7.23842	0.11511	1.10658	0.26743	32	7.13773	0.11718	1.12355	4.12214
3	7.23758	0.11512	1.10668	0.40105	33	7.13579	0.11727	1.12441	4.24363
4	7.2364	0.11514	1.10682	0.53456	34	7.13424	0.11737	1.12527	4.36478
5	7.23489	0.11517	1.10699	0.66792	35	7.1331	0.11746	1.12613	4.48562
6	7.23306	0.11519	1.10721	0.8011	36	7.13235	0.11755	1.12698	4.60617
7	7.23092	0.11523	1.10746	0.93406	37	7.13201	0.11764	1.12783	4.72647
8	7.22851	0.11526	1.10776	1.06677	38	7.13204	0.11773	1.12866	4.84654
9	7.22578	0.11531	1.10808	1.1992	39	7.13243	0.11781	1.12948	4.96641
10	7.22278	0.11535	1.10845	1.33131	40	7.13312	0.11789	1.13028	5.08609
11	7.21954	0.1154	1.10885	1.46308	41	7.13406	0.11797	1.13107	5.20561
12	7.21606	0.11546	1.10929	1.59447	42	7.13519	0.11805	1.13184	5.32496
13	7.21236	0.11552	1.10976	1.72547	43	7.13641	0.11812	1.13258	5.44416
14	7.20847	0.11558	1.11026	1.85604	44	7.13759	0.11819	1.1333	5.5632
15	7.20441	0.11565	1.1108	1.98617	45	7.13861	0.11826	1.13399	5.68205
16	7.20019	0.11572	1.11137	2.11584	46	7.13929	0.11833	1.13465	5.8007
17	7.19585	0.1158	1.11197	2.24503	47	7.13947	0.11839	1.13528	5.91909
18	7.19143	0.11588	1.1126	2.37372	48	7.13889	0.11846	1.13587	6.03715
19	7.18693	0.11596	1.11325	2.5019	49	7.13734	0.11852	1.13644	6.15482
20	7.18241	0.11604	1.11394	2.62957	50	7.1345	0.11858	1.13696	6.27197
21	7.17788	0.11613	1.11464	2.75672	51	7.13008	0.11865	1.13745	6.38849
22	7.17339	0.11622	1.11537	2.88334	52	7.1237	0.11872	1.1379	6.5042
23	7.16896	0.11631	1.11612	3.00943	53	7.11498	0.11878	1.13832	6.61893
24	7.16464	0.1164	1.11689	3.13501	54	7.1035	0.11886	1.1387	6.73246
25	7.16044	0.1165	1.11768	3.26007	55	7.08879	0.11894	1.13904	6.84451
26	7.15642	0.11659	1.11849	3.38462	56	7.07036	0.11903	1.13936	6.9548
27	7.1526	0.11669	1.11931	3.50867	57	7.04767	0.11912	1.13965	7.06299
28	7.14903	0.11679	1.12014	3.63225	58	7.02018	0.11923	1.13991	7.16868
29	7.14572	0.11689	1.12098	3.75536	59	6.98729	0.11936	1.14016	7.27147

Table G.5 (cont'd): Boundary-Layer Parameters For a Circular Pin Between Parallel Planes for b=0.8

θ^0	λ	$\frac{\delta_2}{D}\sqrt{Re_D}$	$\frac{\delta}{D}\sqrt{Re_D}$	$C_f\sqrt{Re_D}$	θ^0	λ	$\frac{\delta_2}{D}\sqrt{Re_D}$	$\frac{\delta}{D}\sqrt{Re_D}$	$C_f\sqrt{Re_D}$
60	6.95	0.1195	1.14041	7.37085	85	2.30969	0.14168	1.23817	6.63043
61	6.91	0.11966	1.14066	7.46633	86	1.90406	0.14409	1.25242	6.38884
62	6.85	0.11984	1.14093	7.5573	87	1.47252	0.14669	1.26823	6.12811
63	6.78967	0.12005	1.14125	7.64316	88	1.013	0.1495	1.28573	5.8486
64	6.72062	0.12029	1.14162	7.72322	89	0.52311	0.15253	1.30506	5.55076
65	6.64248	0.12057	1.14207	7.79677	90	0.0539	0.15546	1.32418	5.26747
66	6.55462	0.12088	1.14263	7.86305	91	-0.55971	0.15932	1.34994	4.90222
67	6.45648	0.12123	1.14333	7.92125	92	-1.1601	0.1631	1.37591	4.55259
68	6.34748	0.12163	1.14421	7.97052	93	-1.80615	0.16716	1.40457	4.18668
69	6.22707	0.12209	1.1453	8.01	94	-2.50408	0.17152	1.43626	3.80482
70	6.09473	0.1226	1.14666	8.03879	95	-3.2618	0.17618	1.4714	3.40708
71	5.94995	0.12317	1.14831	8.05598	96	-4.08965	0.18118	1.51056	2.99311
72	5.79222	0.12381	1.15033	8.06067	97	-4.53406	0.18381	1.53186	2.77976
73	5.62106	0.12453	1.15275	8.05194	98	-5.00165	0.18653	1.55447	2.5619
74	5.43599	0.12533	1.15564	8.02891	99	-5.49511	0.18934	1.57854	2.33923
75	5.23649	0.12622	1.15907	7.99071	100	-6.0177	0.19225	1.60423	2.11133
76	5.02206	0.1272	1.16308	7.93652	101	-6.57352	0.19525	1.63179	1.87763
77	4.79215	0.12829	1.16776	7.86558	102	-7.16781	0.19835	1.66149	1.63732
78	4.54617	0.12948	1.17317	7.77719	103	-7.80739	0.20156	1.69372	1.38929
79	4.28348	0.1308	1.17938	7.67073	104	-8.50158	0.20487	1.72901	1.13193
80	4.00337	0.13224	1.18648	7.54567	105	-9.26357	0.20829	1.76811	0.86288
81	3.70504	0.13382	1.19454	7.40158	106	-10.11336	0.21182	1.81219	0.5784
82	3.3876	0.13554	1.20365	7.23815	107	-11.08387	0.21547	1.86318	0.27218
83	3.05003	0.13742	1.21389	7.05519	108	-11.98712	0.21848	1.91132	0.00372
84	2.69117	0.13946	1.22536	6.8526					

Table G.6: Boundary-Layer Parameters For a Circular Pin Between Parallel Planes for $b=0.5$

θ^0	λ	$\frac{\delta_2}{D}\sqrt{Re_D}$	$\frac{\delta}{D}\sqrt{Re_D}$	$C_f\sqrt{Re_D}$	θ^0	λ	$\frac{\delta_2}{D}\sqrt{Re_D}$	$\frac{\delta}{D}\sqrt{Re_D}$	$C_f\sqrt{Re_D}$
0	7.24	0.12787	1.22928	0.01542	30	6.89	0.13345	1.272	4.23024
1	7.24	0.12788	1.22933	0.1542	31	6.87	0.13385	1.27501	4.34392
2	7.24	0.1279	1.22946	0.30831	32	6.85	0.13427	1.27814	4.45496
3	7.23	0.12793	1.22969	0.46224	33	6.82	0.1347	1.28139	4.56328
4	7.23	0.12797	1.23001	0.61591	34	6.79	0.13514	1.28476	4.66881
5	7.23	0.12802	1.23043	0.76921	35	6.76	0.13561	1.28825	4.77145
6	7.23	0.12809	1.23093	0.92207	36	6.73	0.13609	1.29187	4.87114
7	7.22	0.12816	1.23153	1.07439	37	6.69	0.13659	1.29561	4.9678
8	7.22	0.12825	1.23222	1.22609	38	6.66	0.13711	1.29949	5.06134
9	7.21	0.12836	1.233	1.37708	39	6.63	0.13765	1.30349	5.15168
10	7.20	0.12847	1.23388	1.52726	40	6.59	0.13821	1.30763	5.23876
11	7.19	0.12859	1.23484	1.67656	41	6.55	0.13878	1.31192	5.32248
12	7.19	0.12873	1.23591	1.82487	42	6.51	0.13938	1.31634	5.40277
13	7.18	0.12888	1.23707	1.97213	43	6.47	0.14	1.32091	5.47955
14	7.17	0.12904	1.23832	2.11823	44	6.43	0.14064	1.32562	5.55274
15	7.16	0.12922	1.23967	2.2631	45	6.39	0.14131	1.33049	5.62226
16	7.15	0.12941	1.24111	2.40664	46	6.34	0.14199	1.33552	5.68802
17	7.13	0.12961	1.24266	2.54877	47	6.29	0.14271	1.34071	5.74996
18	7.12	0.12982	1.2443	2.68942	48	6.24	0.14344	1.34607	5.80798
19	7.11	0.13005	1.24604	2.82848	49	6.19	0.1442	1.3516	5.86202
20	7.09	0.13029	1.24788	2.96588	50	6.13	0.14499	1.3573	5.91198
21	7.08	0.13054	1.24982	3.10153	51	6.07	0.14581	1.36319	5.95778
22	7.06	0.13081	1.25186	3.23536	52	6.01	0.14666	1.36927	5.99935
23	7.04	0.13109	1.254	3.36727	53	5.95	0.14753	1.37554	6.03661
24	7.03	0.13138	1.25625	3.49718	54	5.89	0.14844	1.38201	6.06947
25	7.01	0.13169	1.2586	3.62502	55	5.82	0.14938	1.38869	6.09786
26	6.99	0.13201	1.26106	3.75071	56	5.75	0.15035	1.39558	6.1217
27	6.97	0.13235	1.26363	3.87415	57	5.67	0.15136	1.4027	6.1409
28	6.95	0.1327	1.26631	3.99527	58	5.59	0.1524	1.41006	6.15539
29	6.92	0.13307	1.2691	4.11399	59	5.52	0.15348	1.41765	6.16509

Table G.6 (cont'd): Boundary-Layer Parameters For a Circular Pin Between Parallel Planes for b=0.5

θ^0	λ	$\frac{\delta_2}{D}\sqrt{Re_D}$	$\frac{\delta}{D}\sqrt{Re_D}$	$C_f\sqrt{Re_D}$	θ^0	λ	$\frac{\delta_2}{D}\sqrt{Re_D}$	$\frac{\delta}{D}\sqrt{Re_D}$	$C_f\sqrt{Re_D}$
60	5.43	0.1546	1.4255	6.16994	85	1.51	0.20217	1.74875	4.55041
61	5.34	0.15577	1.4336	6.16985	86	1.24	0.20524	1.76969	4.41293
62	5.25	0.15697	1.44198	6.16475	87	0.95	0.20845	1.79162	4.26987
63	5.16	0.15822	1.45064	6.15457	88	0.65	0.2118	1.8146	4.12124
64	5.06	0.15951	1.4596	6.13925	89	0.33	0.2153	1.83872	3.96705
65	4.95	0.16086	1.46887	6.11873	90	0.03	0.21858	1.86147	3.82352
66	4.85	0.16225	1.47846	6.09293	91	-0.35	0.22277	1.89073	3.64194
67	4.73	0.1637	1.48839	6.06181	92	-0.73	0.22676	1.91883	3.47097
68	4.62	0.1652	1.49867	6.0253	93	-1.13	0.23093	1.9485	3.29431
69	4.49	0.16676	1.50932	5.98336	94	-1.55	0.23529	1.97988	3.11186
70	4.36	0.16838	1.52035	5.93594	95	-2.00	0.23985	2.01317	2.92349
71	4.22	0.17006	1.53179	5.88301	96	-2.49	0.24462	2.04857	2.729
72	4.08	0.17181	1.54366	5.82451	97	-2.74	0.24709	2.06714	2.62939
73	3.96	0.17363	1.55597	5.76042	98	-3.00	0.24962	2.08635	2.52813
74	3.78	0.17552	1.56876	5.69072	99	-3.56	0.25486	2.12681	2.3205
75	3.62	0.17748	1.58203	5.61537	100	-4.16	0.26035	2.17036	2.1056
76	3.45	0.17953	1.59583	5.53437	101	-4.82	0.2661	2.2175	1.88271
77	3.27	0.18166	1.61018	5.4477	102	-5.53	0.27214	2.26892	1.65084
78	3.09	0.18387	1.6251	5.35535	103	-6.32	0.27847	2.32555	1.40856
79	2.89	0.18617	1.64063	5.25733	104	-7.20	0.28512	2.3887	1.15371
80	2.69	0.18857	1.6568	5.15364	105	-8.20	0.29211	2.46041	0.88296
81	2.48	0.19107	1.67366	5.04427	106	-9.36	0.29946	2.54409	0.5906
82	2.25	0.19368	1.69124	4.92925	107	-10.76	0.30719	2.64621	0.26566
83	2.02	0.19639	1.70958	4.80859	108	-11.97	0.31284	2.73628	0.00602
84	1.77	0.19922	1.72873	4.68231					

Table G.7: Boundary-Layer Parameters For a Circular Pin Between Parallel Planes for $b=0.2$

θ^0	λ	$\frac{\delta_2}{D}\sqrt{Re_D}$	$\frac{\delta}{D}\sqrt{Re_D}$	$C_f\sqrt{Re_D}$	θ^0	λ	$\frac{\delta_2}{D}\sqrt{Re_D}$	$\frac{\delta}{D}\sqrt{Re_D}$	$C_f\sqrt{Re_D}$
0	7.24	0.13771	1.32383	0.01562	30	6.82	0.14509	1.38036	4.19963
1	7.24	0.13772	1.32386	0.15618	31	6.79	0.14562	1.38437	4.30655
2	7.24	0.13774	1.32407	0.31223	32	6.76	0.14616	1.38849	4.41044
3	7.23	0.13778	1.32437	0.46807	33	6.73	0.14673	1.39281	4.51112
4	7.23	0.13783	1.32481	0.62357	34	6.69	0.14733	1.39727	4.60858
5	7.23	0.1379	1.32532	0.77864	35	6.66	0.14794	1.40187	4.70269
6	7.22	0.13799	1.32602	0.93313	36	6.62	0.14858	1.40671	4.79324
7	7.22	0.13809	1.32675	1.08702	37	6.58	0.14924	1.41163	4.88053
8	7.21	0.13821	1.3277	1.24007	38	6.54	0.14992	1.41677	4.96415
9	7.21	0.13834	1.32873	1.39225	39	6.50	0.15063	1.42208	5.04418
10	7.20	0.13849	1.32988	1.54344	40	6.46	0.15136	1.42754	5.1206
11	7.19	0.13866	1.33116	1.69354	41	6.42	0.15212	1.43324	5.19313
12	7.18	0.13884	1.33257	1.84244	42	6.37	0.1529	1.43908	5.26197
13	7.16	0.13904	1.33409	1.99002	43	6.32	0.15372	1.4451	5.32702
14	7.15	0.13926	1.33577	2.13615	44	6.27	0.15455	1.45134	5.388
15	7.14	0.13949	1.33753	2.28079	45	6.22	0.15542	1.45775	5.44515
16	7.12	0.13973	1.33944	2.42381	46	6.16	0.15632	1.46438	5.49823
17	7.11	0.14	1.34151	2.56504	47	6.11	0.15724	1.47123	5.54723
18	7.09	0.14028	1.34367	2.7045	48	6.05	0.1582	1.47826	5.5922
19	7.08	0.14058	1.34599	2.84197	49	5.99	0.15918	1.48549	5.63307
20	7.06	0.1409	1.34837	2.97755	50	5.93	0.1602	1.49297	5.66971
21	7.04	0.14124	1.351	3.11078	51	5.87	0.16126	1.50071	5.702
22	7.02	0.14159	1.35367	3.24197	52	5.81	0.16234	1.5086	5.73032
23	7.00	0.14196	1.35652	3.37075	53	5.73	0.16346	1.5168	5.75408
24	6.98	0.14235	1.35947	3.49713	54	5.66	0.16462	1.5252	5.77375
25	6.95	0.14276	1.36259	3.62103	55	5.59	0.16582	1.53387	5.78897
26	6.93	0.14318	1.36585	3.74231	56	5.51	0.16705	1.54282	5.79974
27	6.91	0.14363	1.36929	3.86082	57	5.43	0.16832	1.552	5.80624
28	6.88	0.1441	1.37284	3.97662	58	5.35	0.16964	1.56145	5.8084
29	6.85	0.14458	1.3765	4.08962	59	5.27	0.17099	1.57122	5.80596

Table G.7 (cont'd): Boundary-Layer Parameters For a Circular Pin Between Parallel Planes for $b=0.2$

θ^0	λ	$\frac{\delta_2}{D}\sqrt{Re_D}$	$\frac{\delta}{D}\sqrt{Re_D}$	$C_f\sqrt{Re_D}$	θ^0	λ	$\frac{\delta_2}{D}\sqrt{Re_D}$	$\frac{\delta}{D}\sqrt{Re_D}$	$C_f\sqrt{Re_D}$
60	5.18	0.17239	1.58127	5.79912	85	1.40	0.22775	1.96737	4.18313
61	5.09	0.17384	1.5916	5.78795	86	1.14	0.23114	1.99083	4.06157
62	4.99	0.17533	1.60226	5.77221	87	0.88	0.23466	2.01526	3.93564
63	4.89	0.17687	1.61325	5.75194	88	0.63	0.23831	2.04065	3.80547
64	4.79	0.17846	1.62456	5.72724	89	0.31	0.24211	2.06718	3.67084
65	4.69	0.18011	1.63623	5.69806	90	0.03	0.24566	2.09204	3.54595
66	4.58	0.1818	1.6482	5.66452	91	-0.32	0.25018	2.12385	3.38834
67	4.468	0.18355	1.66059	5.62636	92	-0.67	0.25445	2.15417	3.2404
68	4.35	0.18537	1.67334	5.58377	93	-1.04	0.25891	2.18604	3.08775
69	4.225	0.18724	1.6865	5.53668	94	-1.42	0.26355	2.21951	2.93044
70	4.095	0.18917	1.70007	5.48511	95	-1.84	0.26839	2.25481	2.76822
71	3.965	0.19117	1.71405	5.42915	96	-2.28	0.27344	2.29207	2.60099
72	3.83	0.19324	1.7285	5.36865	97	-2.51	0.27605	2.31154	2.51539
73	3.68	0.19537	1.74339	5.30378	98	-2.74	0.27871	2.33162	2.4284
74	3.53	0.19758	1.75878	5.23443	99	-3.25	0.28421	2.37365	2.25023
75	3.38	0.19987	1.77465	5.16073	100	-3.79	0.28996	2.41853	2.06602
76	3.22	0.20224	1.79106	5.08261	101	-4.38	0.29596	2.46677	1.87521
77	3.05	0.20469	1.80804	5.00002	102	-5.02	0.30225	2.51887	1.67711
78	2.87	0.20722	1.82556	4.9132	103	-5.71	0.30882	2.5755	1.4708
79	2.69	0.20985	1.84377	4.82175	104	-6.49	0.31571	2.63782	1.2548
80	2.49	0.21257	1.86254	4.72618	105	-7.35	0.32293	2.70725	1.02709
81	2.29	0.21539	1.88202	4.62618	106	-8.32	0.3305	2.78605	0.78462
82	2.08	0.21831	1.90217	4.52194	107	-9.46	0.33845	2.87785	0.52207
83	1.86	0.22134	1.92313	4.41324	108	-11.74	0.35156	3.06565	0.04825
84	1.64	0.22449	1.9448	4.30042					